NASA TECHNICAL NOTE

NASA TN D-8307

PRESSURE DISTRIBUTIONS ON A 1- BY 3-METER SEMISPAN WING AT SWEEP ANGLES FROM 0° TO 40° IN SUBSONIC FLOW

Long P. Yip and Gary L. Shubert

Langley Research Center
Hampton, Va. 23665

NATIONAL AERONAUTICS AND SPACE ADMINISTRATION • WASHINGTON, D. C. • DECEMBER 1976

1. Report No.	2. Government Accession No.	3. Recipient's Catalog No.
NASA TN D-8307		

4. Title and Subtitle	5. Report Date
PRESSURE DISTRIBUTIONS ON A 1- BY 3-METER SEMISPAN WING AT SWEEP ANGLES FROM 0° TO 40° IN SUBSONIC FLOW	December 1976
	6. Performing Organization Code
7. Author(s)	8. Performing Organization Report No.
Long P. Yip and Gary L. Shubert	L-10969
	10. Work Unit No.
9. Performing Organization Name and Address	505-06-15-02
NASA Langley Research Center Hampton, VA 23665	11. Contract or Grant No.
	13. Type of Report and Period Covered
12. Sponsoring Agency Name and Address	Technical Note
National Aeronautics and Space Administration Washington, DC 20546	14. Sponsoring Agency Code

15. Supplementary Notes

Long P. Yip, Langley Research Center, Hampton, Va.
Gary L. Shubert, JIAFS, George Washington University, Hampton, Va.
Comprehensive tables of the pressure data are available on request in a supplement to this report.

16. Abstract

A 1- by 3-meter semispan wing of taper ratio 1.0 with NACA 0012 airfoil section contours has been tested in the Langley V/STOL tunnel to measure the pressure distributions at five sweep angles, 0°, 10°, 20°, 30°, and 40°, through an angle-of-attack range from -6° to 20°. The pressure data are presented as plots of pressure coefficients at each static-pressure tap location on the wing. Flow-visualization wing-tuft photographs are also presented for a wing of 40° sweep. A comparison between theory and experiment using two inviscid theories and a viscous theory shows good agreement for pressure distributions, normal forces, and pitching moments for the wing at 0° sweep.

17. Key Words (Suggested by Author(s))	18. Distribution Statement
Pressure distributions Sweep Subsonic flow Finite wing	Unclassified - Unlimited Subject Category 02

19. Security Classif. (of this report)	20. Security Classif. (of this page)	21. No. of Pages	22. Price*
Unclassified	Unclassified	174	$6.25

*For sale by the National Technical Information Service, Springfield, Virginia 22161

PRESSURE DISTRIBUTIONS ON A 1- BY 3-METER SEMISPAN WING AT SWEEP ANGLES FROM 0° TO 40° IN SUBSONIC FLOW

Long P. Yip and Gary L. Shubert*
Langley Research Center

SUMMARY

A 1- by 3-meter semispan wing of taper ratio 1.0 with NACA 0012 airfoil section contours has been tested in the Langley V/STOL tunnel to measure the pressure distributions at five sweep angles, 0°, 10°, 20°, 30°, and 40°, through an angle-of-attack range from -6° to 20°. The pressure data are presented as plots of pressure coefficients at each static-pressure tap location on the wing. Flow-visualization wing-tuft photographs are also presented for a wing of 40° sweep. A comparison between theory and experiment using two inviscid theories and a viscous theory shows good agreement for pressure distributions, normal forces, and pitching moments for the wing at 0° sweep.

INTRODUCTION

In recent years, there has been an increasing effort to develop methods to compute the flow-field properties of aircraft wings in three-dimensional, subsonic, viscous flow. Several methods have been developed to compute the potential-flow characteristics of an arbitrary wing-body configuration and are being widely utilized by both NASA and industry to design and analyze aircraft wing performance. In addition, other methods are currently under development within NASA and industry to compute the properties of boundary layers in three dimensions. (See refs. 1 to 3.) The next step in the development of a complete three-dimensional viscous-flow method involves the coupling of the potential-flow and boundary-layer methods. Experimental pressure distributions and boundary-layer properties are needed to verify the viscous-flow method. However, relatively little experimental work has been done to measure the boundary-layer properties on three-dimensional wings. One experiment, described in reference 4, provides a data base for boundary-layer flows under infinite swept-wing conditions. In the experiment of reference 4, a pressure gradient was induced on a flat plate to simulate the desired infinite swept-wing conditions, and boundary-layer properties and static pressures were then measured on the flat plate.

The present investigation was undertaken to provide detailed experimental data on finite, three-dimensional wings for validation of new three-dimensional, viscous computational methods. Previous pressure data on wings (see refs. 5 and 6) generally did not provide sufficient information needed in boundary-layer

*Joint Institute for Advancement of Flight Sciences, George Washington University.

computations. This report presents pressure distributions on a 1- by 3-meter semispan wing with a taper ratio of 1.0 at various sweep angles. The semispan pressure wing was tested in the Langley V/STOL tunnel at five different sweep angles (0° to 40°), and through an angle-of-attack range of -6° to 20°. Pressure data were obtained at 600 pressure tap locations with 60 pressure taps distributed on each of 10 chordwise rows. The wing was tested at free-stream dynamic pressures ranging from 0.48 kPa (10 lbf/ft^2) to 2.87 kPa (60 lbf/ft^2). These pressures correspond to a Reynolds number range based on a 1-meter (3.281-ft) chord of 1.92×10^6 to 4.71×10^6. The pressure data are presented as plots of pressure coefficients at each pressure tap location on the wing. Flow visualization using tufts at a wing sweep angle of 40° is shown in photographs.

Comparisons between experimental and theoretical pressures, normal forces, and pitching moments were made. Although tests were conducted at several sweep conditions, only the zero sweep test data were compared with theory because no interpolation was necessary to obtain chordwise pressures. A viscous-flow program as well as two inviscid-flow programs was used. The inviscid programs include the approximate method of reference 7 and the more exact method of reference 8. The approximate method uses a vortex-lattice and a source-lattice scheme on the wing chord plane to represent the perturbation velocities due to lift and thickness. The more exact method uses finite-strength surface singularity distributions to compute the potential-flow velocities. The viscous program of reference 9 was also used in the comparison which is a method based on the modified lifting-line theory (see ref. 10) using viscous two-dimensional section data computed from a program as described in reference 11. This simplified approach accounts for two-dimensional boundary-layer effects on sectional properties.

SYMBOLS

Values are presented in both SI and U.S. Customary Units. Values were obtained in U.S. Customary Units. Second symbol denotes computer printout symbol. The coefficients and symbols are defined as follows:

A aspect ratio, b^2/S

b span, m (ft)

C_m total pitching-moment coefficient about leading edge

C_N total normal-force coefficient, $\int_0^1 c_n \, d\eta$

C_p,CP pressure coefficient, $\frac{p - p_\infty}{q_\infty}$

c,C chord normal to leading edge, m (ft)

c_m section pitching-moment coefficient about leading edge

c_n section normal-force coefficient, $\int_0^1 (C_{p,\ell} - C_{p,u})\, d\left(\frac{x}{c}\right)$

p local static pressure, kPa (lbf/ft^2)

p_∞ free-stream static pressure, kPa (lbf/ft^2)

q_∞ free-stream dynamic pressure, kPa (lbf/ft^2)

S wing area, m^2 (ft^2)

U_∞ free-stream velocity, m/sec (ft/sec)

x,X distance in chordwise direction, m (ft)

y,Y distance in spanwise direction, m (ft)

z,Z normal distance from x,y plane, m (ft)

α geometric angle of attack, deg

α_i induced local angle of attack, deg

η semispan location, $\frac{y}{b/2}$

Λ sweep angle, deg

$\sqrt{\ },SQRT$ square root

Subscripts:

ℓ,L lower surface

u,U upper surface

MODEL DESCRIPTION

A semispan pressure wing of taper ratio 1.0 was constructed with NACA 0012 airfoil section contours. The NACA 0012 airfoil section was selected because of its good low- and high-speed performance characteristics and because of the availability of additional test data over a wide range of test conditions. (See refs. 12 to 14.) Coordinates of the NACA 0012 airfoil are given in reference 12 and are also presented in table I as pressure tap locations. A schematic drawing of the model and support system is shown in figure 1. The range of sweep angles, 0° to 40°, was made possible by the movement in the pitch mechanisms of the model support system with the addition of one of the two wedge blocks (i.e., 12° or 33°) at the wing root. The wing slot inserts prevented flow through the reflection plate. The wing tips were kept parallel to the free-stream flow as

the wing was swept by attaching an appropriate wing-tip fairing. These tip fairings did not contain static-pressure taps.

To insure sufficient available data, 60 pressure orifices were installed in each of 10 chordwise stations making a total of 600. The spanwise distributions of the pressure taps are presented in table II and were determined by the following equation for $\Lambda = 0^{\circ}$:

$$\eta = 0.05 + 0.95 \cos\left[\frac{\pi(10 - k)}{20}\right] \qquad (0 \leq k \leq 9)$$

where k is the station number starting near the wing root. This distribution allowed for a concentration of pressure taps in the outboard section of the wing where the pressure gradients are the largest. Values of wing span and aspect ratio for the wing at different sweep angles are presented in table III.

A circular reflection plate with a diameter of 3.05 meters (10 ft) was designed to simulate a full-span wing and to move the semispan model away from the tunnel-wall boundary layer and the model support system.

The model was fabricated by covering a solid aluminum spar with a fiber glass skin. The pressure tubings were embedded in the fiber glass skin and routed to a set of scanivalves attached to the sting mount below the reflection plate. A photograph of the model mounted in the Langley V/STOL tunnel at 30° sweep is shown in figure 2.

TESTS AND CORRECTIONS

The investigation was conducted in the Langley V/STOL tunnel over a range of free-stream dynamic pressures of 0.48 kPa (10 lbf/ft^2) to 2.87 kPa (60 lbf/ft^2). This pressure range corresponds to a Reynolds number range based on a wing chord of 1 meter (3.281 ft) from 1.92×10^6 to 4.71×10^6 at Mach numbers 0.08 to 0.20, respectively. Pressure measurements were obtained through an angle-of-attack range from approximately -6° to 20° for each of the five sweep conditions, 0°, 10°, 20°, 30°, and 40°. A transition strip consisting of No. 80 carborundum grit was installed on the upper and lower surfaces at 0.05x/c. The grit size was selected according to reference 15.

A correction due to the blockage effects of the model and support systems was applied to the free-stream dynamic pressure by using the method described in reference 16. A correction due to the jet-boundary effects was applied to the angle of attack by using the method described in reference 17. In addition, a correction due to flow angularity of the wind tunnel and the misalinement of the model in the tunnel was applied to the angle of attack. The flow-angularity correction was obtained by plotting and matching the upper and lower surface c_n obtained from a pressure integration at the indicated angle of attack for 0° sweep. The angle correction is the offset angle from 0° to the intersection of the upper and lower surface c_n curves because the NACA 0012 airfoil is a symmetric section.

The normal forces were obtained by integrating the surface pressures. The section pitching moments were computed by using the following summation equation:

$$c_m = \sum_{i=1}^{n-1} \left[\frac{\left(x_{i+1}^2 - x_i^2\right) + \left(z_{i+1}^2 - z_i^2\right)}{c^2} \right] \left(\frac{C_{p,i+1} + C_{p,i}}{4} \right)$$

where n is the number of pressure taps per station and i is the ith pressure tap. This moment equation accounts for the moment contribution along the Z-axis in addition to the moments computed along the X-axis.

PRESENTATION OF RESULTS

The pressure data are presented as plots of pressure coefficient against the square root of x/c locations. Plotting the pressures against the square root of x/c instead of against x/c has the effect of spreading the nose pressure distribution. The data are presented as indicated in the following table:

Type of data	Sweep angle, deg	α, deg	q_∞, kPa (lbf/ft^2)	Figure
Pressure distribution	0	-5.71 to 19.55	1.47 (30.8)	3
	10	-5.69 to 21.38	2.46 (51.3)	4
	20	-5.67 to 17.42	2.46 (51.3)	5
	30	-5.88 to 21.07	1.47 (30.8)	6
	40	-7.92 to 19.08	1.47 (30.8)	7
Flow visualization	40	0.39 to 19.08	1.68 (35.0)	8

Data points that were in obvious error due to instrumentation malfunction or tube blockage were corrected by linear interpolation between the adjacent values. These modified data points are indicated by a flag on the plotted data symbol. Comprehensive tables of the pressure data are available in a "Supplement to NASA TN D-8307," which is available on request.*

*Supplement to NASA TN D-8307 may be obtained on request from

Long P. Yip
Low-Speed Aerodynamics Branch
Subsonic-Transonic Aerodynamics Division
Langley Research Center
Hampton, VA 23665

RESULTS AND DISCUSSION

In each figure of the pressure plots (figs. 3 to 7), a sketch is provided near the upper left-hand corner to illustrate the sweep of the wing and the relative location of the rows of pressure stations. In general, all configurations show that sufficient data were taken to insure full definition of the pressure distribution. However, as the wing is swept beyond 10°, a number of pressure taps are lost into the reflection plate, which accounts for the blank data near the trailing edge of pressure station 0 for sweeps of 20°, 30°, and 40°. In figure 3, a tip vortex flow is in evidence at pressure station 9 as a pressure bubble near the trailing edge which starts to develop at an angle of attack of 4.65°. However, at the other sweep conditions (figs. 4 to 7), there is no evidence of tip vortex flow because there were no pressure orifices in the tip fairings.

Flow visualization using tufts on a wing at 40° sweep is shown in figure 8. These photographs show the movement of the surface streamlines as a function of angle of attack at 40° sweep. At low angles of attack, the tufts are alined with the free stream. As angle of attack is increased, spanwise flow and tip vortex flow become more noticeable, particularly near the trailing edge. At an angle of attack of 17°, the spanwise flow is predominant, and some of the tufts near the outboard region begin to fluctuate and indicate near-stall conditions. At an angle of attack of 19°, the flow has separated in the outboard region of the wing and the wing has stalled.

Pressure data were obtained over a range of free-stream dynamic pressures from approximately 0.48 kPa (10 lbf/ft^2) to 2.87 kPa (60 lbf/ft^2) which corresponds to a Reynolds number based on a chord of 1 meter (3.281 ft) of 1.92×10^6 to 4.71×10^6. The effects of Reynolds number are shown in figure 9 in the form of a plot of C_N against α. At the lower q_∞ condition, values of C_N are consistently lower at each α, and the stall begins at a lower α than for the higher q_∞ values. The pressure data presented in this report were obtained at q_∞ settings equal to or higher than 1.44 kPa (30.1 lbf/ft^2).

As mentioned previously, only data at 0° sweep angle were compared with theoretical predictions. Viscous predictions as well as inviscid predictions of normal force, pitching moments, and pressures are used in comparisons with experimental data.

An inviscid theory described in reference 7 was used to compute the potential-flow pressure coefficients on the wing surfaces. This theory uses a vortex-lattice-type singularity to represent the perturbation velocities due to lift and a source singularity to represent the perturbation velocities due to thickness. This theoretical method is one of many such linearized methods that use singularities on the wing chord plane to obtain the inviscid three-dimensional flow properties. Another prediction method for computing potential flow (ref. 8) was used for comparison with experimental results. This method uses finite-strength surface singularity distributions to compute the potential-flow velocities.

A simplified viscous method (ref. 9) was used to analyze the results on the unswept wing. This method accounts for the two-dimensional boundary-layer

effects on section properties. Viscous airfoil properties are used in a modified lifting-line theory (ref. 10) to obtain the span loading and induced angles of attack at various spanwise locations. Pressure coefficients were obtained from the viscous, two-dimensional airfoil computer program (ref. 11) by using the effective angle of attack. This simplified method is applicable to unswept wings with varying taper ratio.

In figure 10, a comparison of total normal force against angle of attack is made between theory and experiment. Predictions for inviscid theories as well as the viscous theory were in good agreement with the experimental results. In the viscous theory, the addition of boundary-layer displacement causes an overprediction of normal force due to increased thickness, but this overprediction is offset because the displacement thickness reduces the effective wing camber near the trailing edge. (See ref. 18.) The predictions of the surface singularity method of reference 8 also show good agreement with experiment at angles of attack up to 15°. At this angle of attack, viscous effects become noticeable. The values of normal forces predicted by the two inviscid theories are similar, even though the method of reference 7 does not use the contributions from source singularities in this computation.

In figure 11, a comparison of the span-load distributions at an angle of attack of 6.75° is made between theory and experiment. The experimental values of section normal force c_n, normalized by total normal force C_N, are plotted against the semispan location. Both inviscid and viscous theories agree well with experiment except near the root and tip locations of the wing. Near the root, the experimental section normal force is decreased by the partial effectiveness of the reflection plate. This result indicates that the reflection plate was not large enough to fully reflect the properties of a full-span wing. At the wing tip, the experimental section normal force is increased by the influence of the tip vortex flow.

In figure 12, a comparison of section normal force at the effective angle of attack $(\alpha - \alpha_i)$ is made between theory and experiment for several values of η. The section normal forces derived from the experimental pressures are plotted against the effective angle of attack predicted by the method of reference 9. A two-dimensional theoretical curve predicted by the two-dimensional airfoil program of reference 11 is plotted for comparison. The experimental data begin to deviate from theory in the outboard wing-tip region of the wing. This result is consistent with the results in the span-load comparison between theory and experiment.

In figure 13, a comparison of the total pitching moment about the leading edge against angle of attack is made between theory and experiment. Better agreement is obtained for the inviscid predictions than for the viscous predictions which are slightly more negative than the experimental results. A study of the section pitching moments c_m (fig. 14) shows that the experimental value strongly deviates from theory only near the wing tip.

In figure 15, a comparison of pressure coefficients against the $\sqrt{x/c}$ at several η stations is made between theory and experiment. Plotting the pressure against the square root of x/c expands the region near the leading edge for a more detailed look at the nose region. The comparisons indicate generally

good agreement between theory and experiment. However, near the nose region, the inviscid chord-plane singularity method overpredicted the leading-edge pressure peak. The inviscid surface singularity method and viscous method predicted the leading-edge pressures with more accuracy. Two sets of experimental values at different free-stream dynamic pressures were plotted on the same figure. The experimental values of C_p were in good agreement with each other at the two values of free-stream dynamic pressure. Both sets of experimental pressure coefficients show disagreement with theory near the reflection plate and near the tip stations. However, good agreement between theory and experiment was obtained at the midpanel stations.

CONCLUDING REMARKS

Pressure data were obtained on a 1- by 3-meter semispan wing through an angle-of-attack range of about -6° to 20° for each of the sweep angles, 0°, 10°, 20°, 30°, and 40°. Values of pressure coefficients, normal forces, and pitching moments obtained from two inviscid theories and one viscous theory compared well with the experimental results. Disagreement between theory and experiment occurred generally at sections of the wing near the root and near the tip. A reduction in wing loading near the reflection plate indicates that the sizing of the reflection plate was inadequate to simulate the full-span wing properties. At the wing tip, the tip vortex was not accounted for in theory which caused disagreement between theory and experiment. In the midpanel stations, however, very good agreement was obtained between theory and experiment.

All theories predicted very good results for the normal force. However, in the pressure coefficient comparison, the surface singularity method and the viscous theory gave a better definition of the pressures near the leading-edge nose than did the chord-plane singularity method.

Langley Research Center
National Aeronautics and Space Administration
Hampton, VA 23665
October 13, 1976

REFERENCES

1. Harris, Julius E.: Calculation of Three-Dimensional Compressible Laminar and Turbulent Boundary Layers. Aerodynamic Analyses Requiring Advanced Computers, Pt. I, NASA SP-347, 1975, pp. 17-18.

2. Harris, Julius E.: Calculation of Three-Dimensional Compressible Laminar and Turbulent Boundary Layers - An Implicit Finite-Difference Procedure for Solving the Three-Dimensional Compressible Laminar, Transitional, and Turbulent Boundary-Layer Equations. Aerodynamic Analyses Requiring Advanced Computers, Pt. I, NASA SP-347, 1975, pp. 19-40.

3. Cebeci, Tuncer; Kaups, Kalle; Ramsey, Judy; and Moser, Alfred: Calculation of Three-Dimensional Compressible Laminar and Turbulent Boundary Layers - Calculation of Three-Dimensional Compressible Boundary Layers on Arbitrary Wings. Aerodynamic Analyses Requiring Advanced Computers, Pt. I, NASA SP-347, 1975, pp. 41-76.

4. Van den Berg, B.; and Elsenaar, A.: Measurements in a Three-Dimensional Incompressible Turbulent Boundary Layer in an Adverse Pressure Gradient Under Infinite Swept Wing Conditions. NRL TR 72092, Nat. Lucht-Ruimtevaartlab. (Amsterdam), Aug. 15, 1972.

5. Lamar, John E.; and McKinney, L. Wayne: Low-Speed Static Wind-Tunnel Investigation of a Half-Span Fuselage and Variable-Sweep Pressure Wing Model. NASA TN D-6215, 1971.

6. Henderson, William P.: Pressure Distributions on a Cambered Wing-Body Configuration at Subsonic Mach Numbers. NASA TN D-7946, 1975.

7. Tulinius, J.; Clever, W.; Niemann, A.; Dunn, K.; and Gaither, B.: Theoretical Prediction of Airplane Stability Derivatives at Subcritical Speeds. NASA CR-132681, 1975.

8. Hess, John L.: Calculation of Potential Flow About Arbitrary Three-Dimensional Lifting Bodies. Rep. No. MDC J5679-01 (Contract N00019-71-C-0524), Naval Air Systems Command, Oct. 1972.

9. McVeigh, M. A.; and Kisielowski, E.: A Design Summary of Stall Characteristics of Straight Wing Aircraft. NASA CR-1646, 1971.

10. Sivells, James C.; and Neely, Robert H.: Method for Calculating Wing Characteristics by Lifting-Line Theory Using Nonlinear Section Lift Data. NACA Rep. 865, 1947. (Supersedes NACA TN 1269.)

11. Stevens, W. A.; Goradia, S. H.; and Braden, J. A.: Mathematical Model for Two-Dimensional Multi-Component Airfoils in Viscous Flow. NASA CR-1843, 1971.

12. Abbott, Ira H.; and Von Doenhoff, Albert E.: Theory of Wing Sections. Dover Publ., Inc., c.1959.

13. Gregory, N.; and Wilby, P. G.: NPL 9615 and NACA 0012 - A Comparison of Aerodynamic Data. C.P. No. 1261, Brit. A.R.C., 1973.

14. Gregory, N.; and O'Reilly, C. L.: Low-Speed Aerodynamic Characteristics of NACA 0012 Aerofoil Section, Including the Effects of Upper-Surface Roughness Simulating Hoar Frost. R. & M. No. 3726, Brit. A.R.C., 1973.

15. Braslow, Albert L.; and Knox, Eugene C.: Simplified Method for Determination of Critical Height of Distributed Roughness Particles for Boundary-Layer Transition at Mach Numbers From 0 to 5. NACA TN 4363, 1958.

16. Herriot, John G.: Blockage Corrections for Three-Dimensional-Flow Closed-Throat Wind Tunnels, With Consideration of the Effect of Compressibility. NACA Rep. 995, 1950. (Supersedes NACA RM A7B28.)

17. Polhamus, Edward C.: Jet-Boundary-Induced-Upwash Velocities for Swept Reflection-Plane Models Mounted Vertically in 7- by 10-Foot, Closed, Rectangular Wind Tunnels. NACA TN 1752, 1948.

18. Margason, Richard J.; and Morgan, Harry L., Jr.: High-Lift Aerodynamics - Trends, Trades, and Options. AGARD-CP-160, Take-Off and Landing, Apr. 1974, pp. 1-1 - 1-11.

TABLE I.- CHORDWISE LOCATION OF STATIC-PRESSURE TAPS

x/c	z/c for -	
	Upper surface	Lower surface
0	0	0
.001938	.007786	-.007786
.005101	.012371	-.012371
.008412	.015751	-.015751
.012003	.018643	-.018643
.015533	.021081	-.021081
.020164	.023692	-.023692
.026691	.026927	-.026927
.043449	.033474	-.033474
.068029	.040393	-.040393
.096415	.046215	-.046215
.127694	.050912	-.050912
.161629	.054573	-.054573
.197963	.057260	-.057260
.236335	.059018	-.059018
.276981	.059893	-.059893
.319422	.059933	-.059933
.363751	.059168	-.059168
.410335	.057631	-.057631
.458507	.055365	-.055365
.508984	.052366	-.052366
.561119	.048693	-.048693
.615491	.044342	-.044342
.671552	.039352	-.039352
.728190	.033838	-.033838
.785998	.027770	-.027770
.843881	.021246	-.021246
.900483	.014420	-.014420
.956240	.007242	-.007242
.99619	.001793	-.001793
1.0000	0	0

TABLE II.- SPANWISE LOCATION OF PRESSURE ROWS

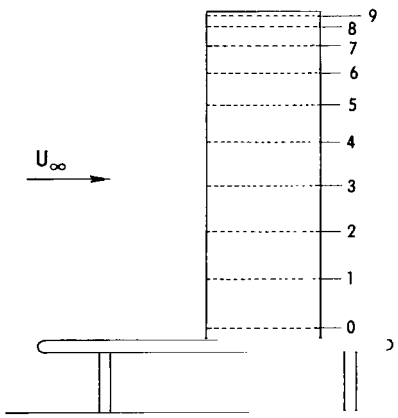

Pressure station	$\eta(\Lambda = 0^\circ)$
0	0.05
1	.1986
2	.3436
3	.4813
4	.6084
5	.7218
6	.8186
7	.8965
8	.9539
9	.9883

TABLE III.- WING SPAN AND ASPECT RATIO FOR WING PLANFORM AT DIFFERENT SWEEP ANGLES

Sweep, deg	b/2, m	Aspect ratio, A
0	2.95	5.90
10	2.98	5.87
20	2.91	5.47
30	2.83	4.90
40	2.53	3.88

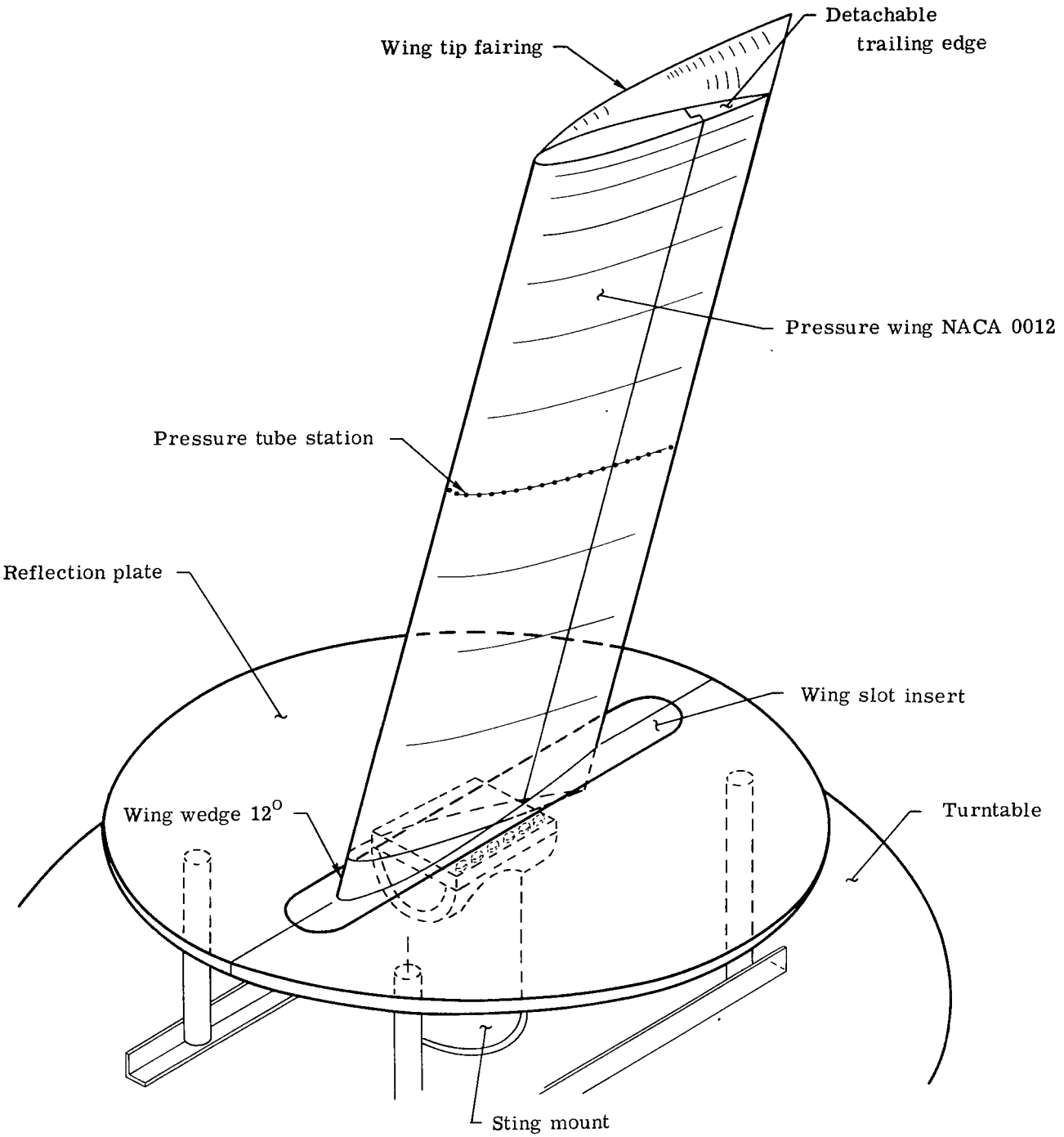

Figure 1.- Schematic drawing of semispan pressure wing model.

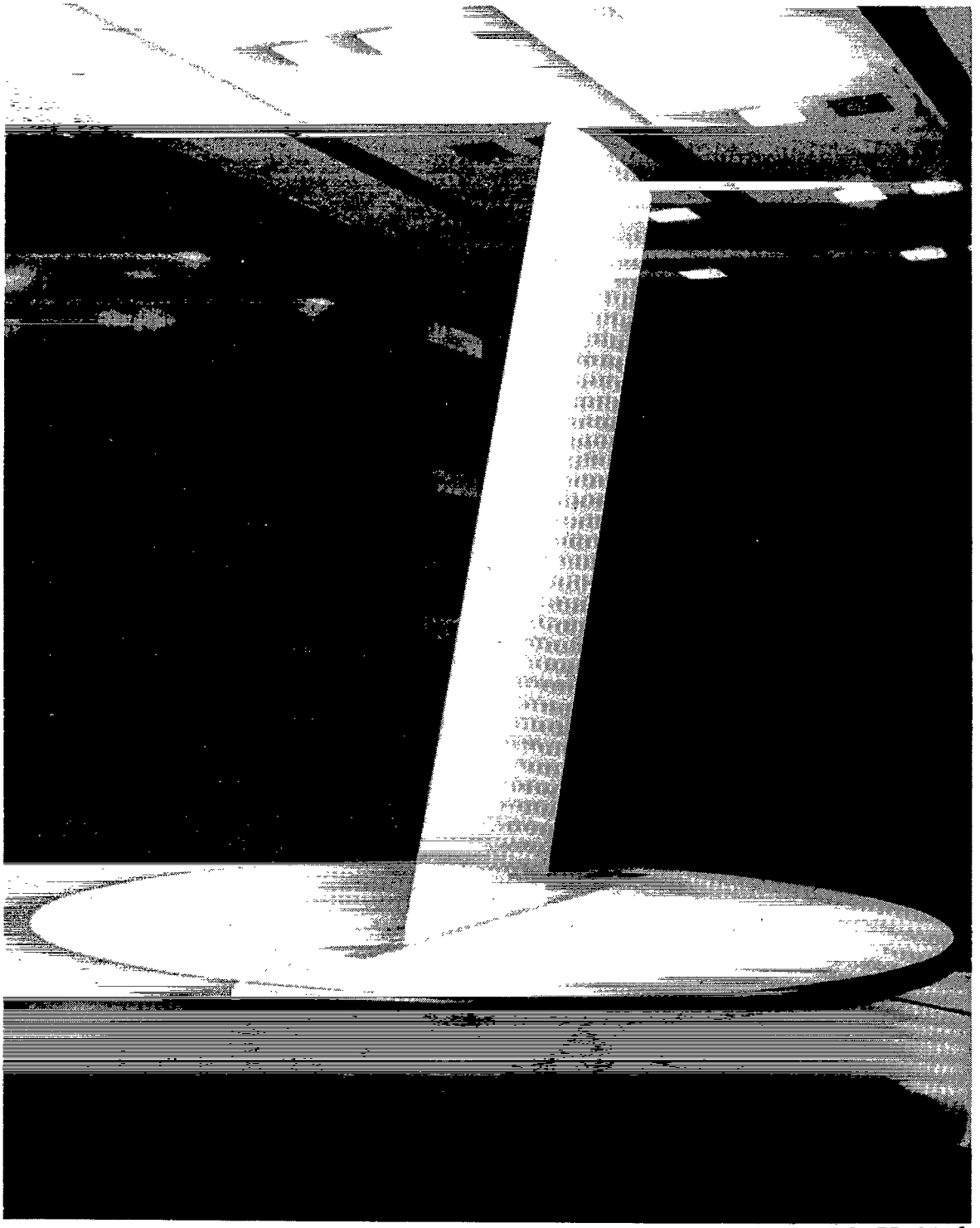

L-75-3706

Figure 2.- Photograph of 1- by 3-meter semispan model at 30° sweep in the Langley V/STOL tunnel.

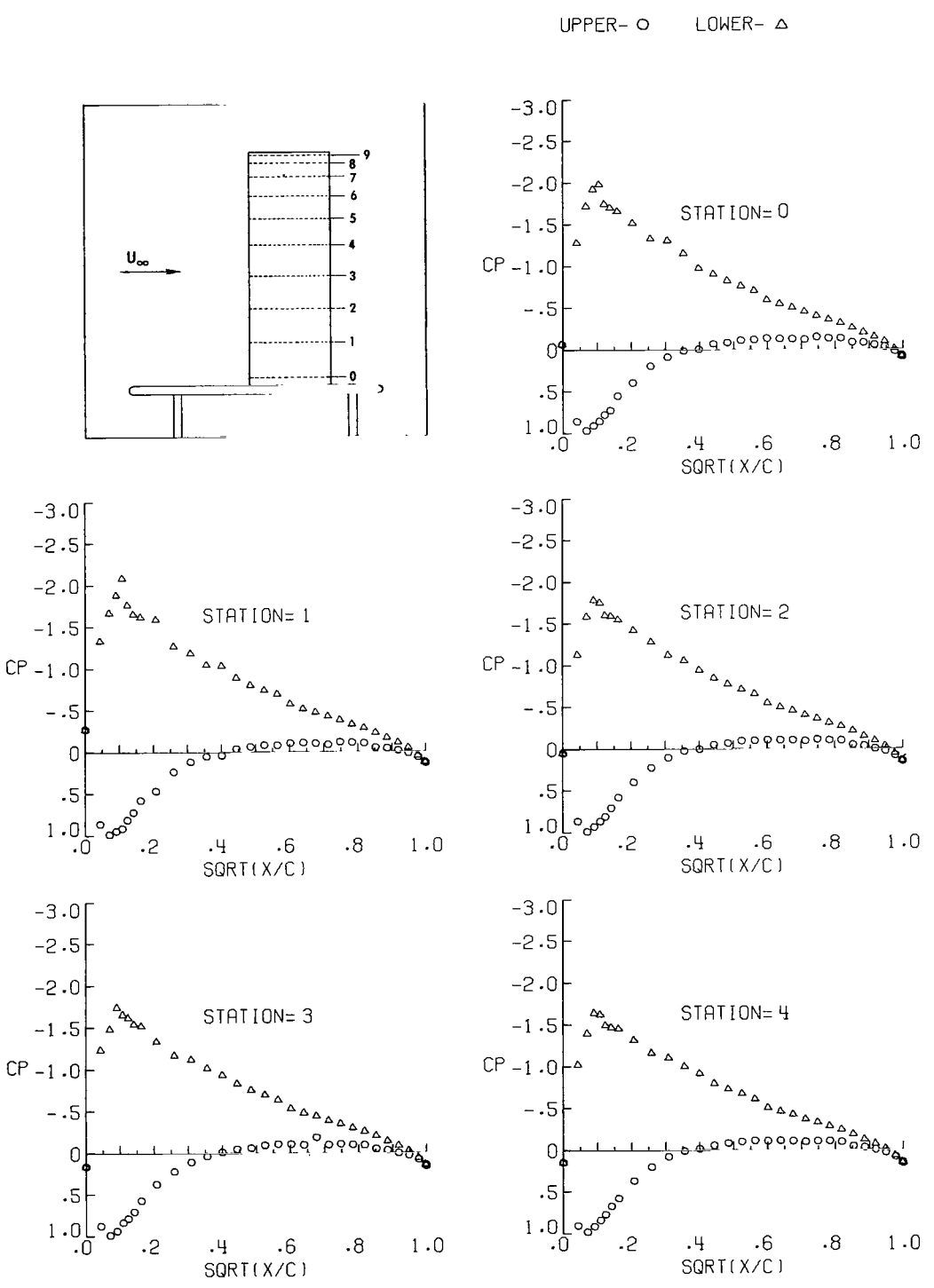

(a) α = -5.91°; q_∞ = 1.48 kPa (30.84 lb/ft^2).

Figure 3.- Pressure distributions at sweep angle of 0°.

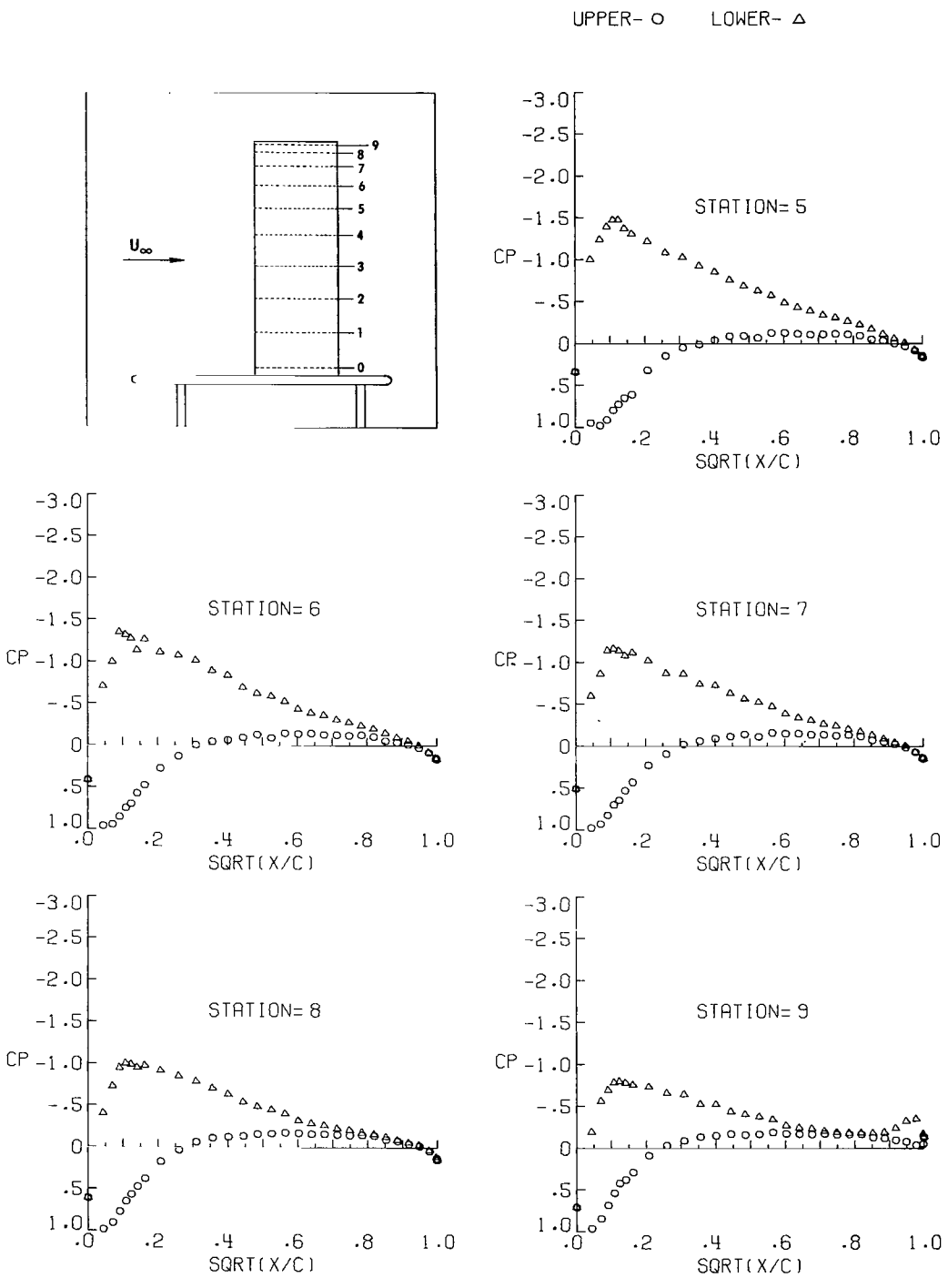

(a) Concluded.

Figure 3.- Continued.

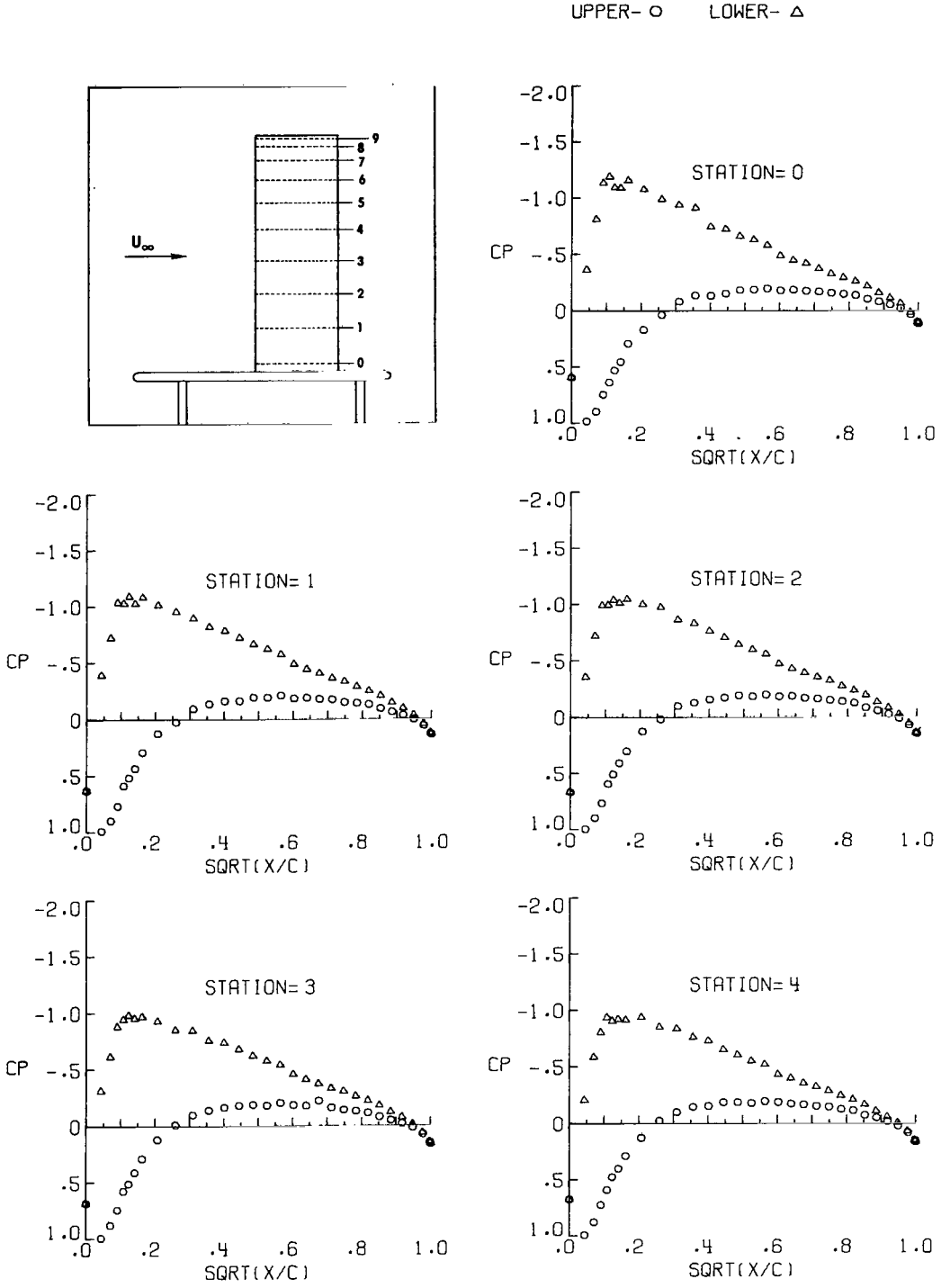

(b) $\alpha = -3.78^{\circ}$; $q_\infty = 1.48$ kPa (30.87 lb/ft^2).

Figure 3.- Continued.

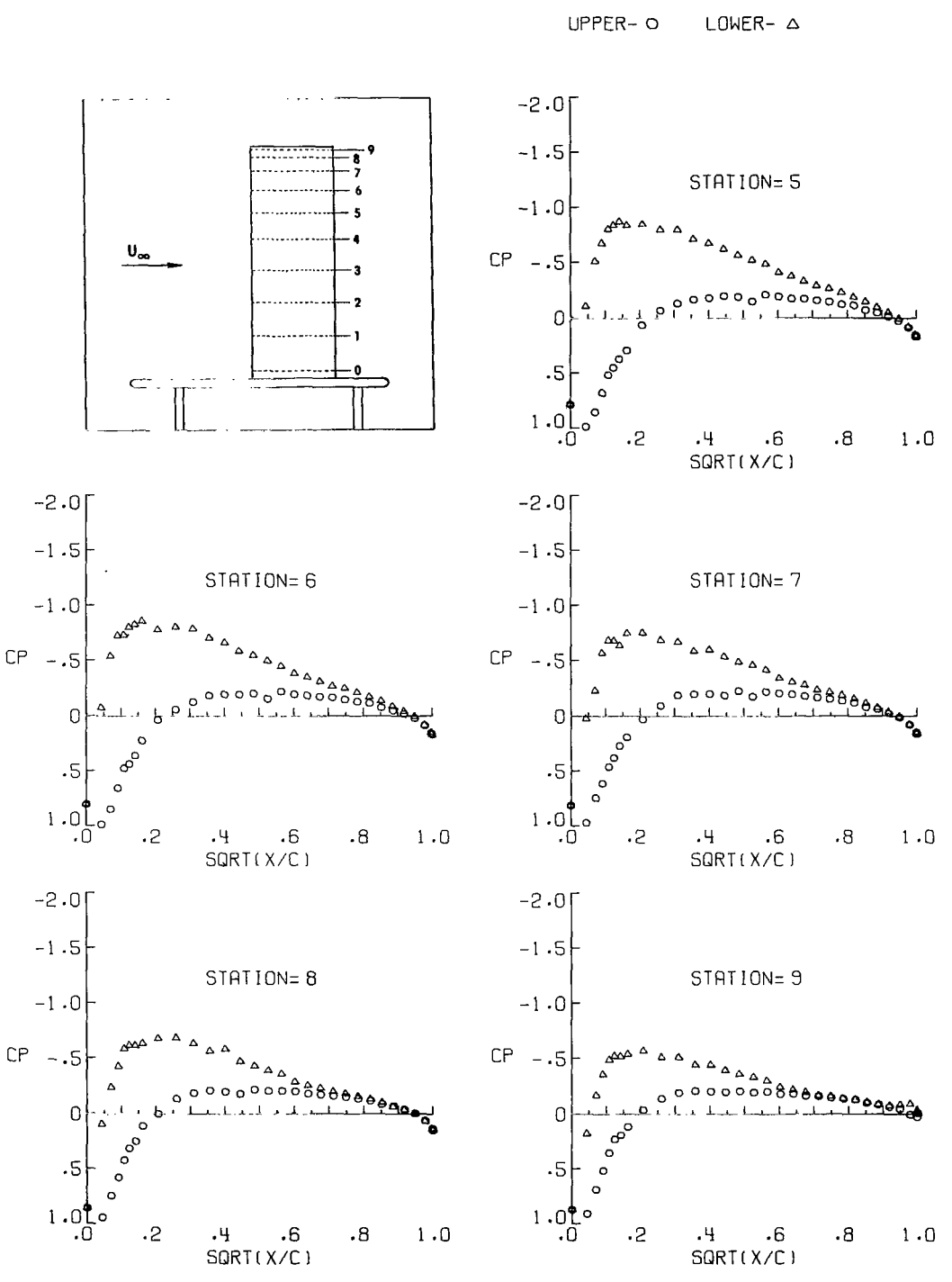

(b) Concluded.

Figure 3.- Continued.

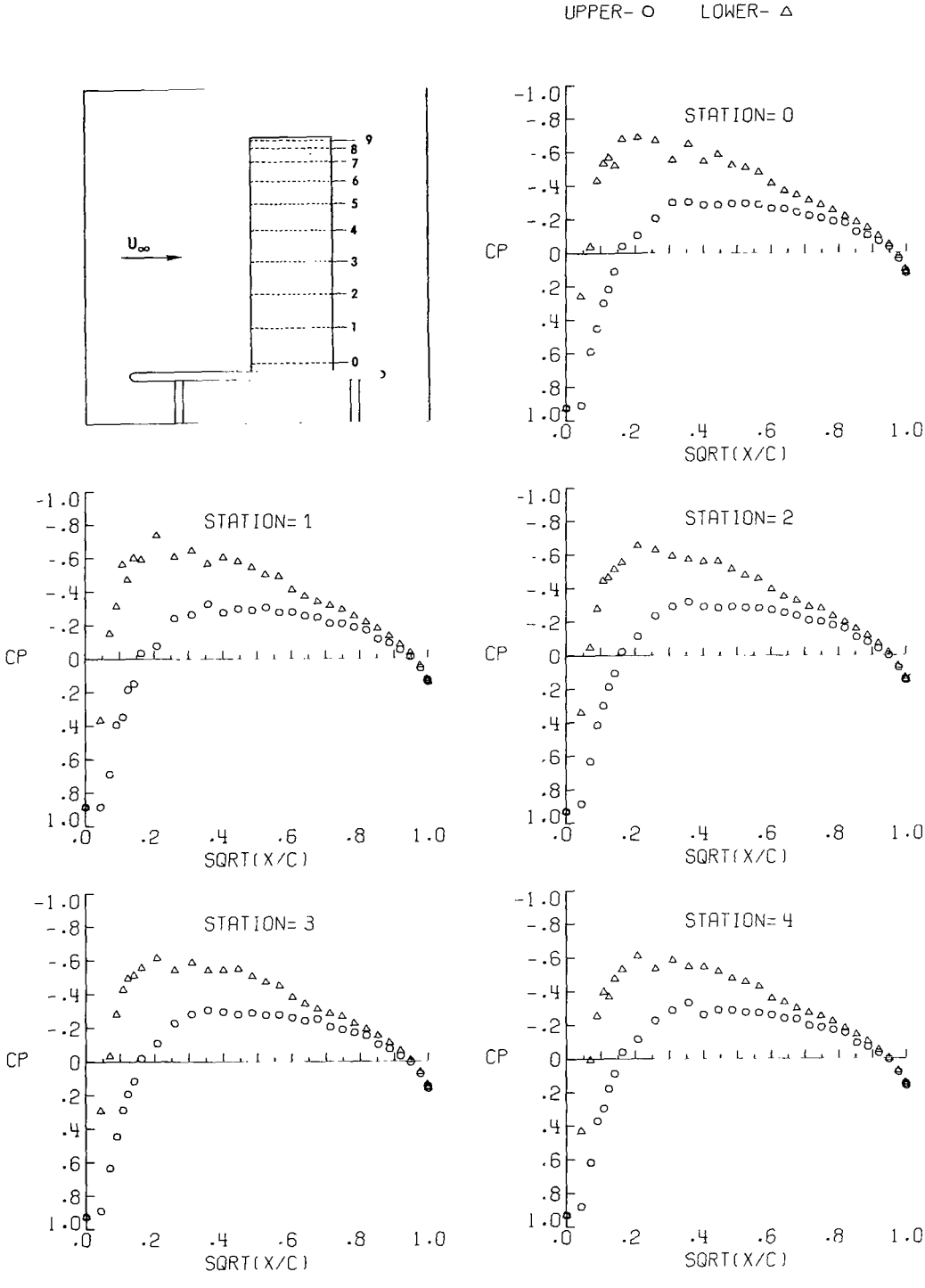

(c) α ▫ -1.69^{o}; q_∞ = 1.47 kPa (30.66 lb/ft^2).

Figure 3.- Continued.

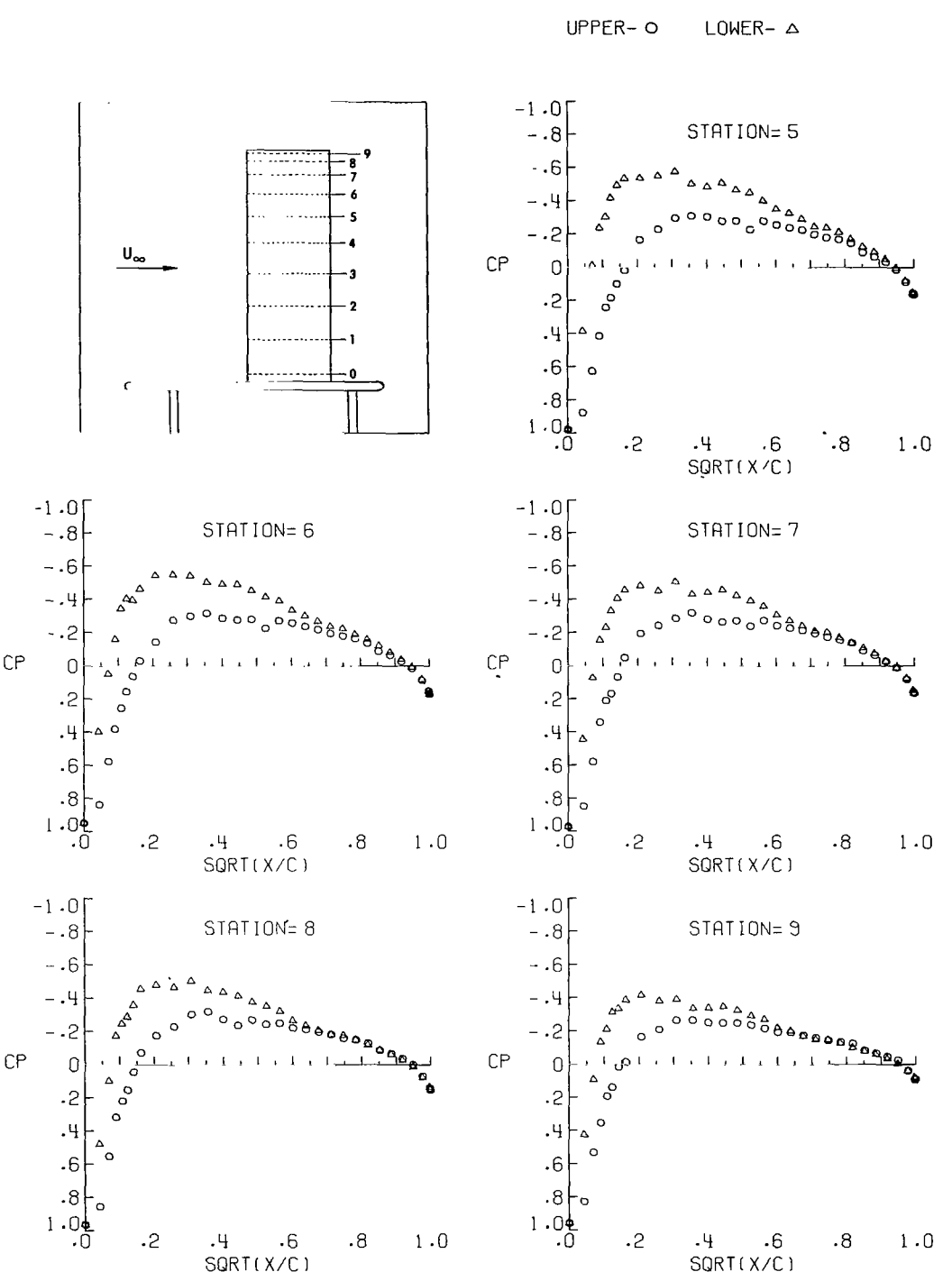

(c) Concluded.

Figure 3.- Continued.

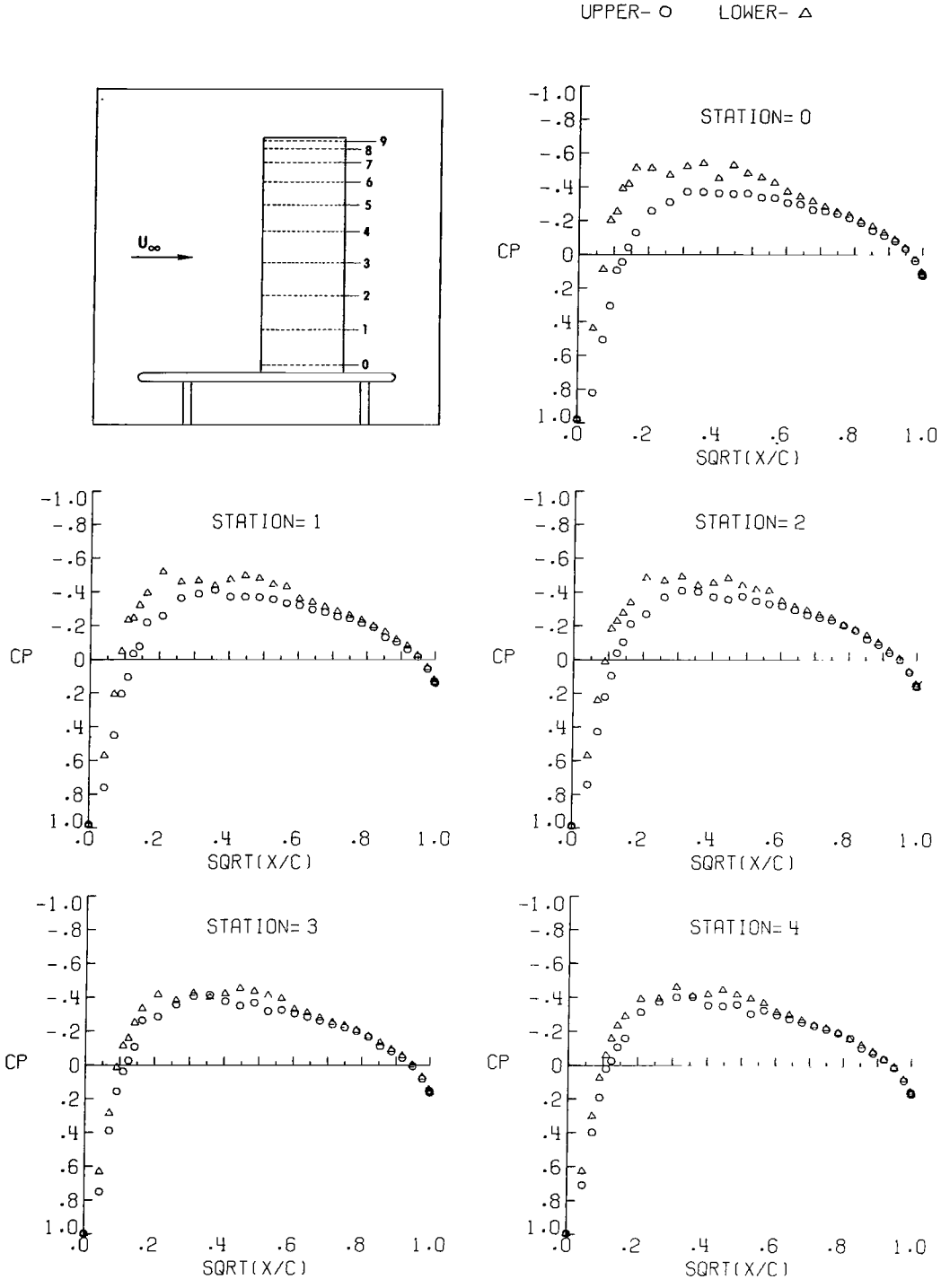

(d) $\alpha = -0.62^{\circ}$; $q_\infty = 1.47$ kPa (30.78 lb/ft^2).

Figure 3.- Continued.

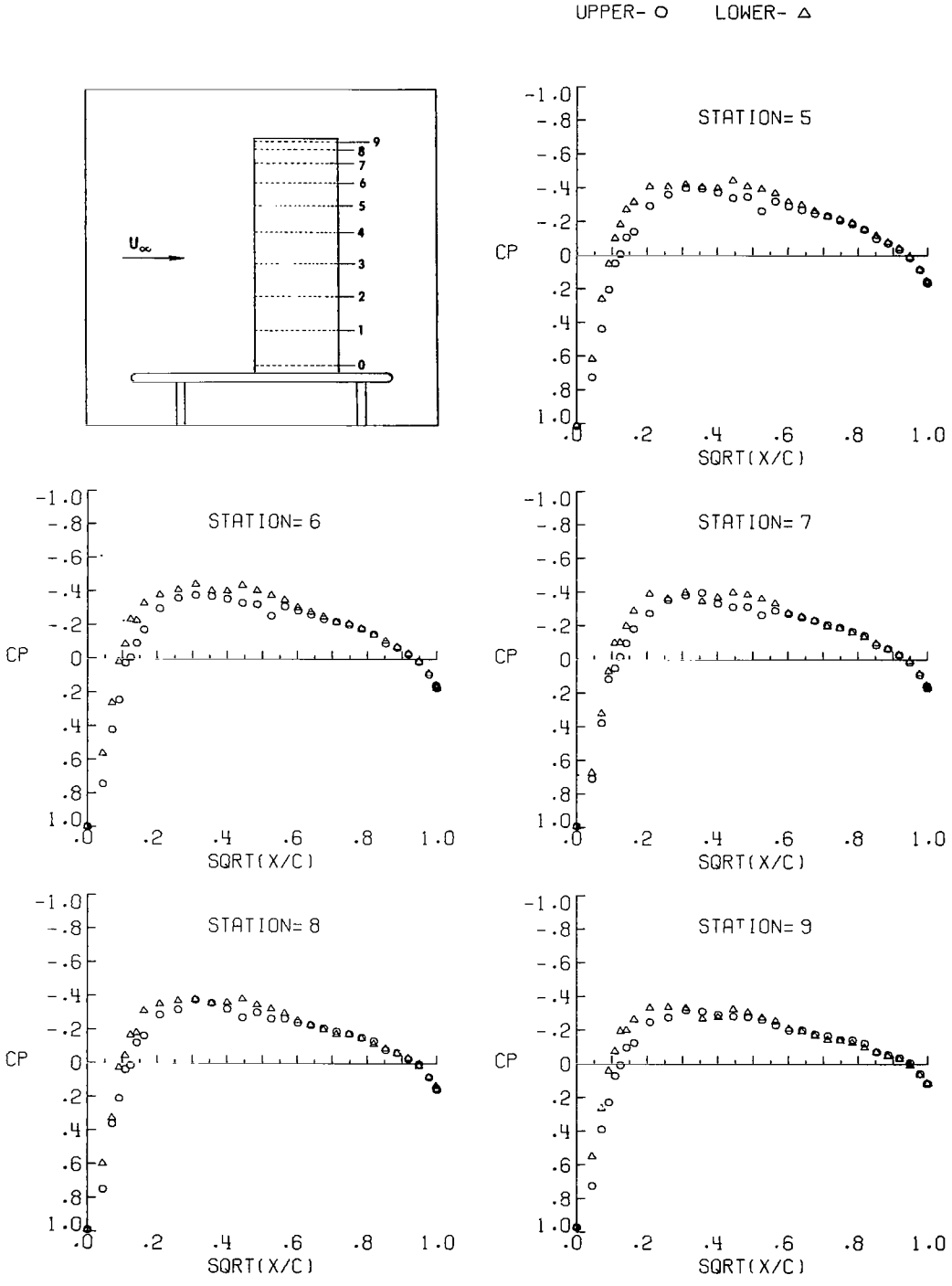

(d) Concluded.

Figure 3.- Continued.

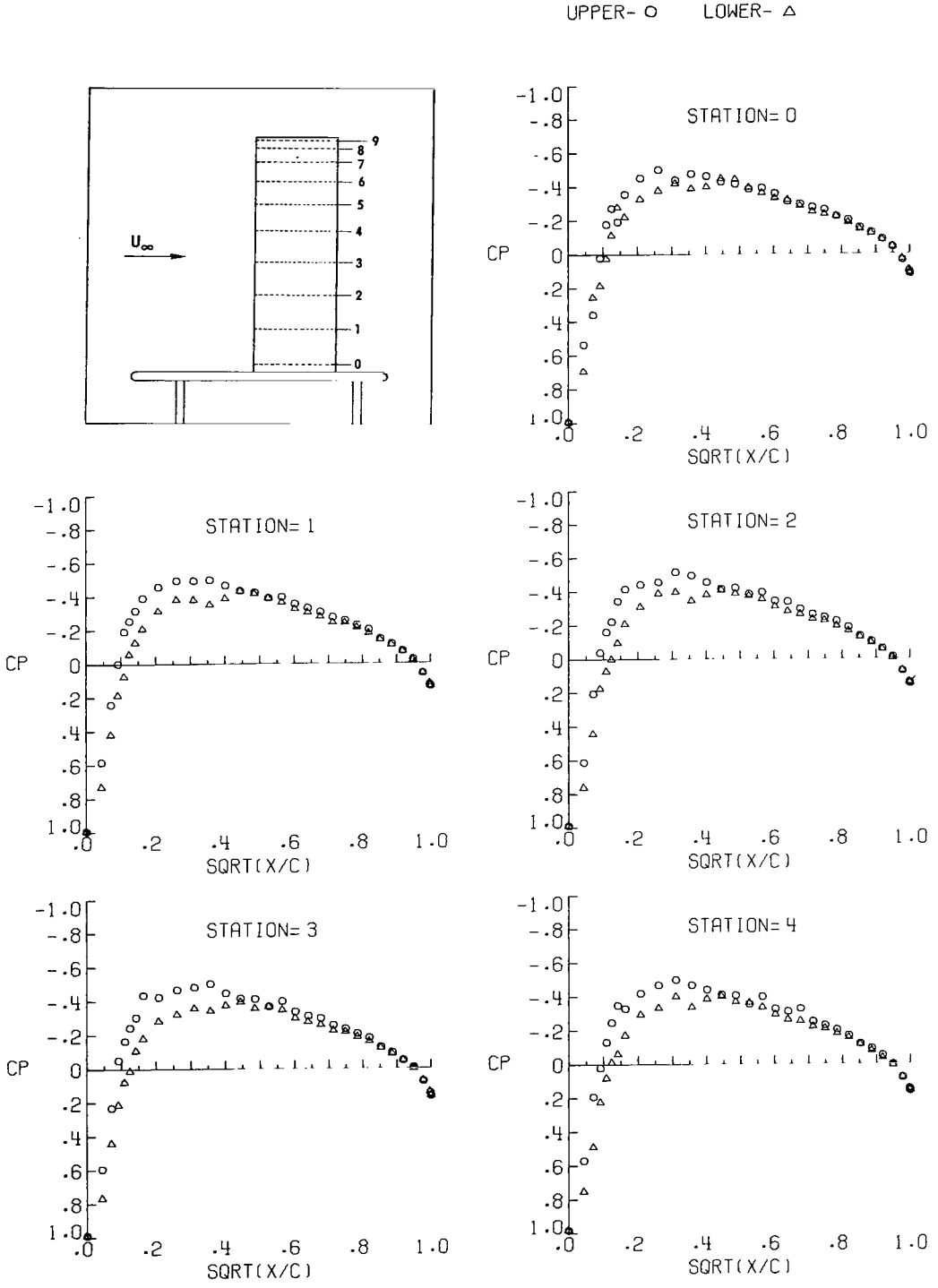

(e) α = 0.42°; q_∞ = 1.47 kPa (30.76 lb/ft^2).

Figure 3.- Continued.

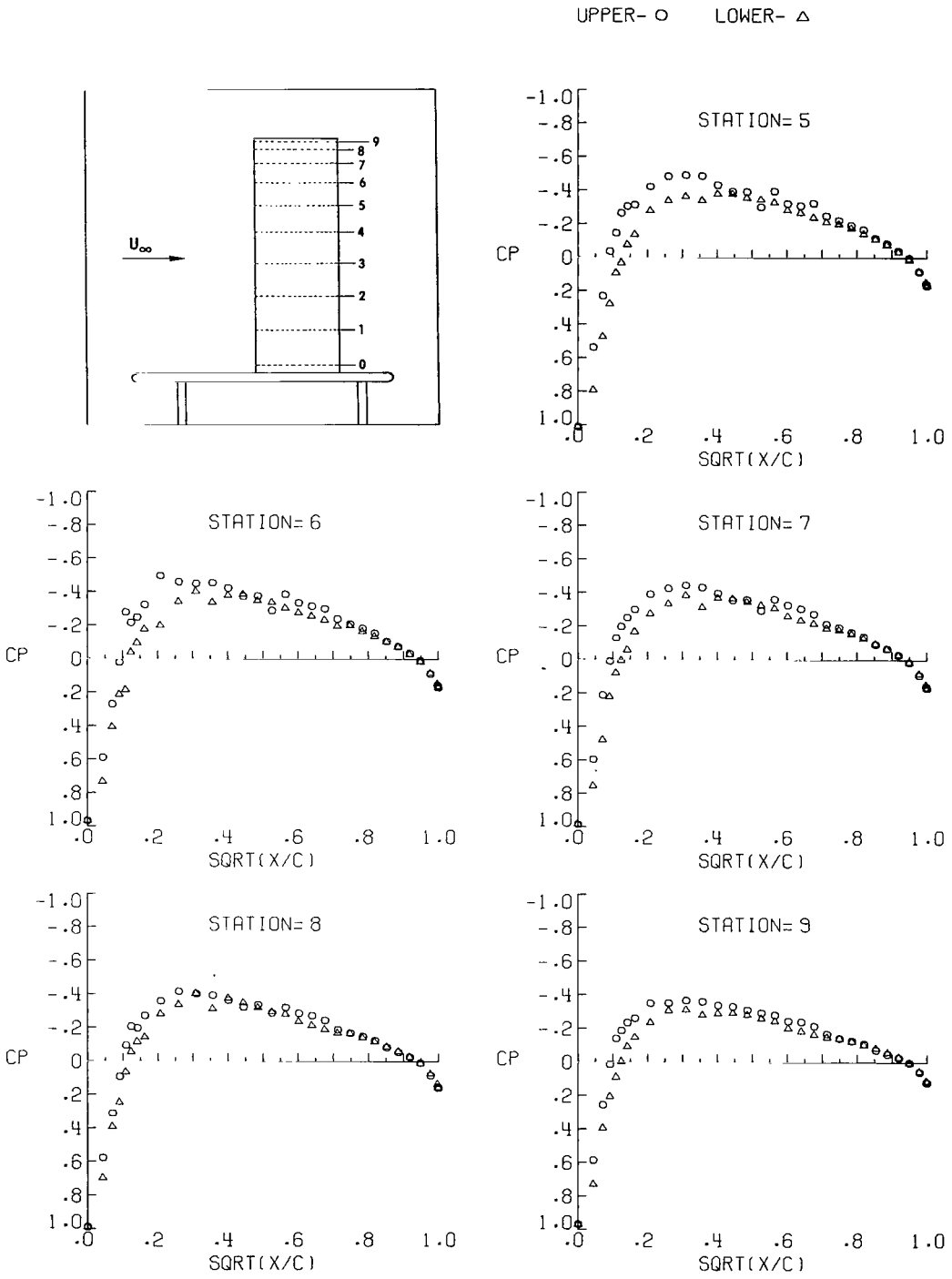

(e) Concluded.

Figure 3.- Continued.

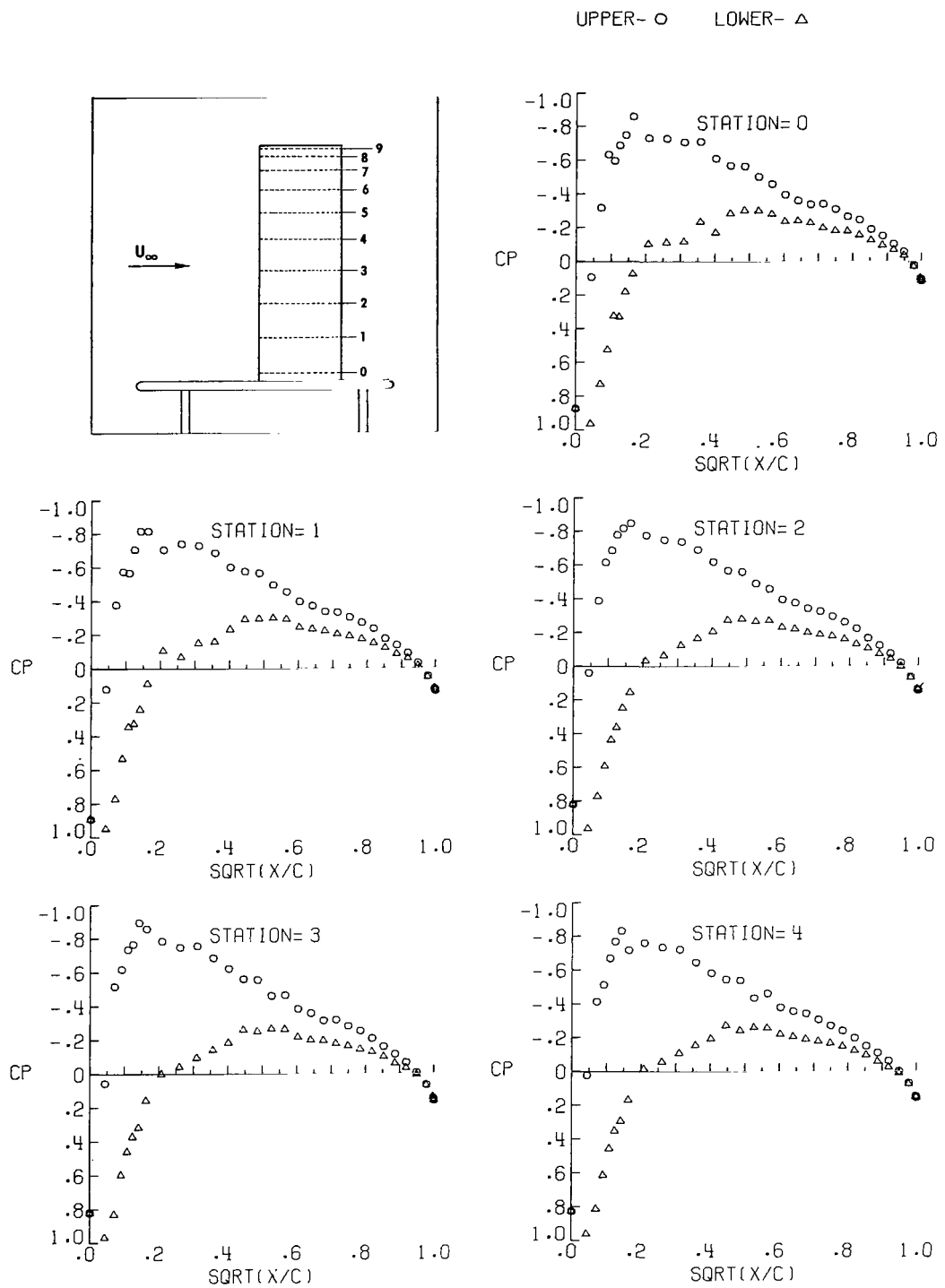

(f) α = 2.53°; q_∞ = 1.47 kPa (30.71 lb/ft^2).

Figure 3.- Continued.

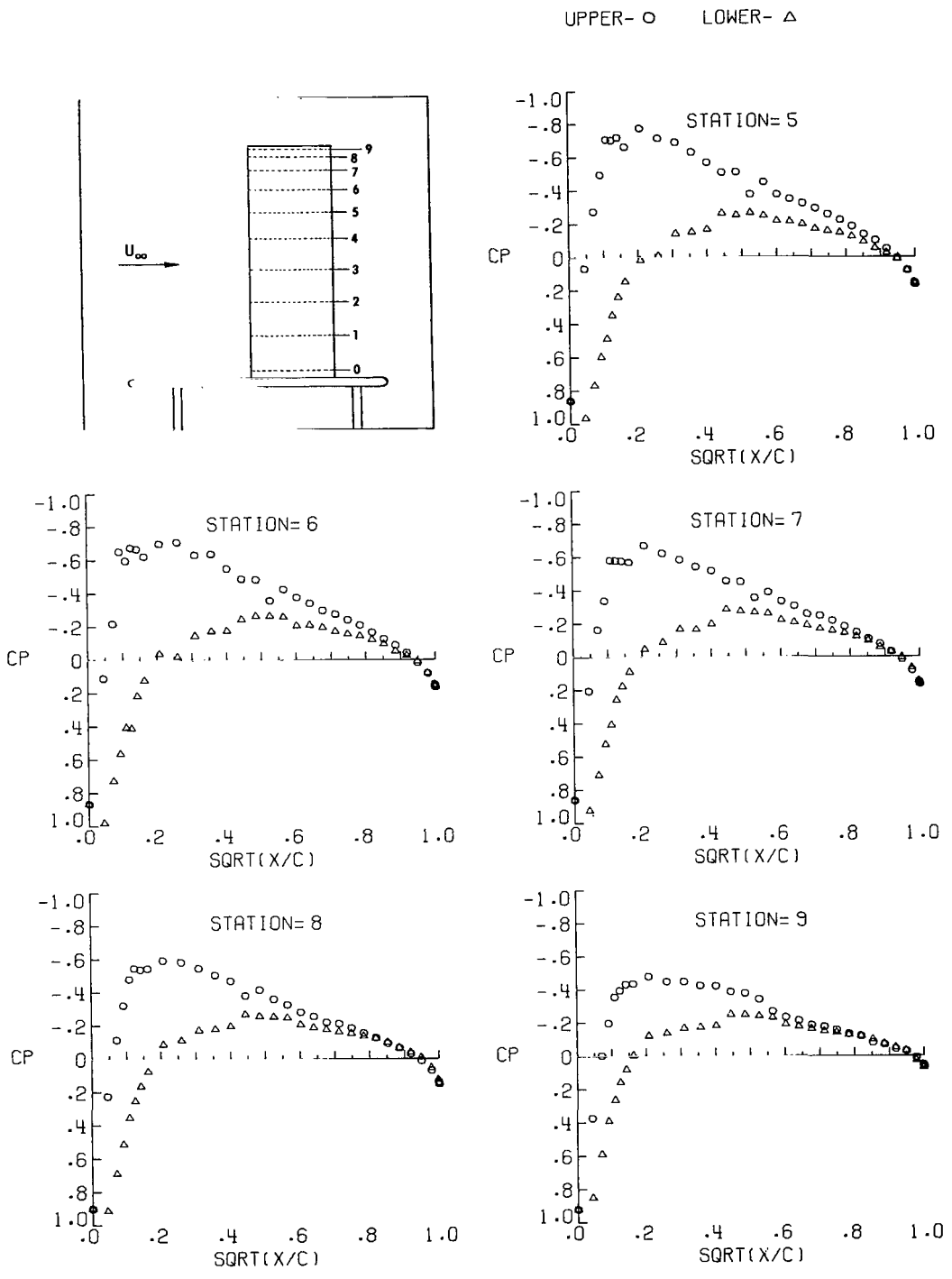

(f) Concluded.

Figure 3.- Continued.

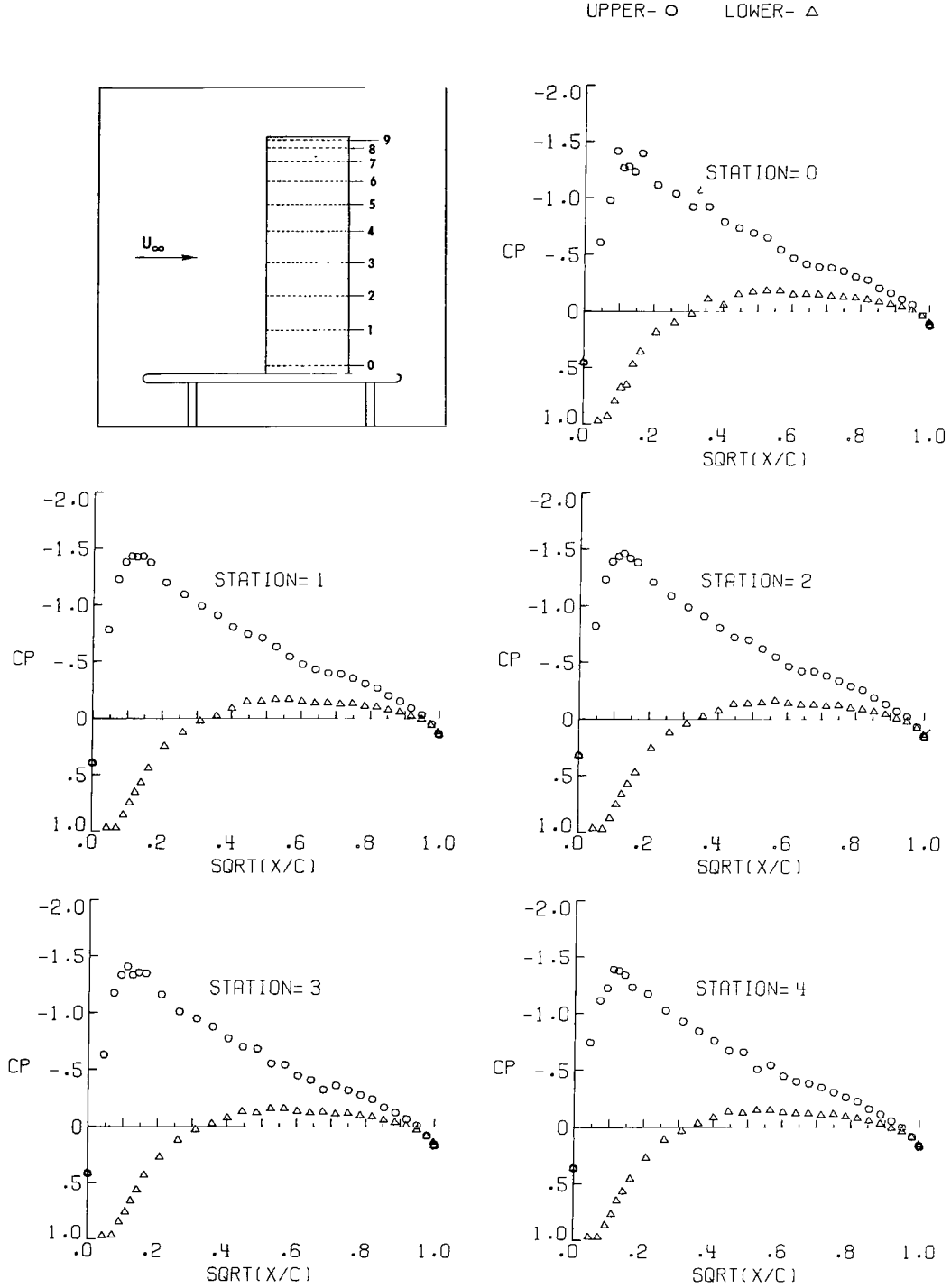

(g) $\alpha = 4.64^{o}$; $q_\infty = 1.48$ kPa (30.92 lb/ft^2).

Figure 3.- Continued.

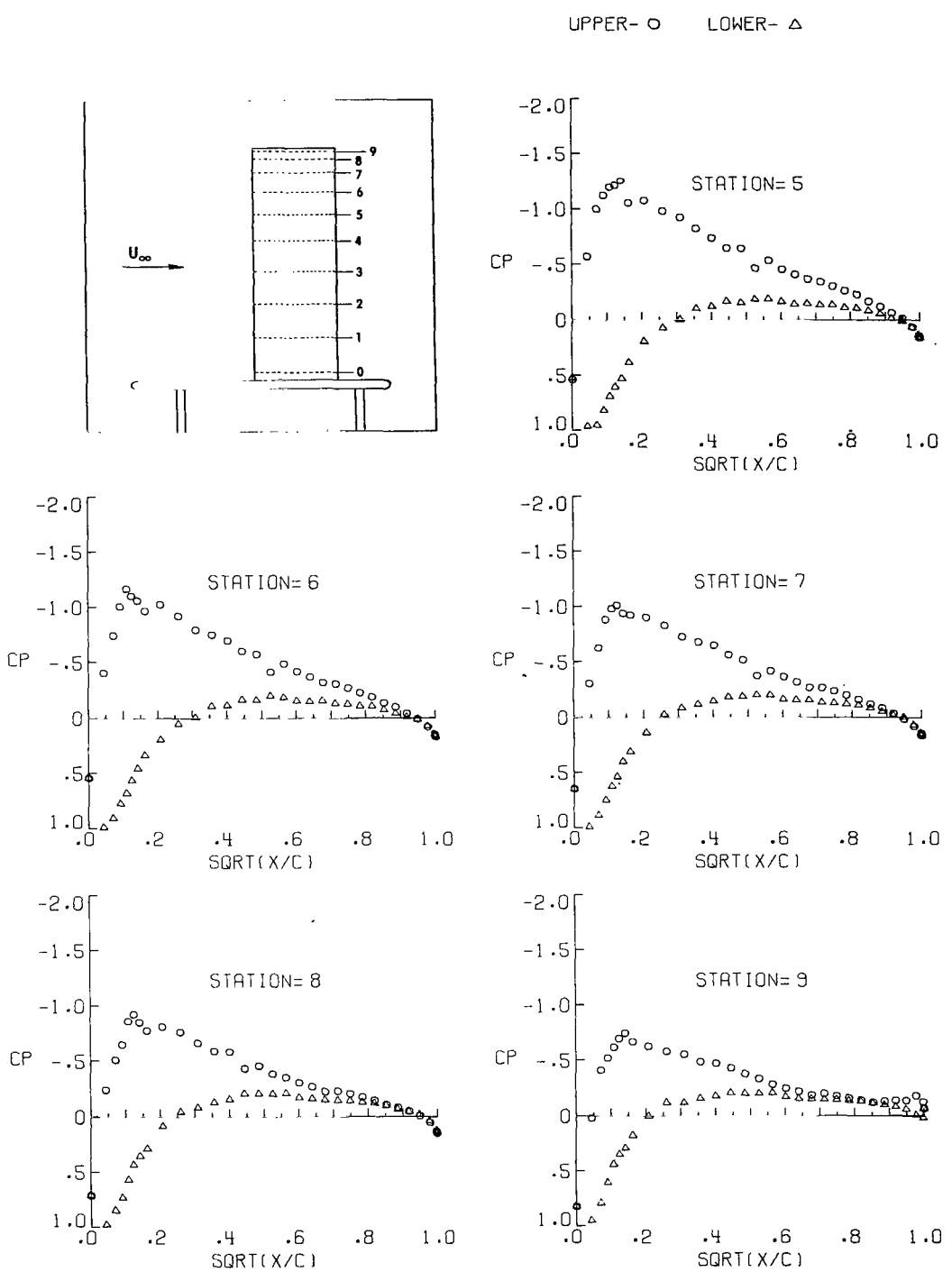

(g) Concluded.

Figure 3.- Continued.

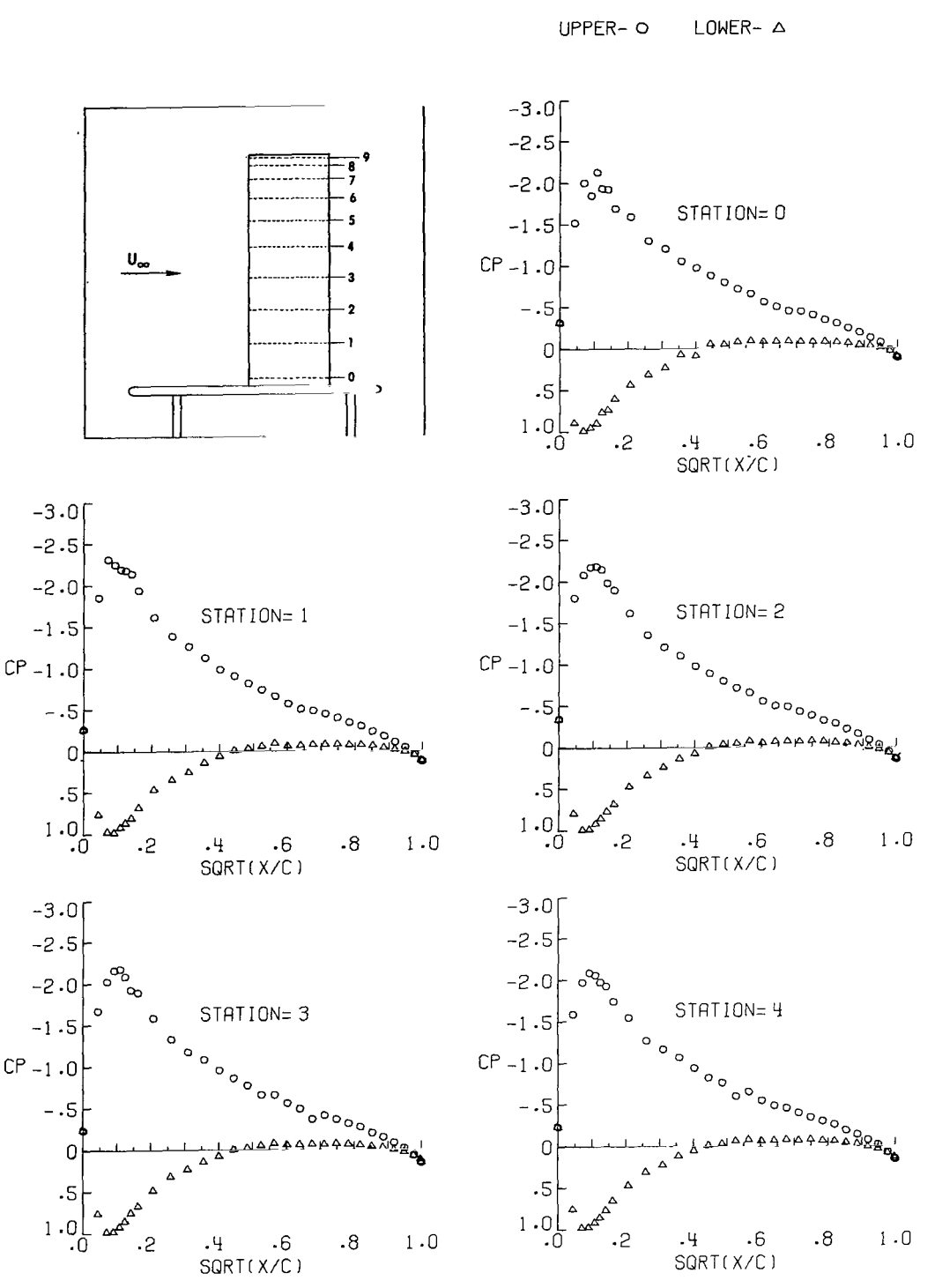

(h) $\alpha = 6.75^{\circ}$; $q_\infty = 1.47$ kPa (30.68 lb/ft^2).

Figure 3.- Continued.

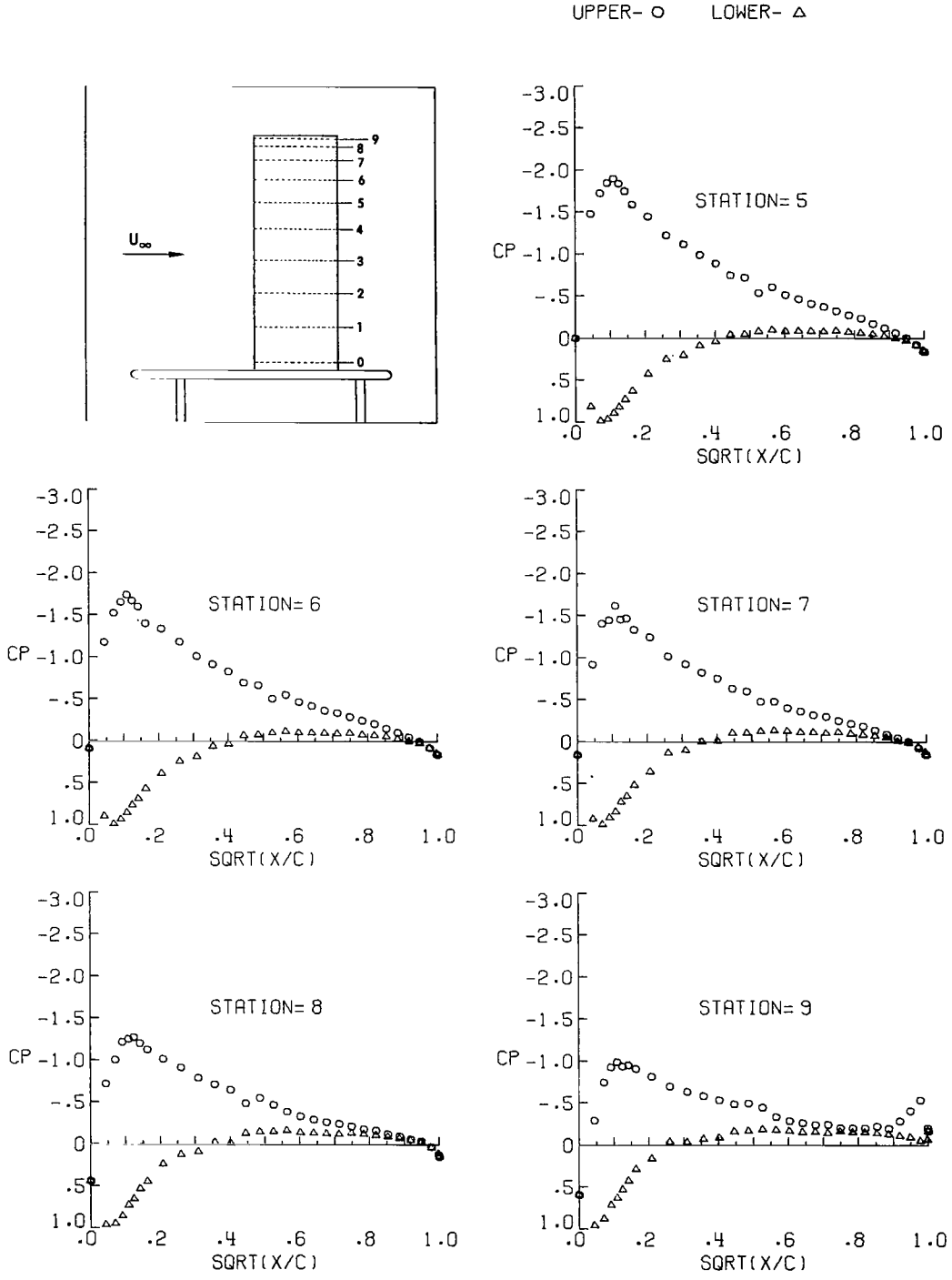

(h) Concluded.

Figure 3.- Continued.

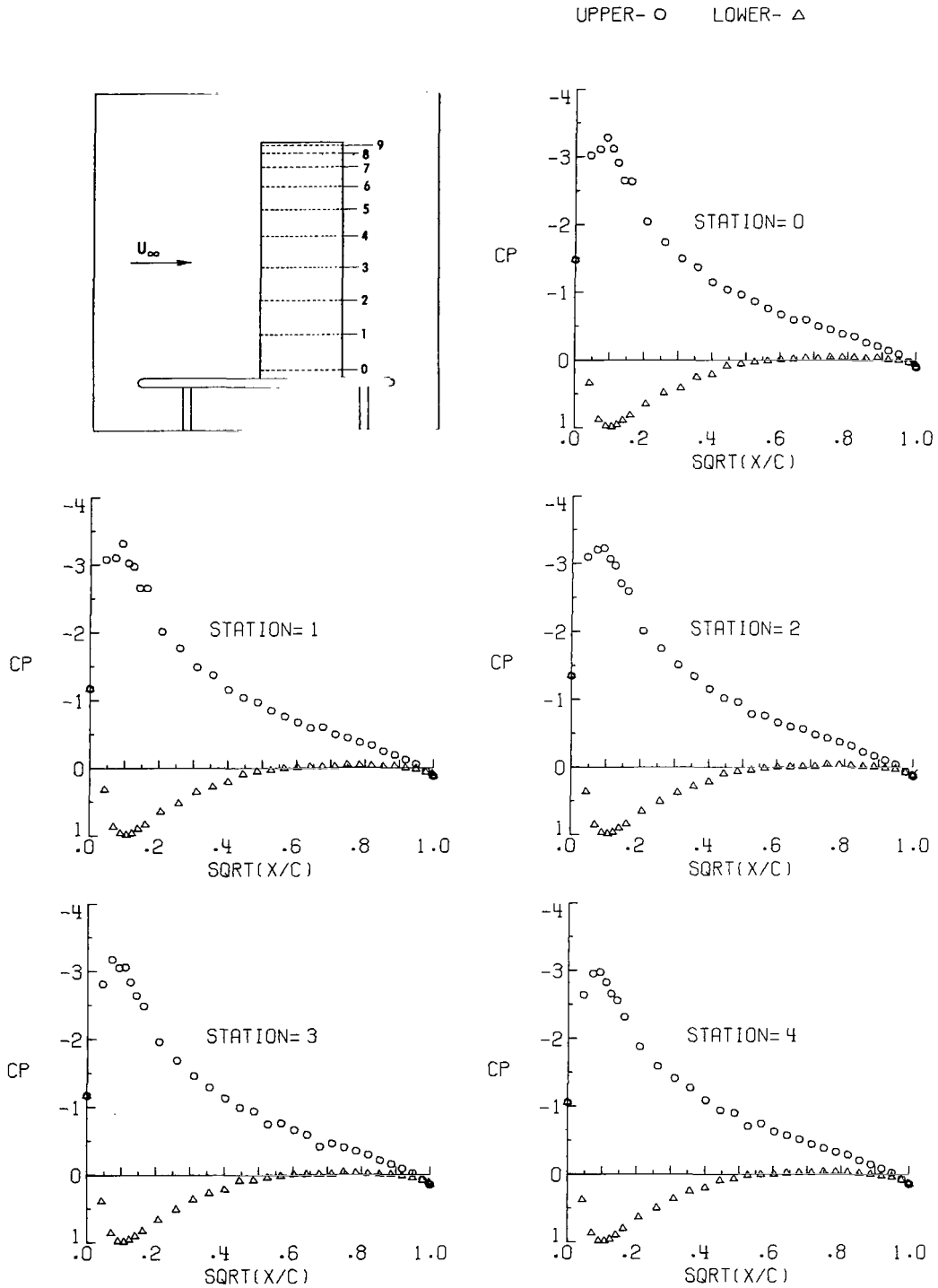

(i) $\alpha = 8.85^{o}$; $q_\infty = 1.48$ kPa (30.85 lb/ft^2).

Figure 3.- Continued.

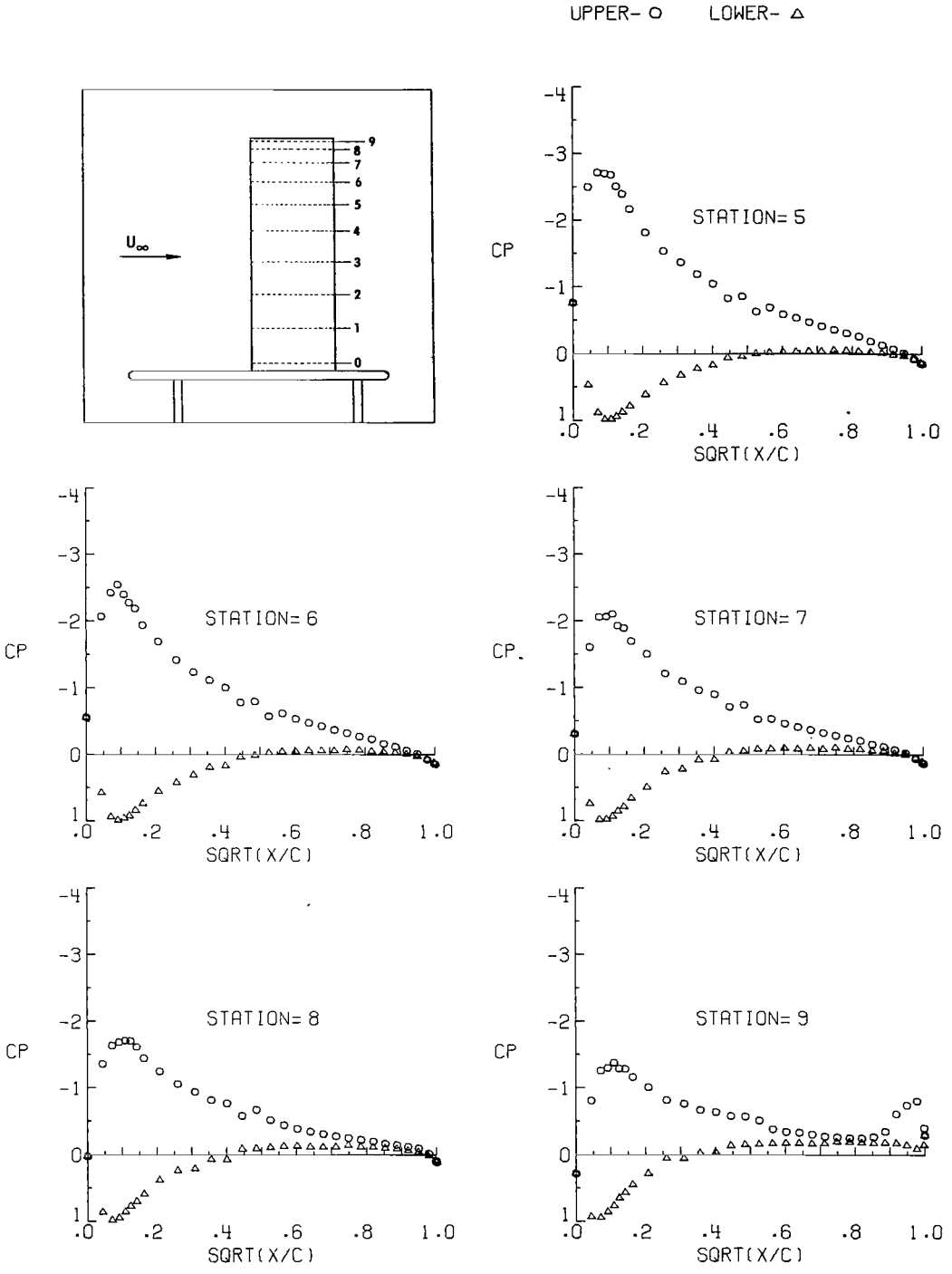

(i) Concluded.

Figure 3.- Continued.

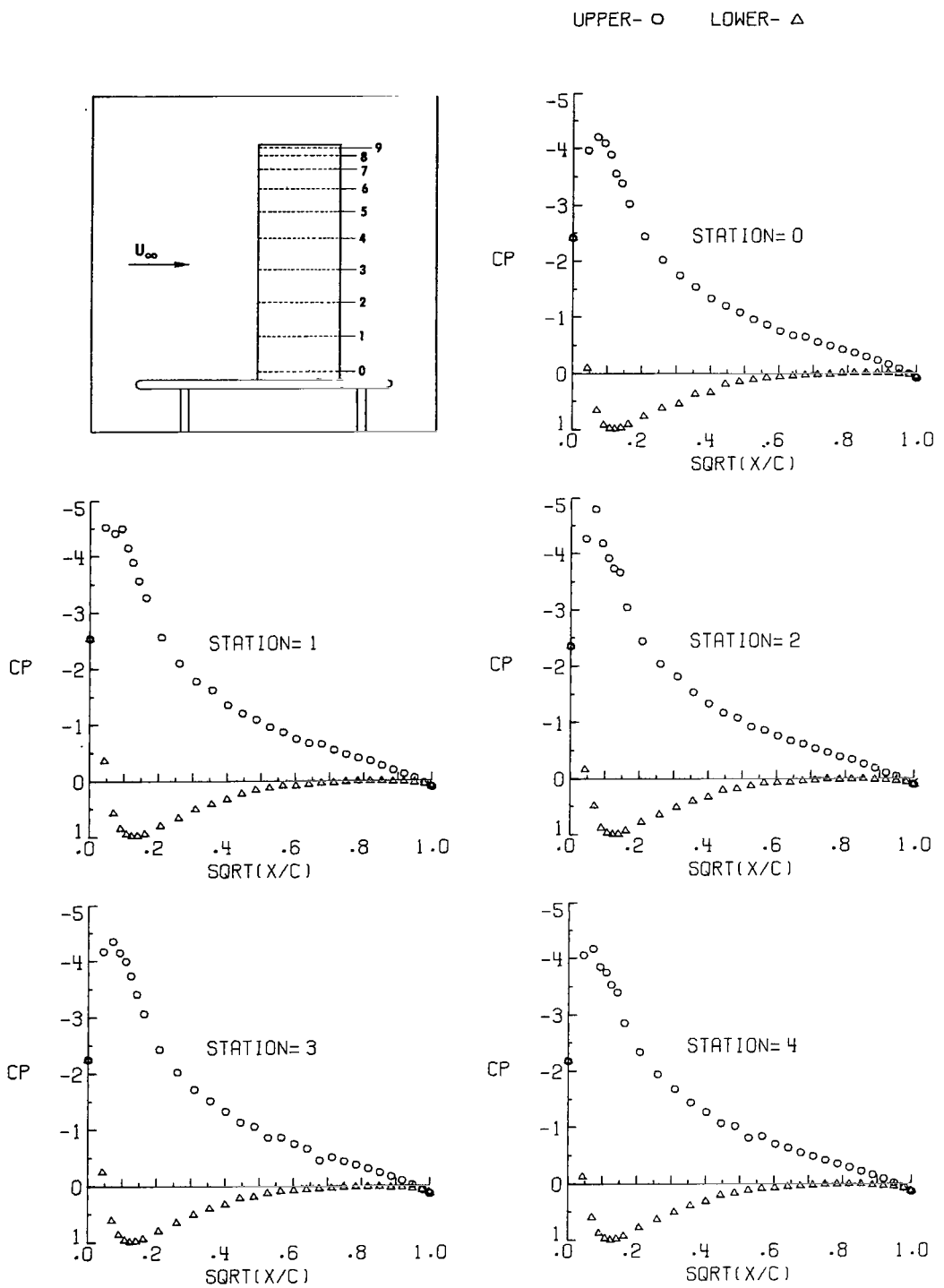

(j) $\alpha = 10.97^{\circ}$; $q_\infty = 1.47$ kPa (30.80 lb/ft^2).

Figure 3.- Continued.

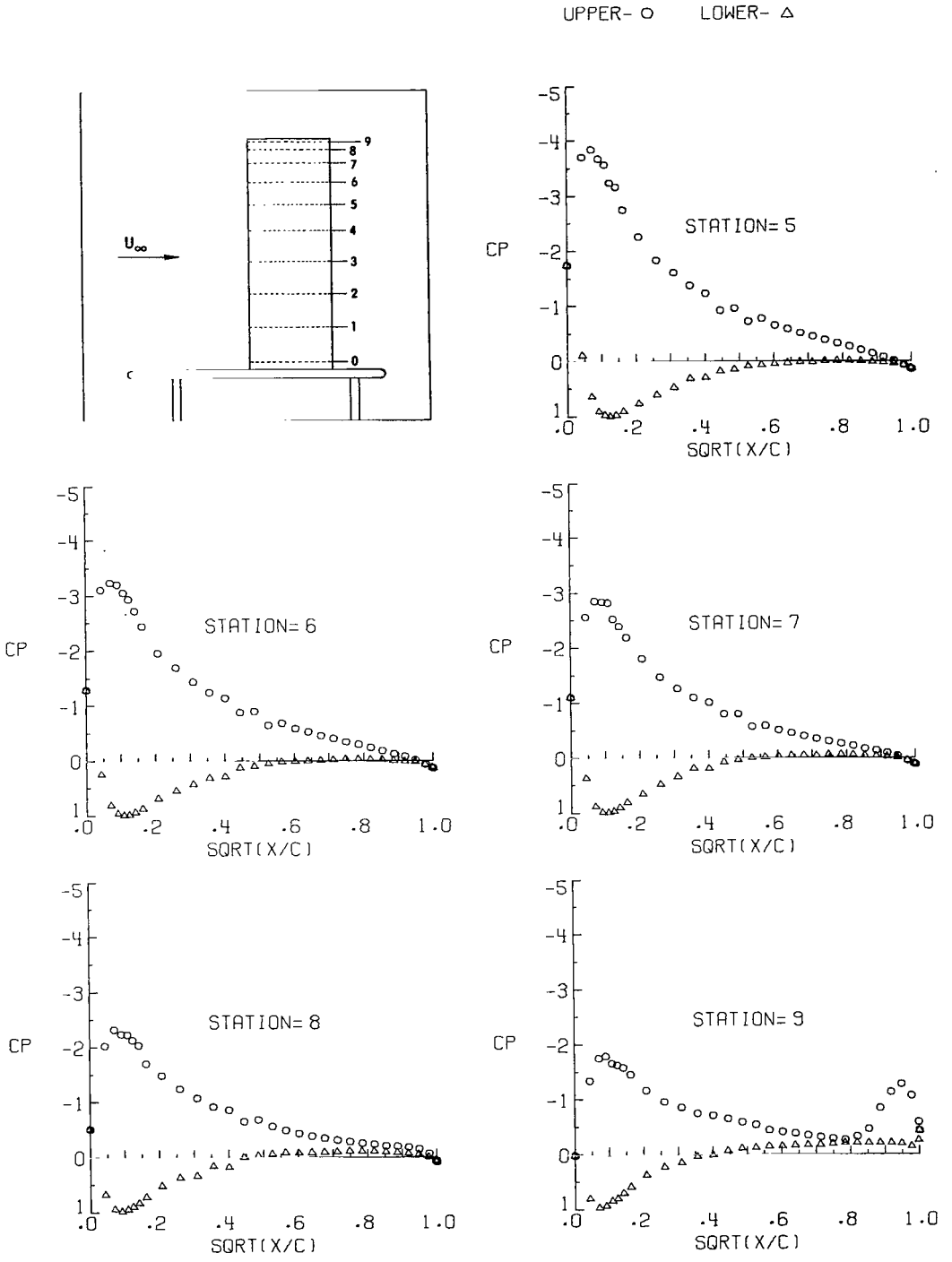

(j) Concluded.

Figure 3.- Continued.

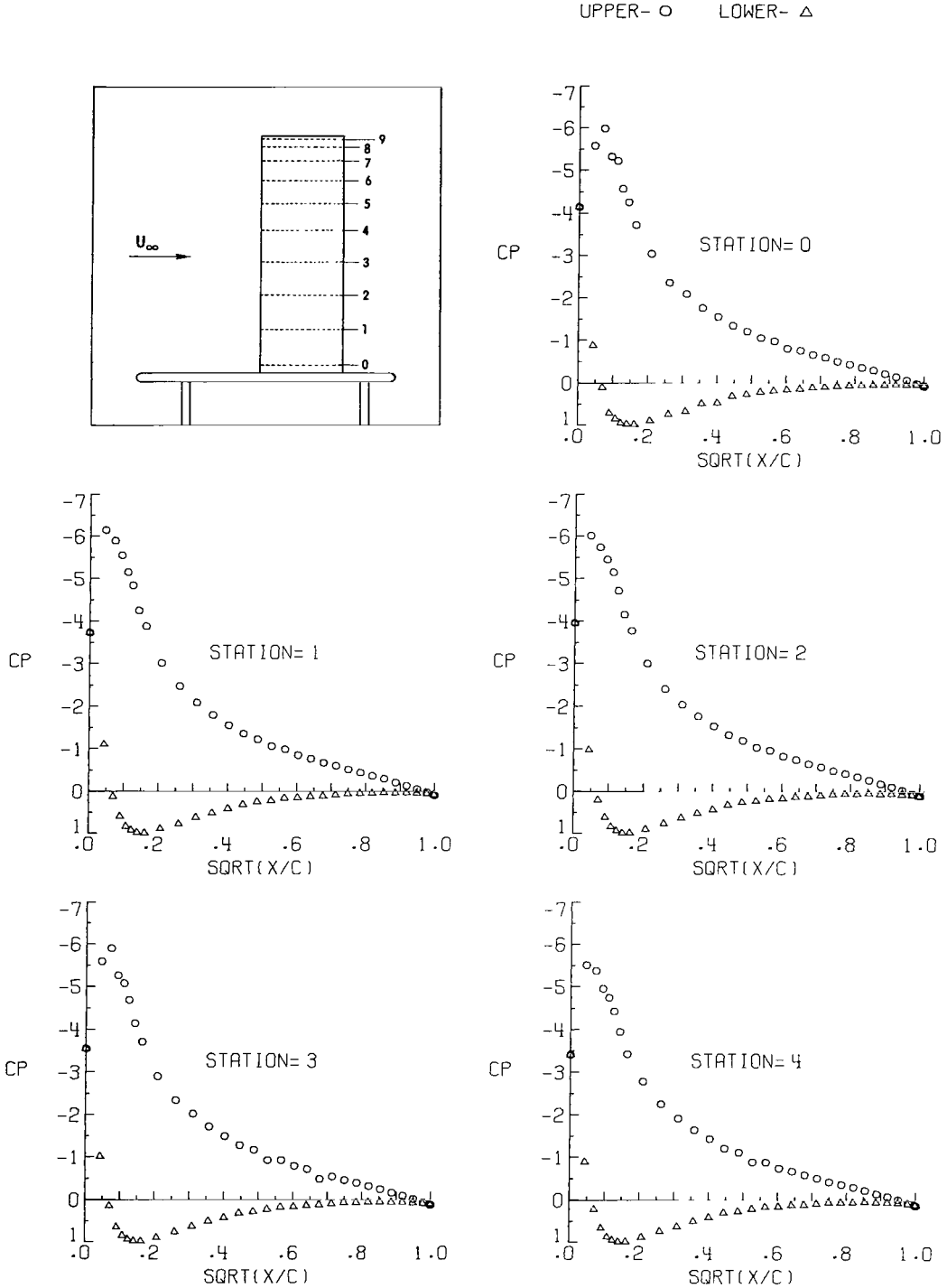

(k) $\alpha = 13.06^{\circ}$; $q_\infty = 1.48$ kPa (30.85 lb/ft^2).

Figure 3.- Continued.

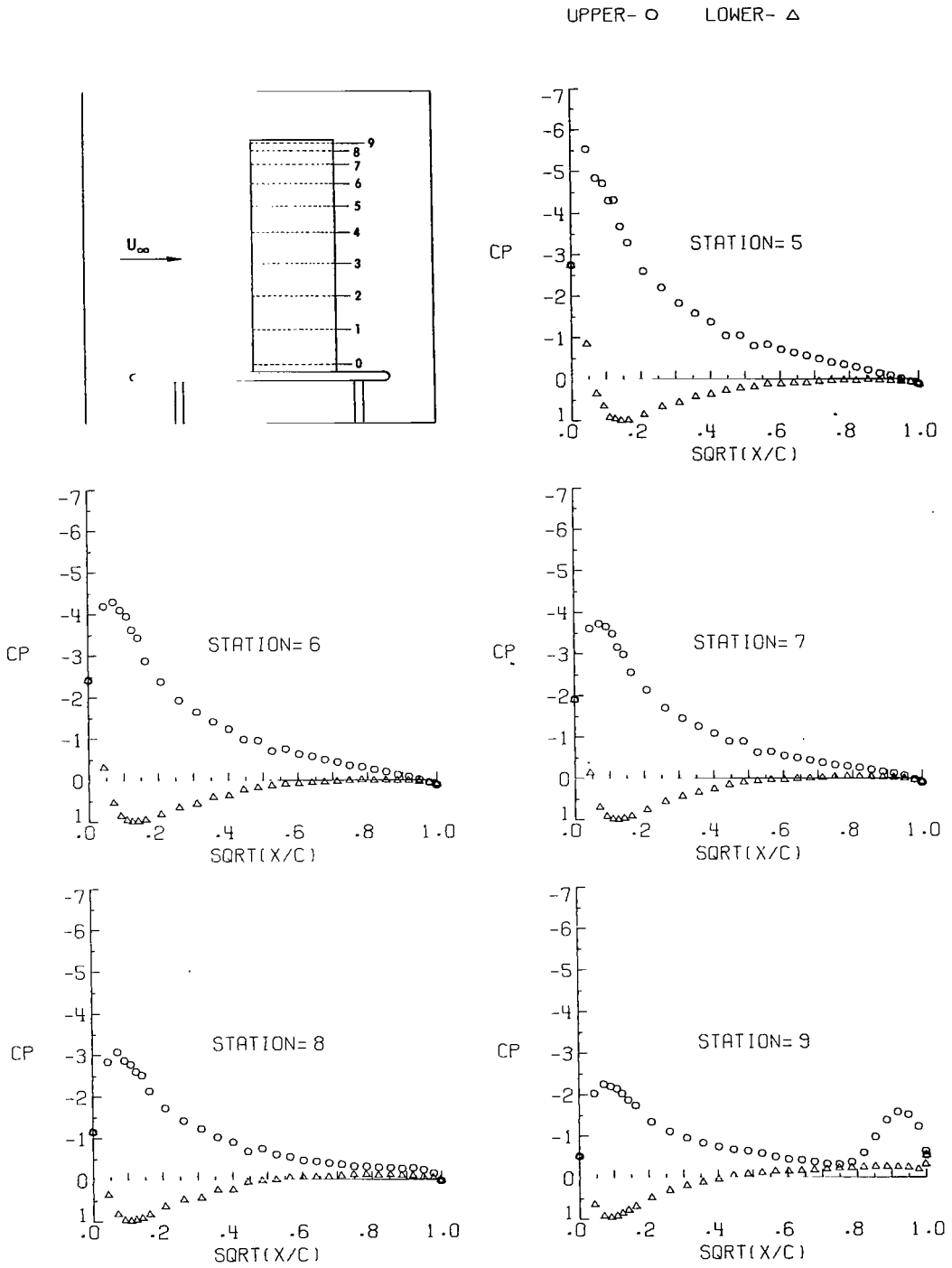

(k) Concluded.

Figure 3.- Continued.

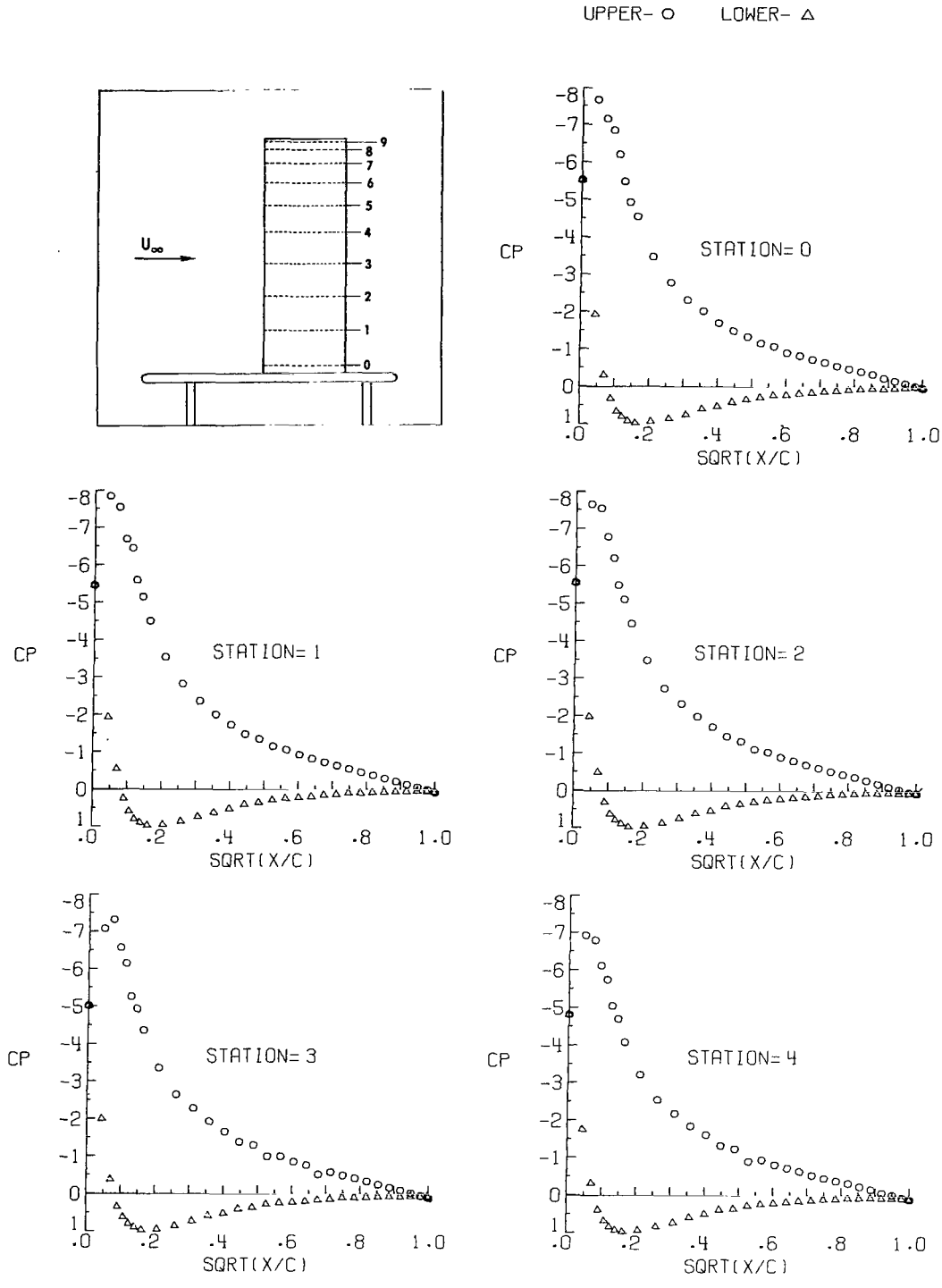

(l) $\alpha = 15.16^{o}$; $q_\infty = 1.46$ kPa (30.55 lb/ft^2).

Figure 3.- Continued.

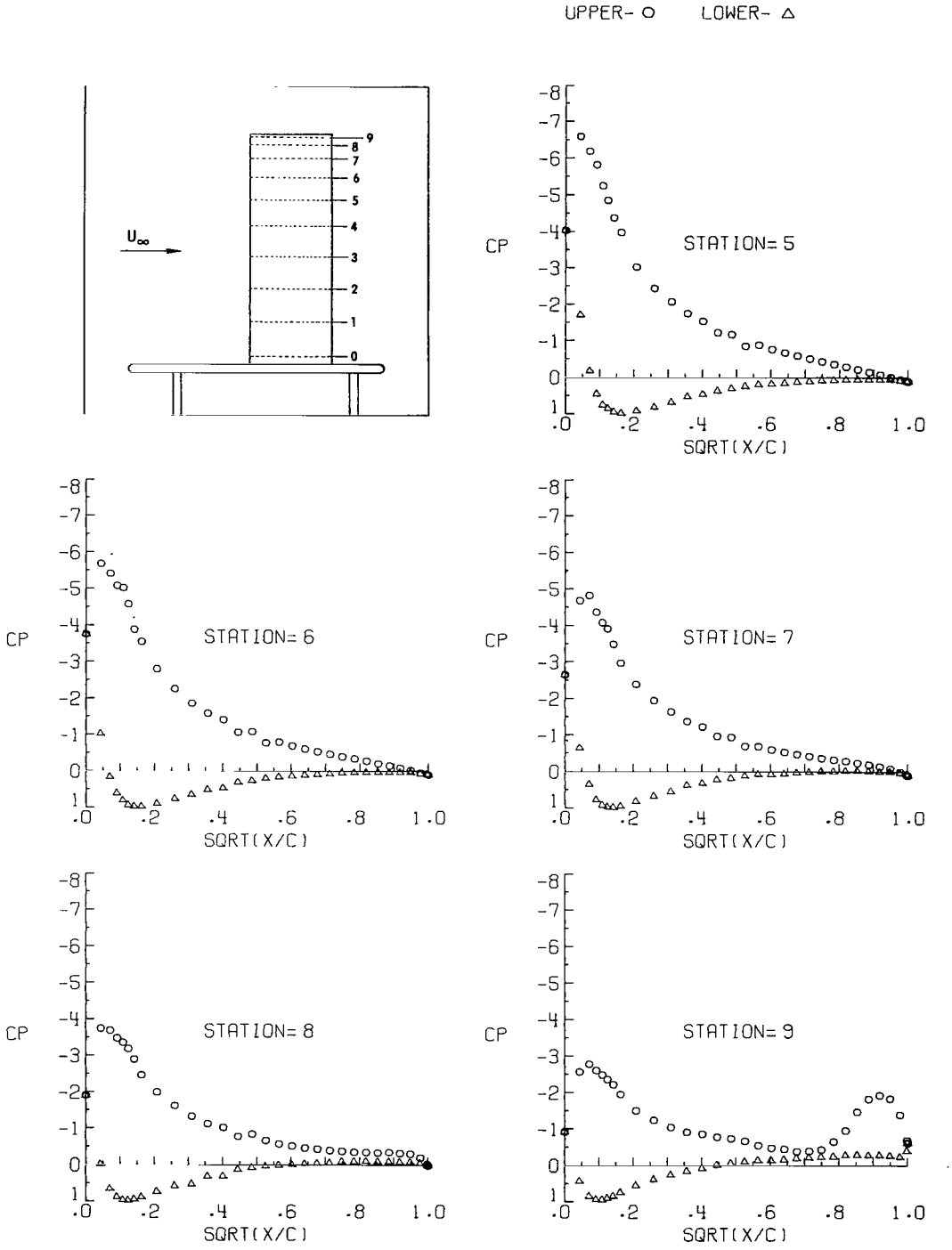

(1) Concluded.

Figure 3.- Continued.

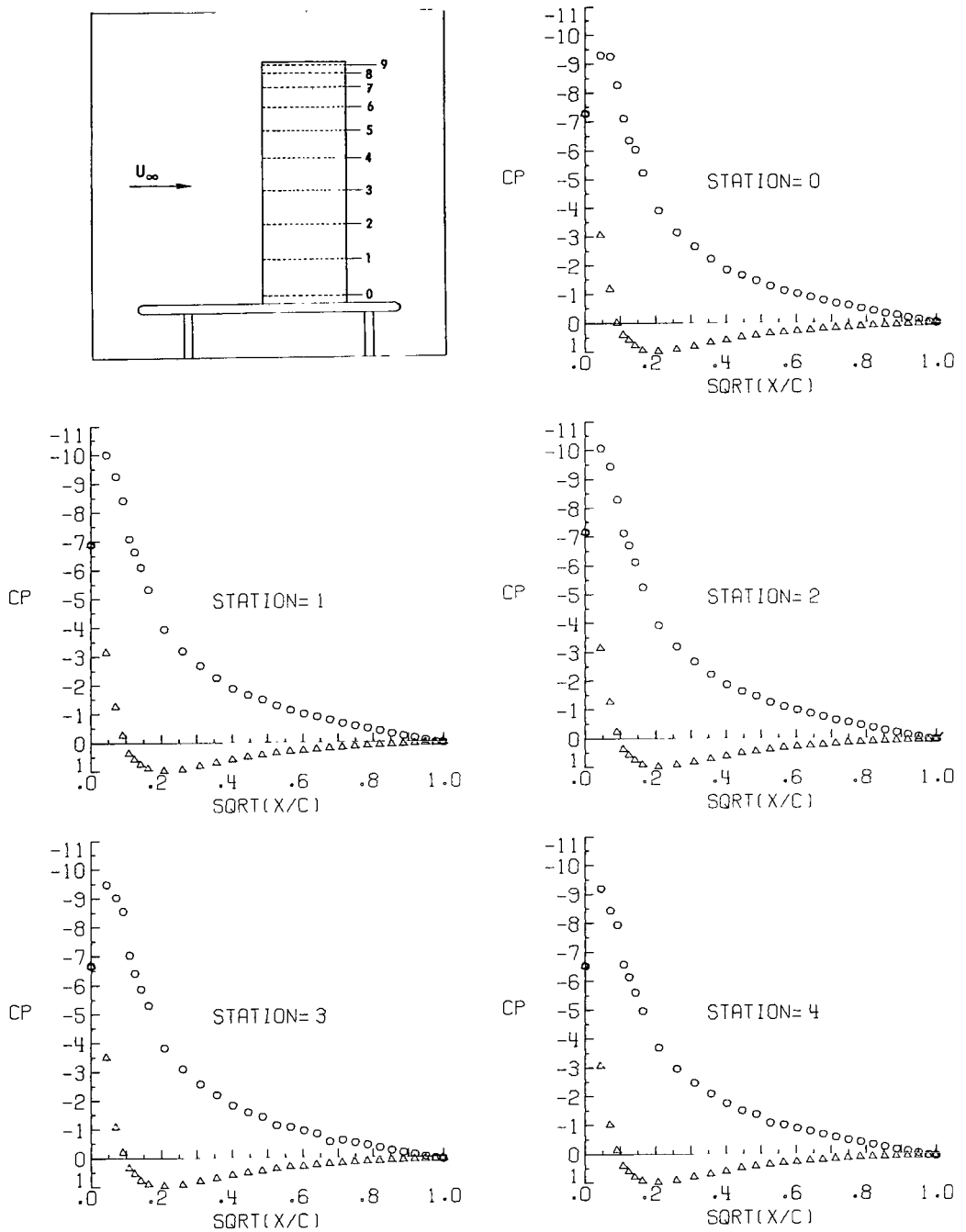

(m) $\alpha = 17.26^{o}$; $q_\infty = 1.48$ kPa (30.84 lb/ft^2).

Figure 3.- Continued.

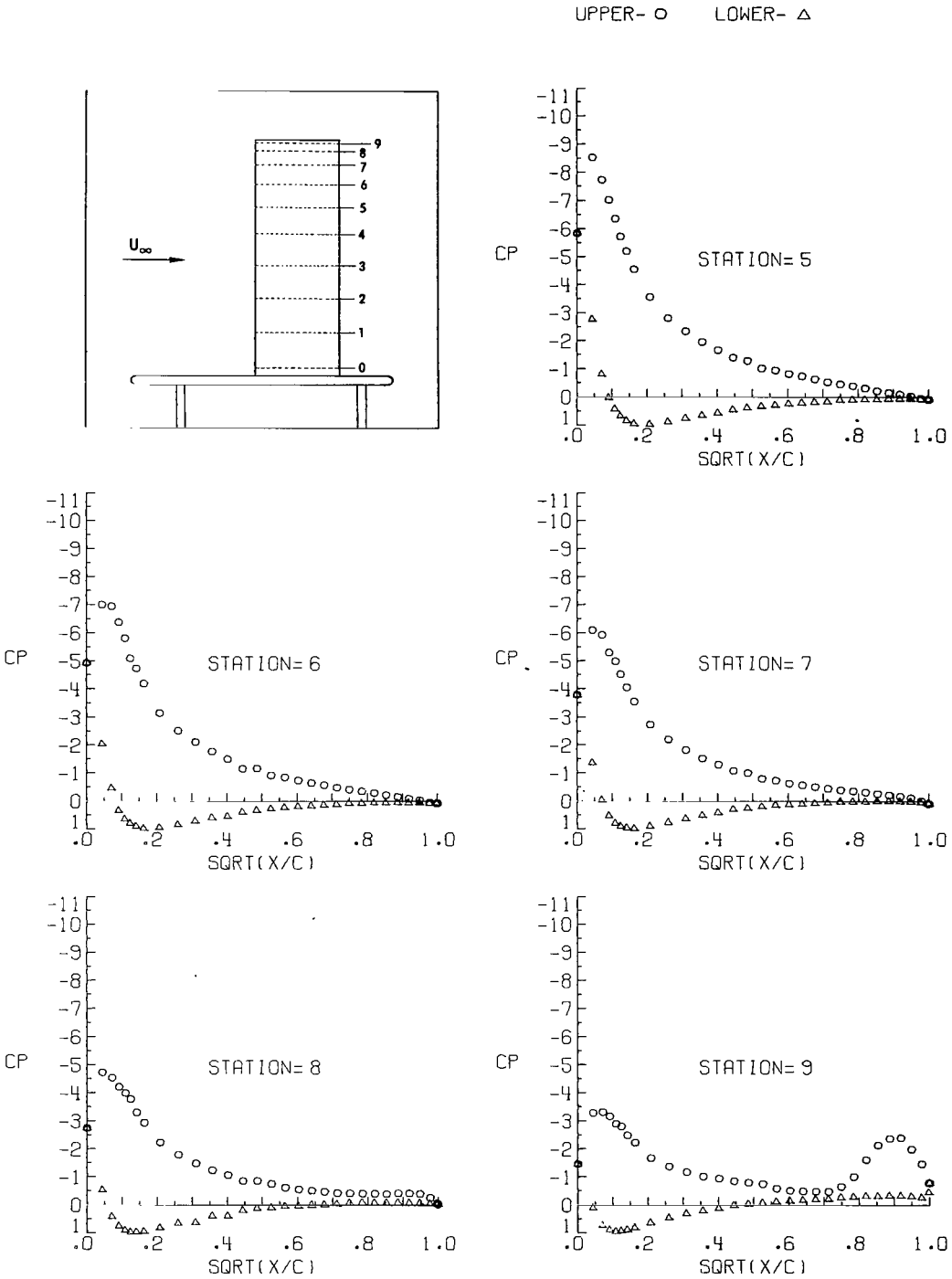

(m) Concluded.

Figure 3.- Continued.

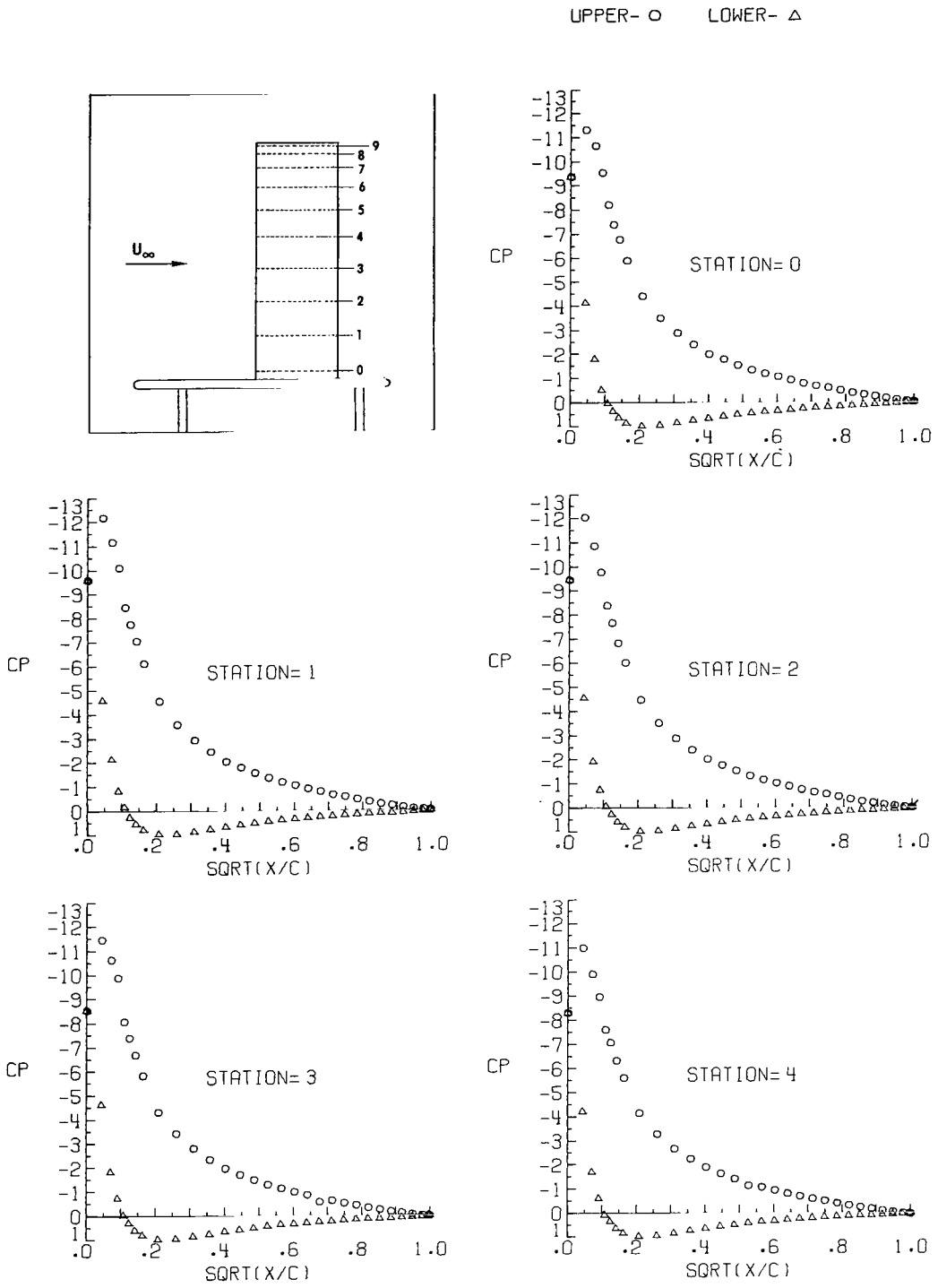

(n) $\alpha = 19.35^{\circ}$; $q_\infty = 1.48$ kPa (30.85 lb/ft^2).

Figure 3.- Continued.

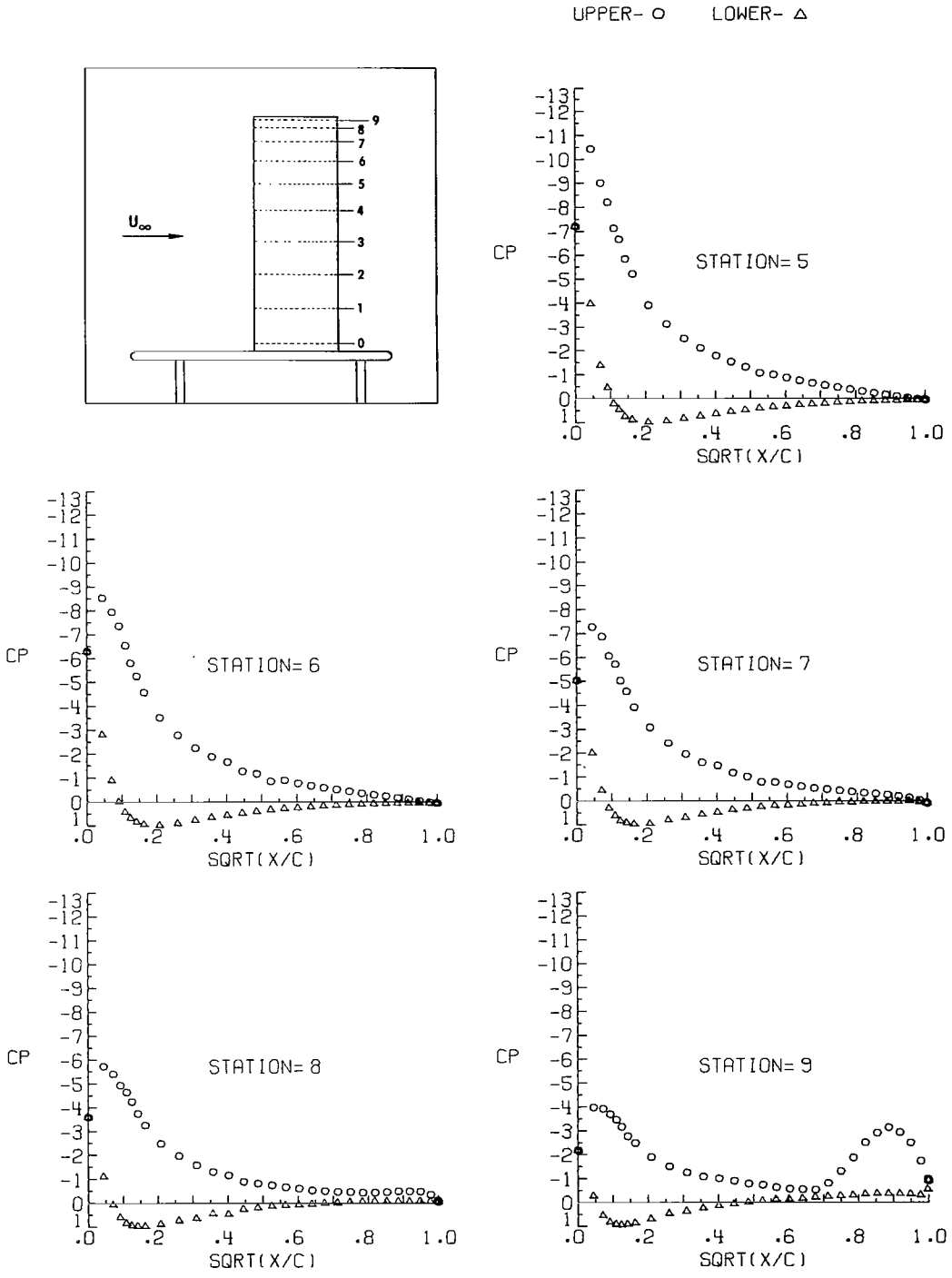

(n) Concluded.

Figure 3.- Concluded.

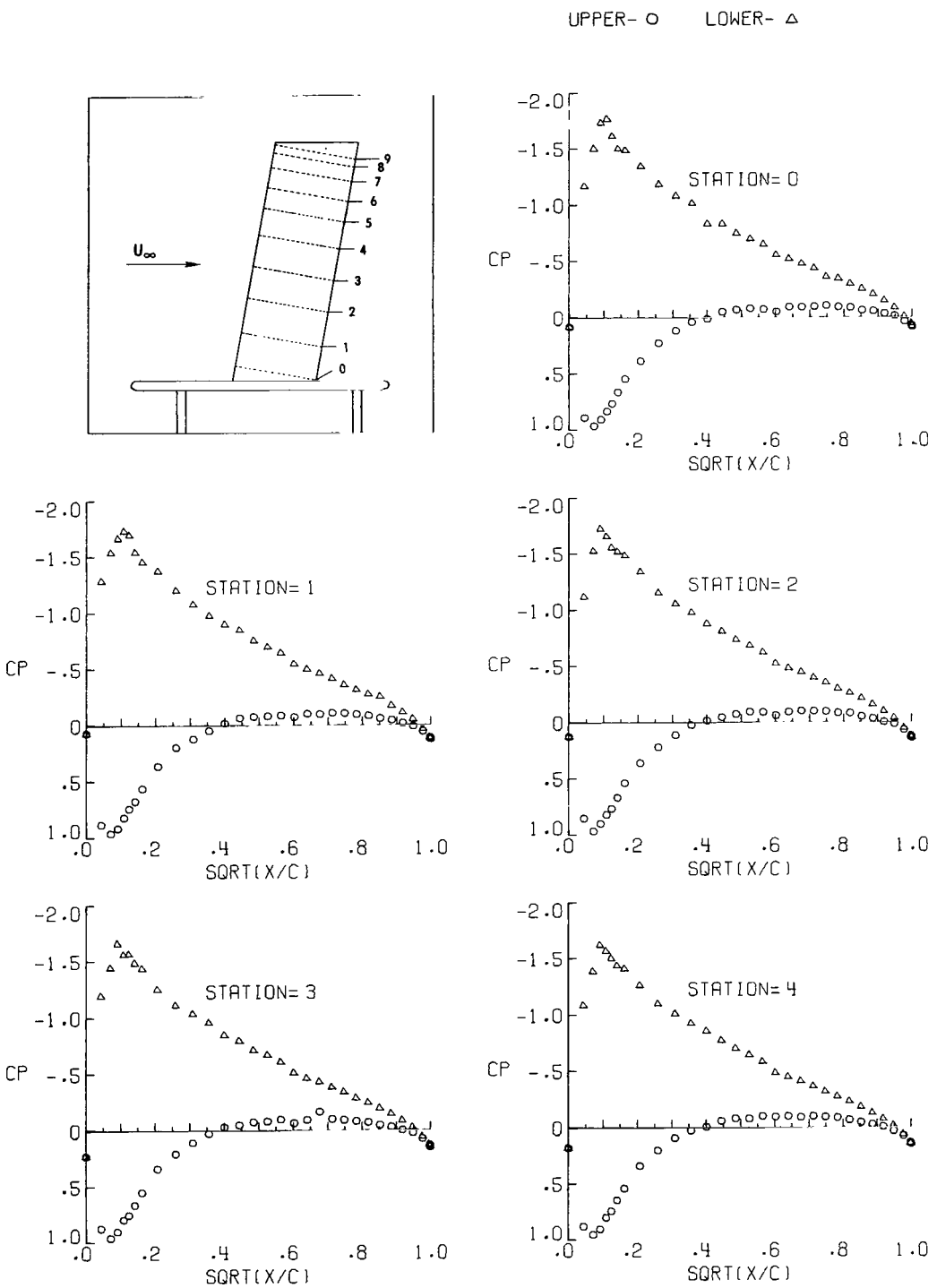

(a) $\alpha = -5.89^{\circ}$; $q_\infty = 2.47$ kPa (51.58 lb/ft^2).

Figure 4.- Pressure distributions at sweep angle of 10°.

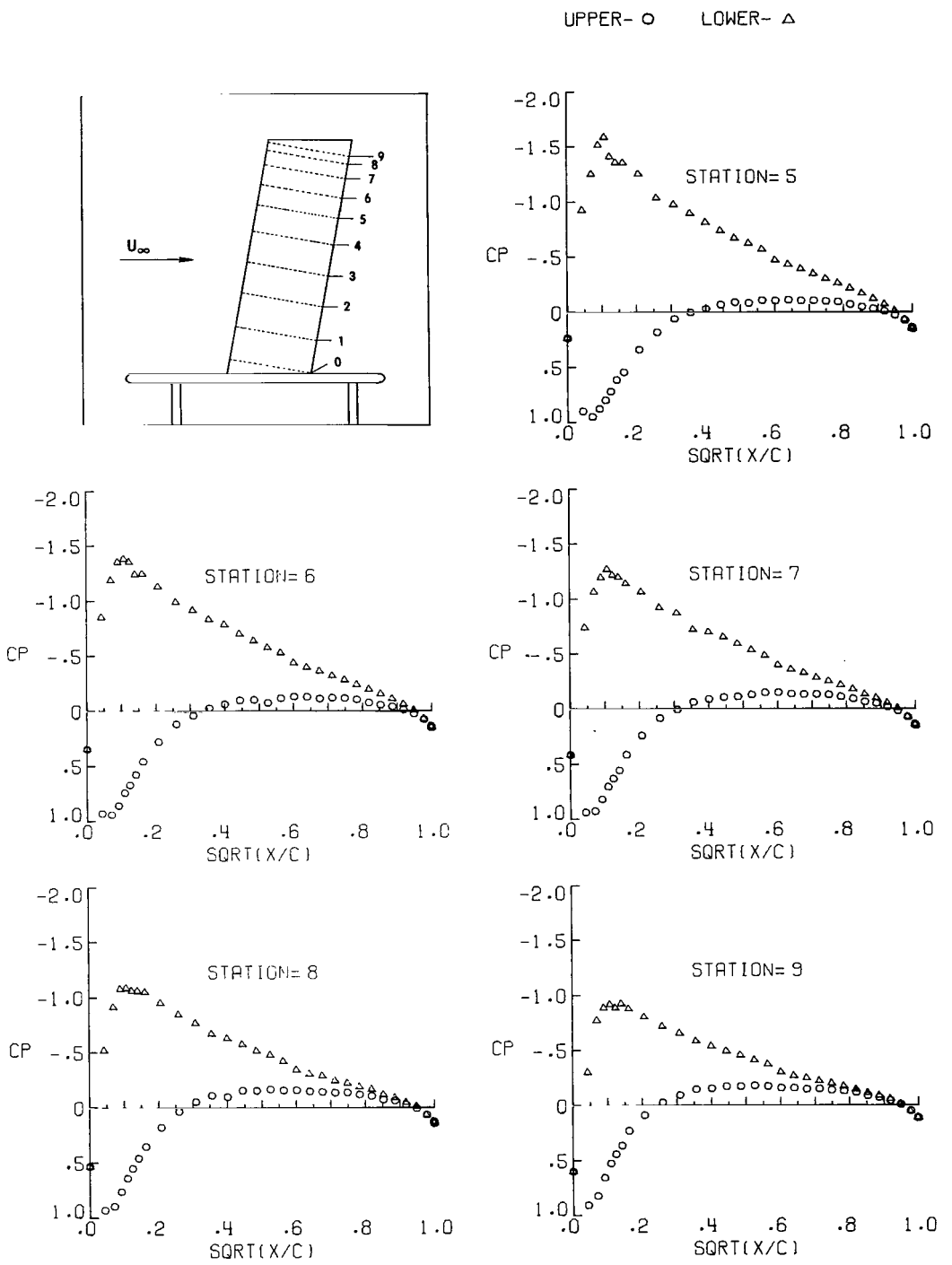

(a) Concluded.

Figure 4.- Continued.

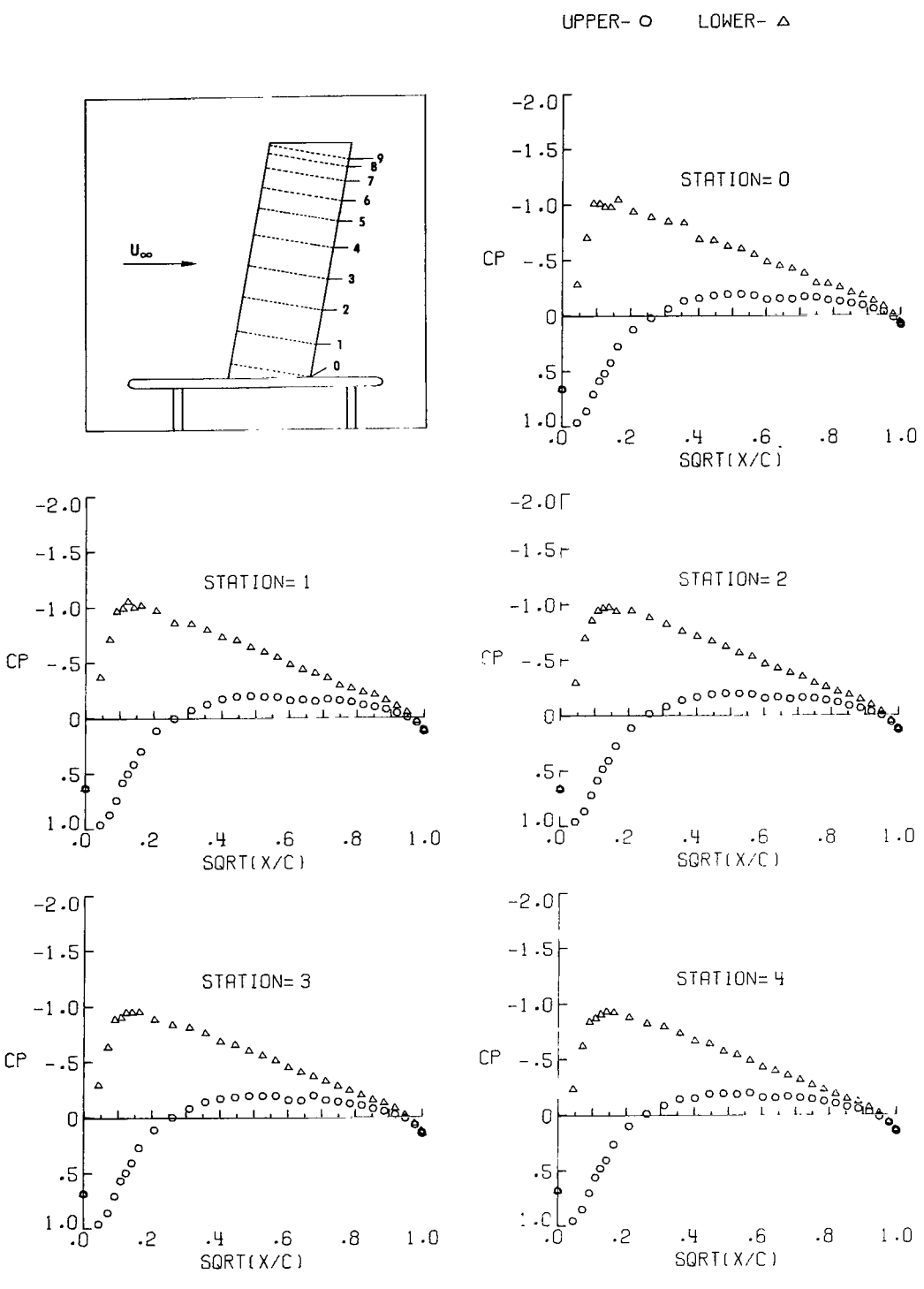

(b) $\alpha = -3.78^{\circ}$; $q_\infty = 2.47$ kPa (51.52 lb/ft^2).

Figure 4.- Continued.

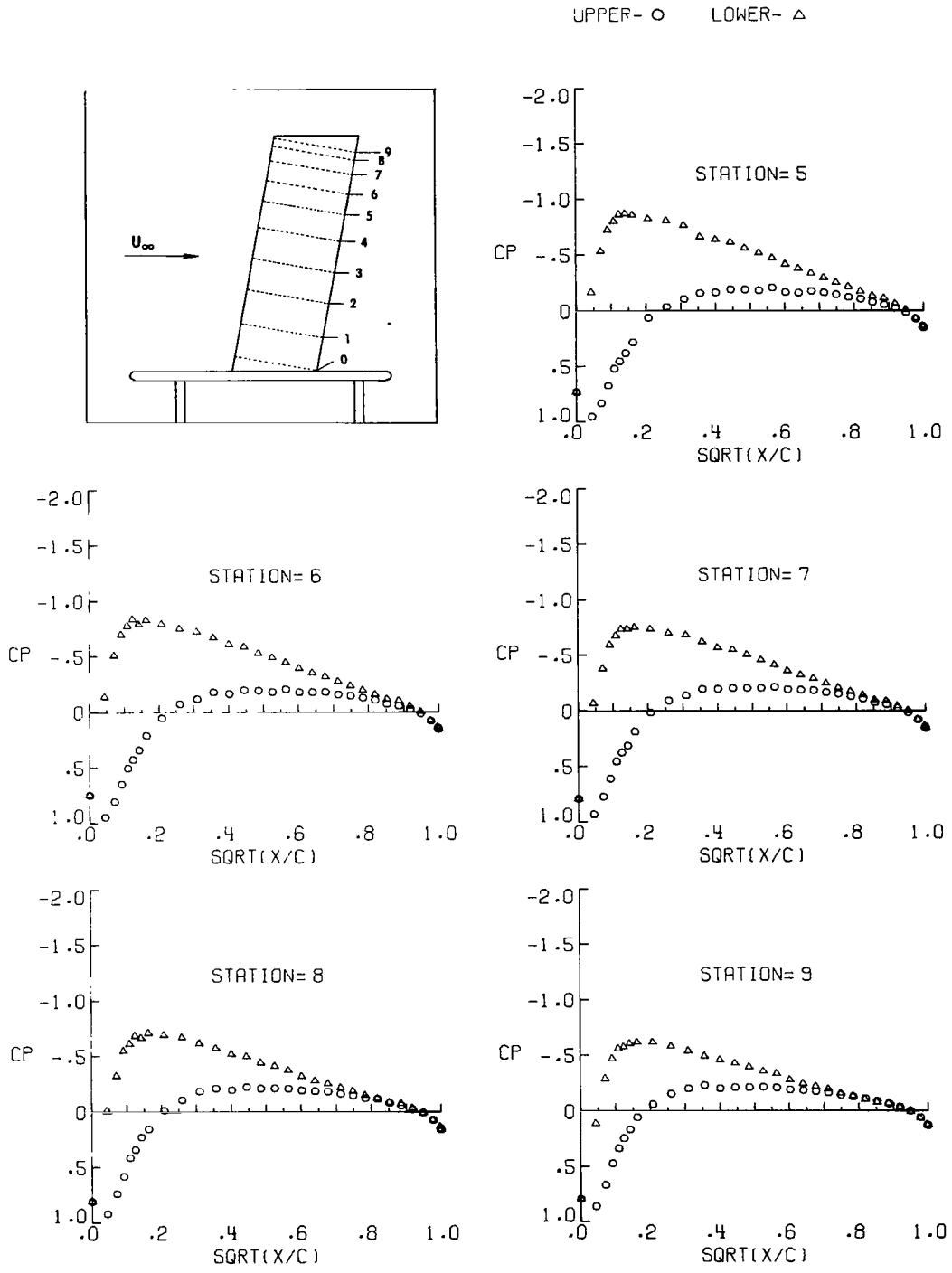

(b) Concluded.

Figure 4.- Continued.

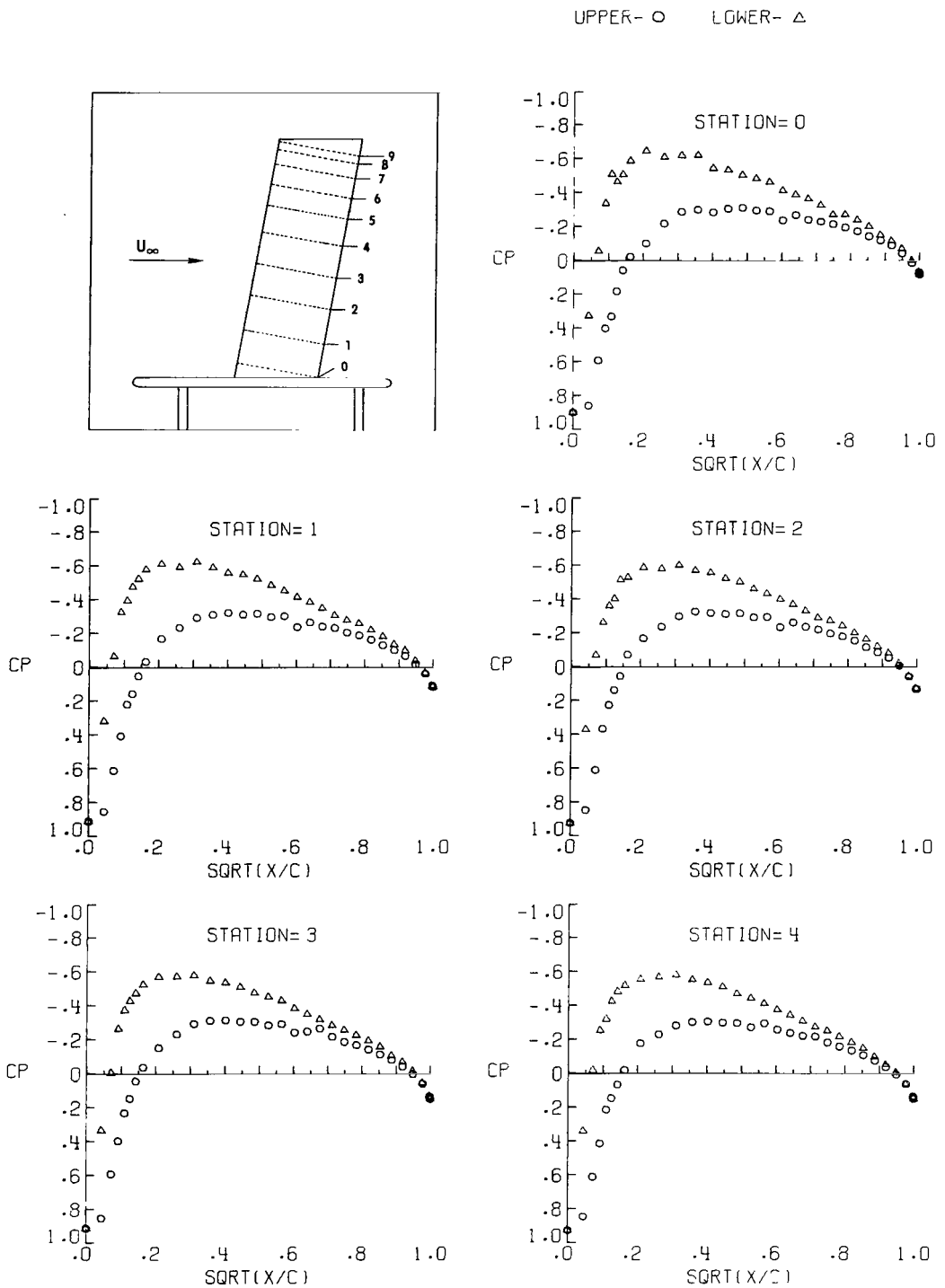

(c) $\alpha = -1.67^{\circ}$; $q_\infty = 2.47$ kPa (51.55 lb/ft^2).

Figure 4.- Continued.

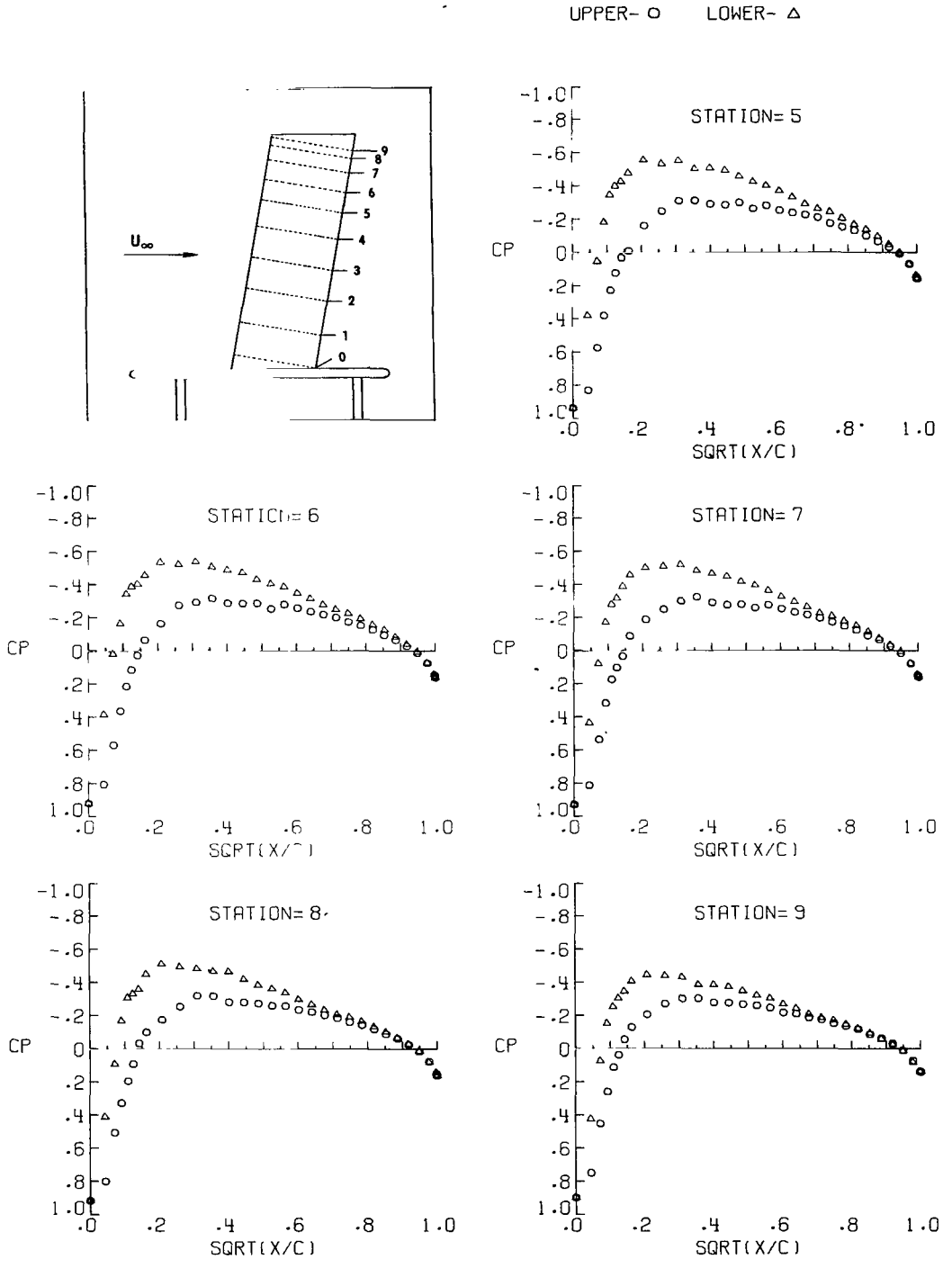

(c) Concluded.

Figure 4.- Continued.

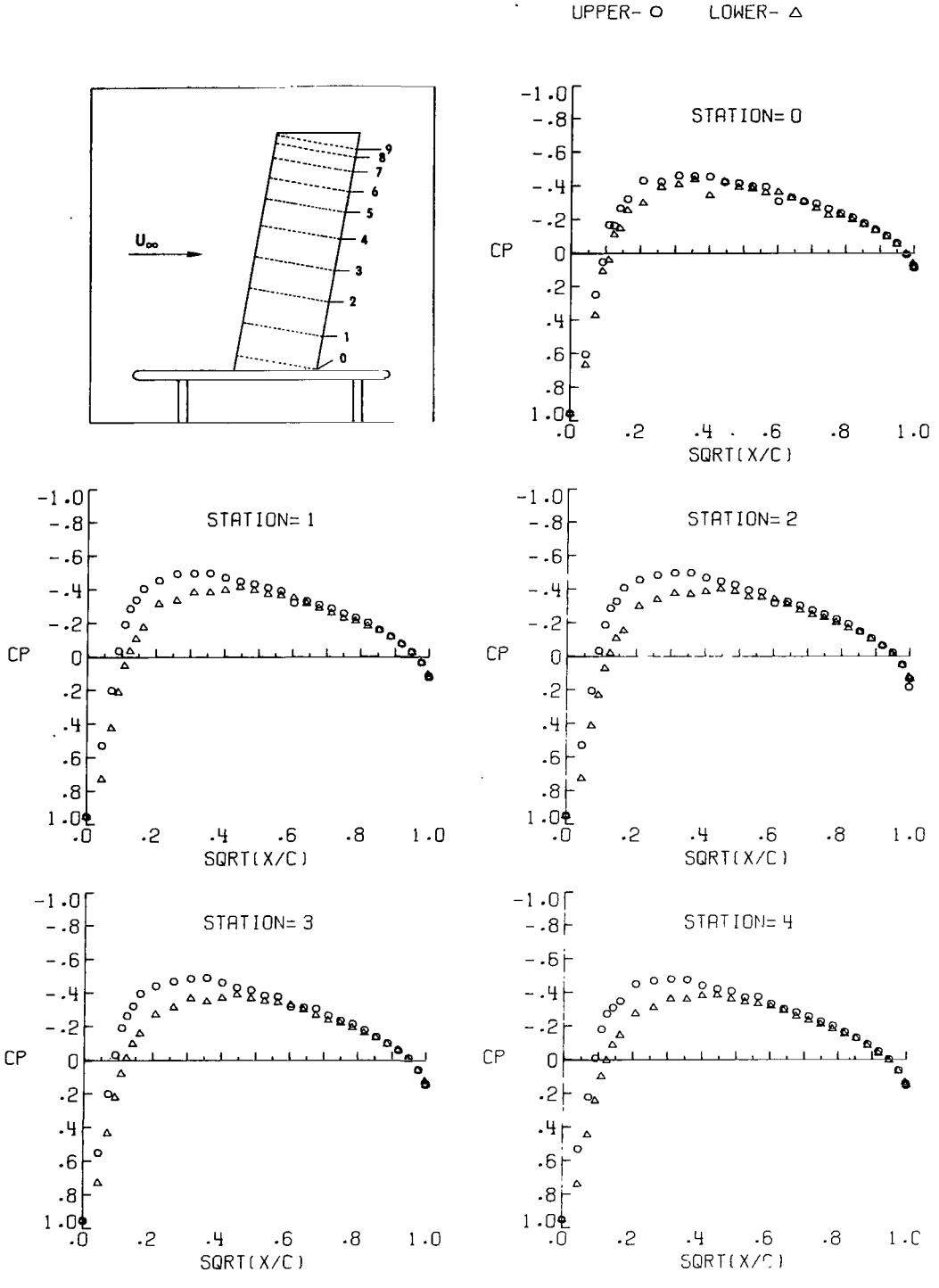

(d) $\alpha = 0.42^{o}$; $q_\infty = 2.46$ kPa (51.35 lb/ft^2).

Figure 4.- Continued.

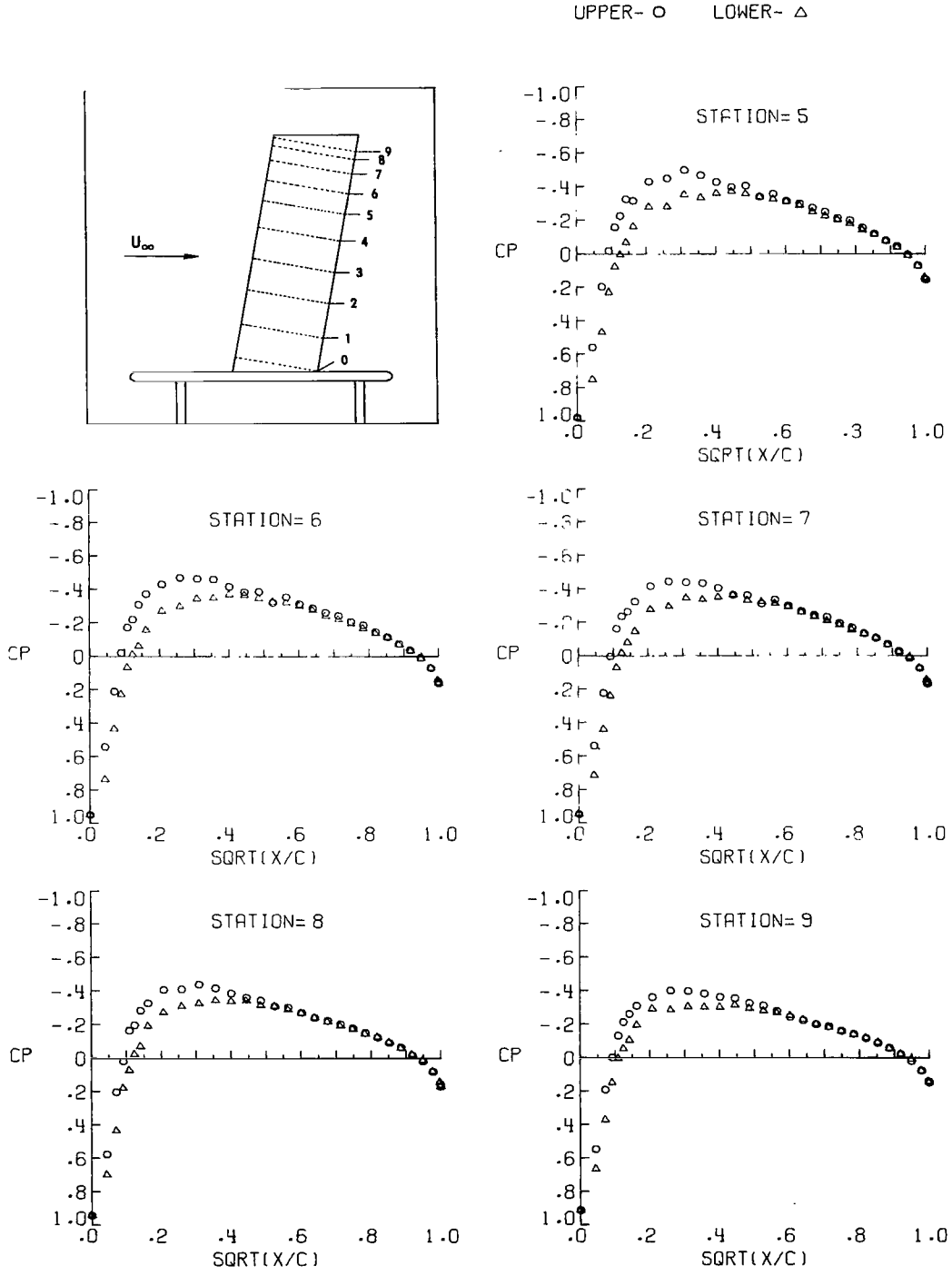

(d) Concluded.

Figure 4.- Continued.

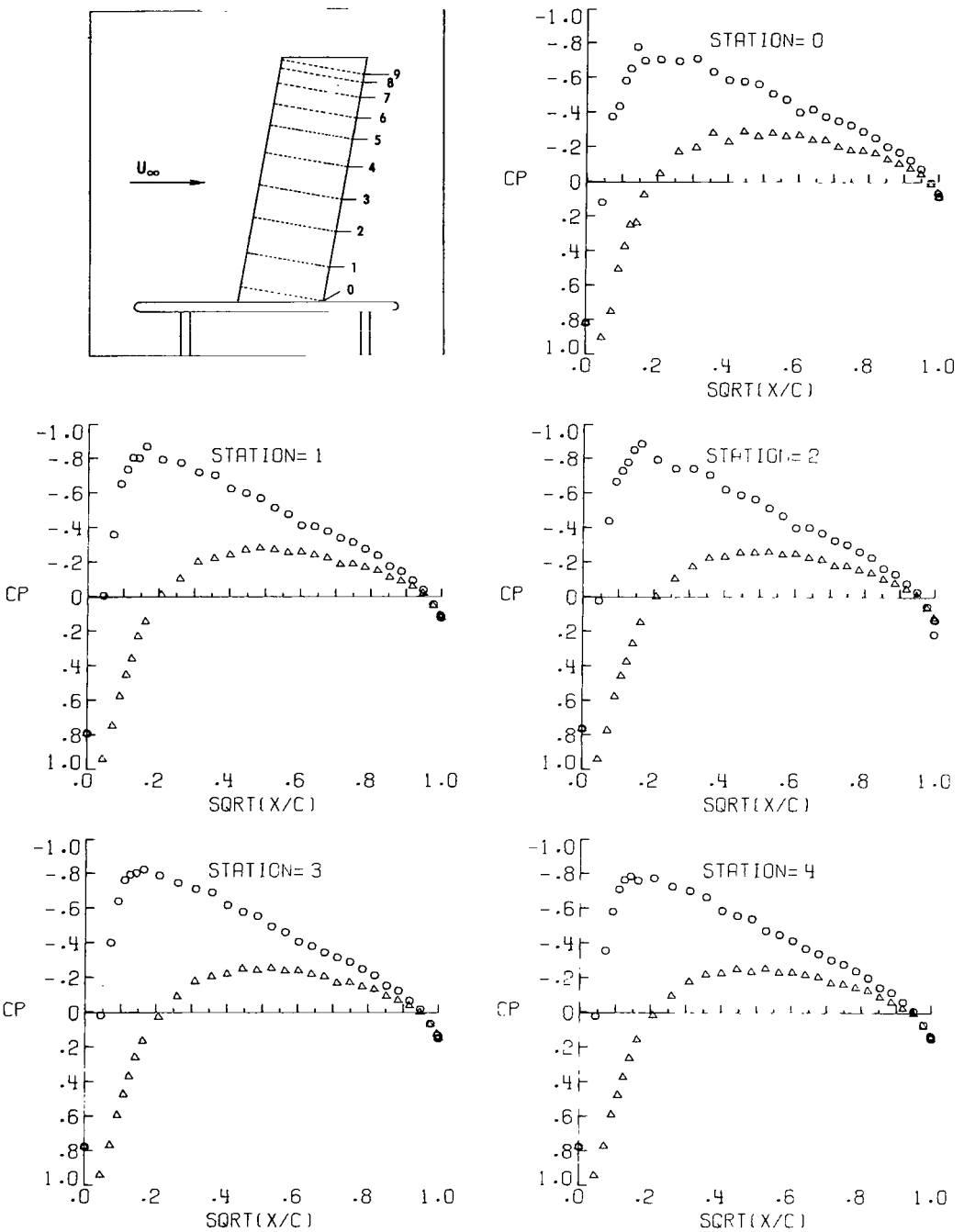

(e) α = 2.54°; q_∞ = 2.46 kPa (51.42 lb/ft^2).

Figure 4.- Continued.

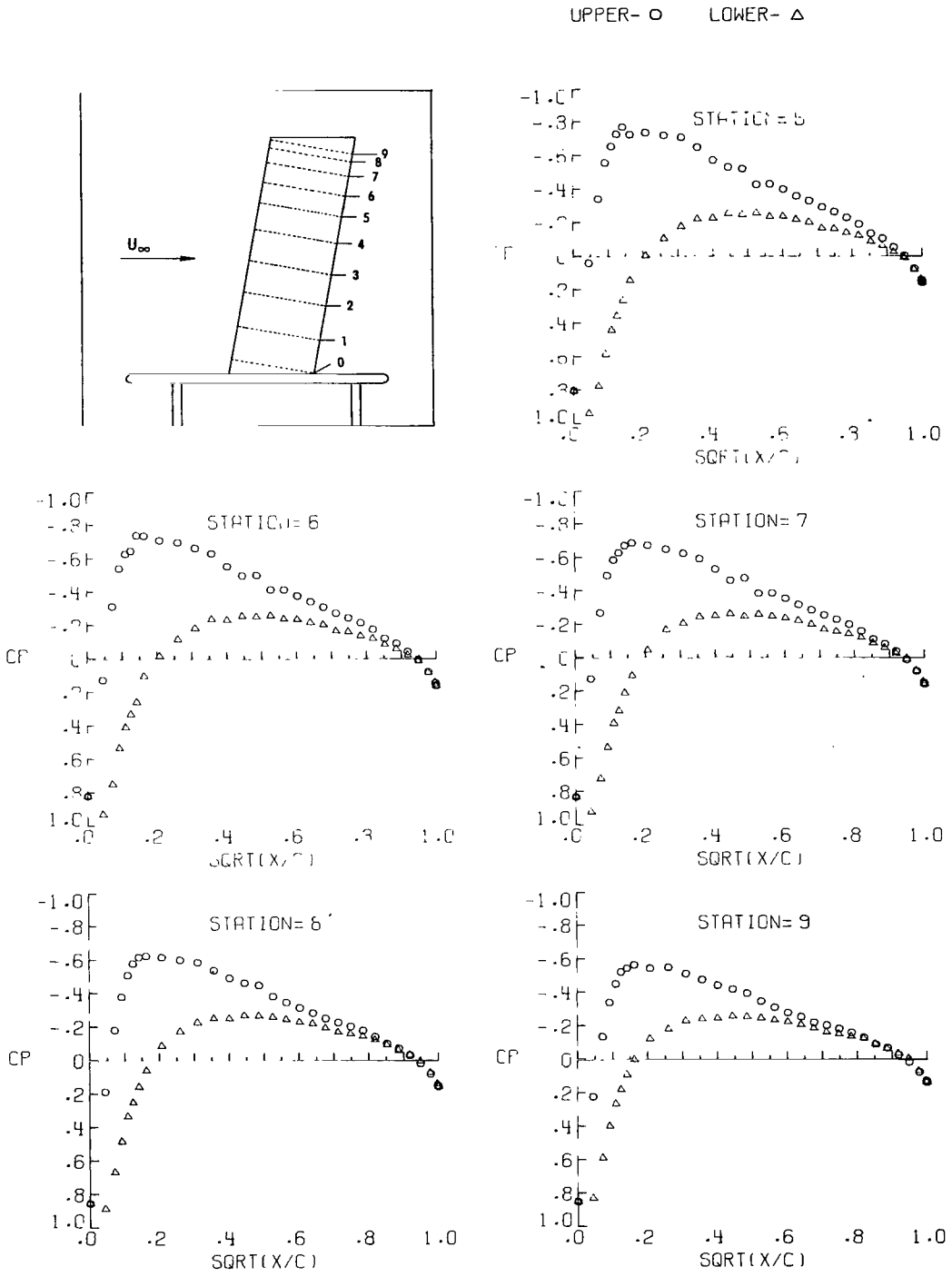

(e) Concluded.

Figure 4.- Continued.

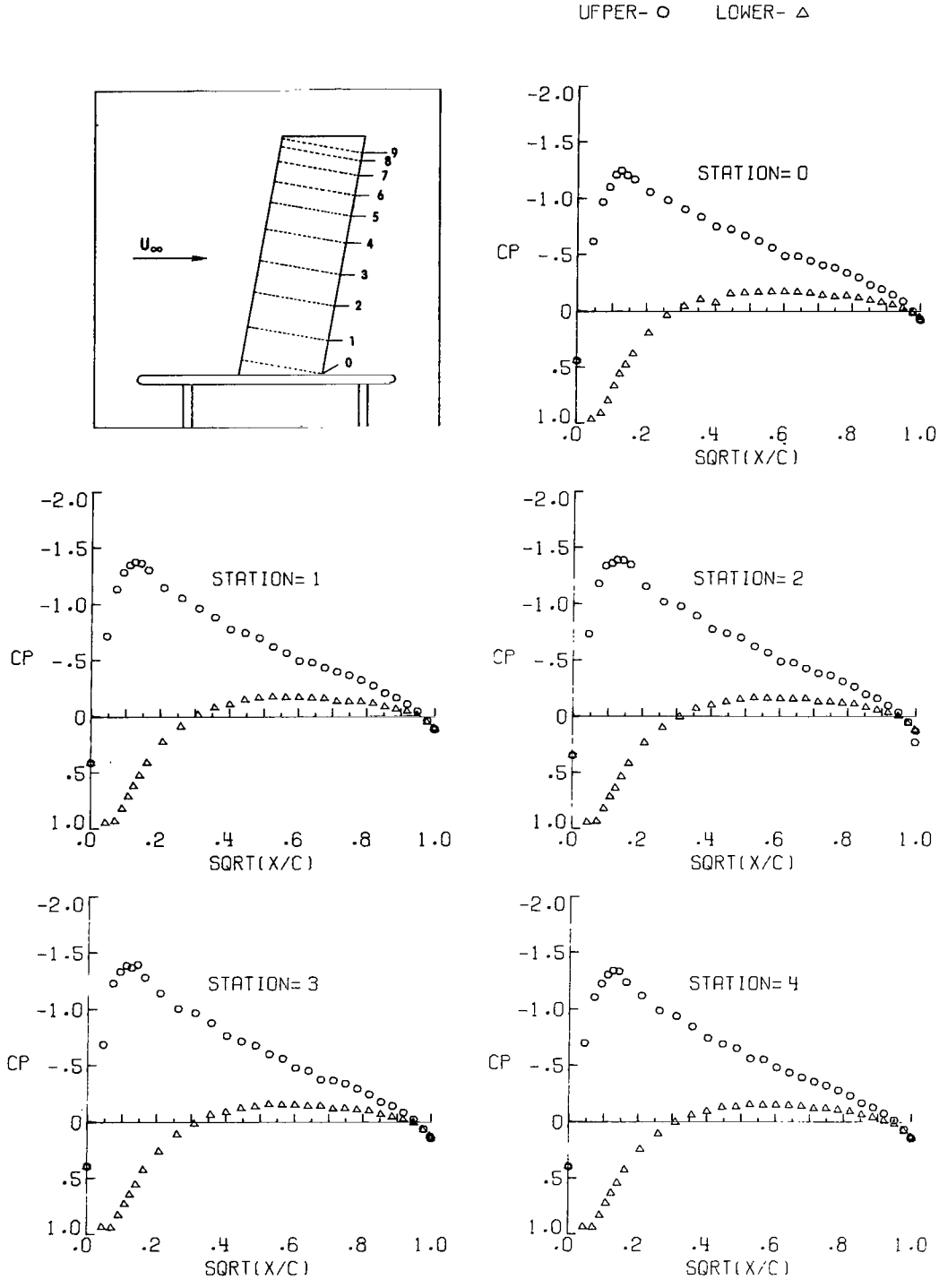

(f) $\alpha = 4.65^{\circ}$; $q_\infty = 2.46$ kPa (51.30 lb/ft^2).

Figure 4.- Continued.

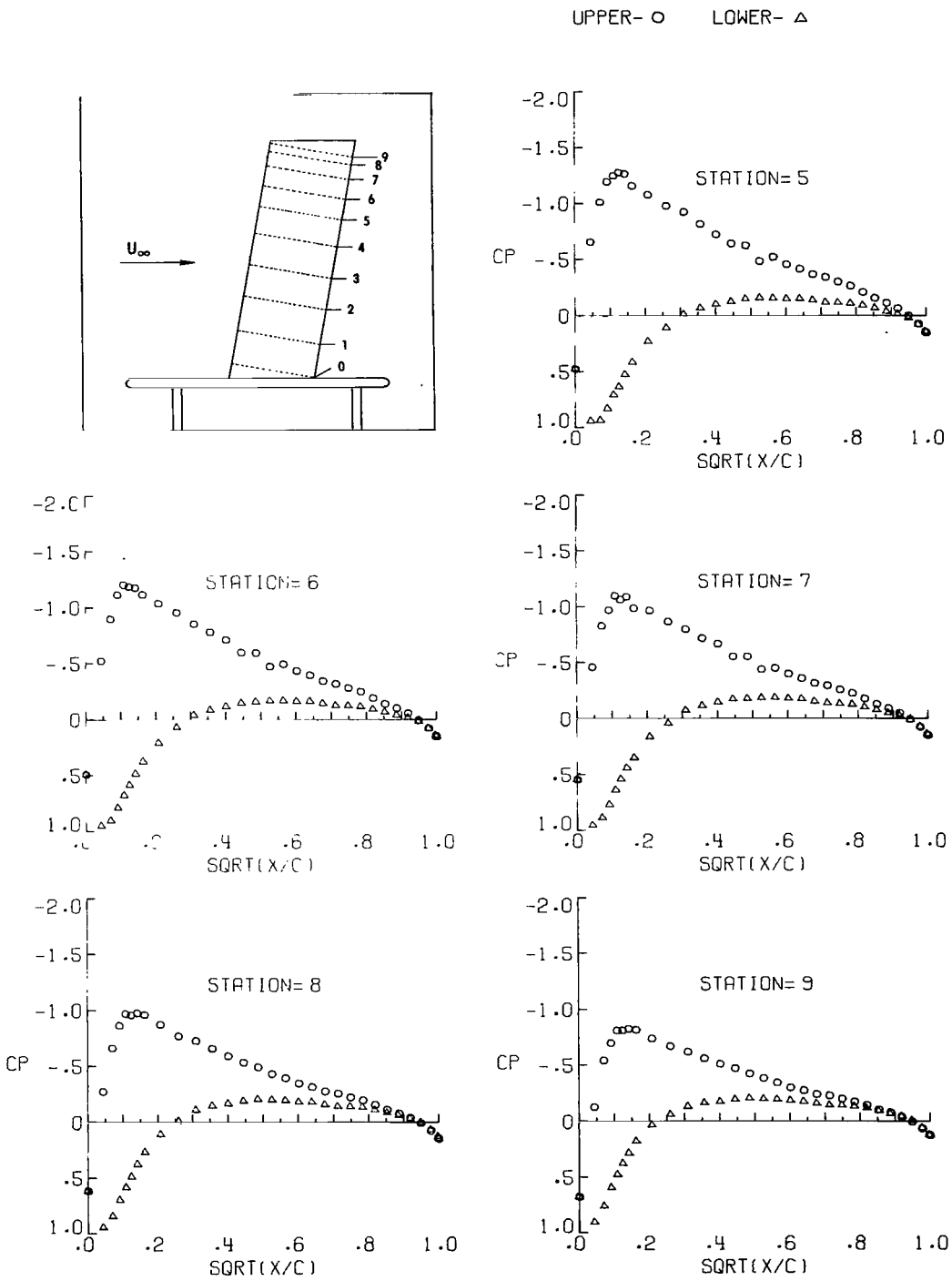

(f) Concluded.

Figure 4.- Continued.

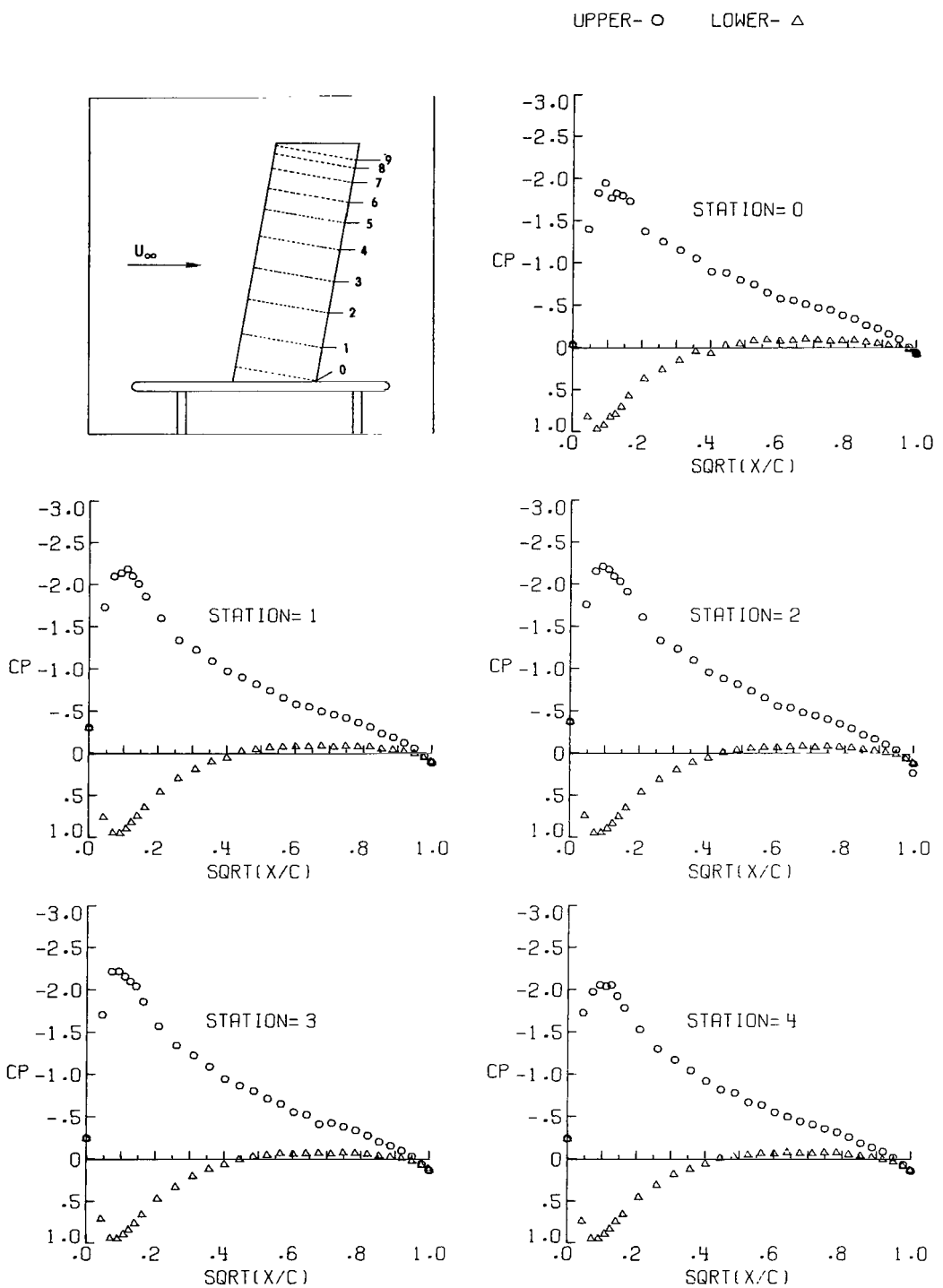

(g) $\alpha = 6.76^{\circ}$; $q_\infty = 2.46$ kPa (51.47 lb/ft^2).

Figure 4.- Continued.

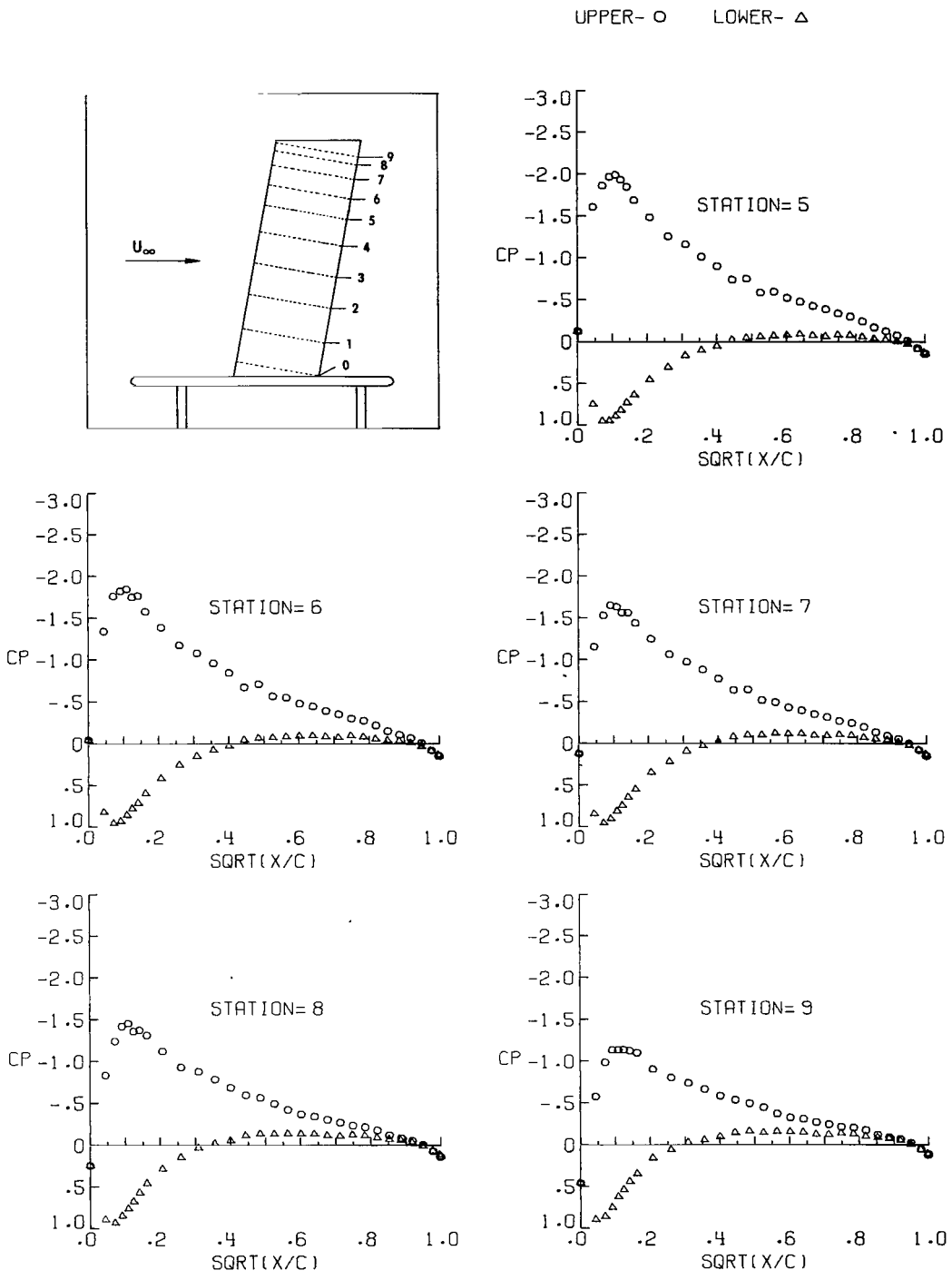

(g) Concluded.

Figure 4.- Continued.

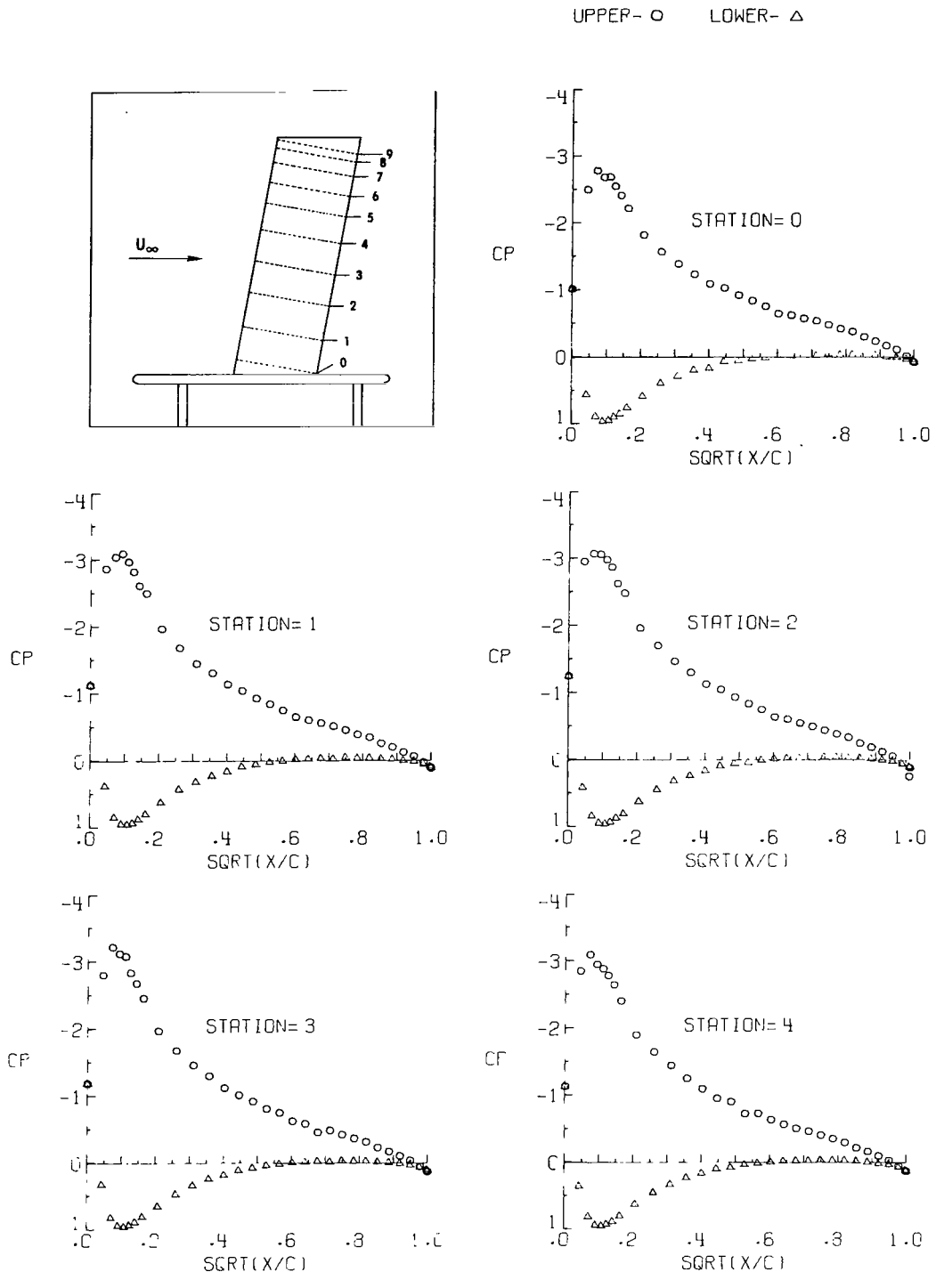

(h) $\alpha = 8.86^{\circ}$; $q_\infty = 2.45$ kPa (51.22 lb/ft^2).

Figure 4.- Continued.

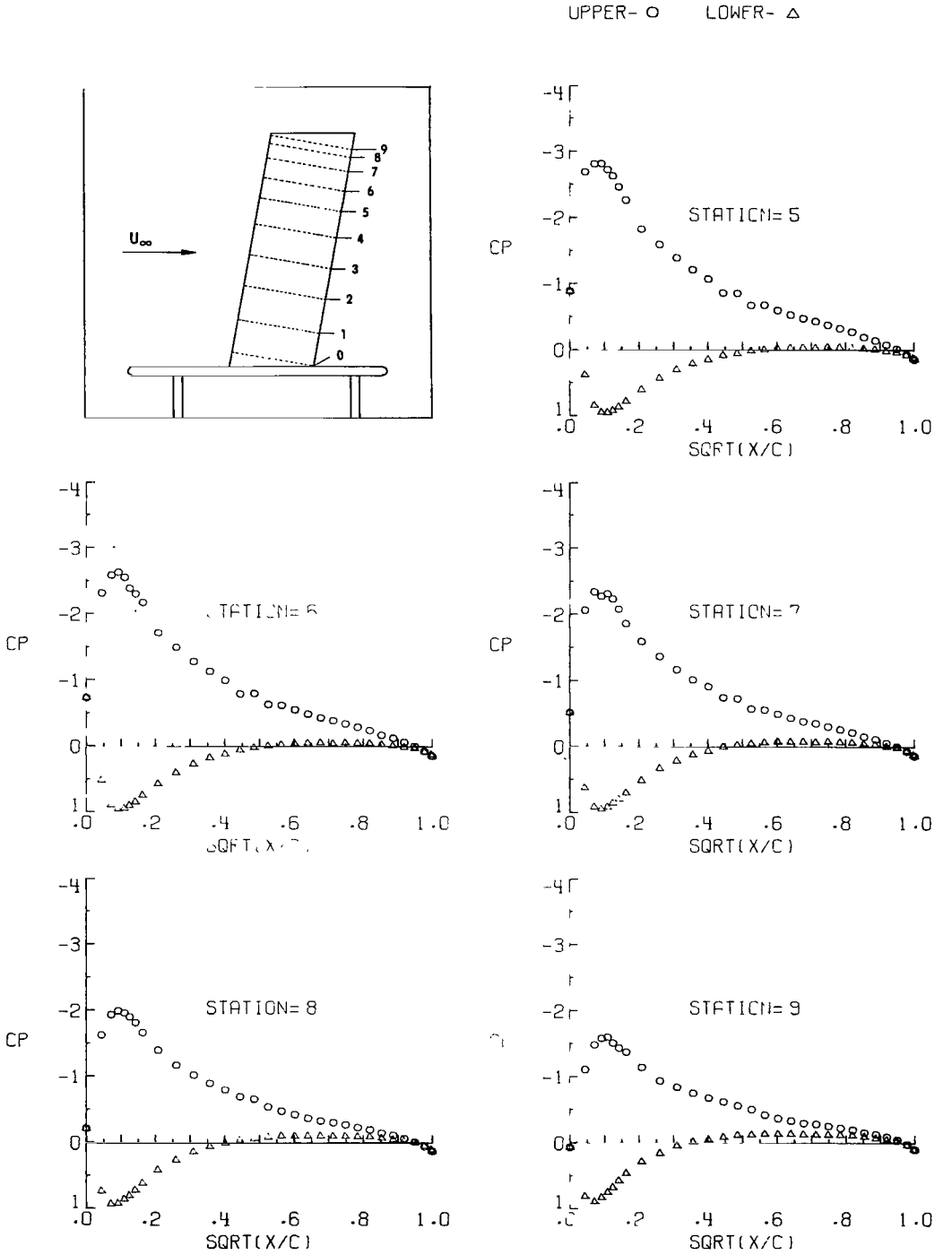

(h) Concluded.

Figure 4.- Continued.

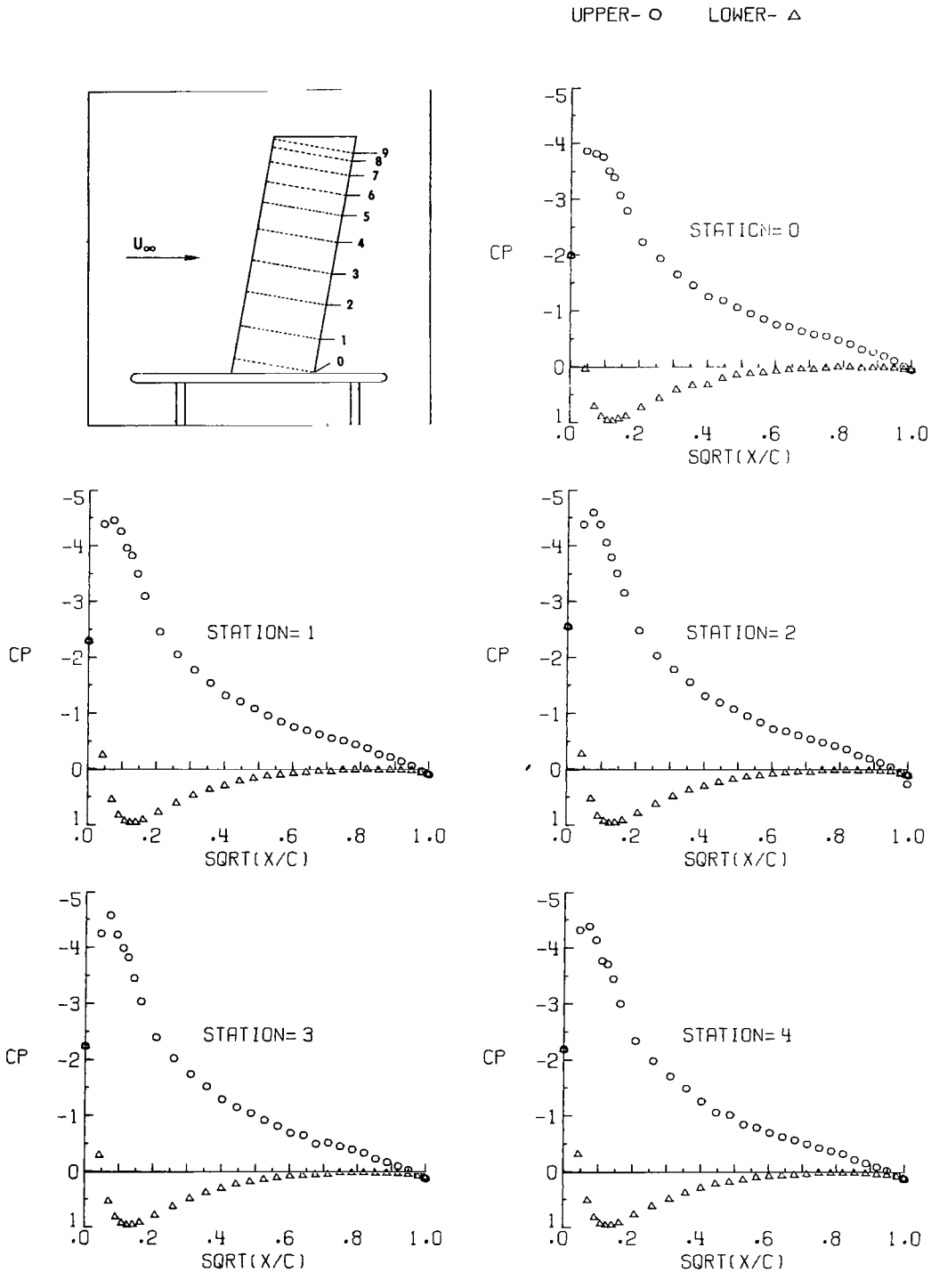

(i) $\alpha = 10.98^{o}$; $q_\infty = 2.45$ kPa (51.17 lb/ft^2).

Figure 4.- Continued.

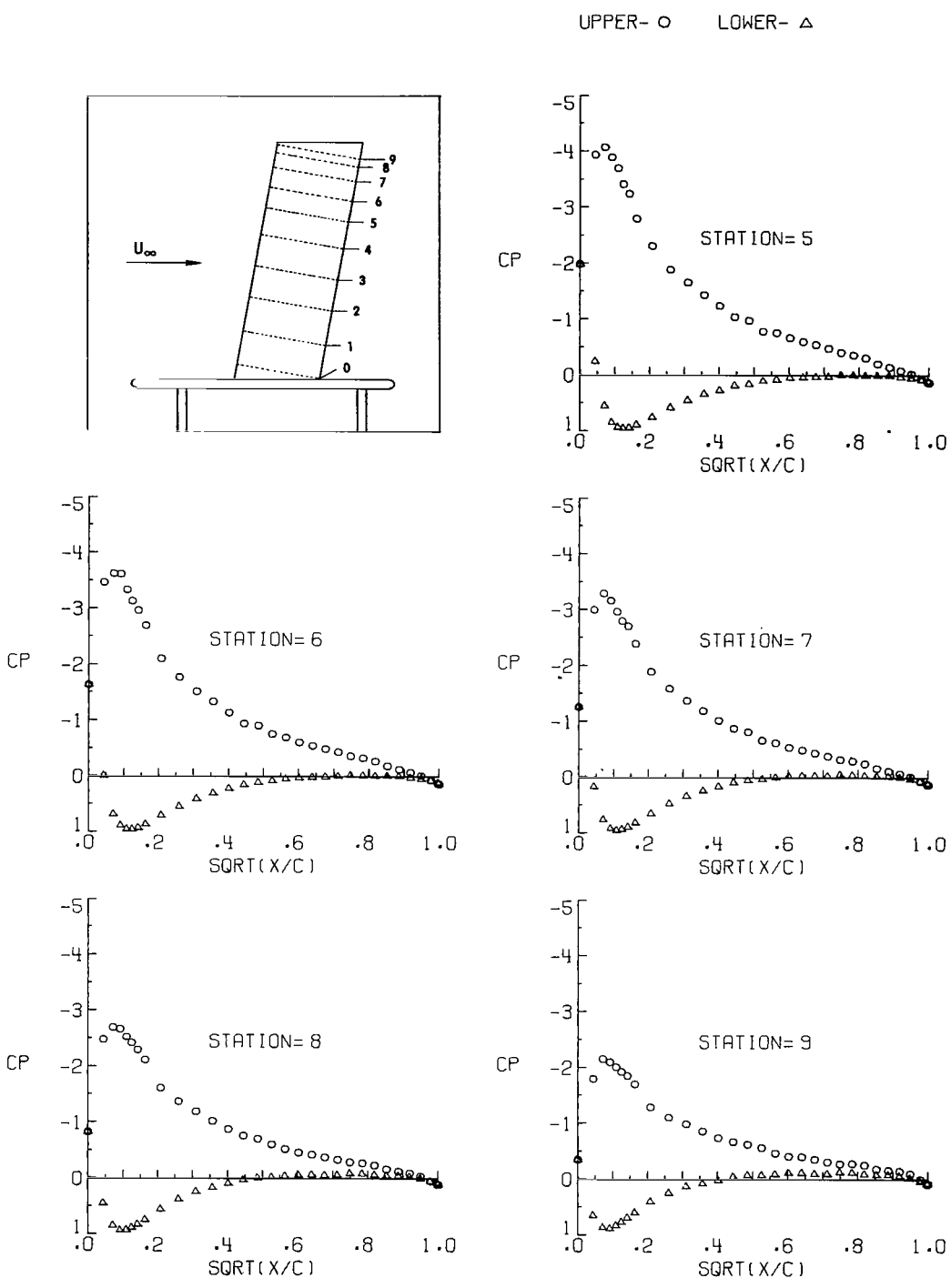

(i) Concluded.

Figure 4.- Continued.

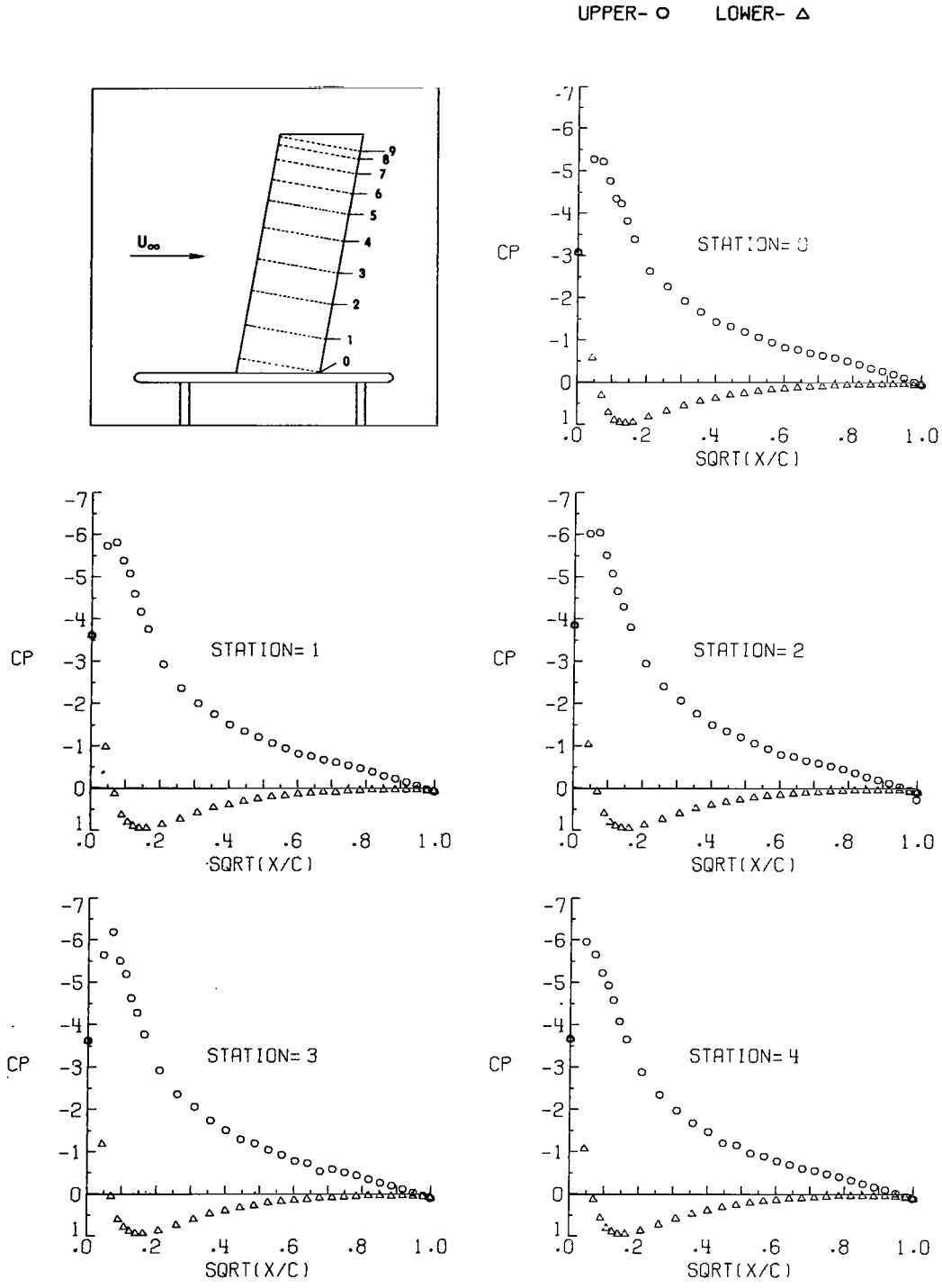

(j) $\alpha = 13.08^{o}$; $q_\infty = 2.46$ kPa (51.33 lb/ft^2).

Figure 4.- Continued.

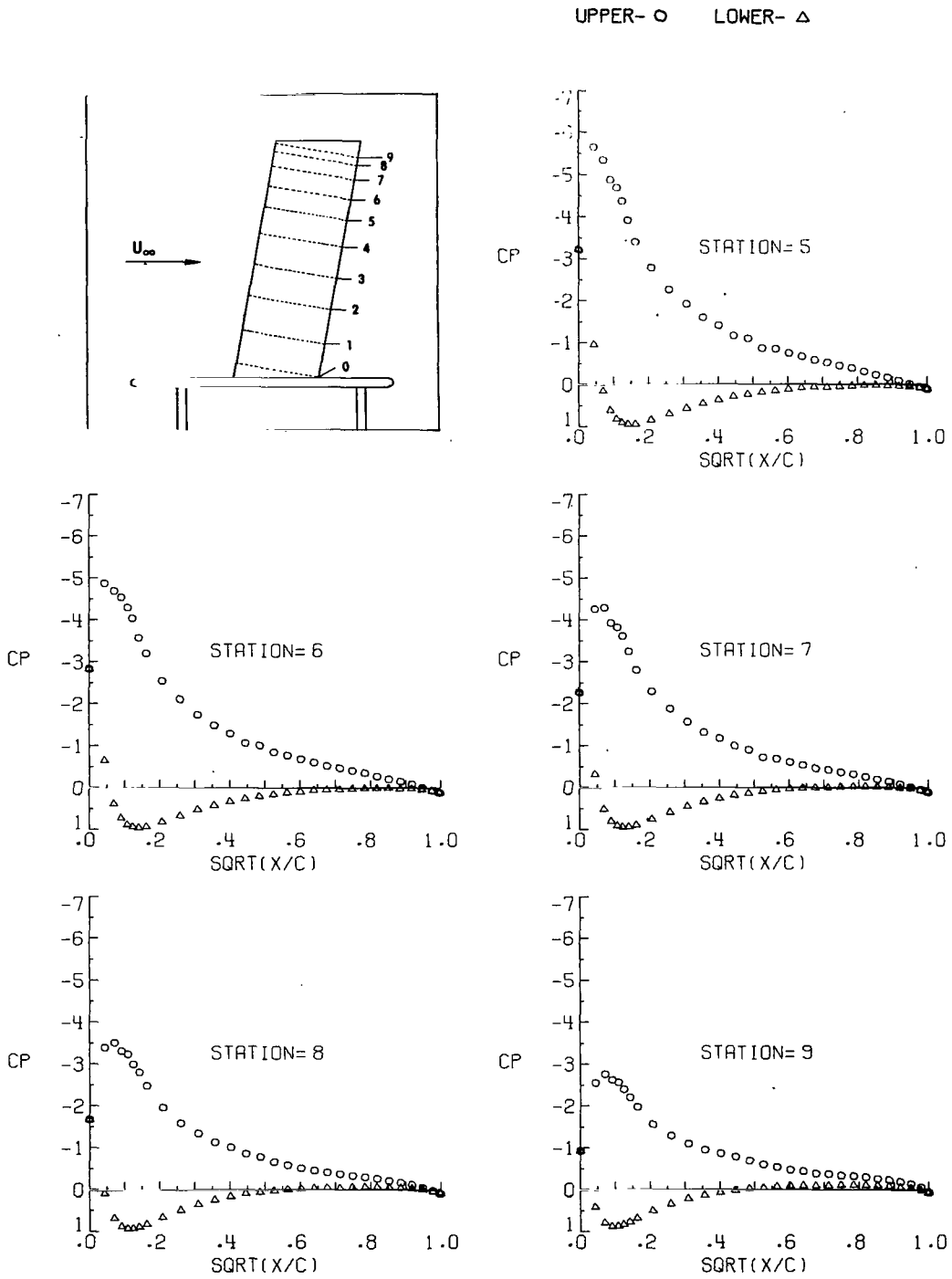

(j) Concluded.

Figure 4.- Continued.

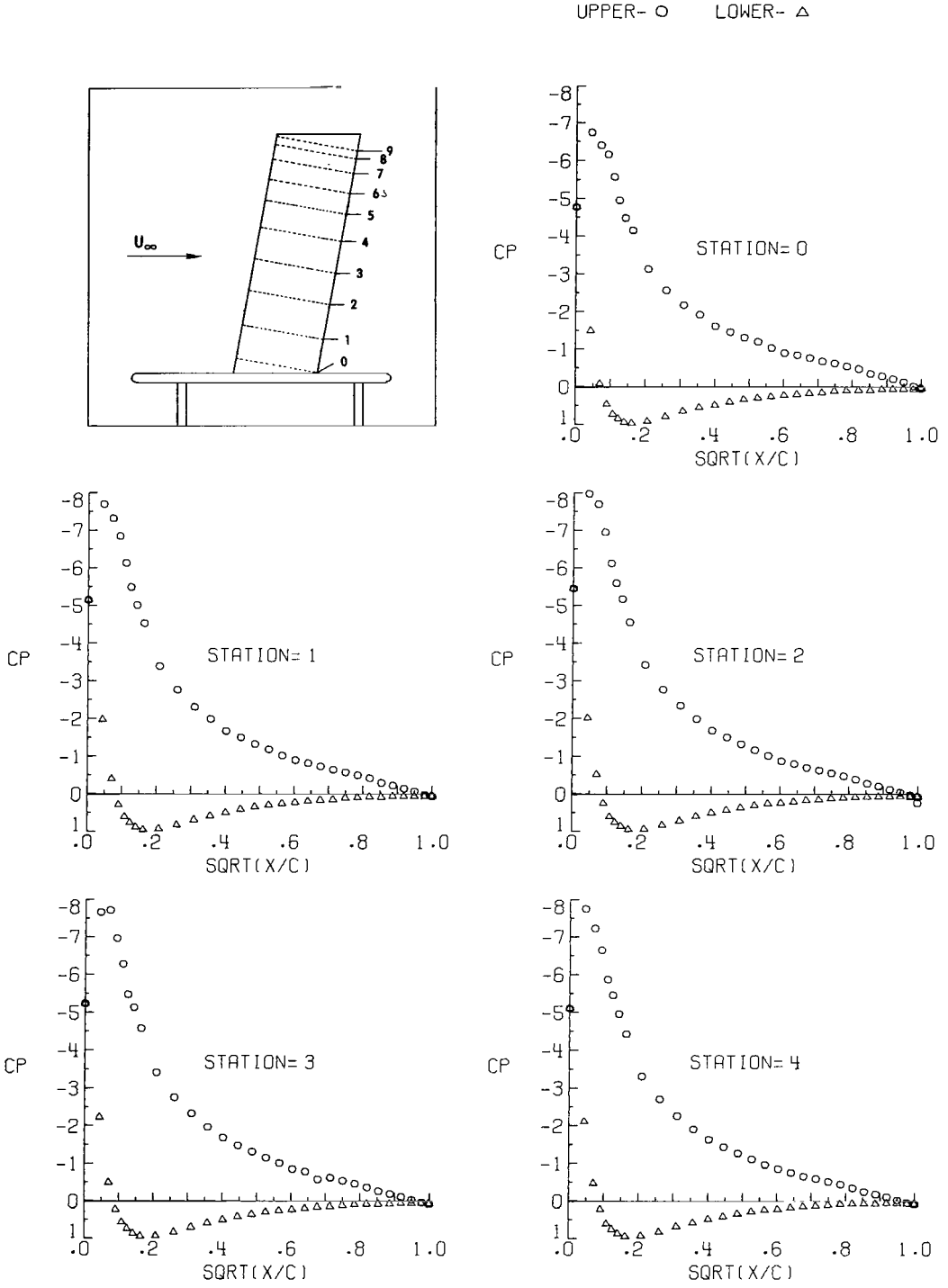

(k) $\alpha = 15.18^{o}$; $q_{\infty} = 2.46$ kPa (51.45 lb/ft^2).

Figure 4.- Continued.

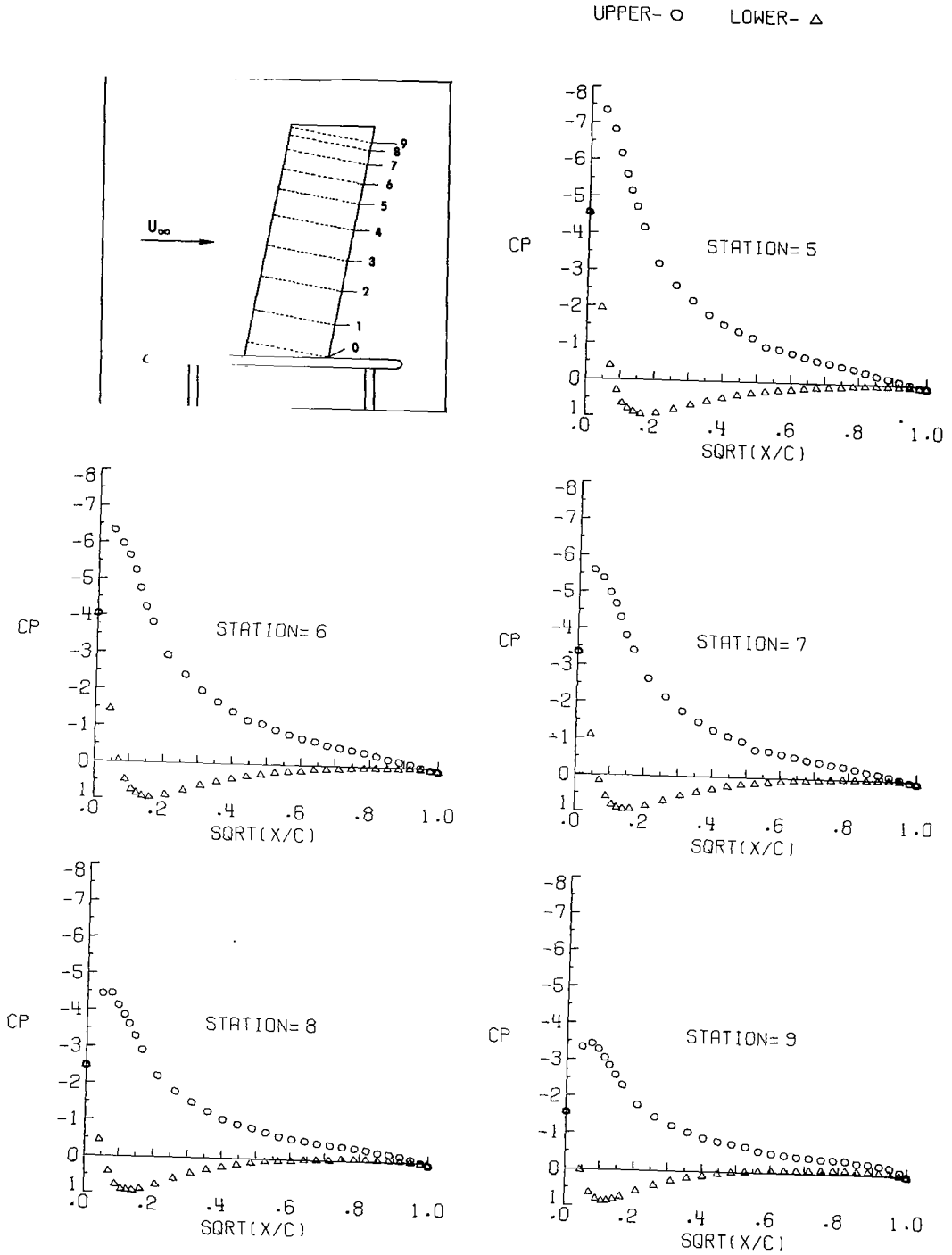

(k) Concluded.

Figure 4.- Continued.

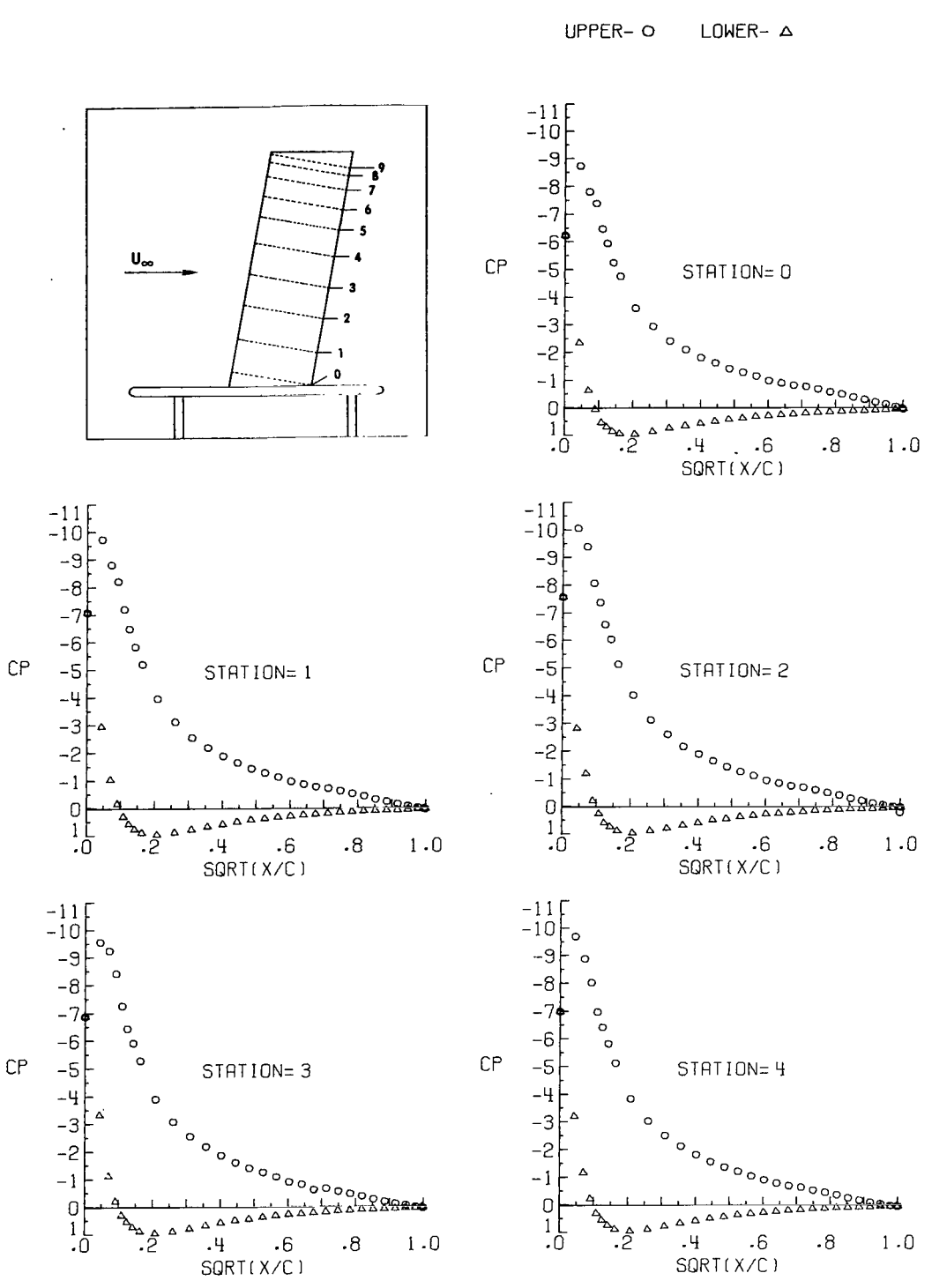

(1) $\alpha = 17.28^{o}$; $q_\infty = 2.46$ kPa (51.34 lb/ft^2).

Figure 4.- Continued.

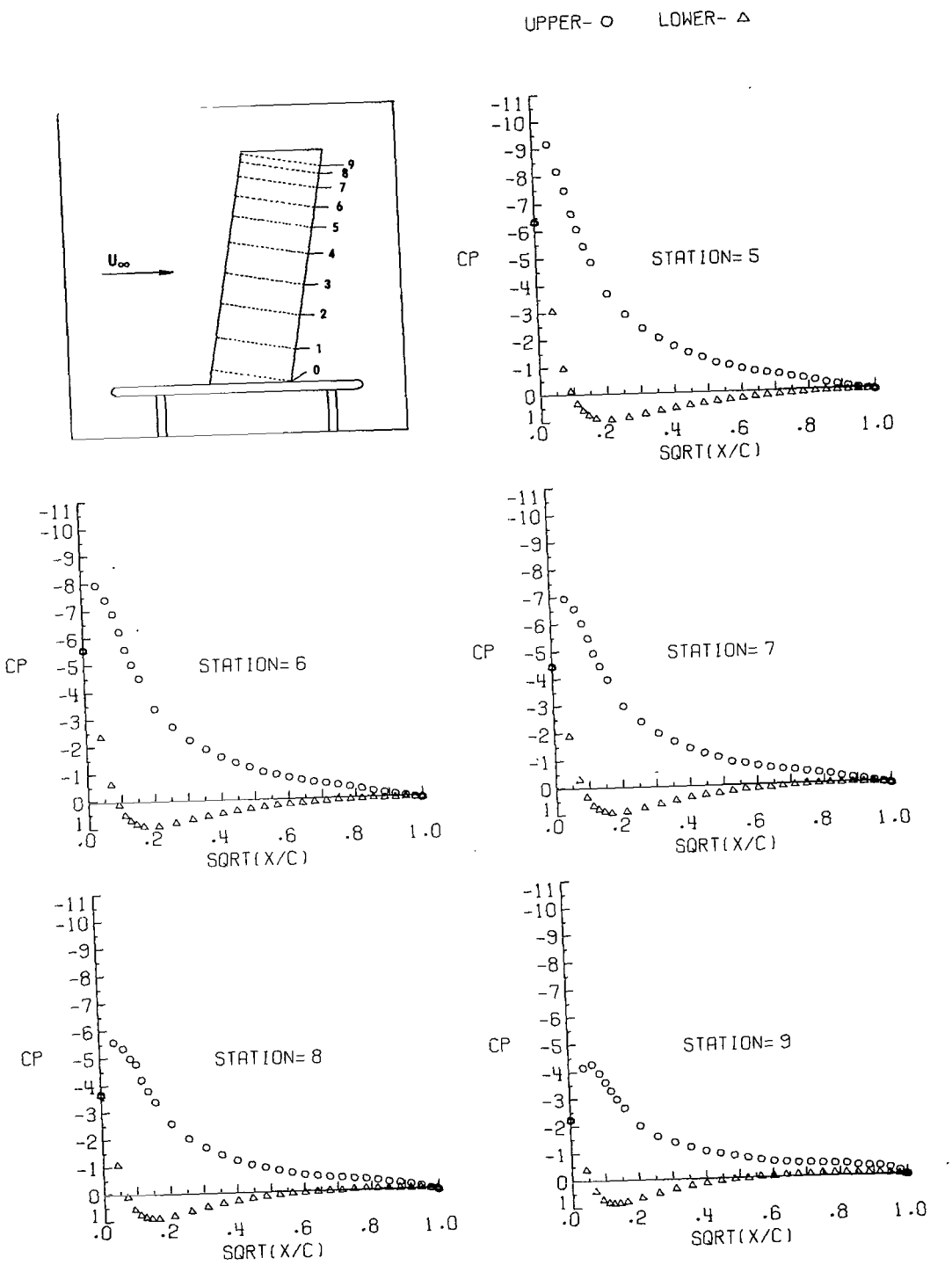

(1) Concluded.

Figure 4.- Continued.

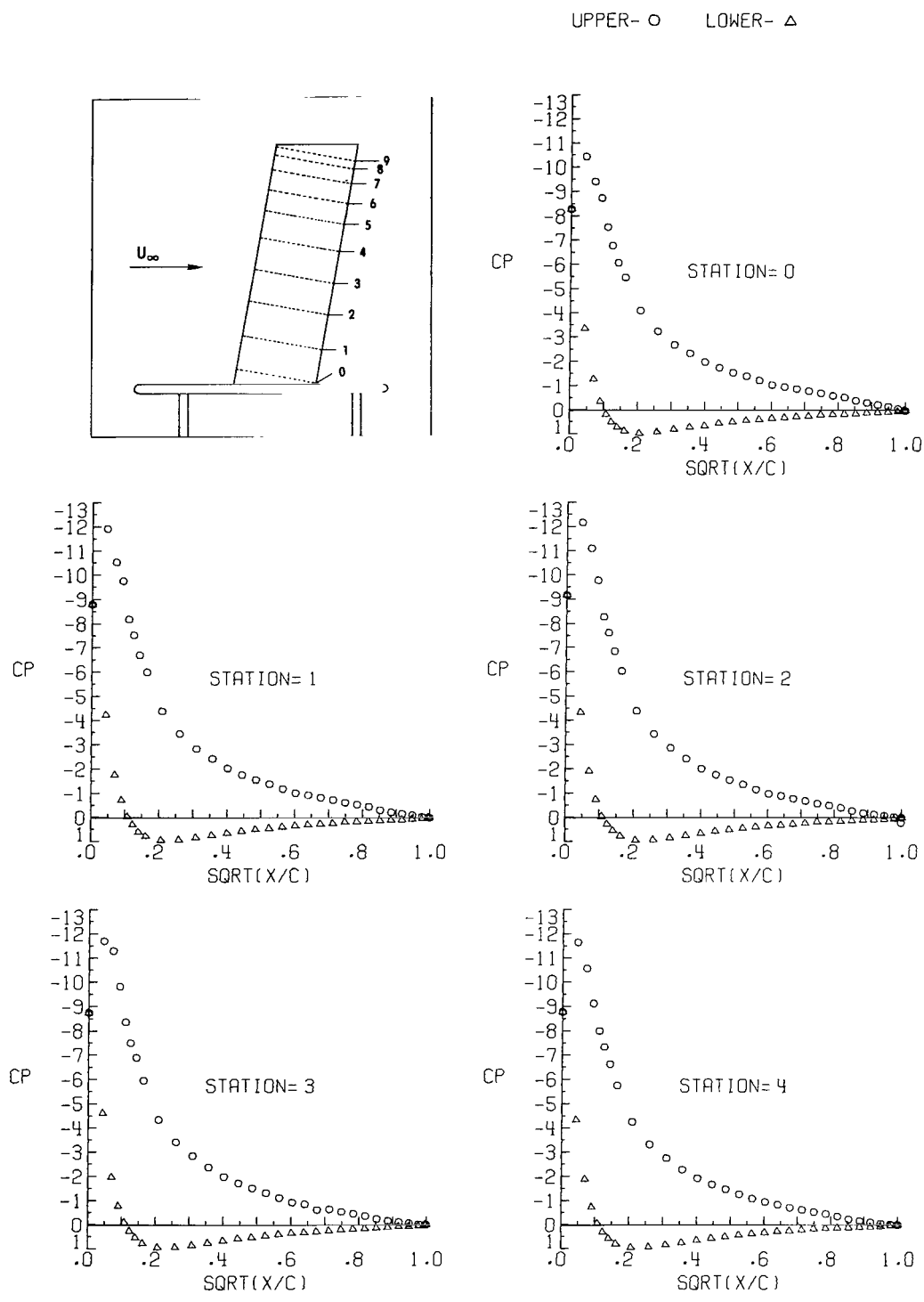

(m) $\alpha = 19.35^{o}$; $q_\infty = 2.45$ kPa (51.17 lb/ft^2).

Figure 4.- Continued.

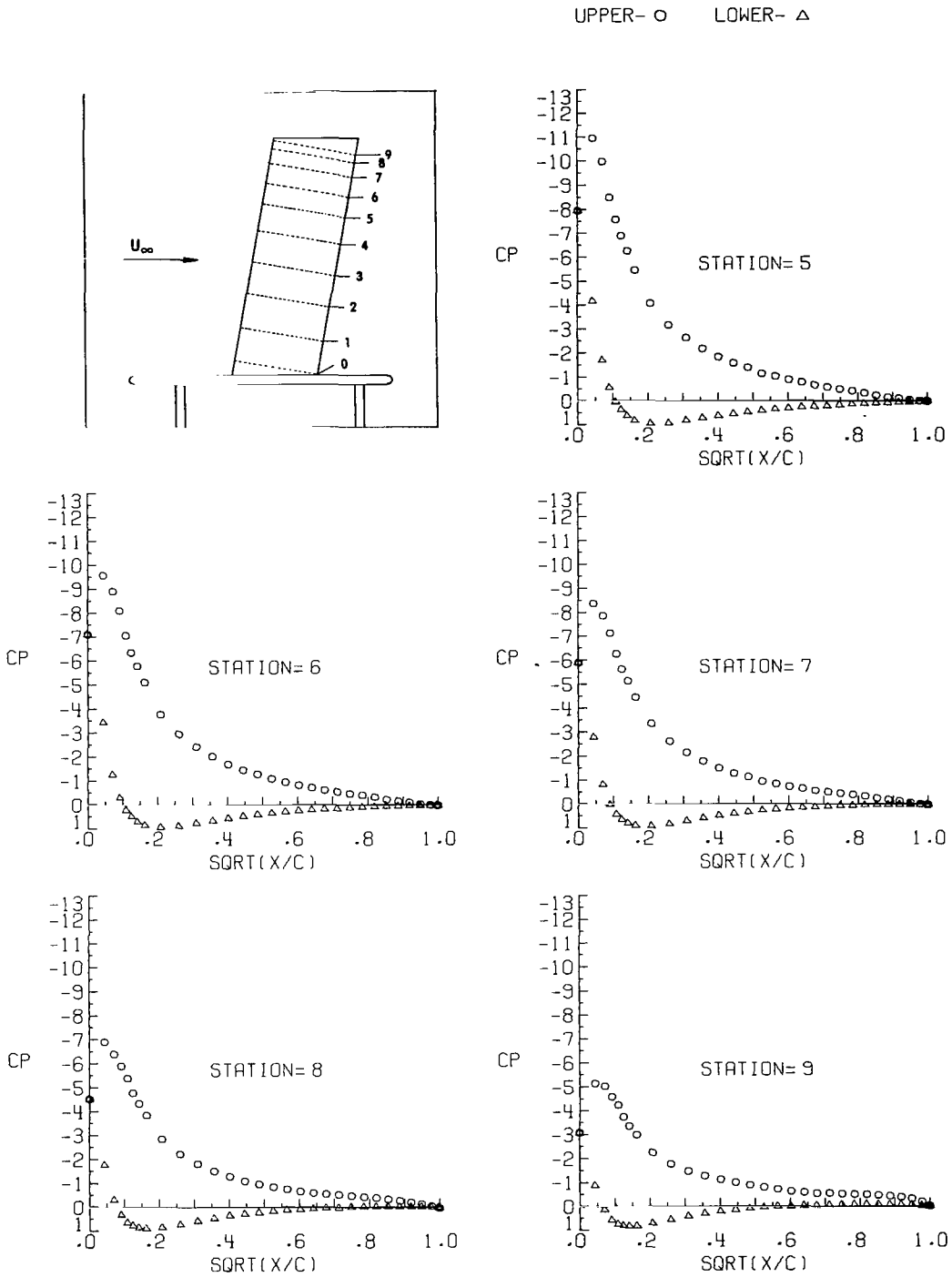

(m) Concluded.

Figure 4.- Continued.

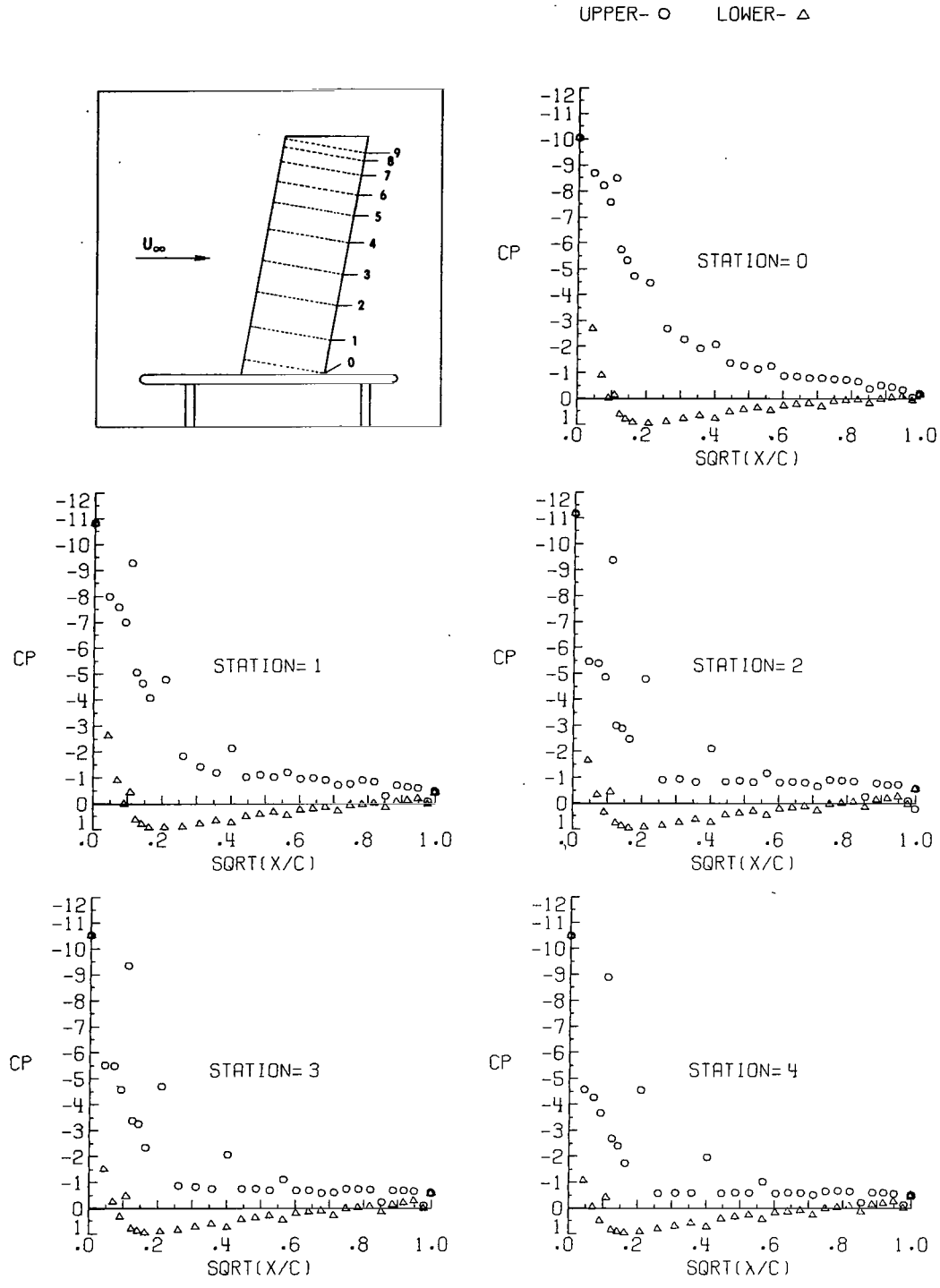

(n) $\alpha = 21.18^{\circ}$; $q_\infty = 2.47$ kPa (51.68 lb/ft^2).

Figure 4.- Continued.

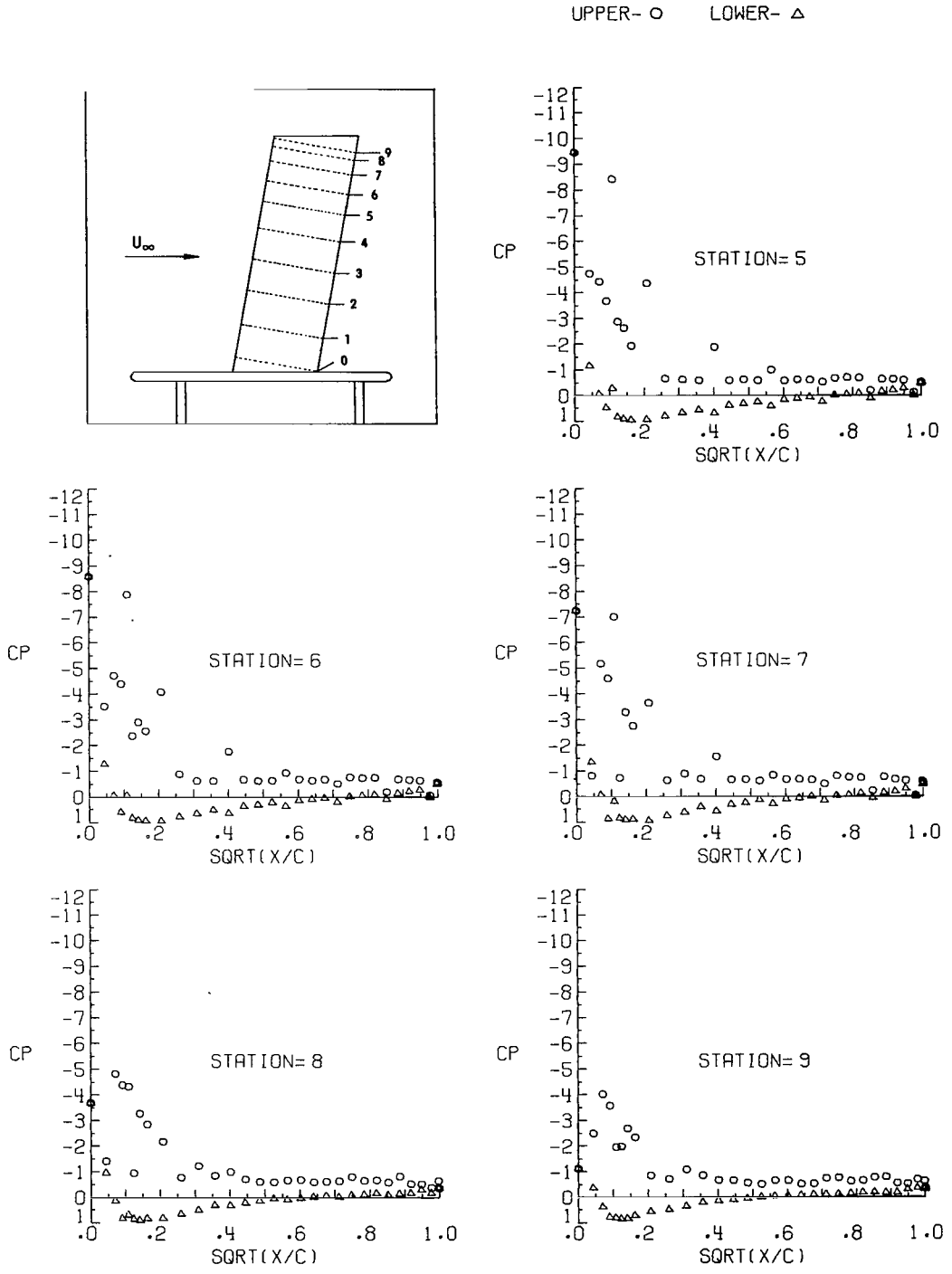

(n) Concluded.

Figure 4.- Concluded.

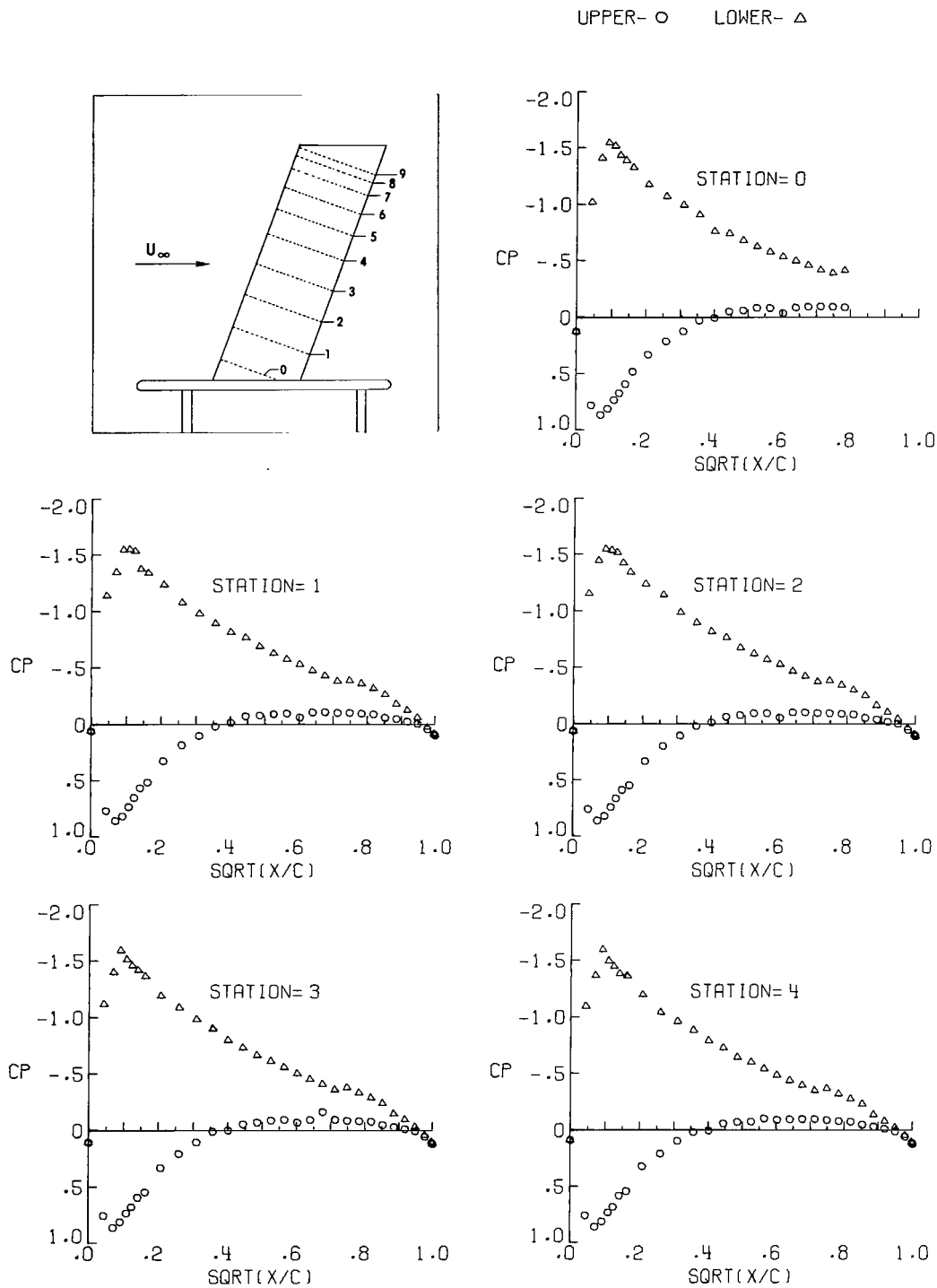

(a) $\alpha = -5.87^{\circ}$; $q_\infty = 2.44$ kPa (50.97 lb/ft^2).

Figure 5.- Pressure distributions at sweep angle of 20°.

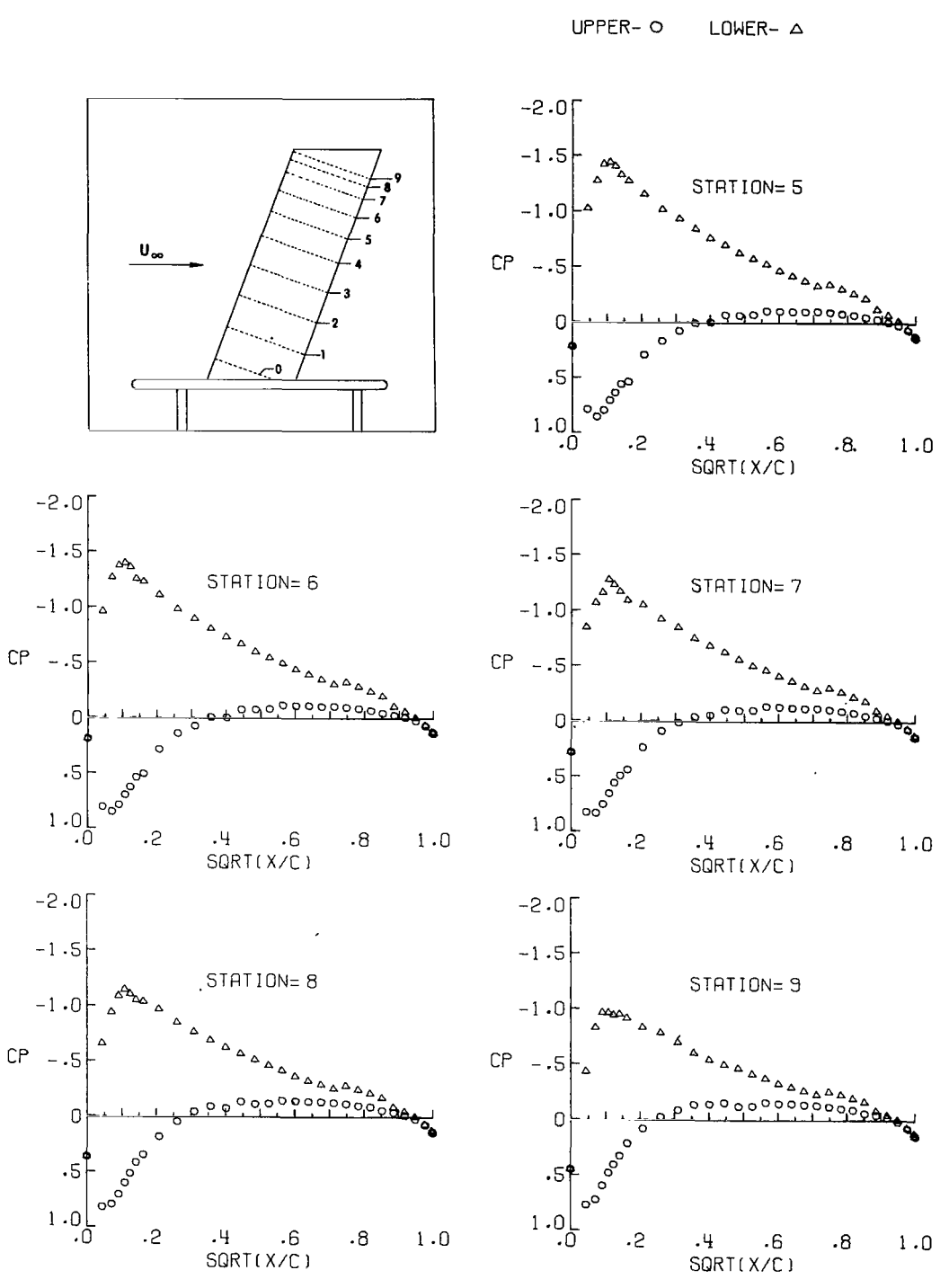

(a) Concluded.

Figure 5.- Continued.

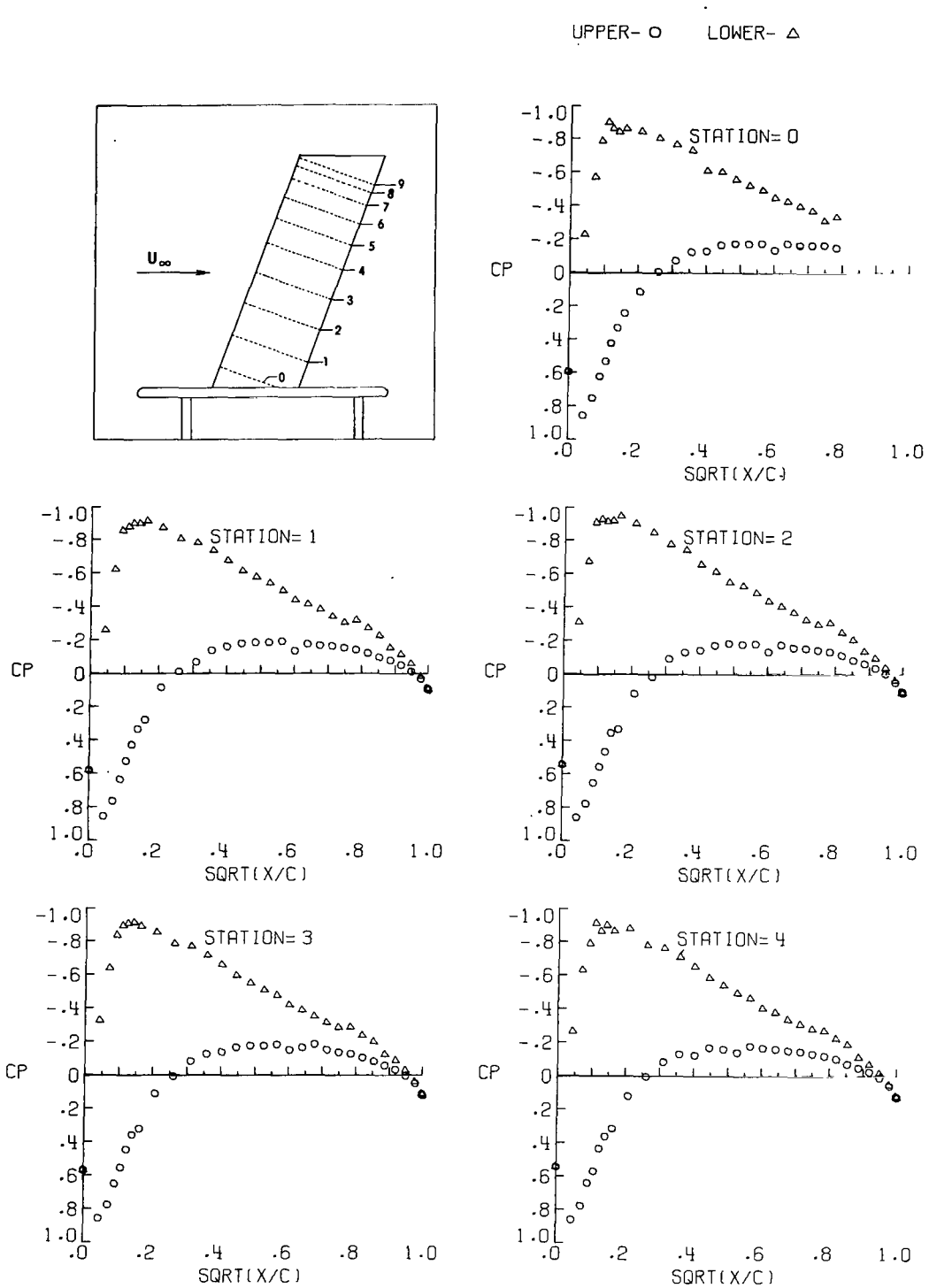

(b) $\alpha = -3.77^{o}$; $q_\infty = 2.46$ kPa (51.44 lb/ft^2).

Figure 5.- Continued.

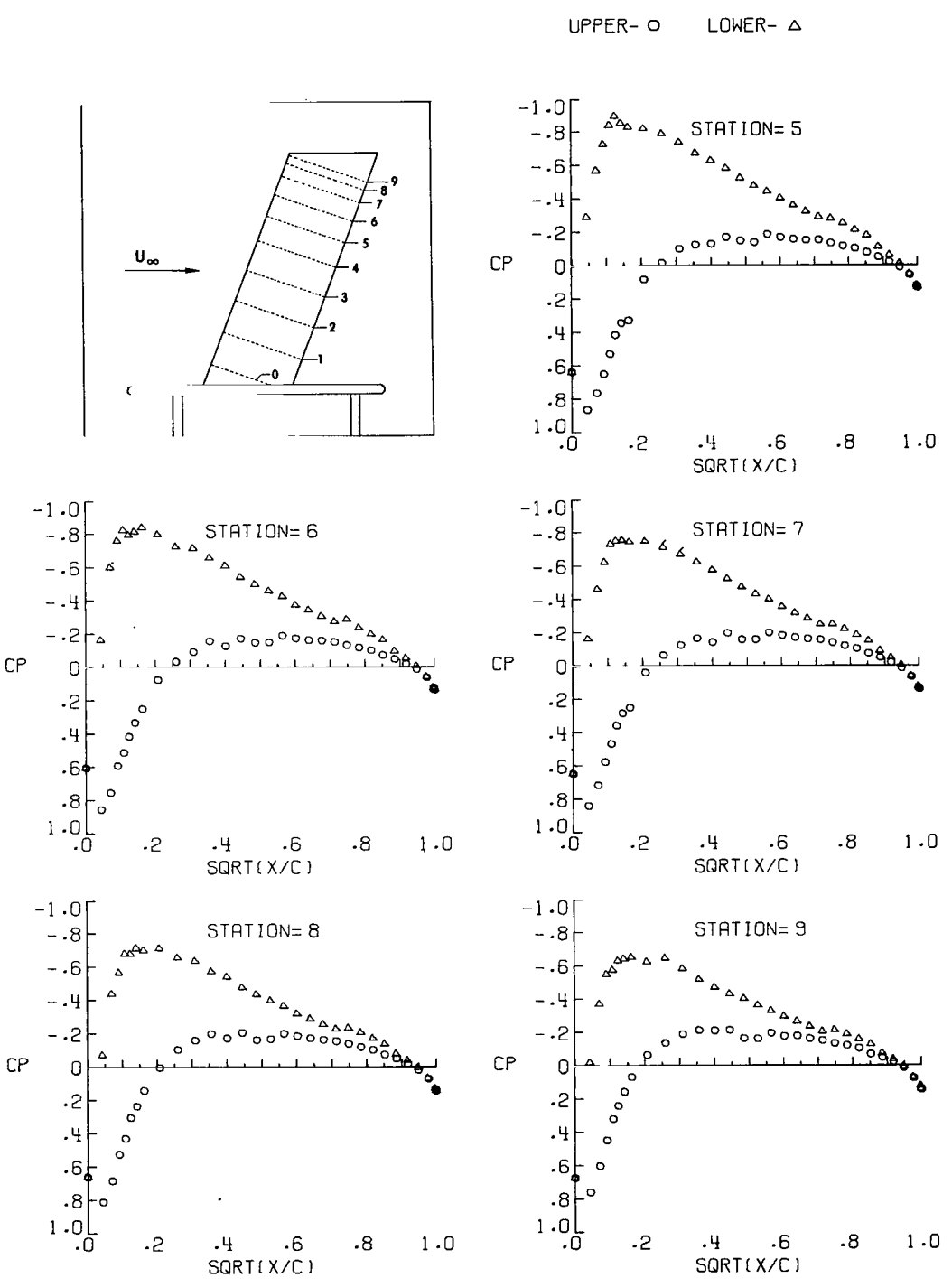

(b) Concluded.

Figure 5.- Continued.

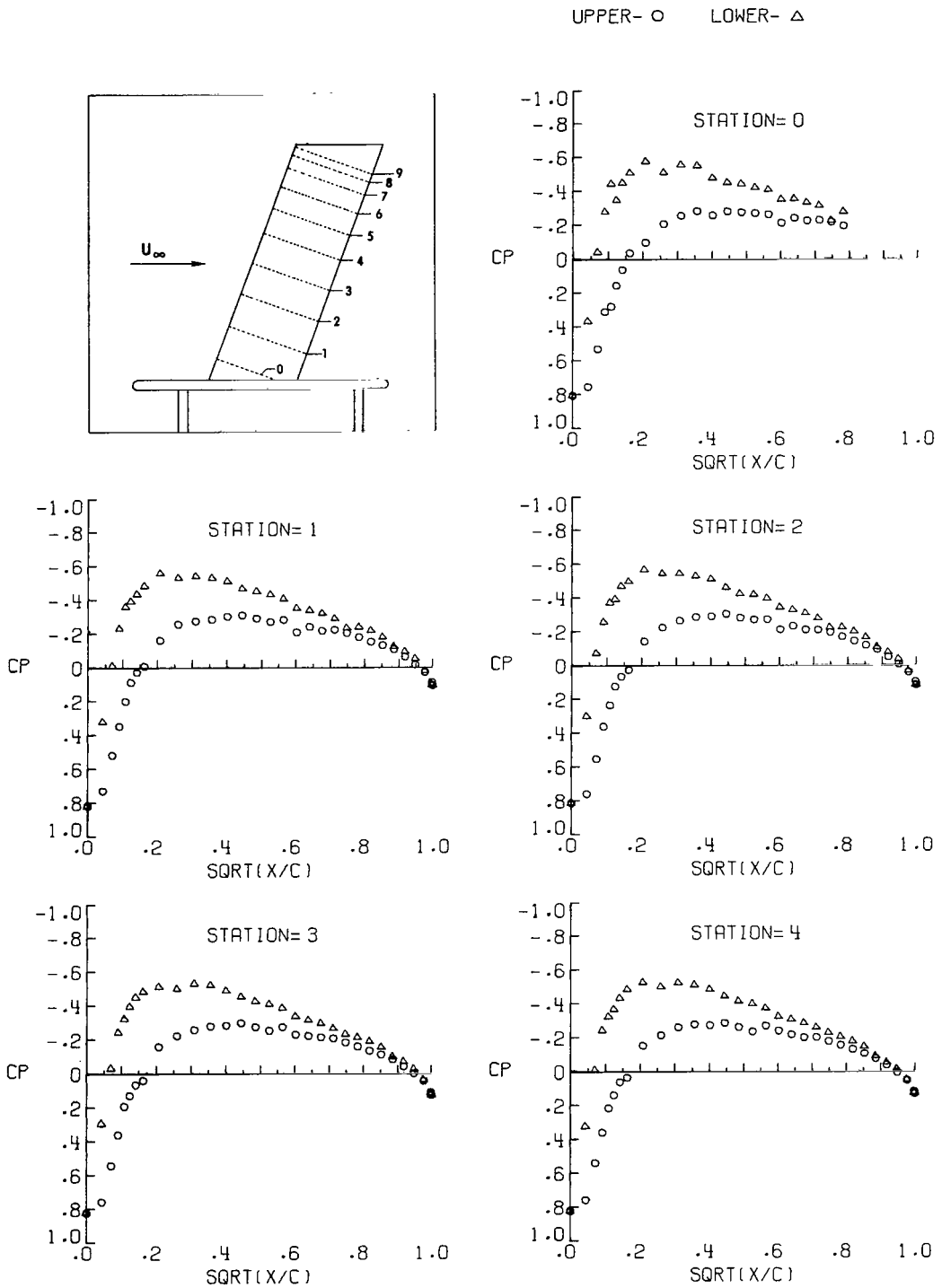

(c) $\alpha = -1.65^{o}$; $q_\infty = 2.46$ kPa (51.48 lb/ft^2).

Figure 5.- Continued.

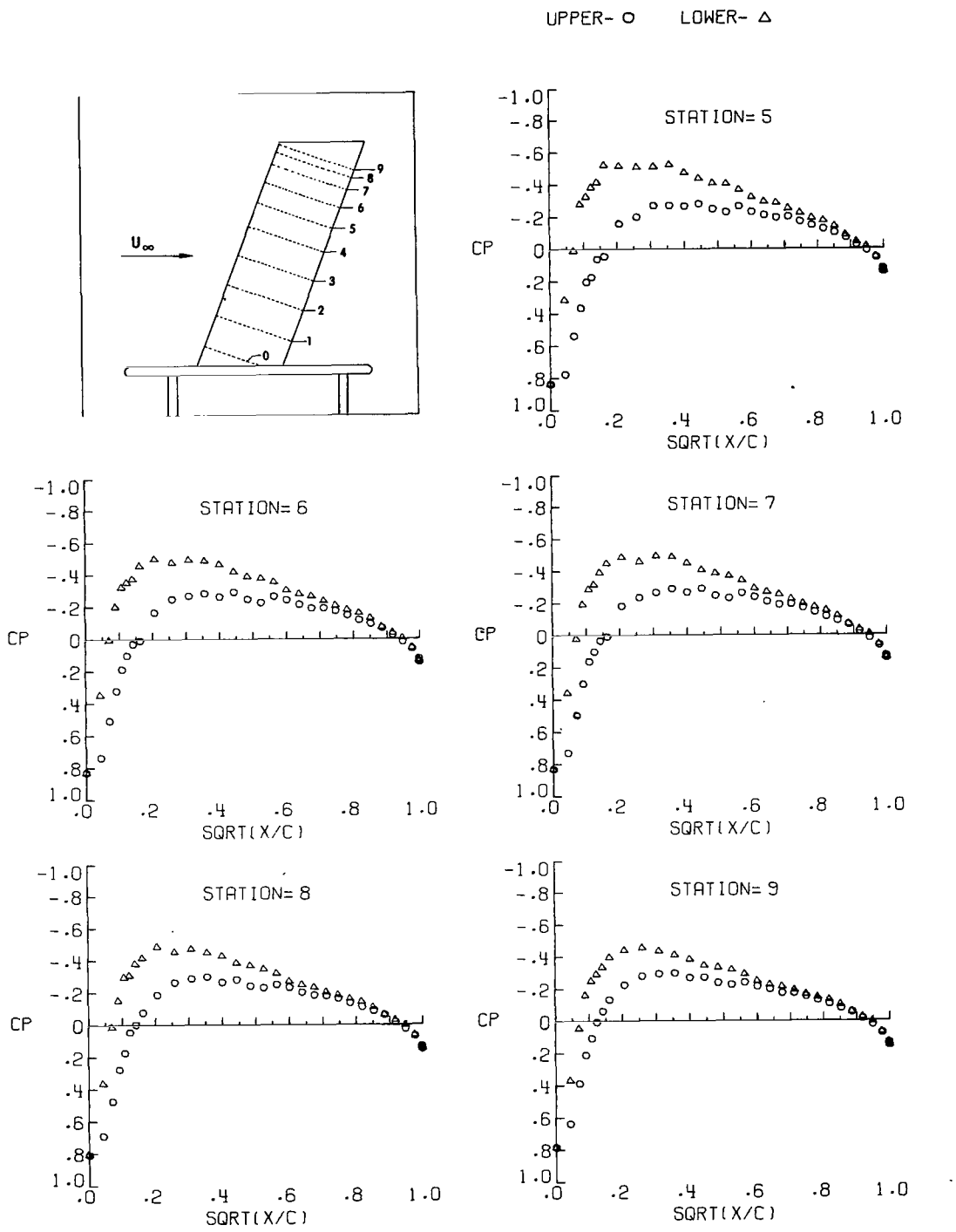

(c) Concluded.

Figure 5.- Continued.

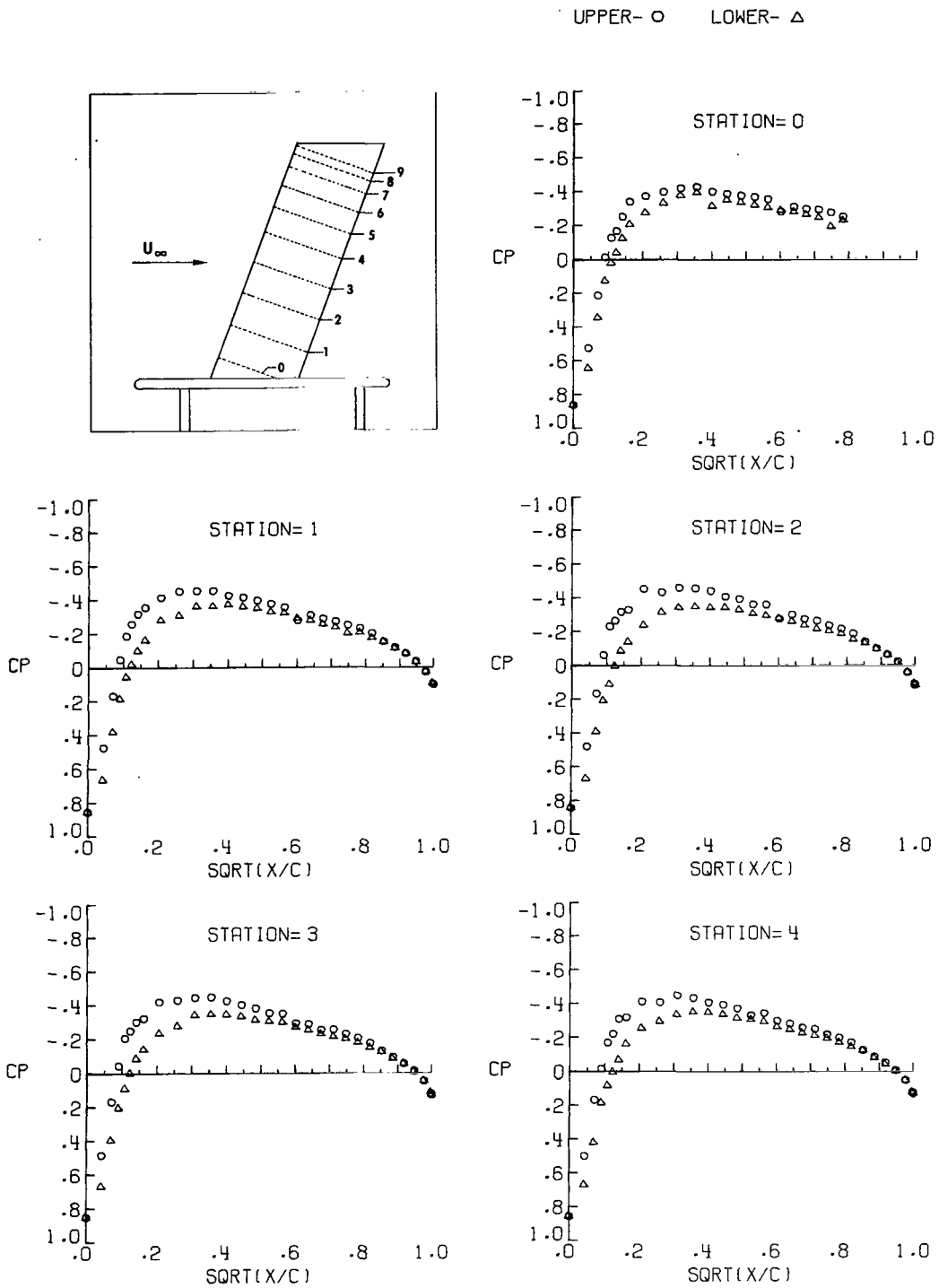

(d) $\alpha = 0.43^{o}$; $q_\infty = 2.46$ kPa (51.30 lb/ft^2).

Figure 5.- Continued.

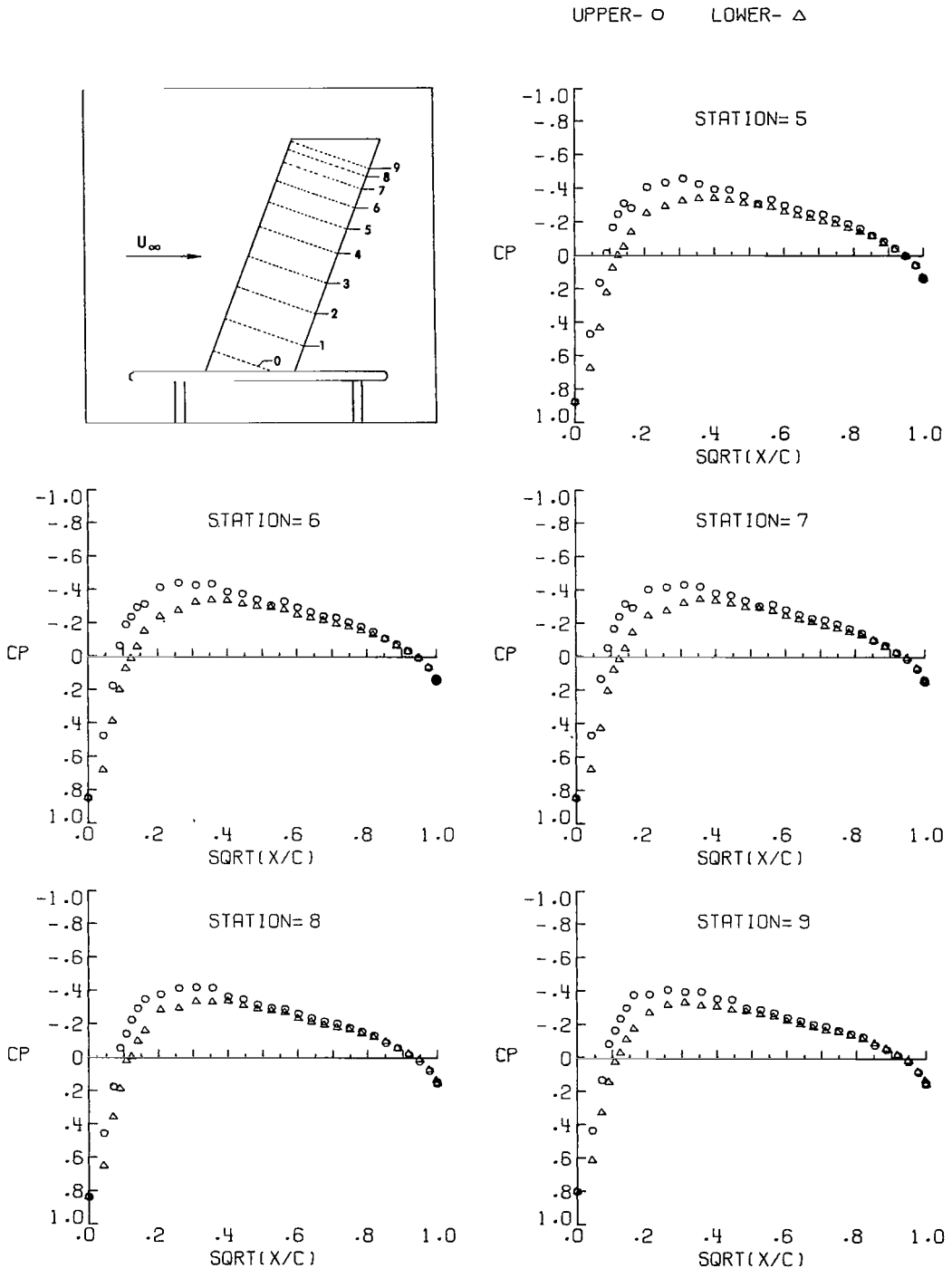

(d) Concluded.

Figure 5.- Continued.

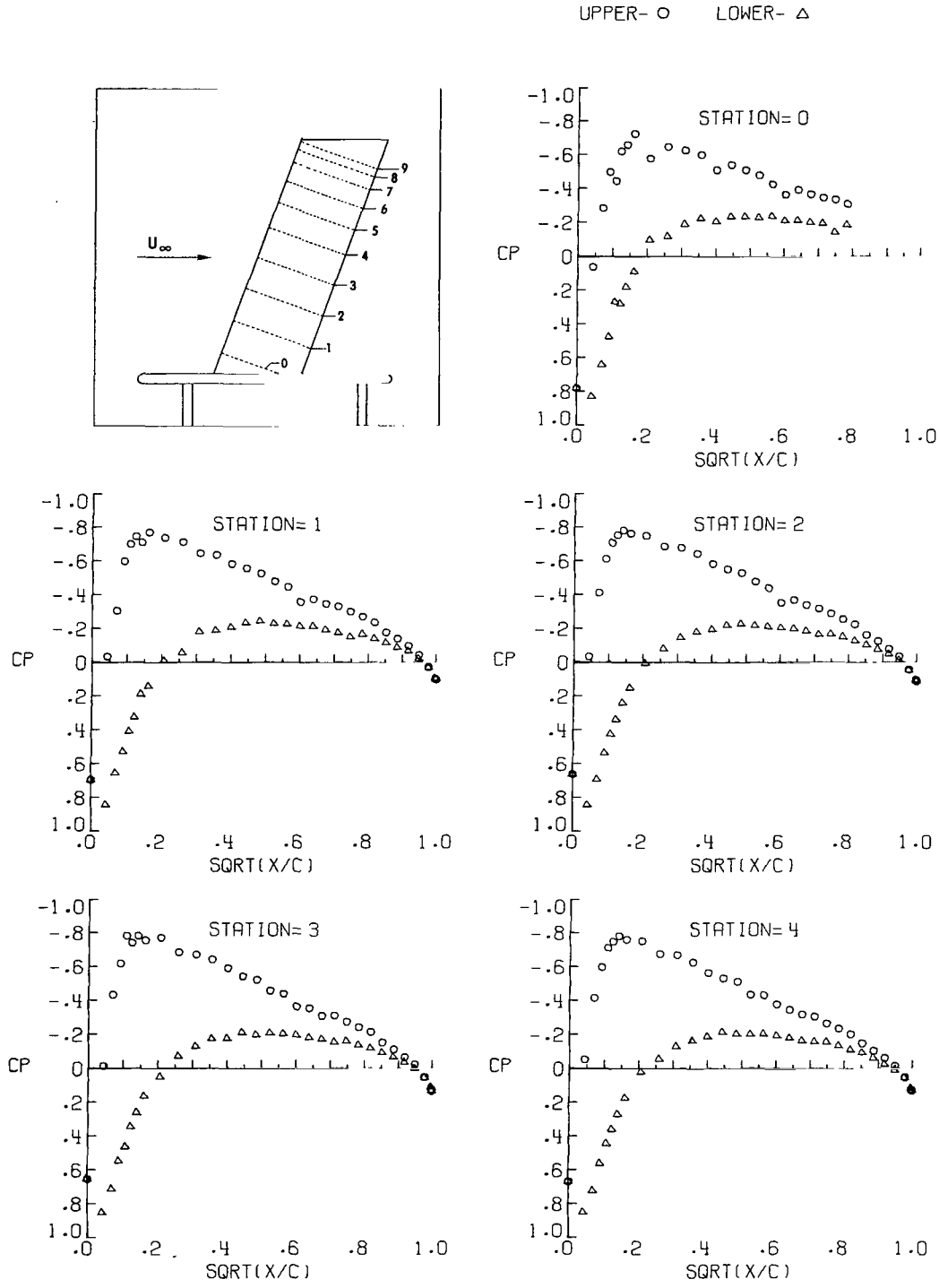

(e) $\alpha = 2.59^{\circ}$; $q_\infty = 2.45$ kPa (51.21 lb/ft^2).

Figure 5.- Continued.

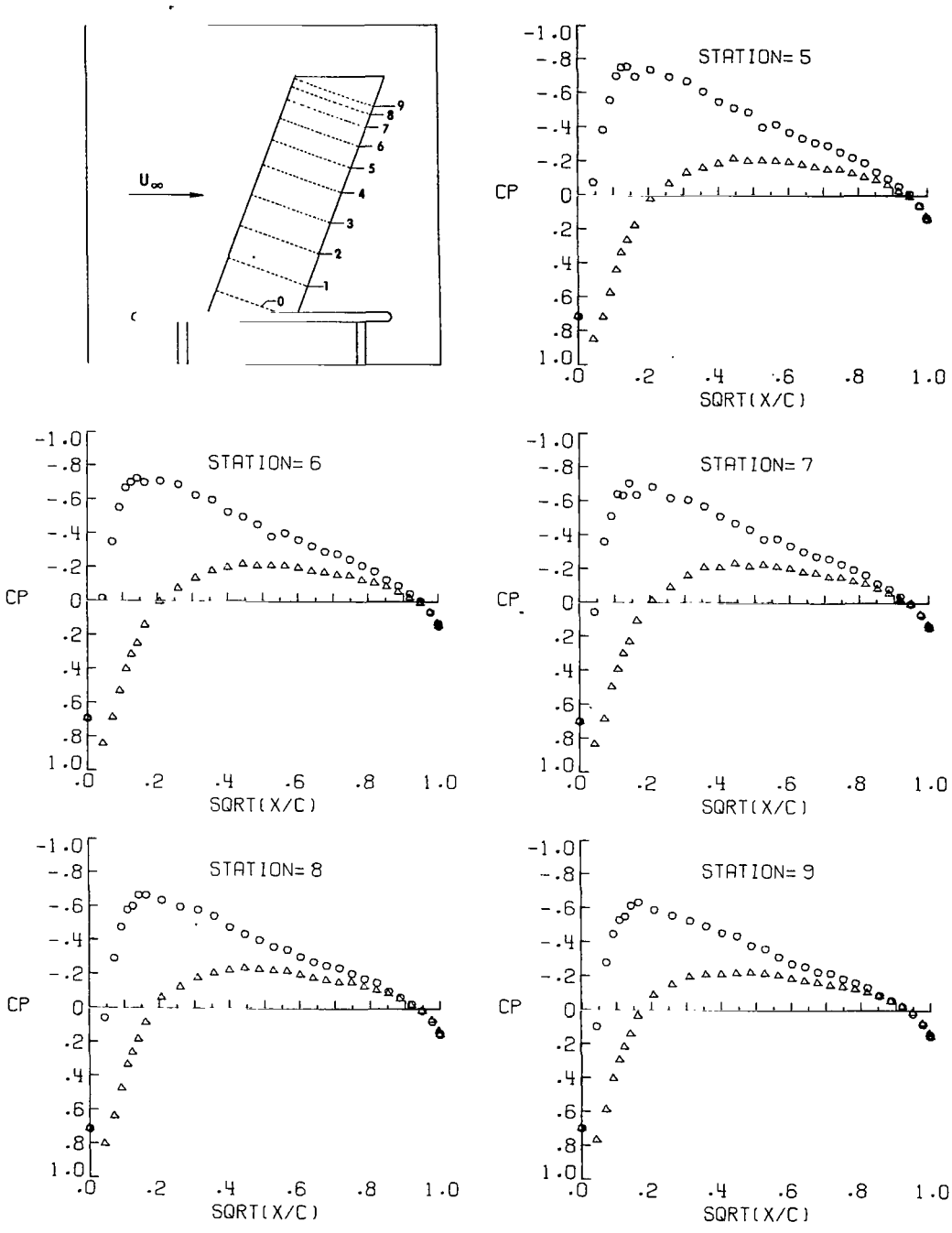

(e) Concluded.

Figure 5.- Continued.

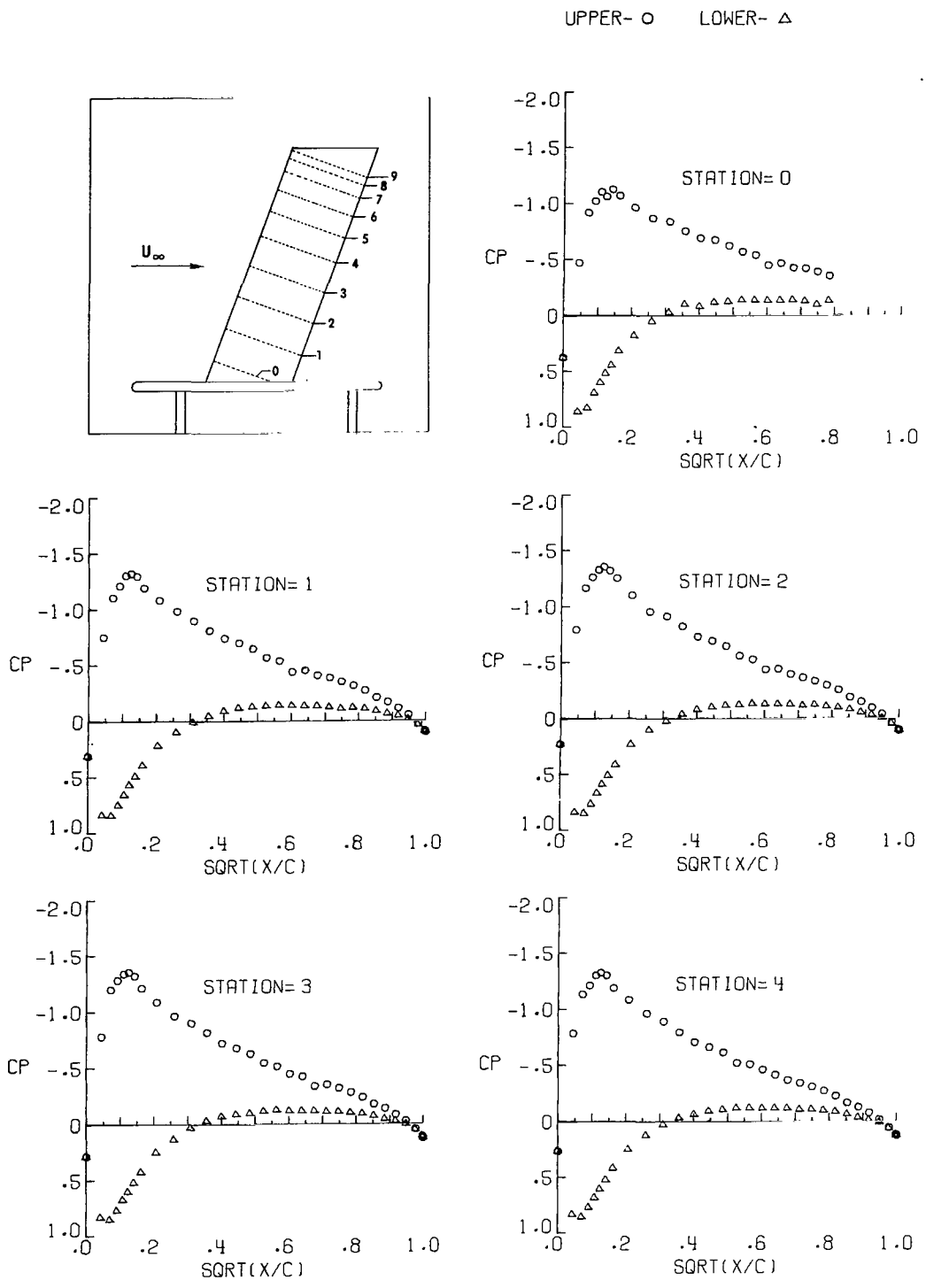

(f) $\alpha = 4.65^{o}$; $q_\infty = 2.46$ kPa (51.32 lb/ft^2).

Figure 5.- Continued.

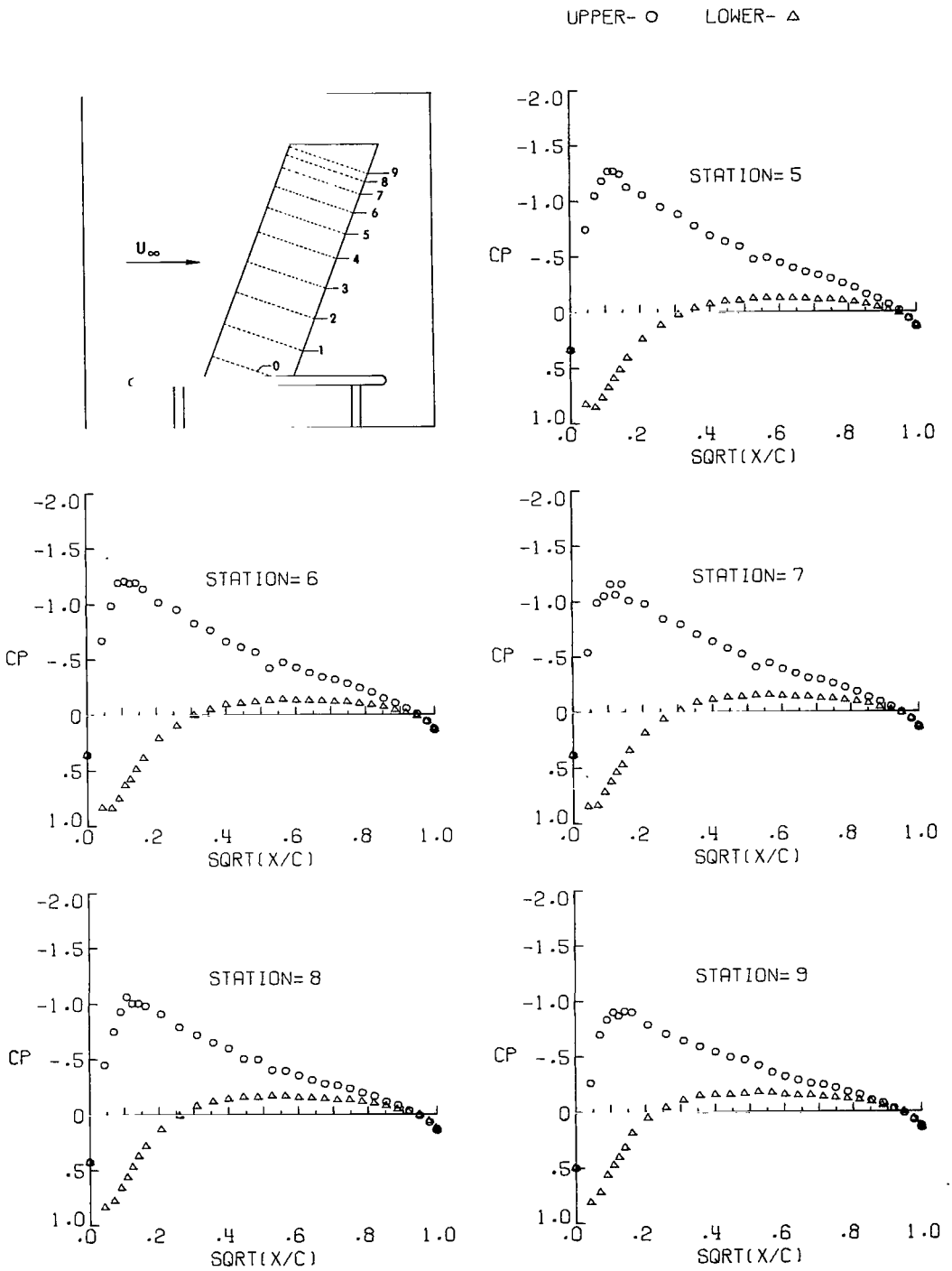

(f) Concluded.

Figure 5.- Continued.

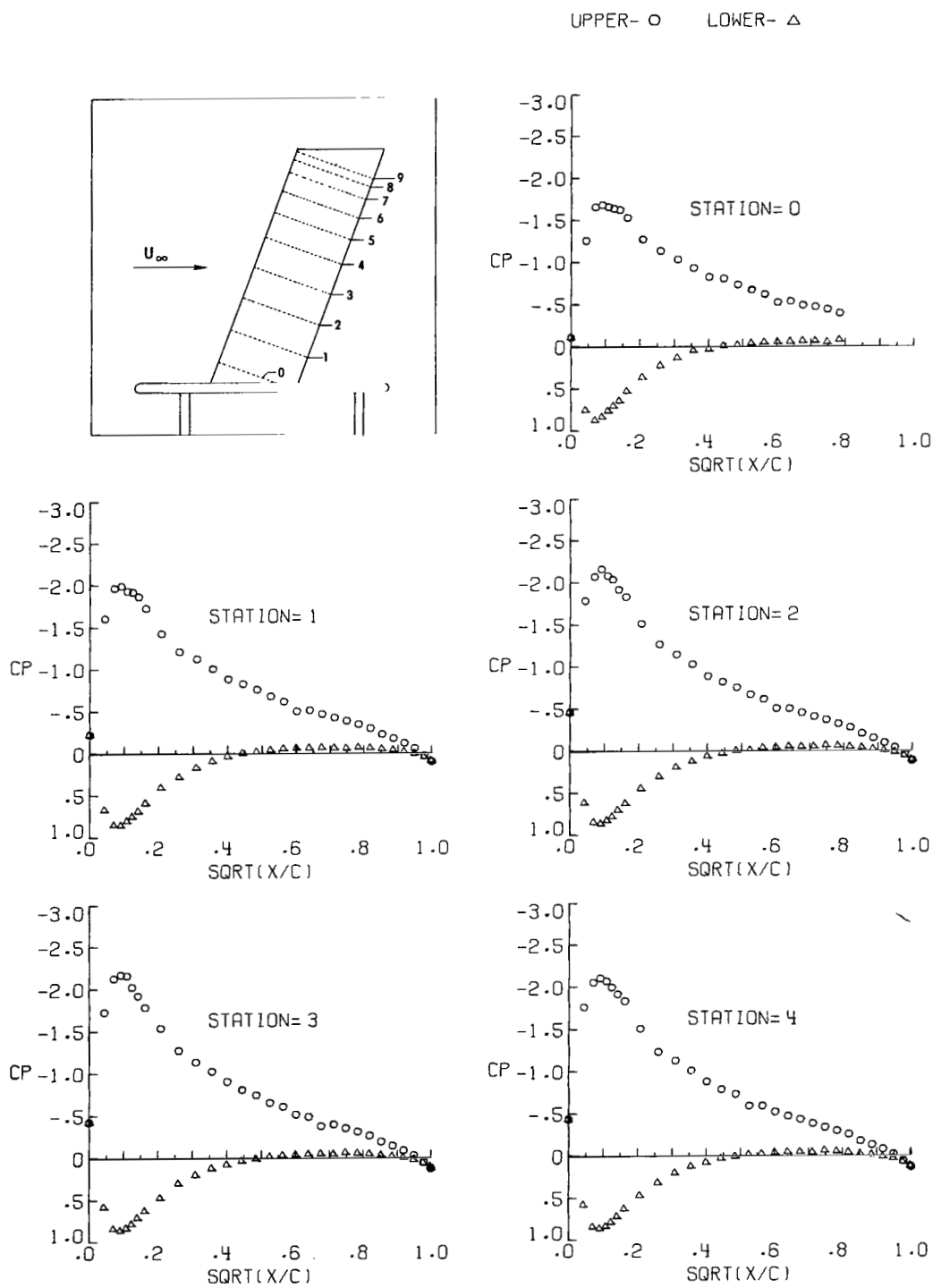

(g) $\alpha = 6.76^{o}$; $q_\infty = 2.45$ kPa (51.25 lb/ft^2).

Figure 5.- Continued.

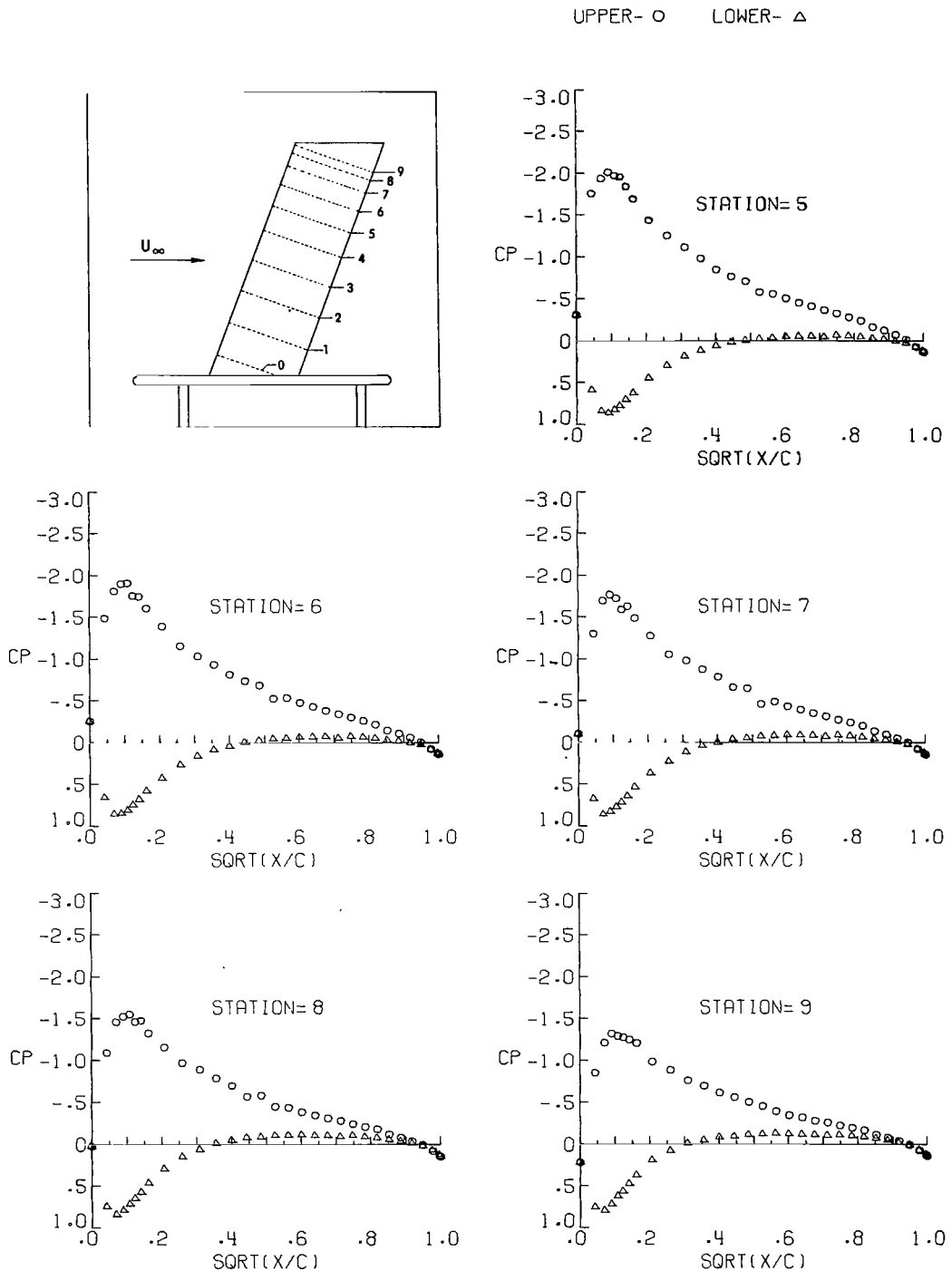

(g) Concluded.

Figure 5.- Continued.

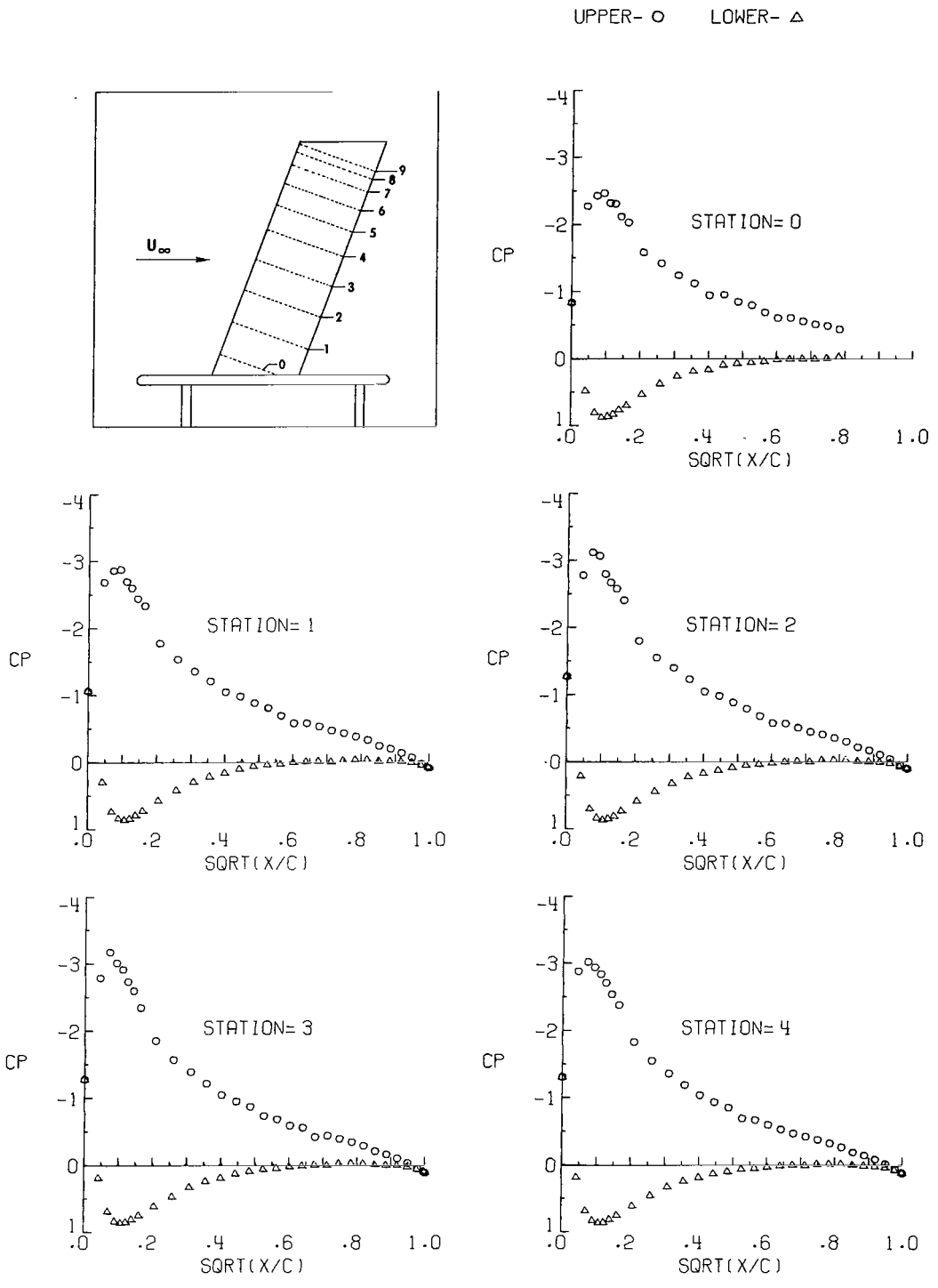

(h) $\alpha = 8.84^{o}$; $q_\infty = 2.46$ kPa (51.30 lb/ft^2).

Figure 5.- Continued.

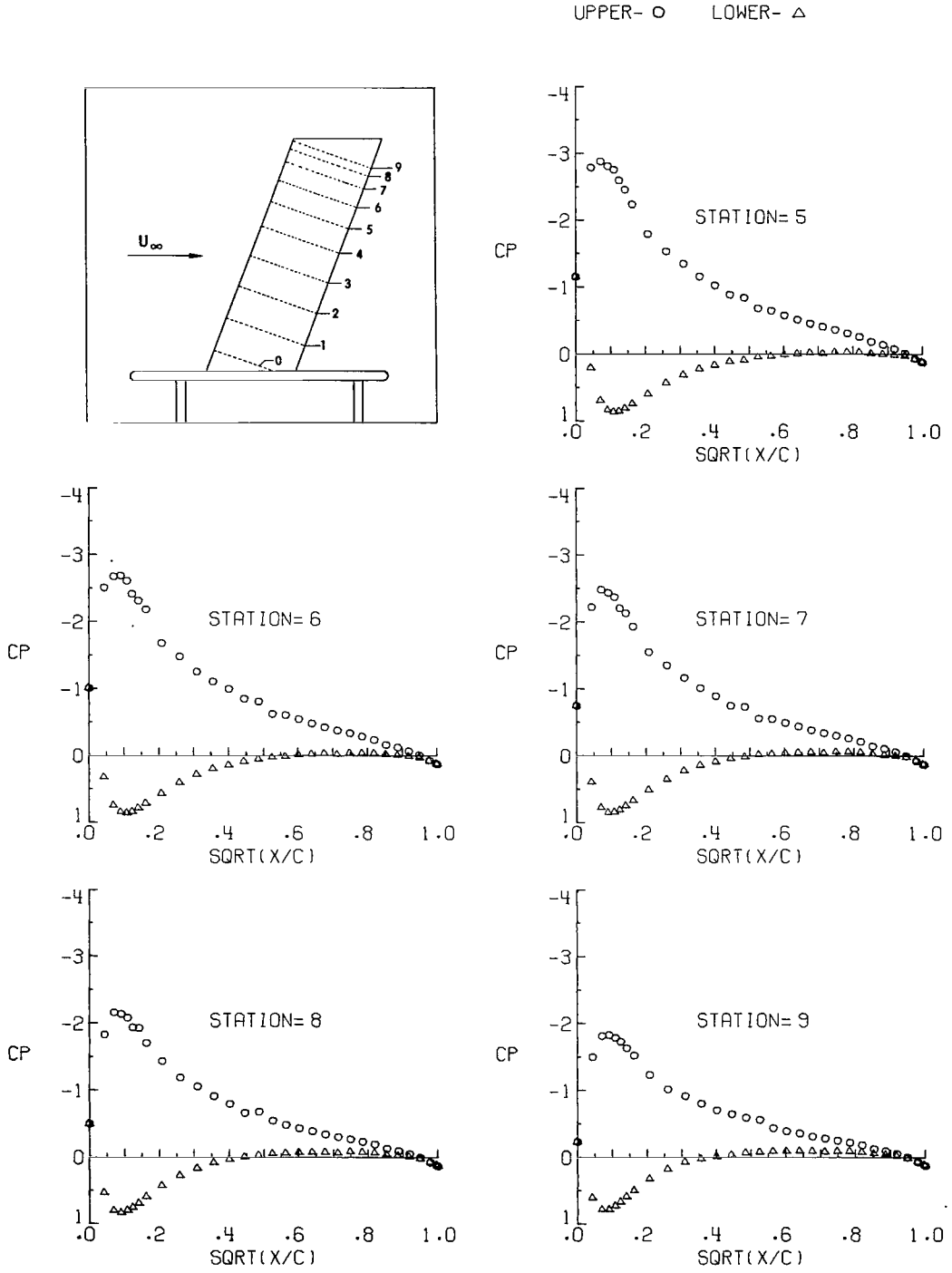

(h) Concluded.

Figure 5.- Continued.

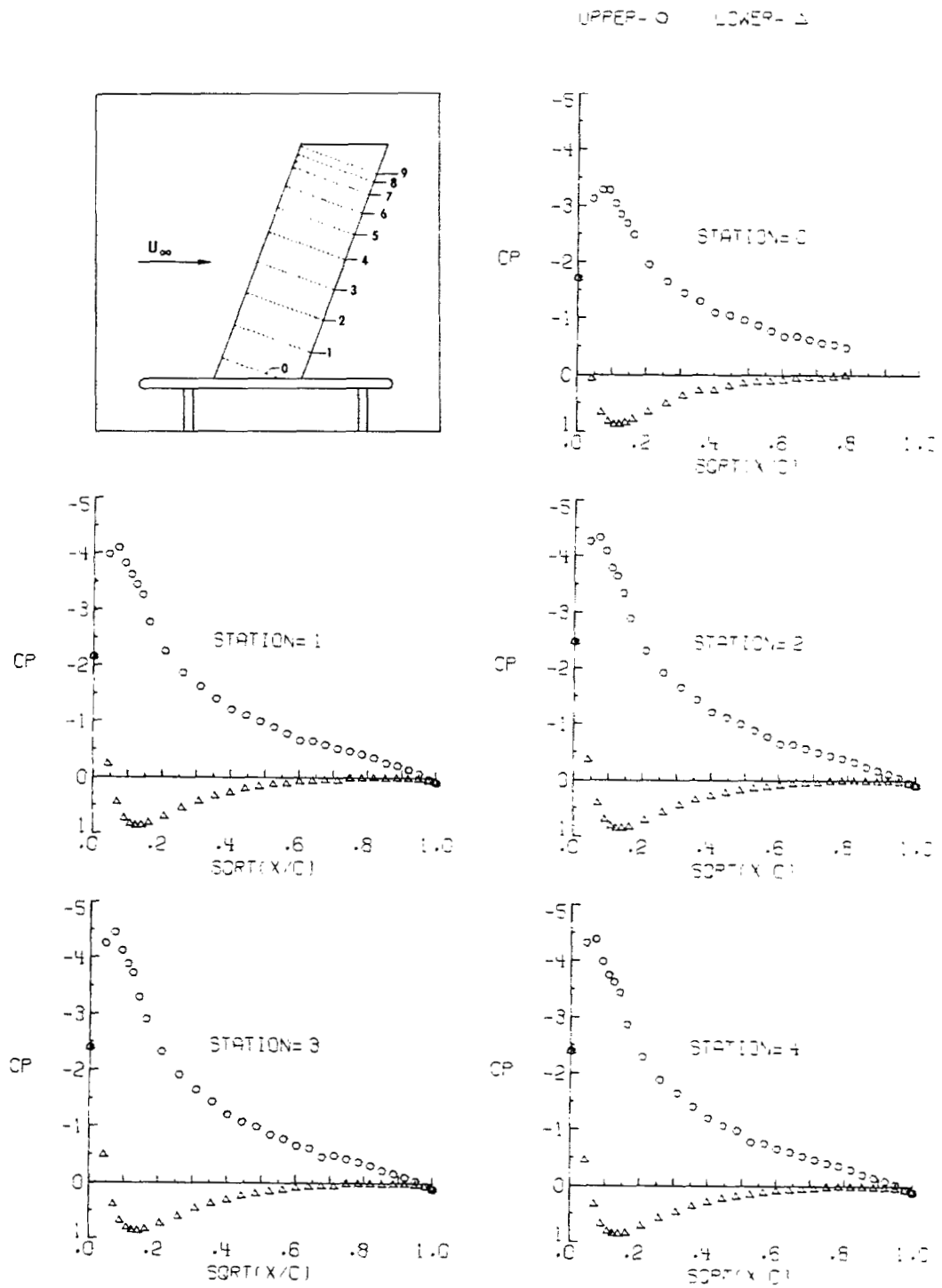

(i) $\alpha = 10.94^{o}$; $q_\infty = 2.46$ kPa (51.38 lb/ft^2).

Figure 5.- Continued.

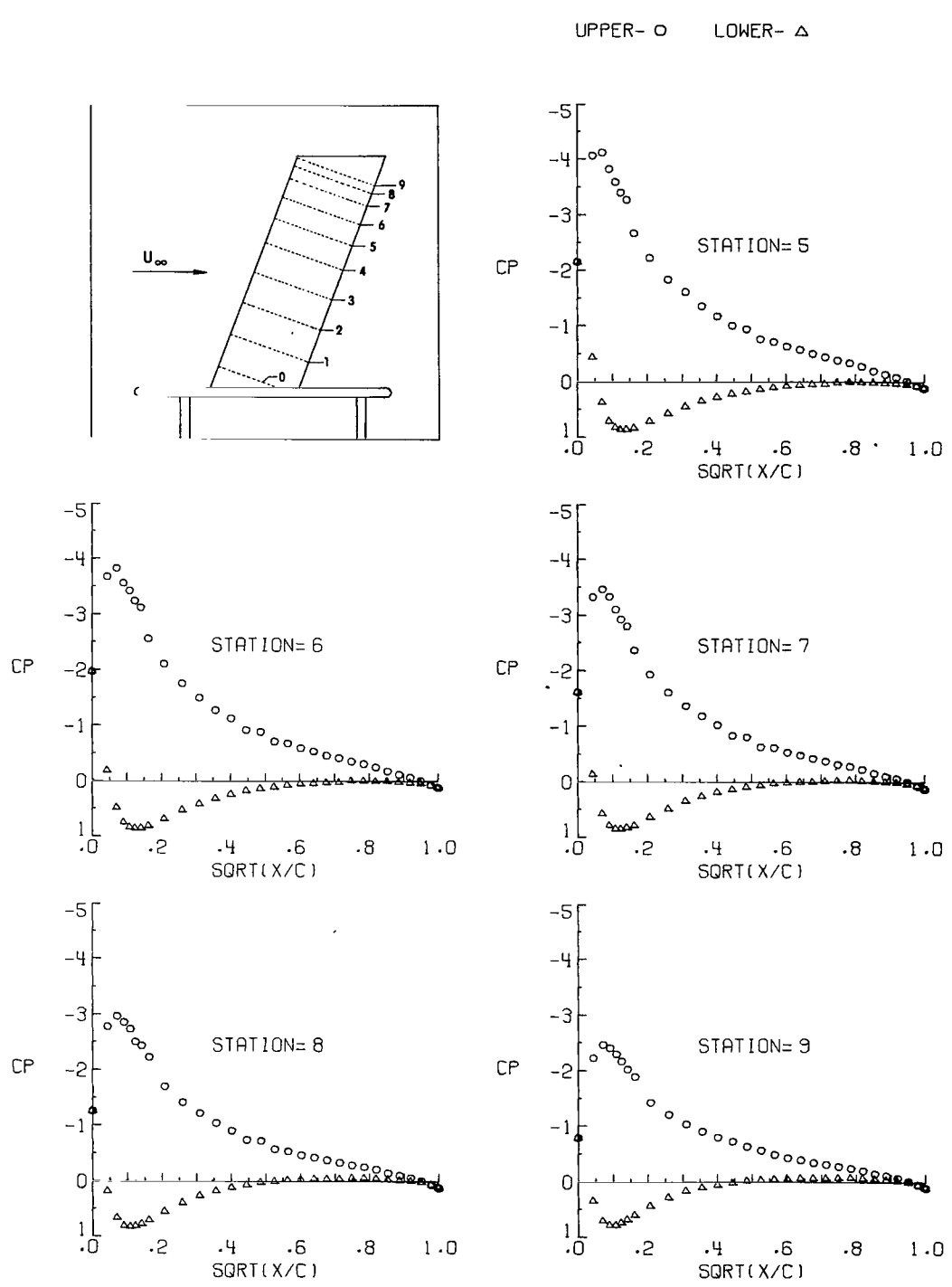

(i) Concluded.

Figure 5.- Continued.

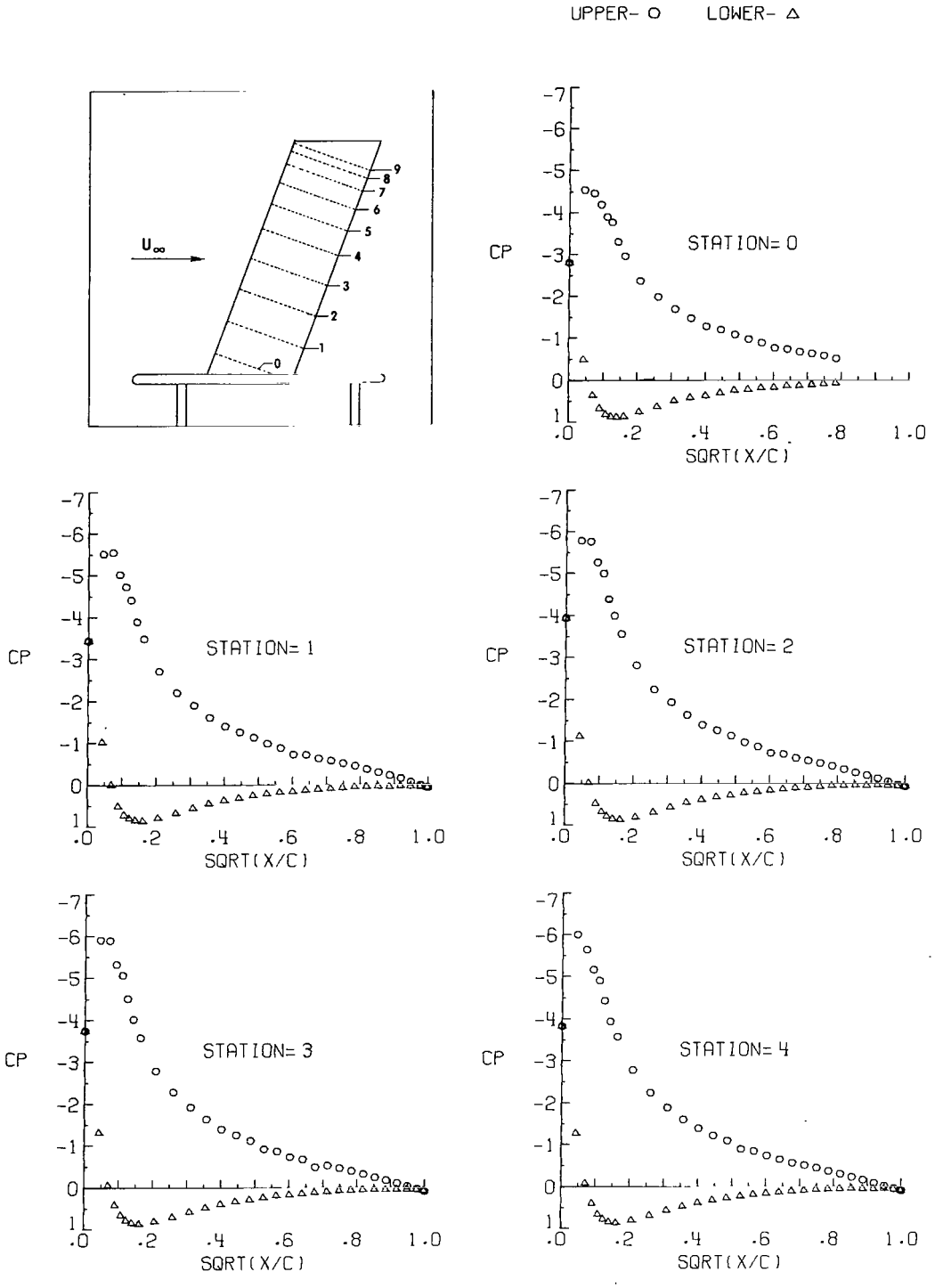

(j) $\alpha = 13.06^{o}$; $q_\infty = 2.46$ kPa (51.41 lb/ft^2).

Figure 5.- Continued.

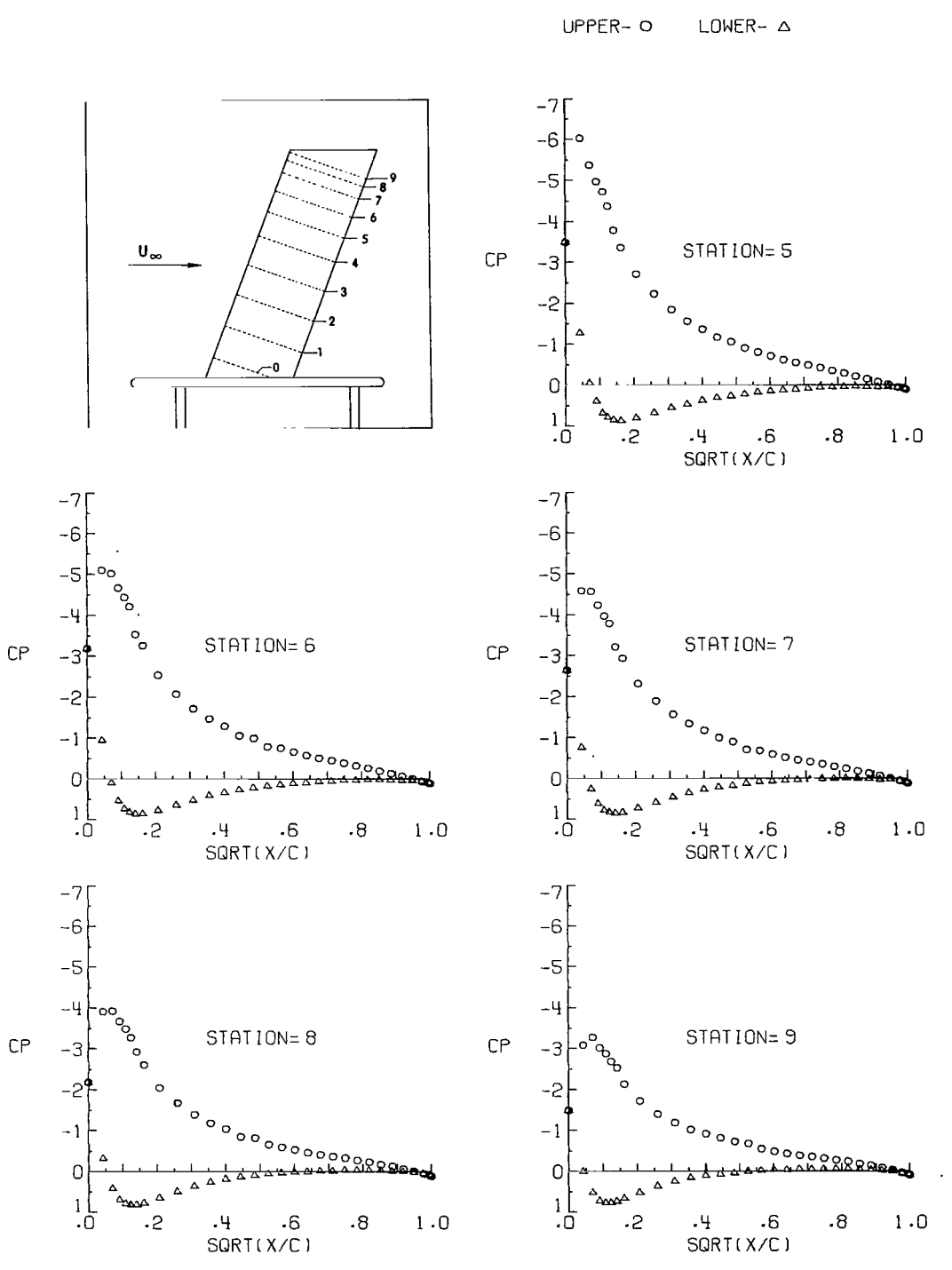

(j) Concluded.

Figure 5.- Continued.

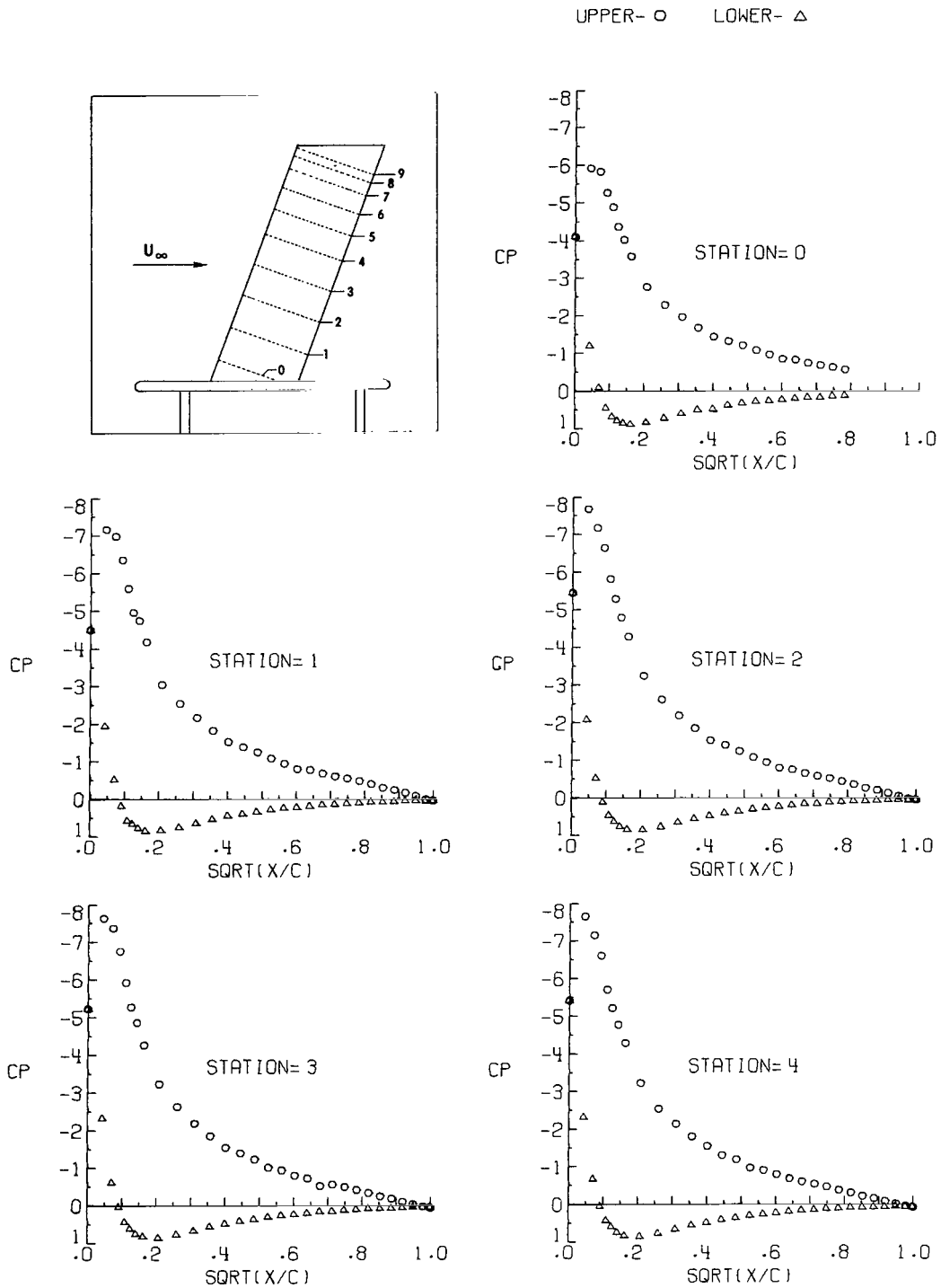

(k) $\alpha = 15.14^{o}$; $q_\infty = 2.46$ kPa (51.29 lb/ft^2).

Figure 5.- Continued.

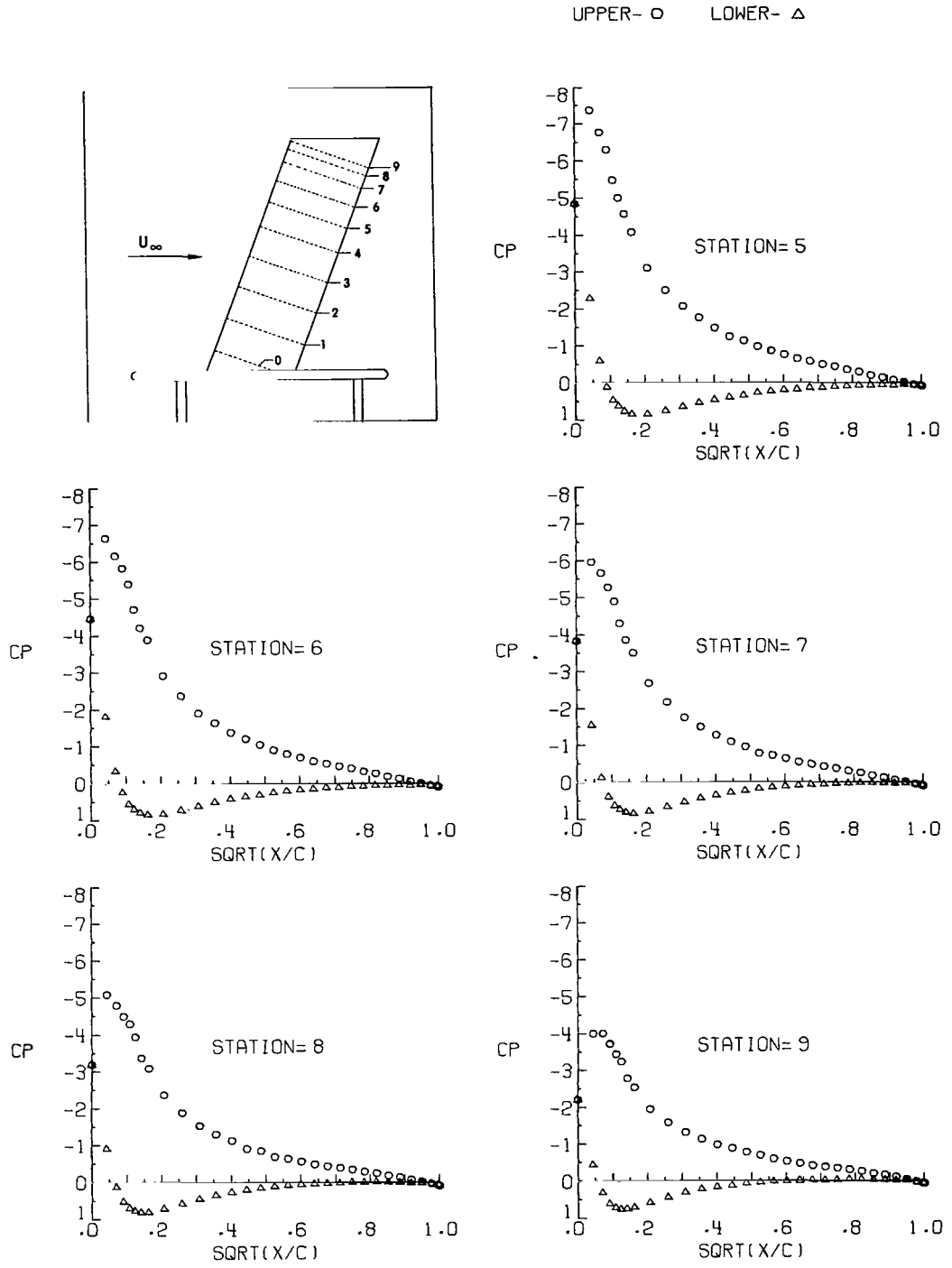

(k) Concluded.

Figure 5.- Continued.

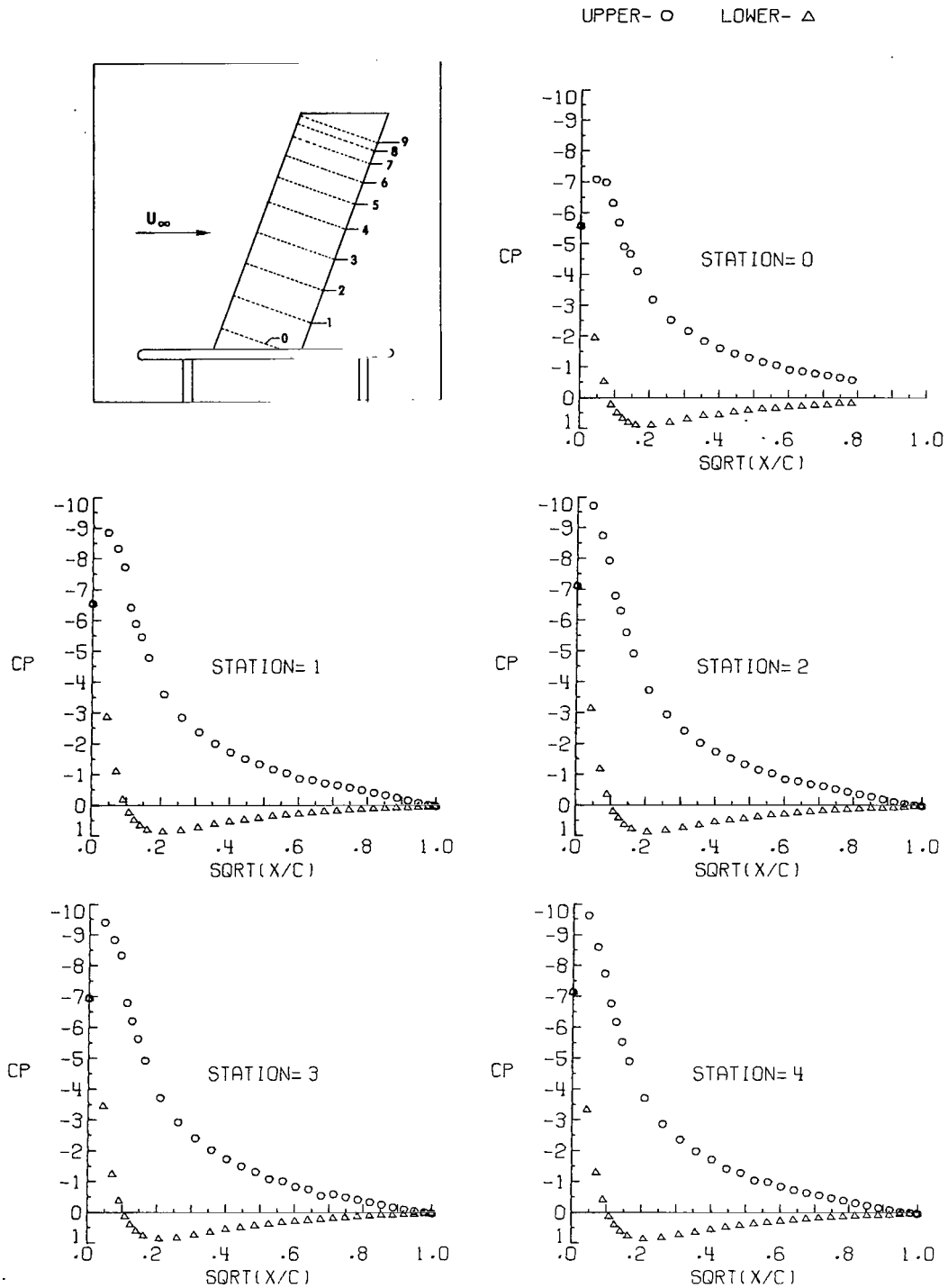

(1) $\alpha = 17.22^{o}$; $q_\infty = 2.46$ kPa (51.33 lb/ft^2).

Figure 5.- Continued.

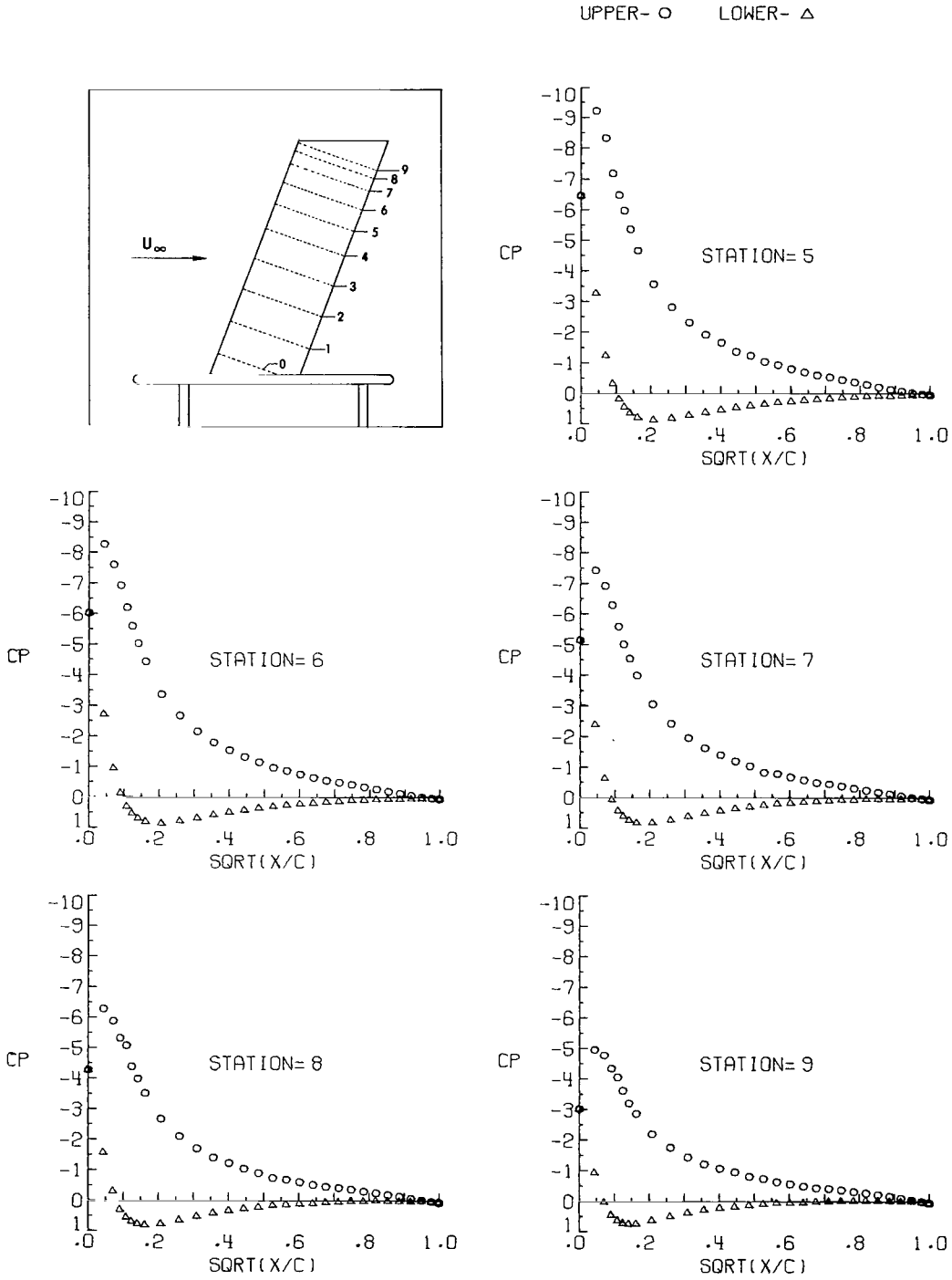

(1) Concluded.

Figure 5.- Concluded.

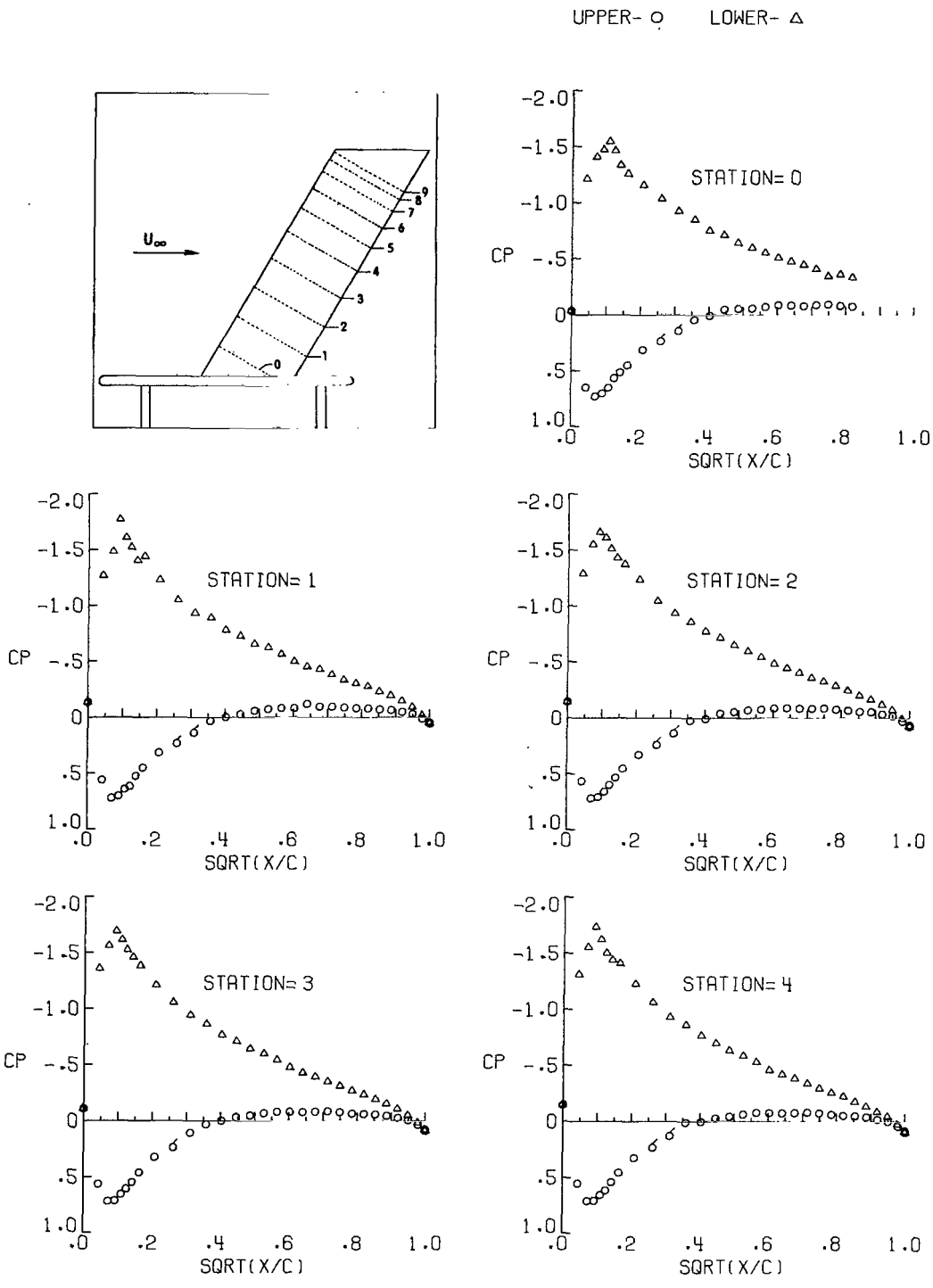

(a) $\alpha = -5.88^{\circ}$; $q_\infty = 1.47$ kPa (30.73 lb/ft^2).

Figure 6.- Pressure distributions at sweep angle of 30°.

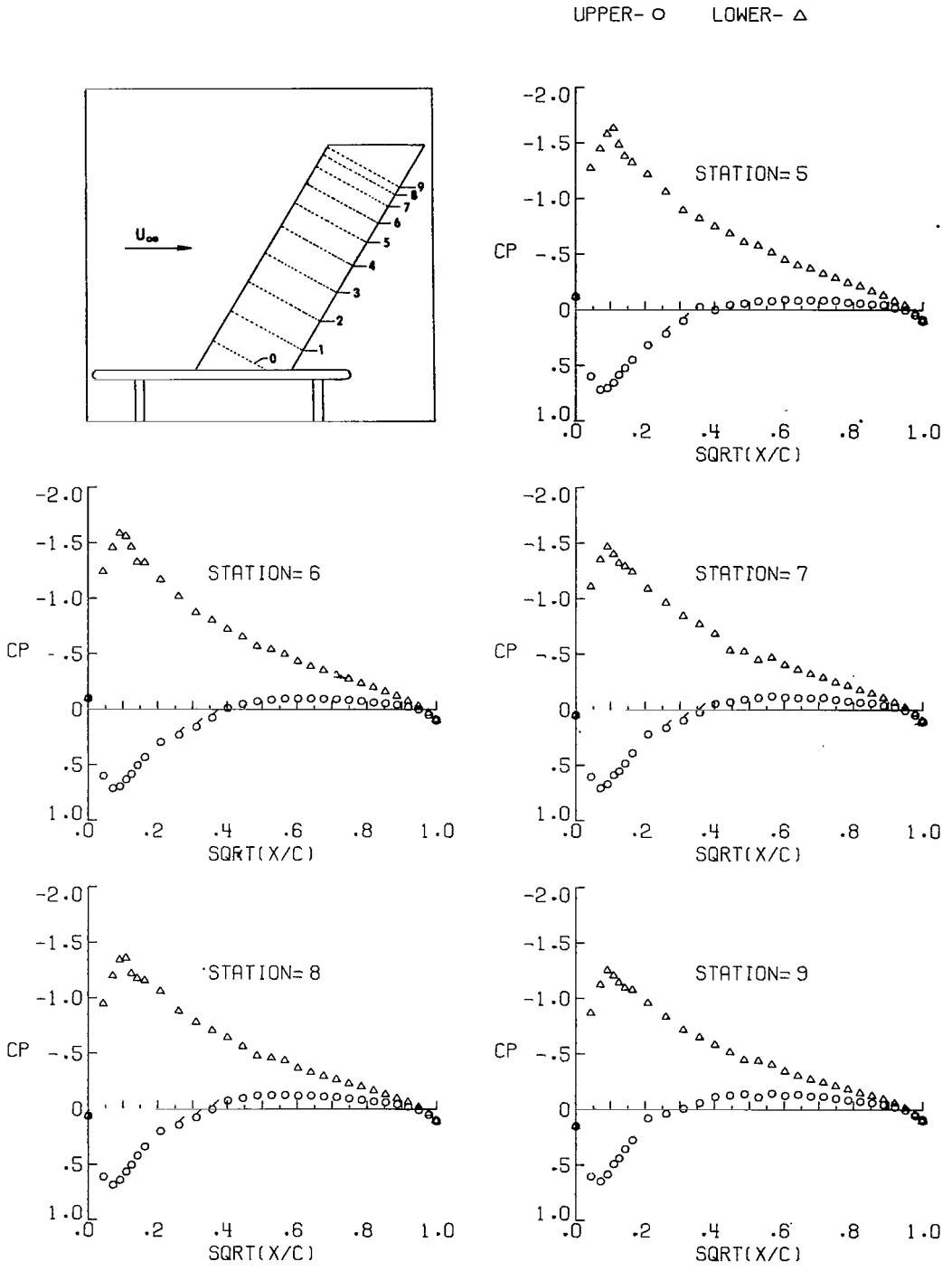

(a) Concluded.

Figure 6.- Continued.

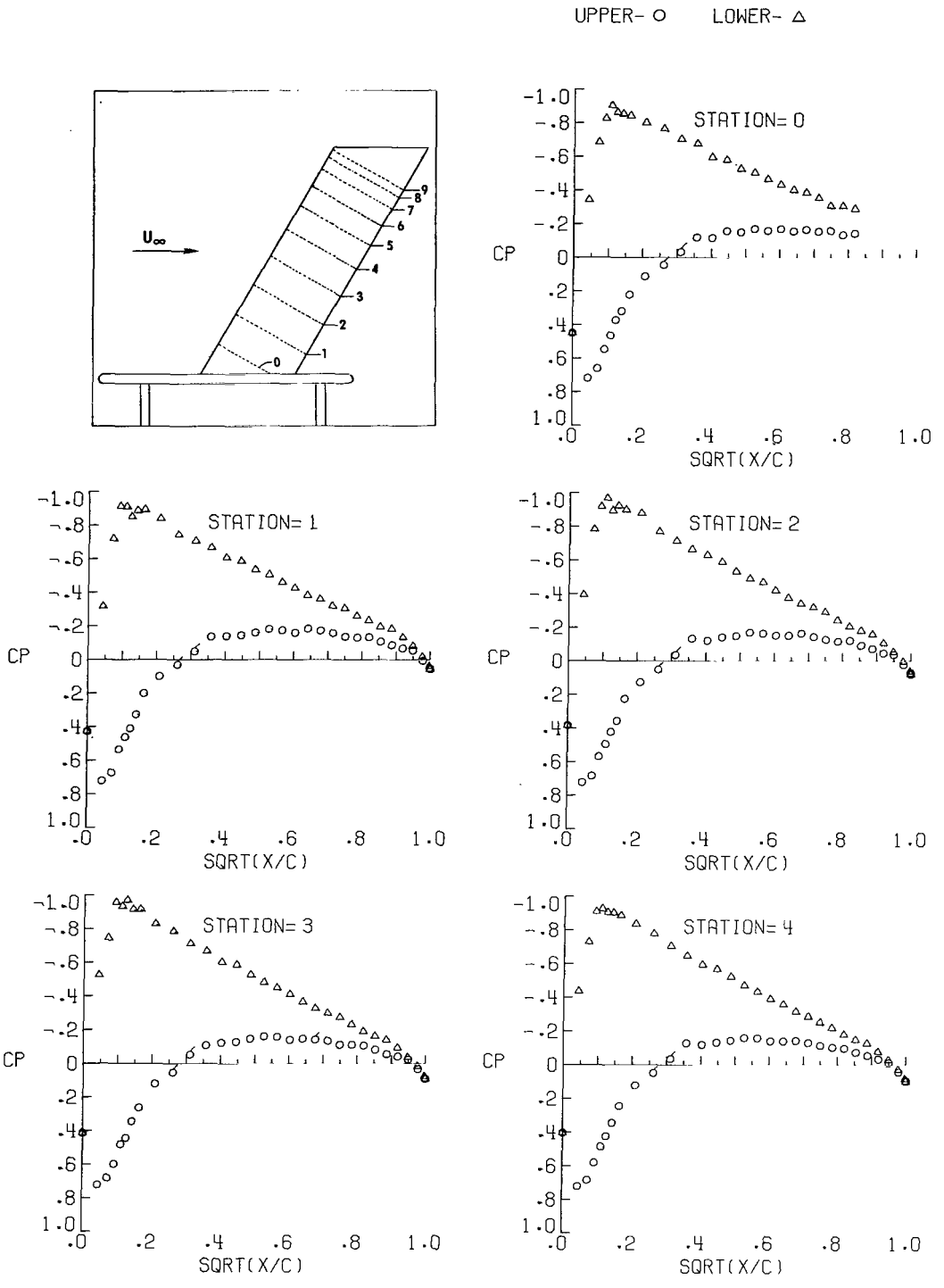

(b) $\alpha = -3.76^{o}$; $q_\infty = 1.48$ kPa (30.81 lb/ft^2).

Figure 6.- Continued.

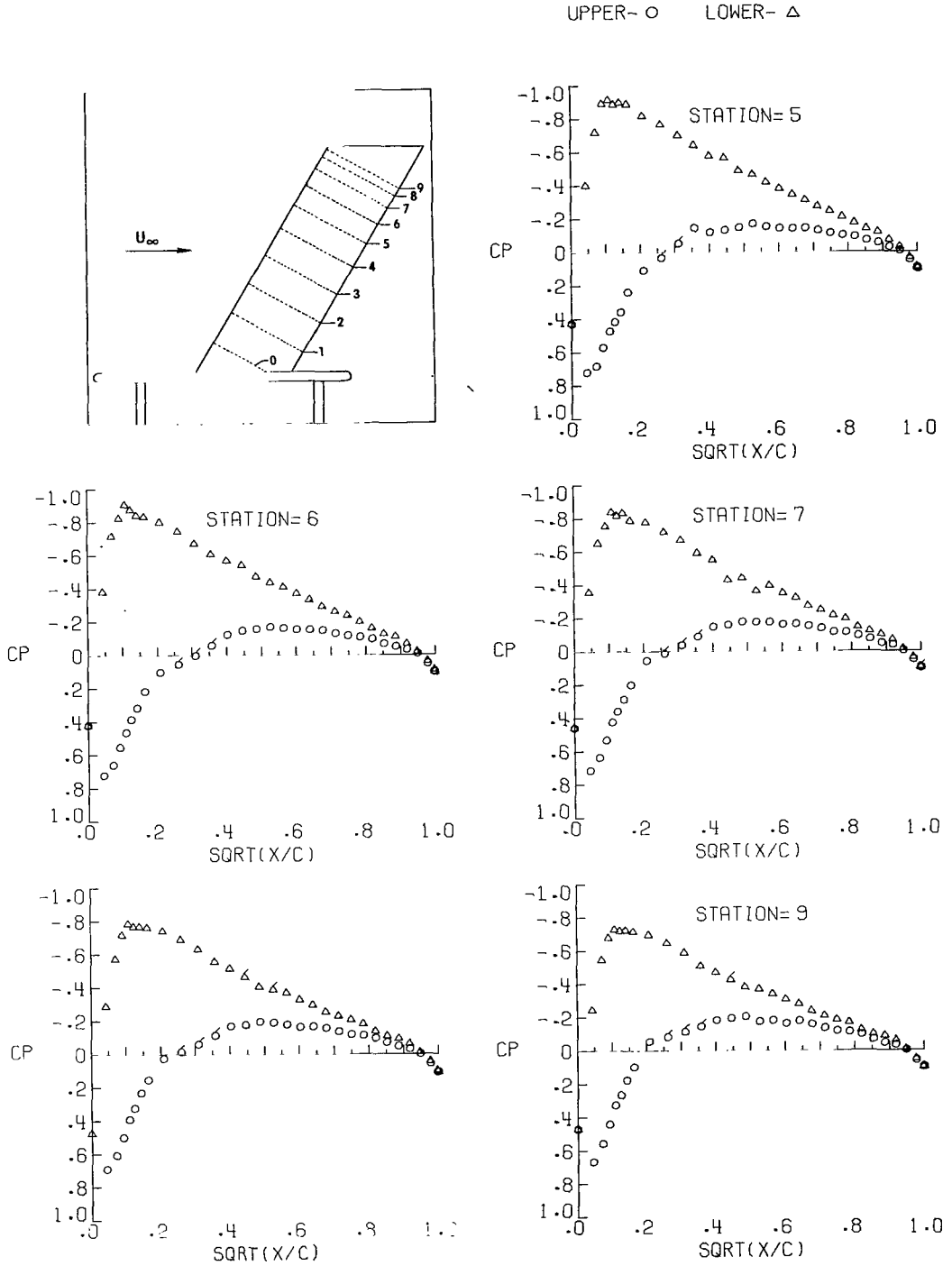

(b) Concluded.

Figure 6.- Continued.

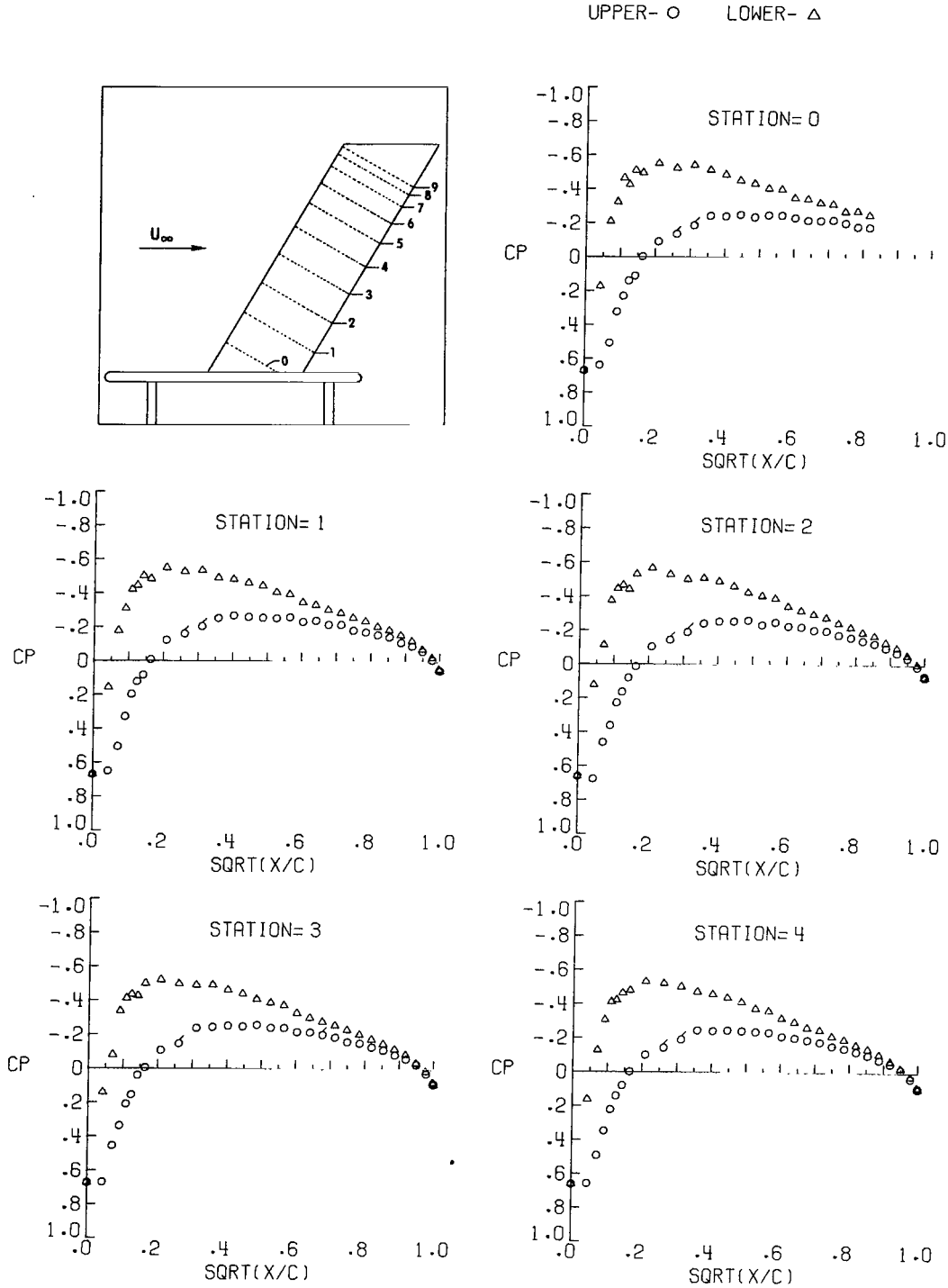

(c) $\alpha = -1.67^{\circ}$; $q_\infty = 1.47$ kPa (30.80 lb/ft^2).

Figure 6.- Continued.

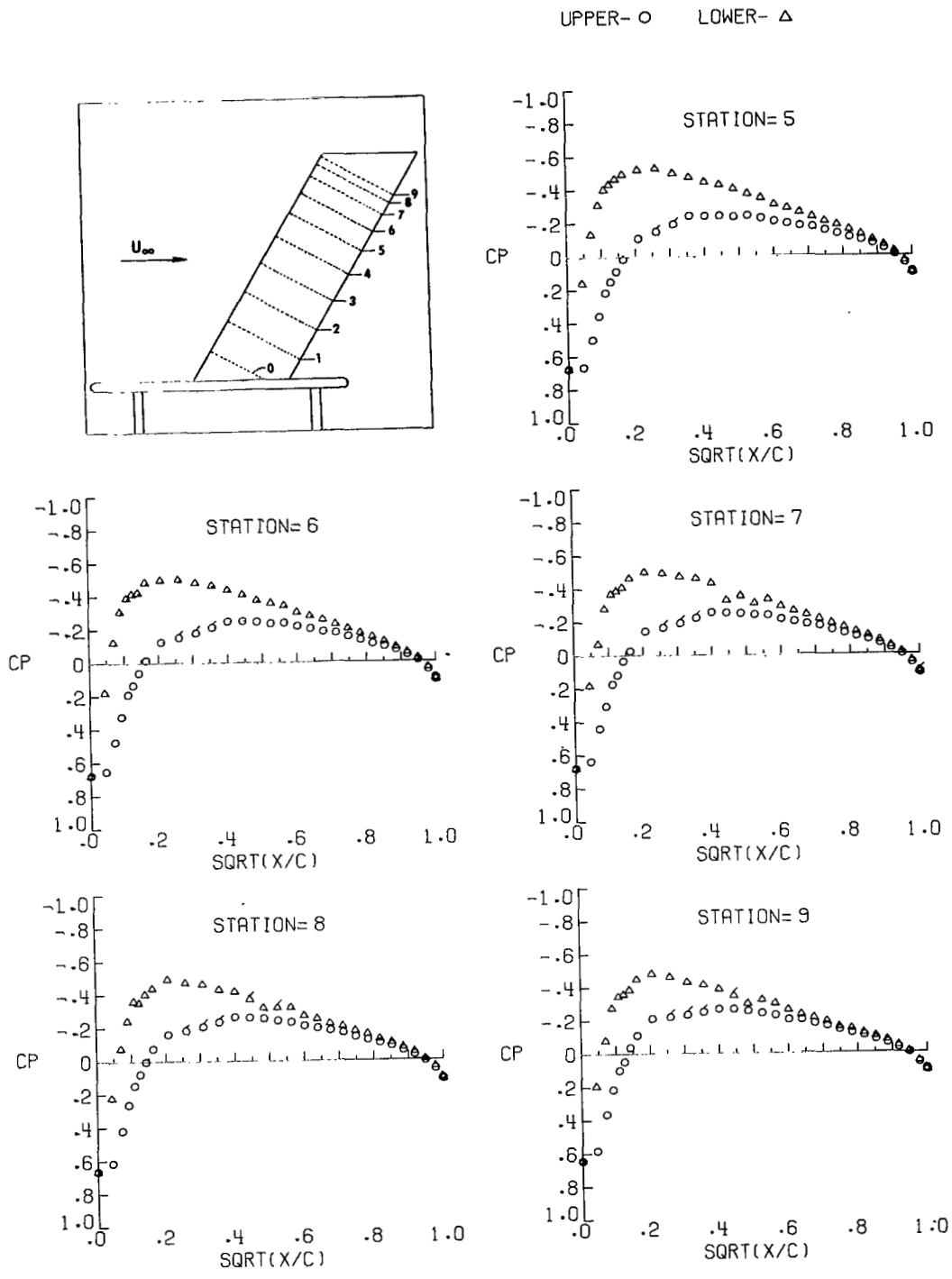

(c) Concluded.

Figure 6.- Continued.

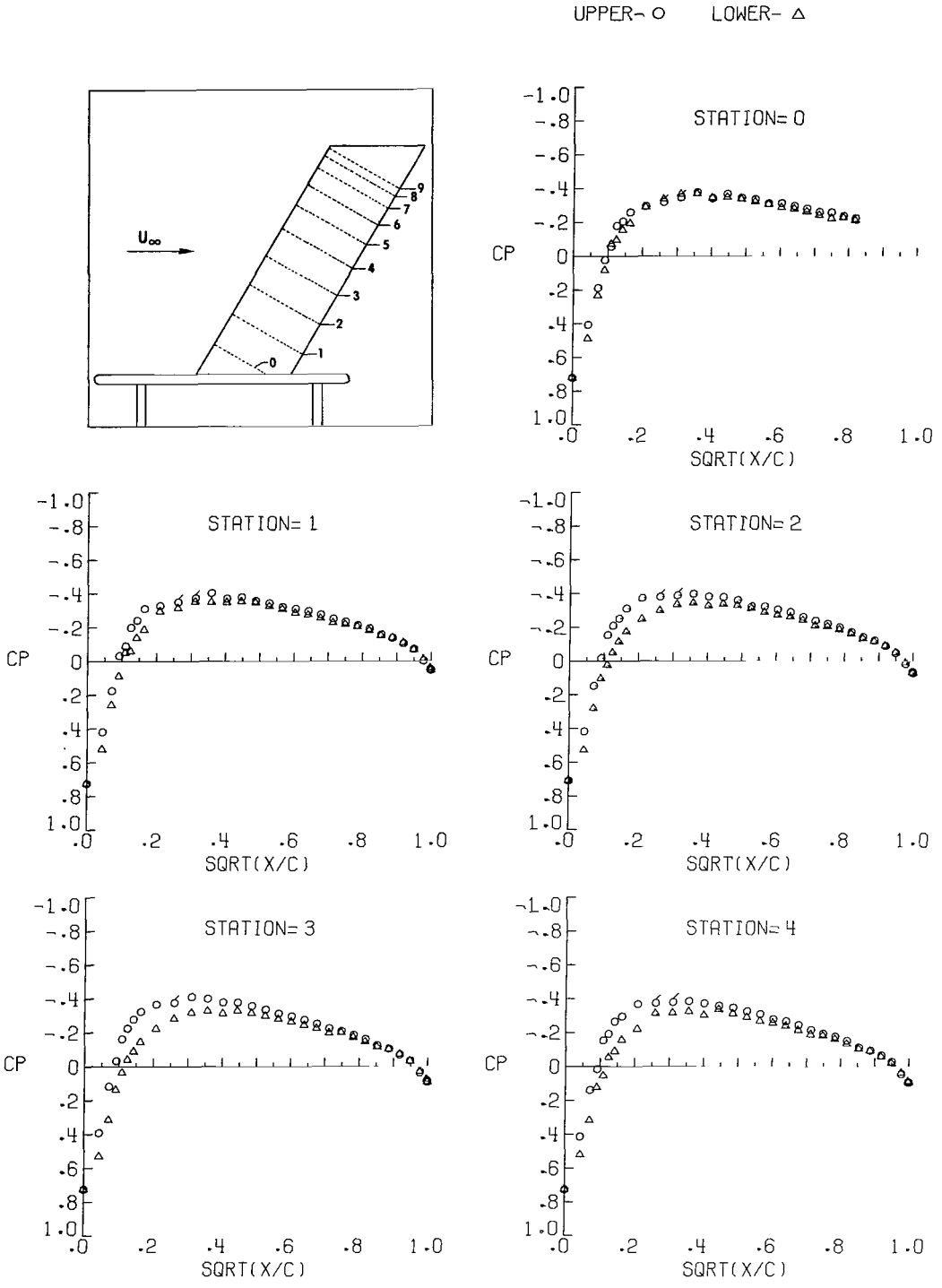

(d) $\alpha = 0.42^{o}$; $q_\infty = 1.47$ kPa (30.79 lb/ft^2).

Figure 6.- Continued.

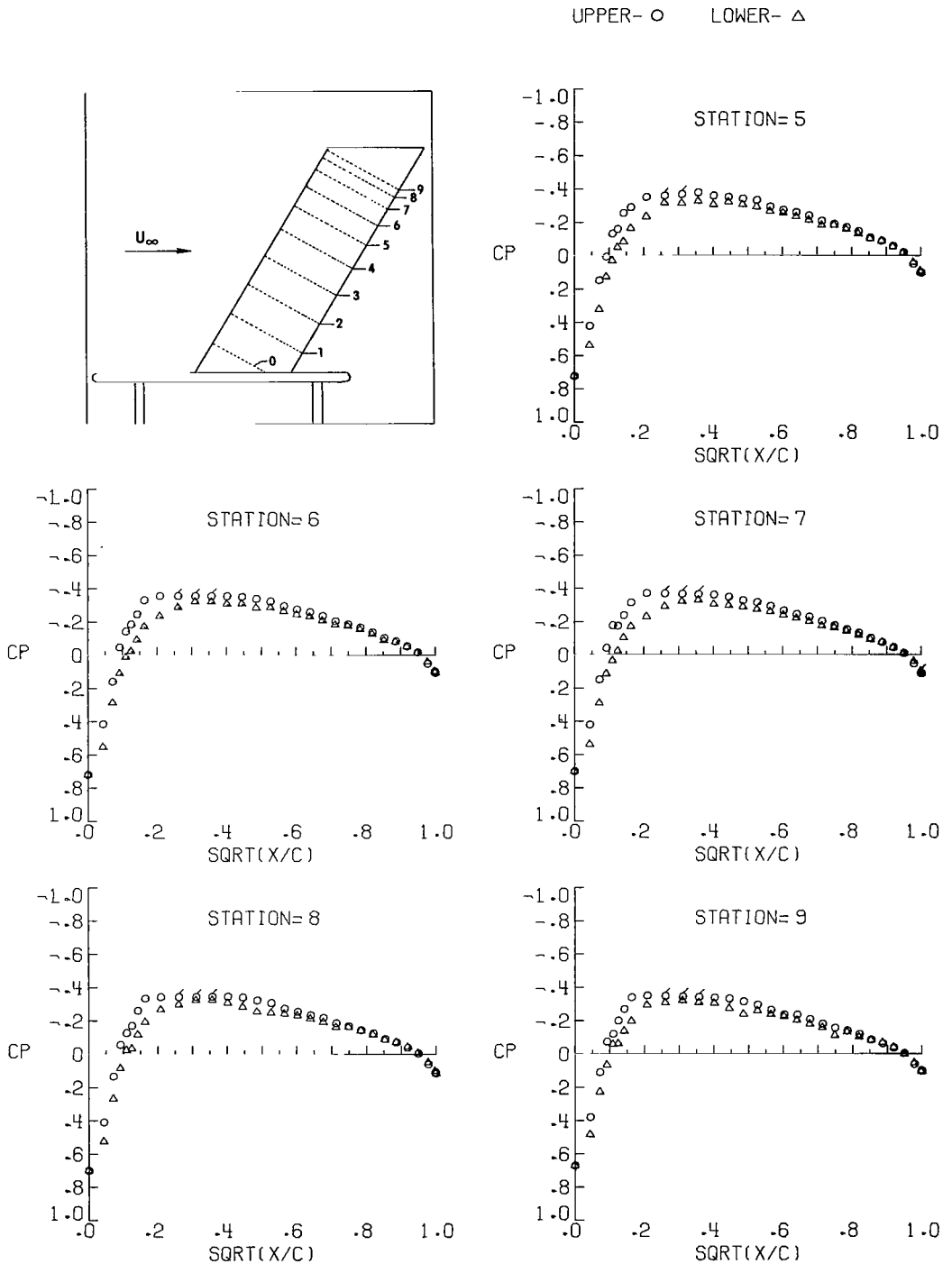

(d) Concluded.

Figure 6.- Continued.

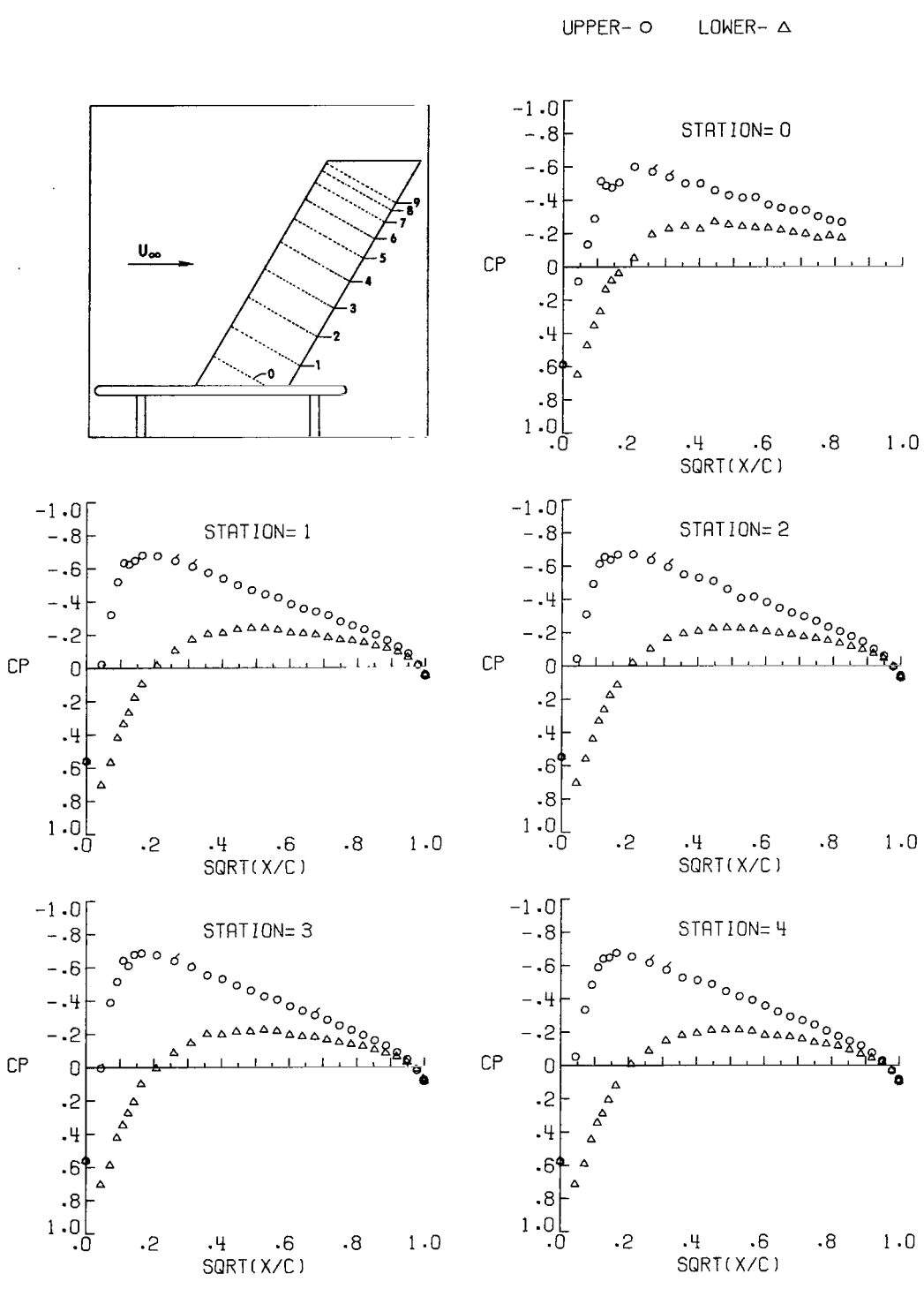

(e) $\alpha = 2.51^{o}$; $q_\infty = 1.47$ kPa (30.77 lb/ft^2).

Figure 6.- Continued.

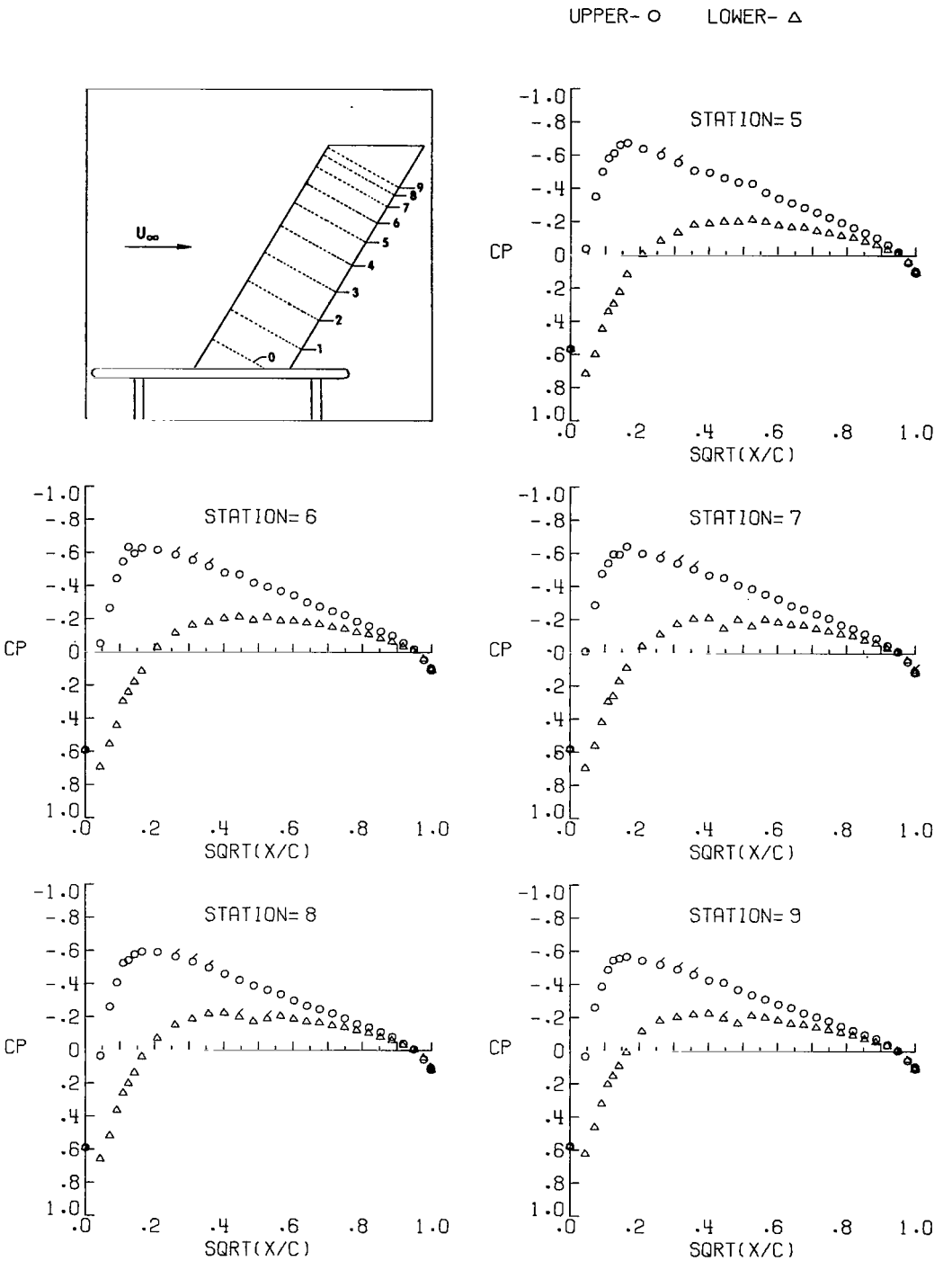

(e) Concluded.

Figure 6.- Continued.

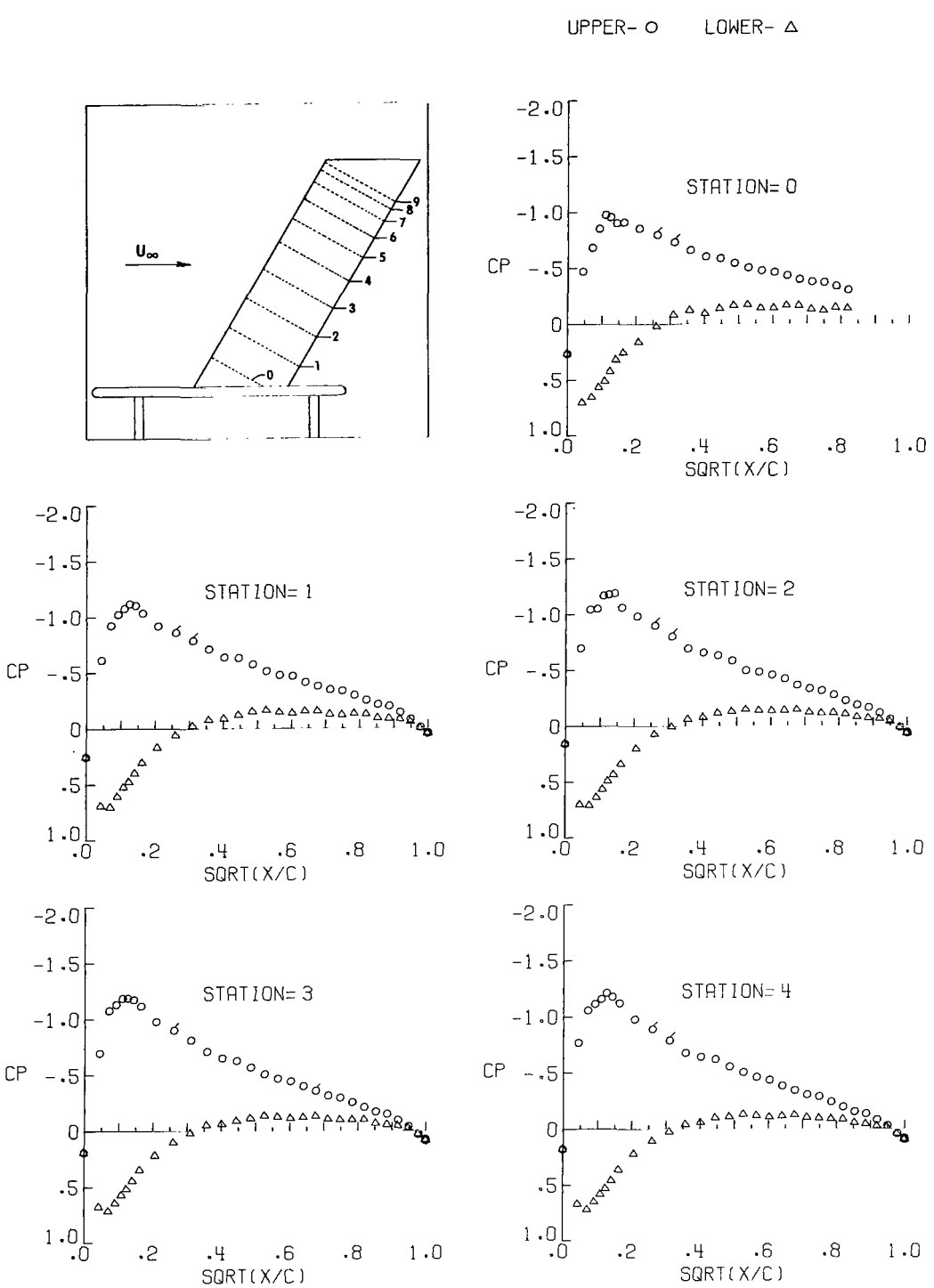

(f) $\alpha = 4.62^{\circ}$; $q_{\infty} = 1.48$ kPa (30.83 lb/ft^2).

Figure 6.- Continued.

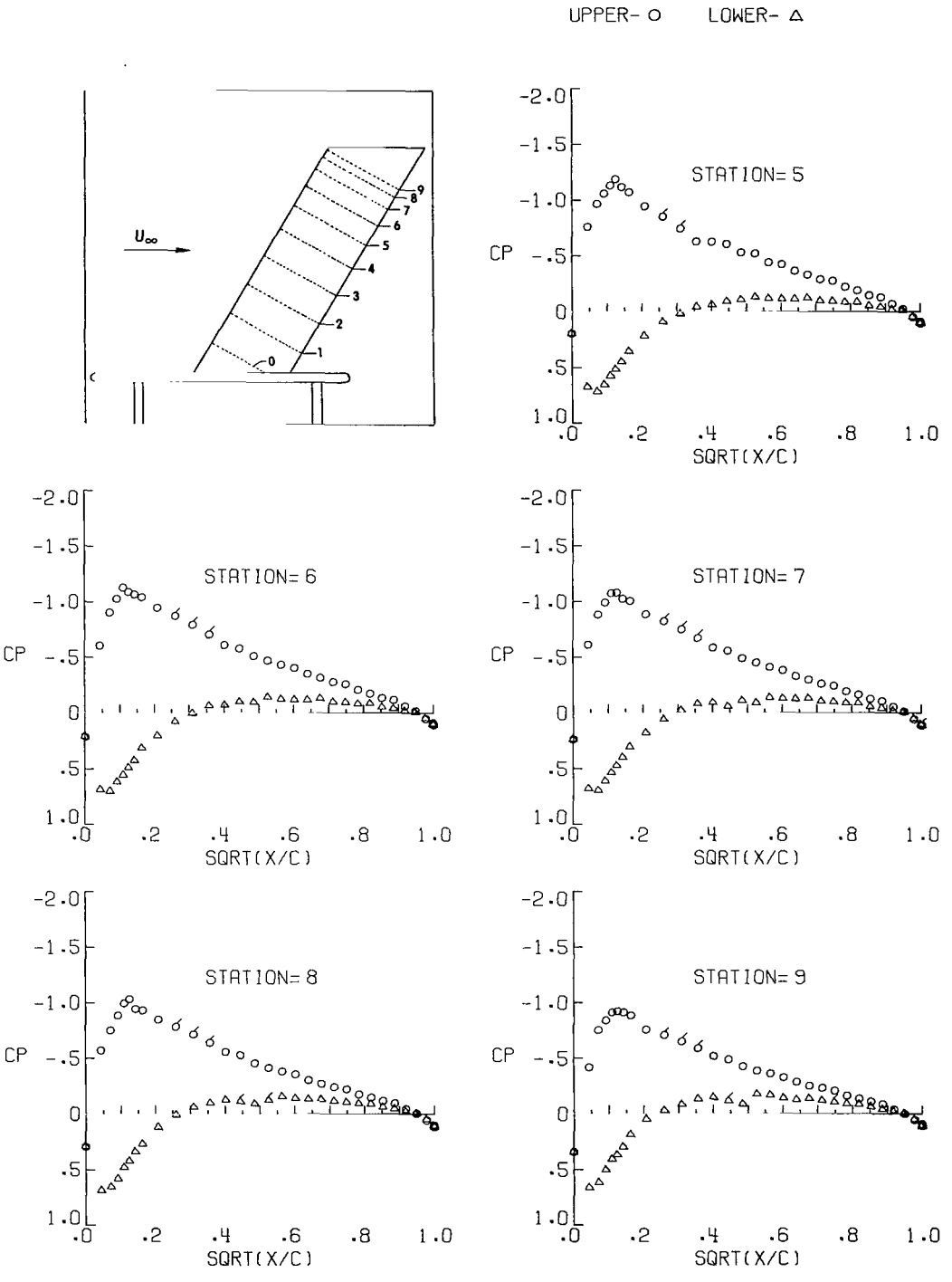

(f) Concluded.

Figure 6.- Continued.

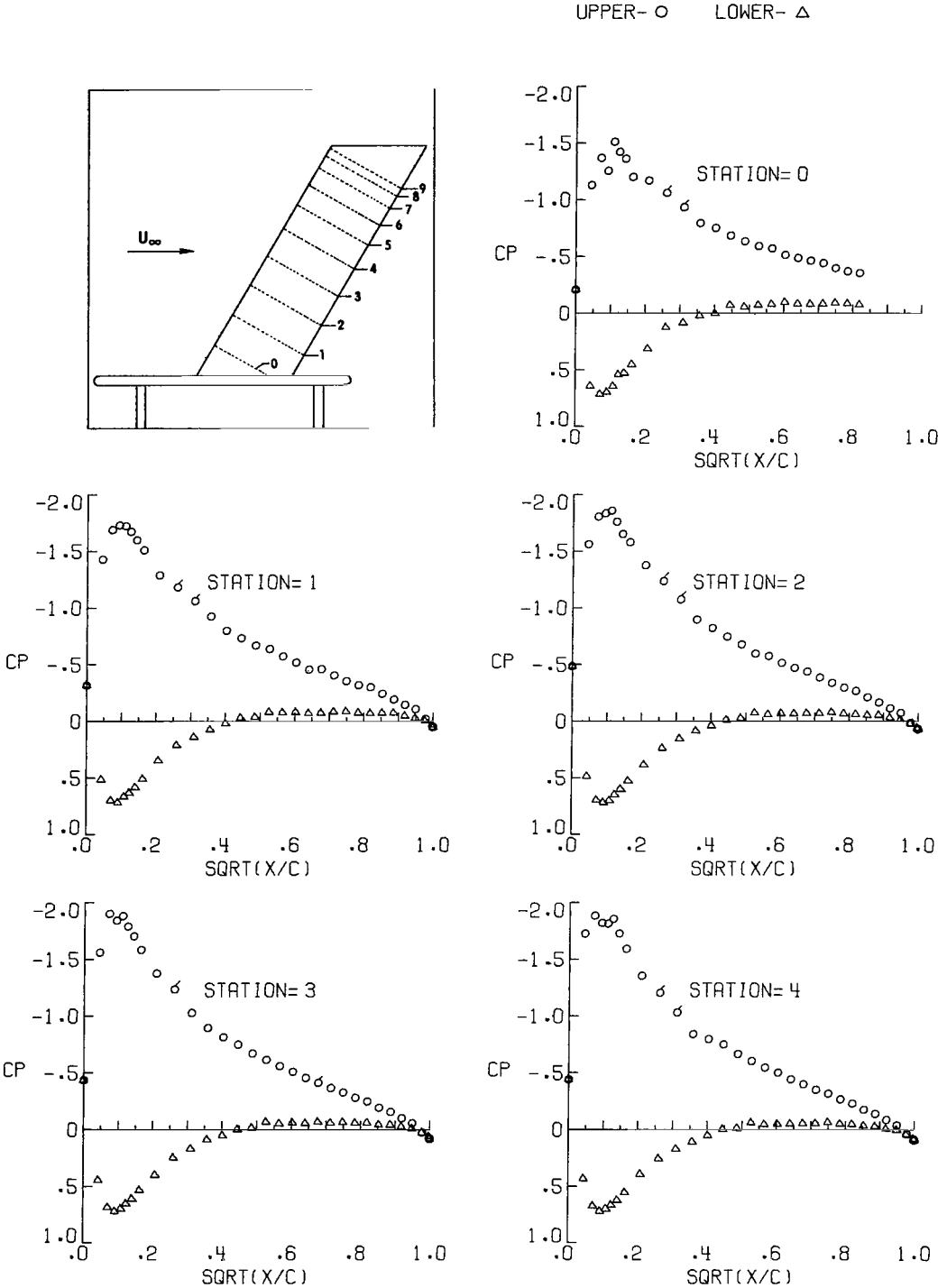

(g) $\alpha = 6.73^{o}$; $q_\infty = 1.48$ kPa (30.82 lb/ft^2).

Figure 6.- Continued.

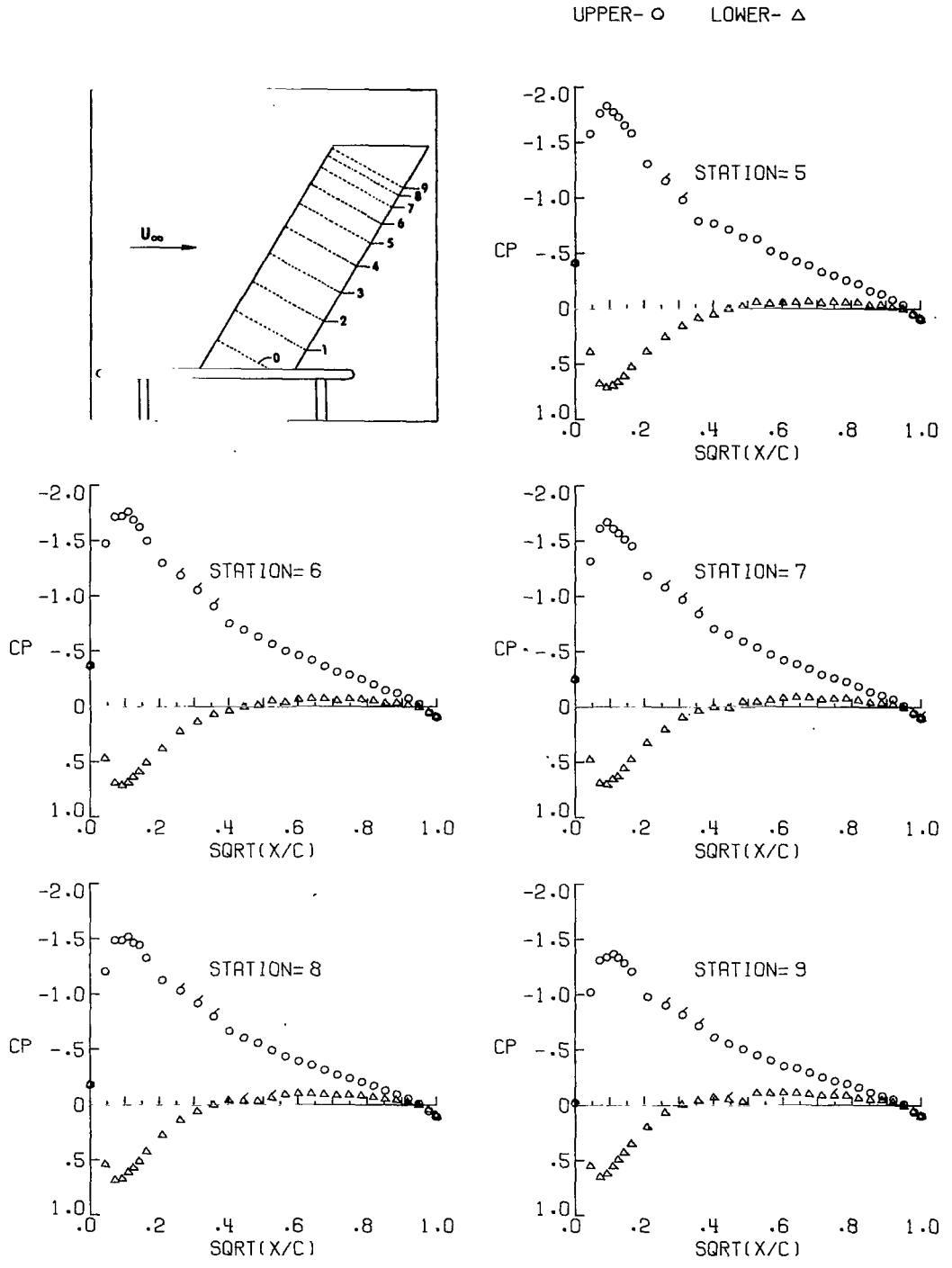

(g) Concluded.

Figure 6.- Continued.

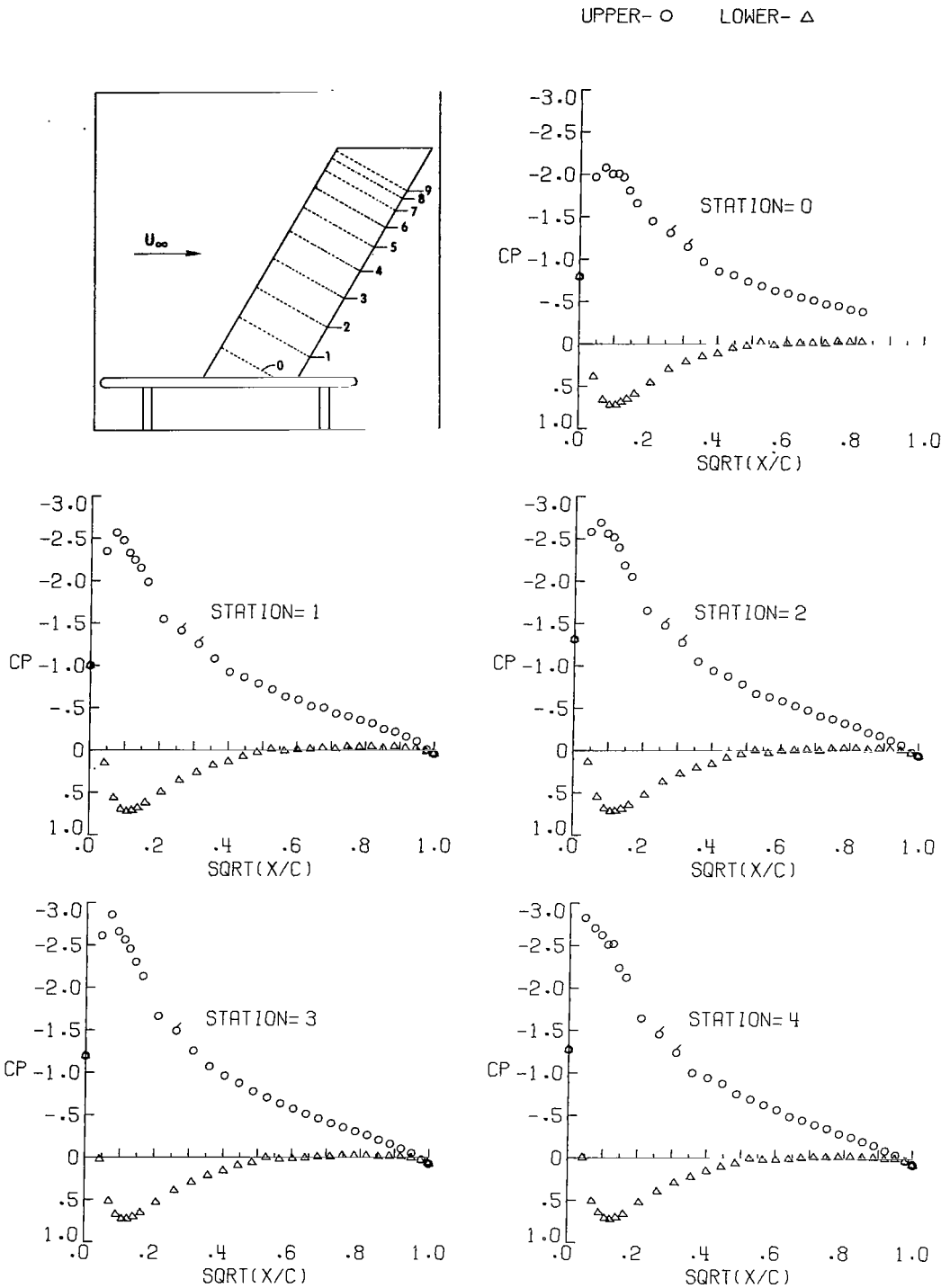

(h) $\alpha = 8.80^{\circ}$; $q_\infty = 1.48$ kPa (30.86 lb/ft^2).

Figure 6.- Continued.

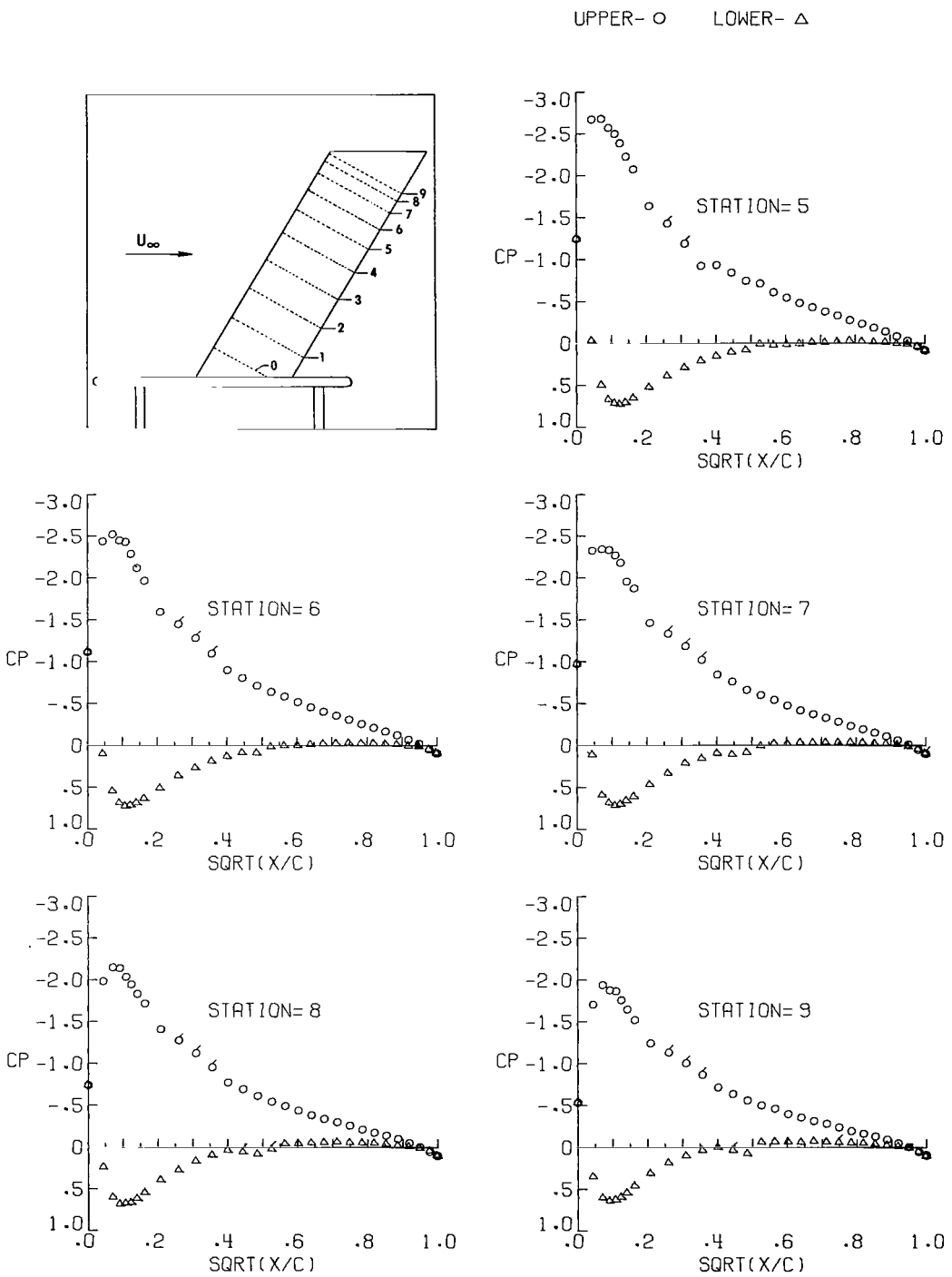

(h) Concluded.

Figure 6.- Continued.

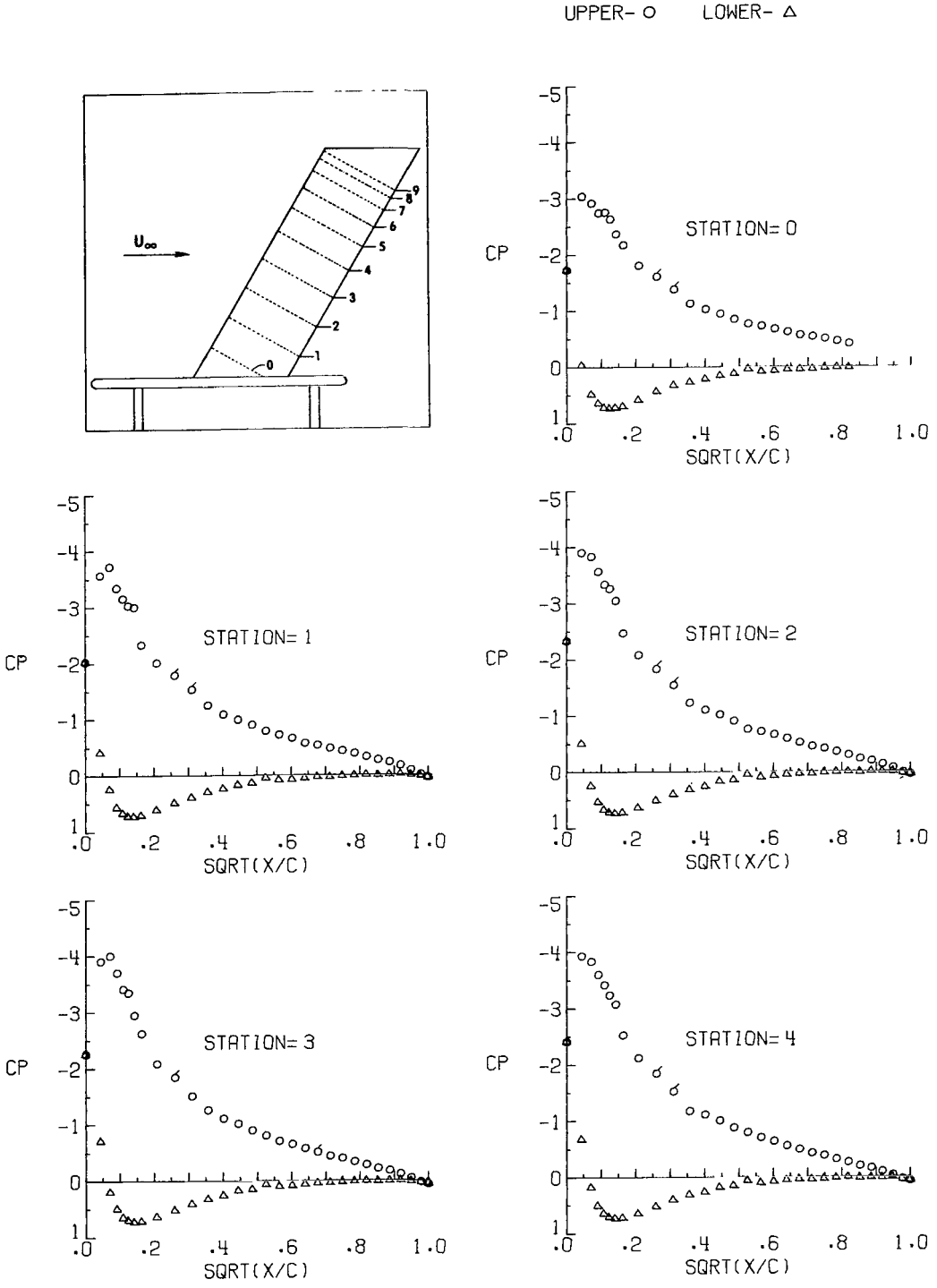

(i) $\alpha = 10.90^{o}$; $q_\infty = 1.48$ kPa (30.88 lb/ft^2).

Figure 6.- Continued.

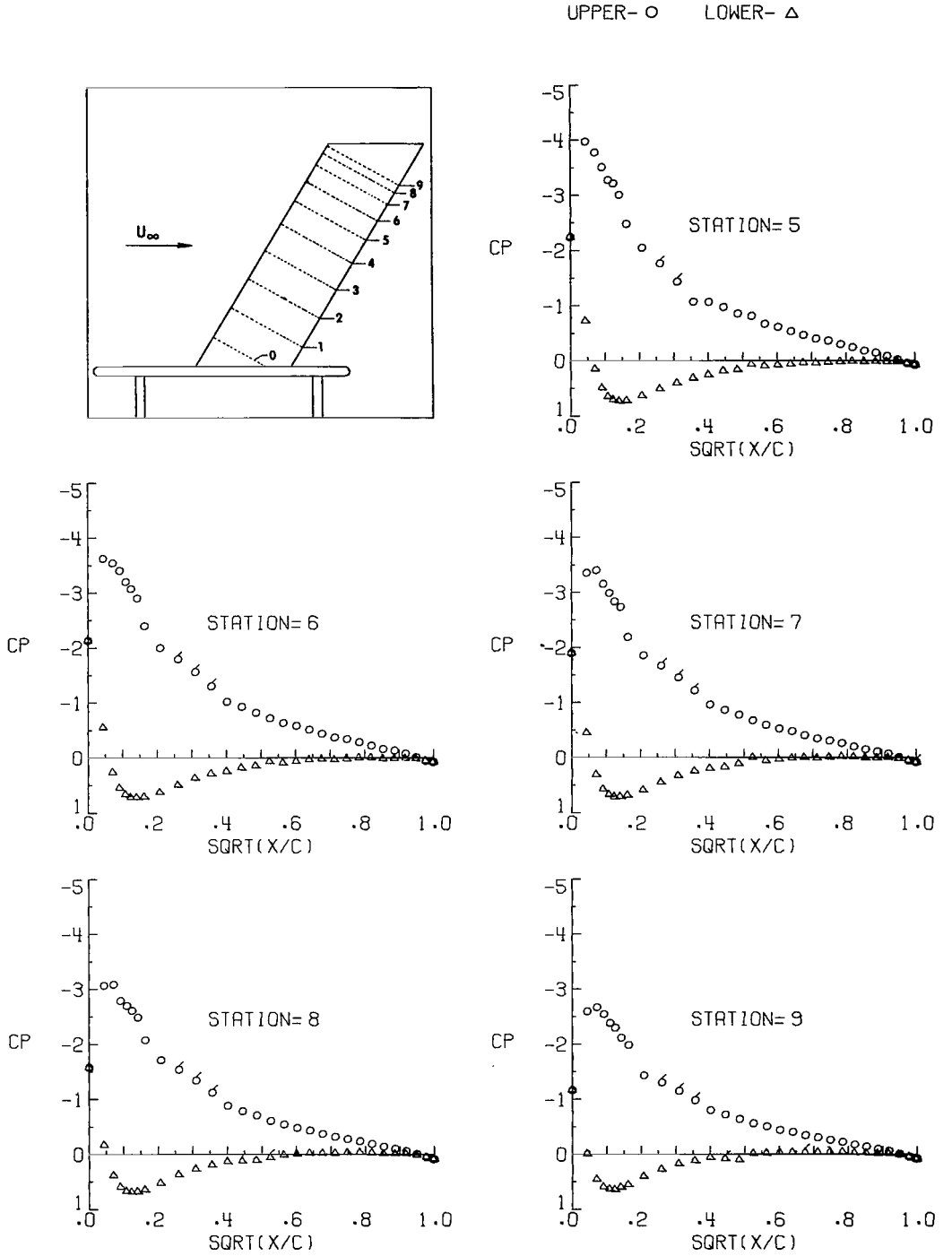

(i) Concluded.

Figure 6.- Continued.

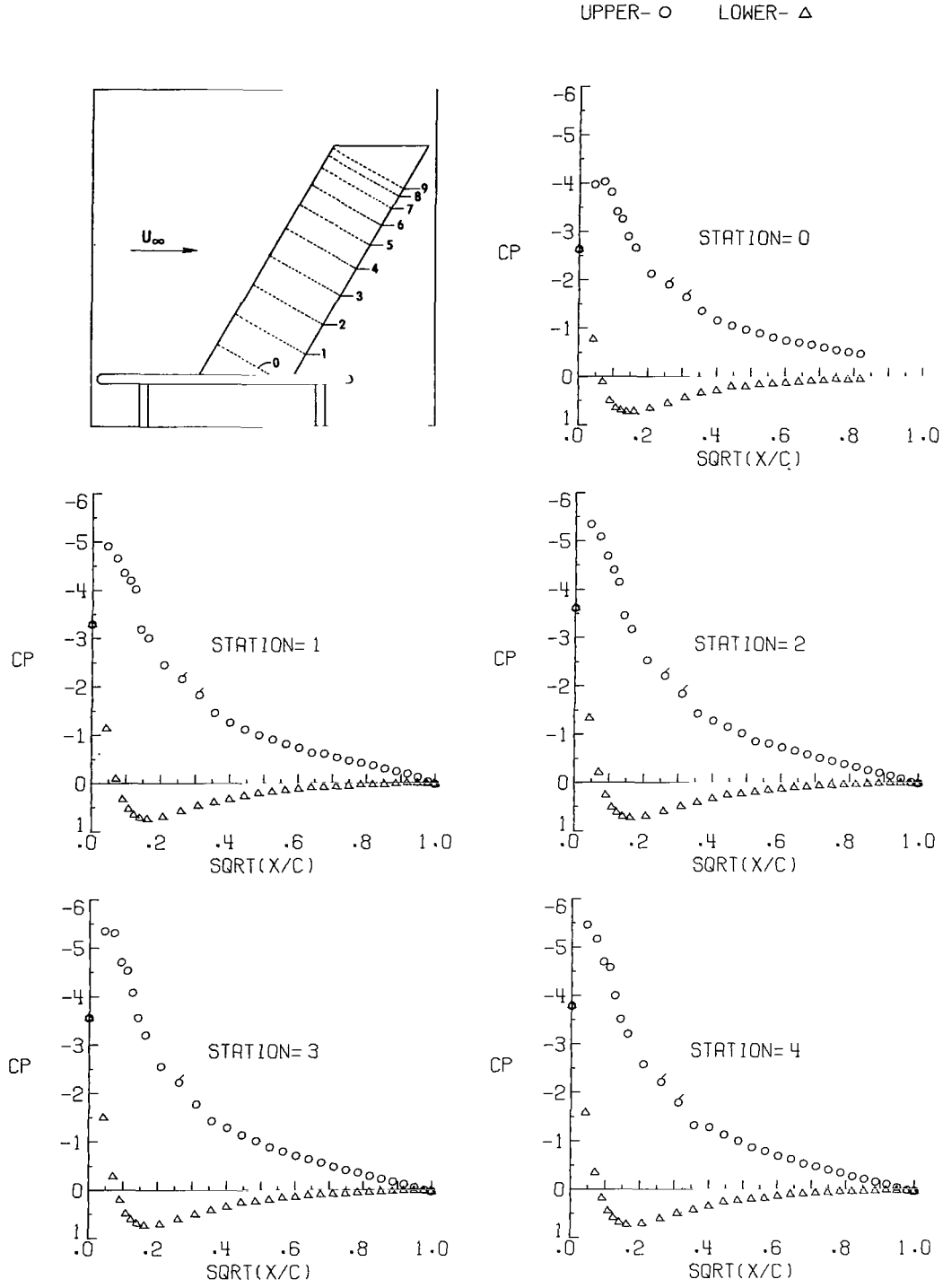

(j) $\alpha = 13.00^{o}$; $q_\infty = 1.47$ kPa (30.77 lb/ft^2).

Figure 6.- Continued.

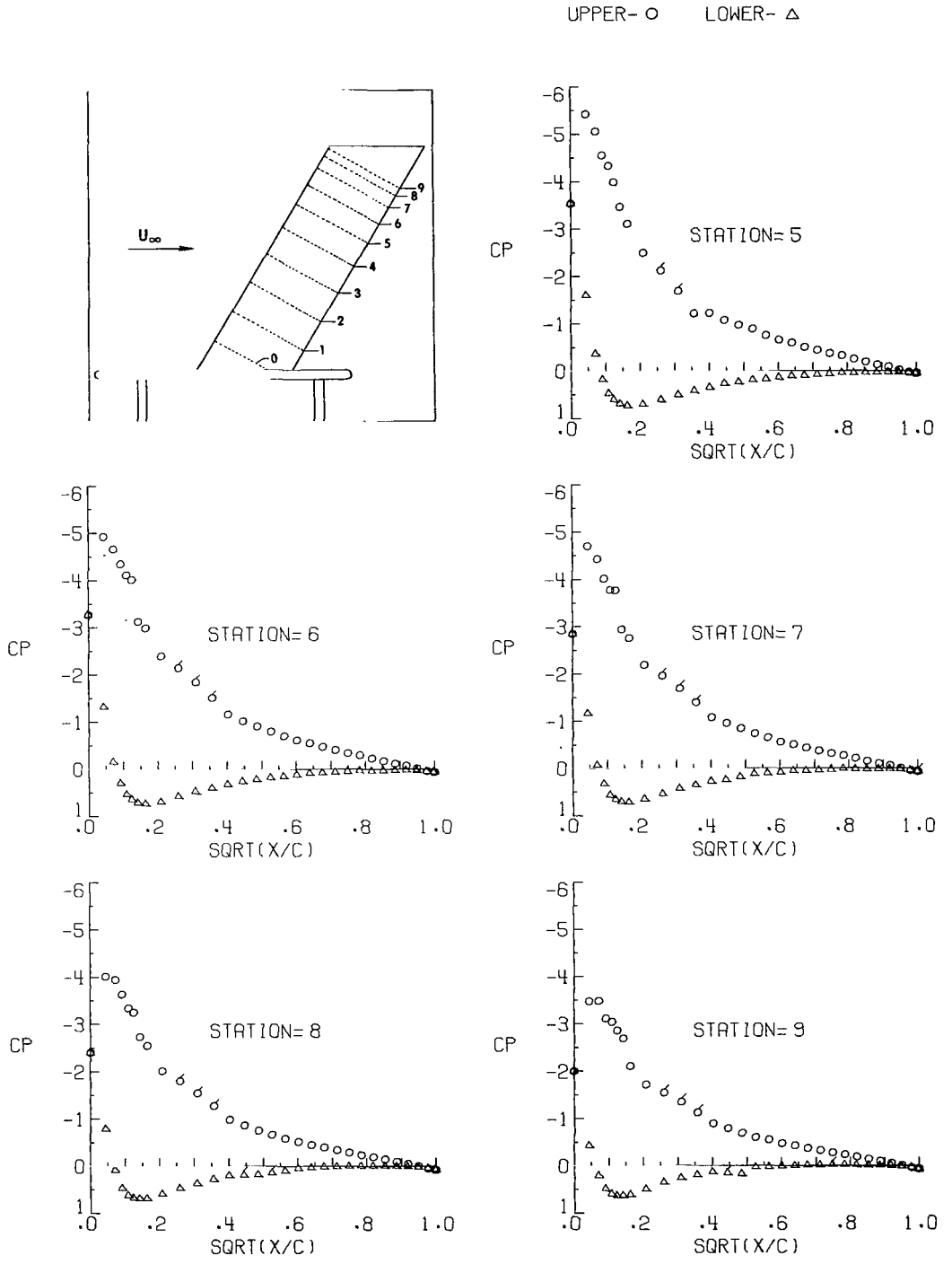

(j) Concluded.

Figure 6.- Continued.

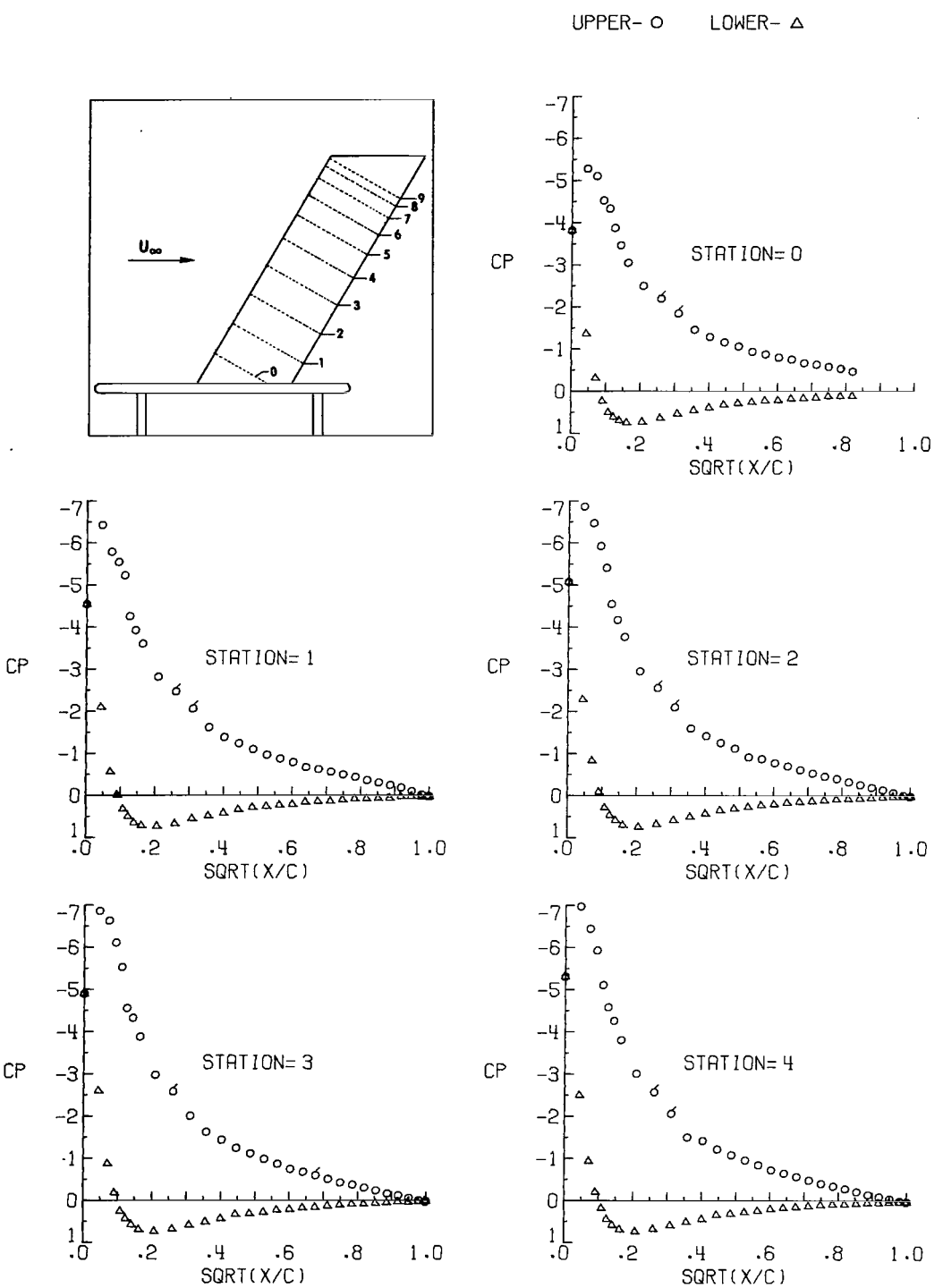

(k) $\alpha = 15.08^{o}$; $q_\infty = 1.48$ kPa (30.94 lb/ft^2).

Figure 6.- Continued.

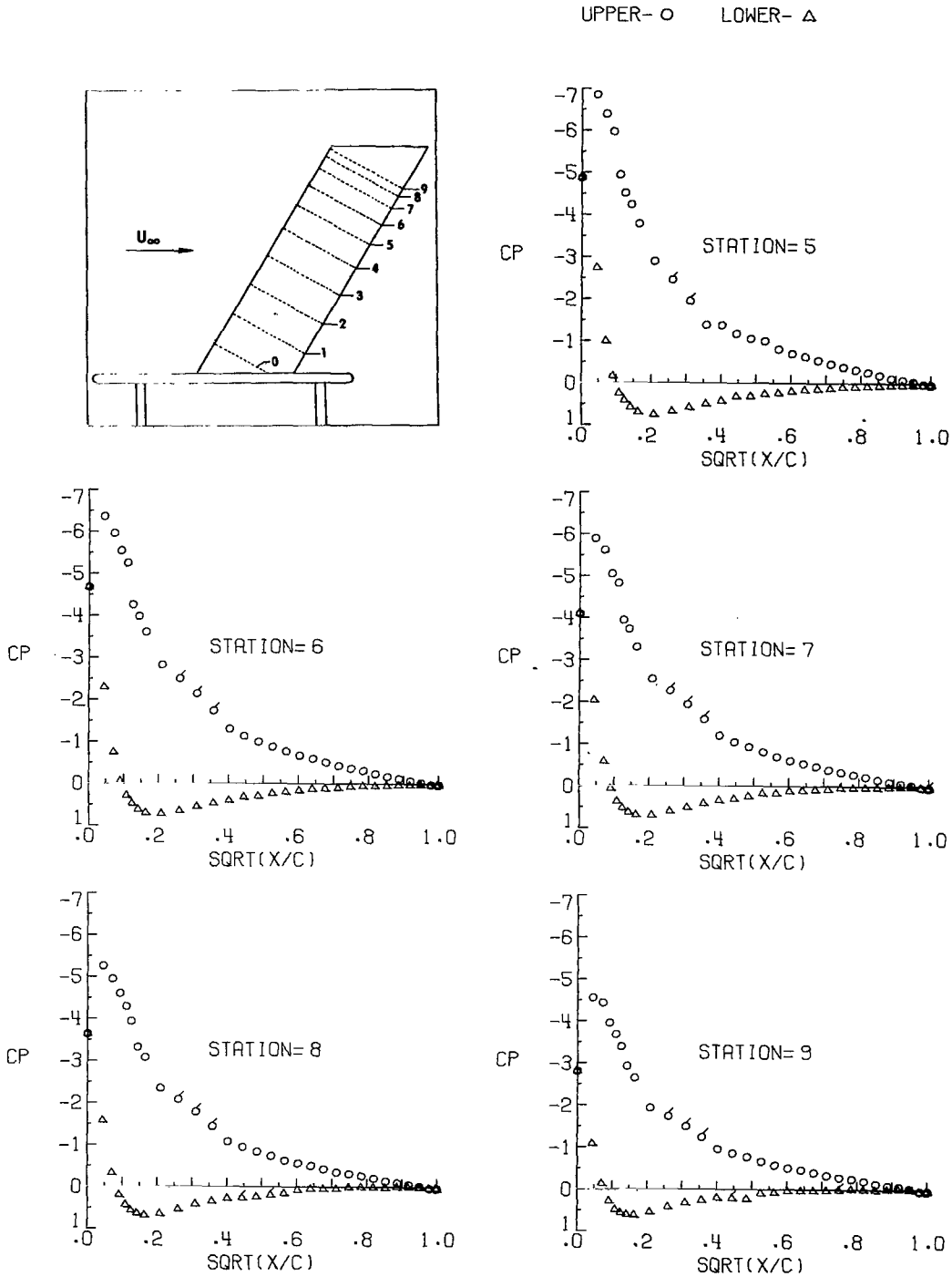

(k) Concluded.

Figure 6.- Continued.

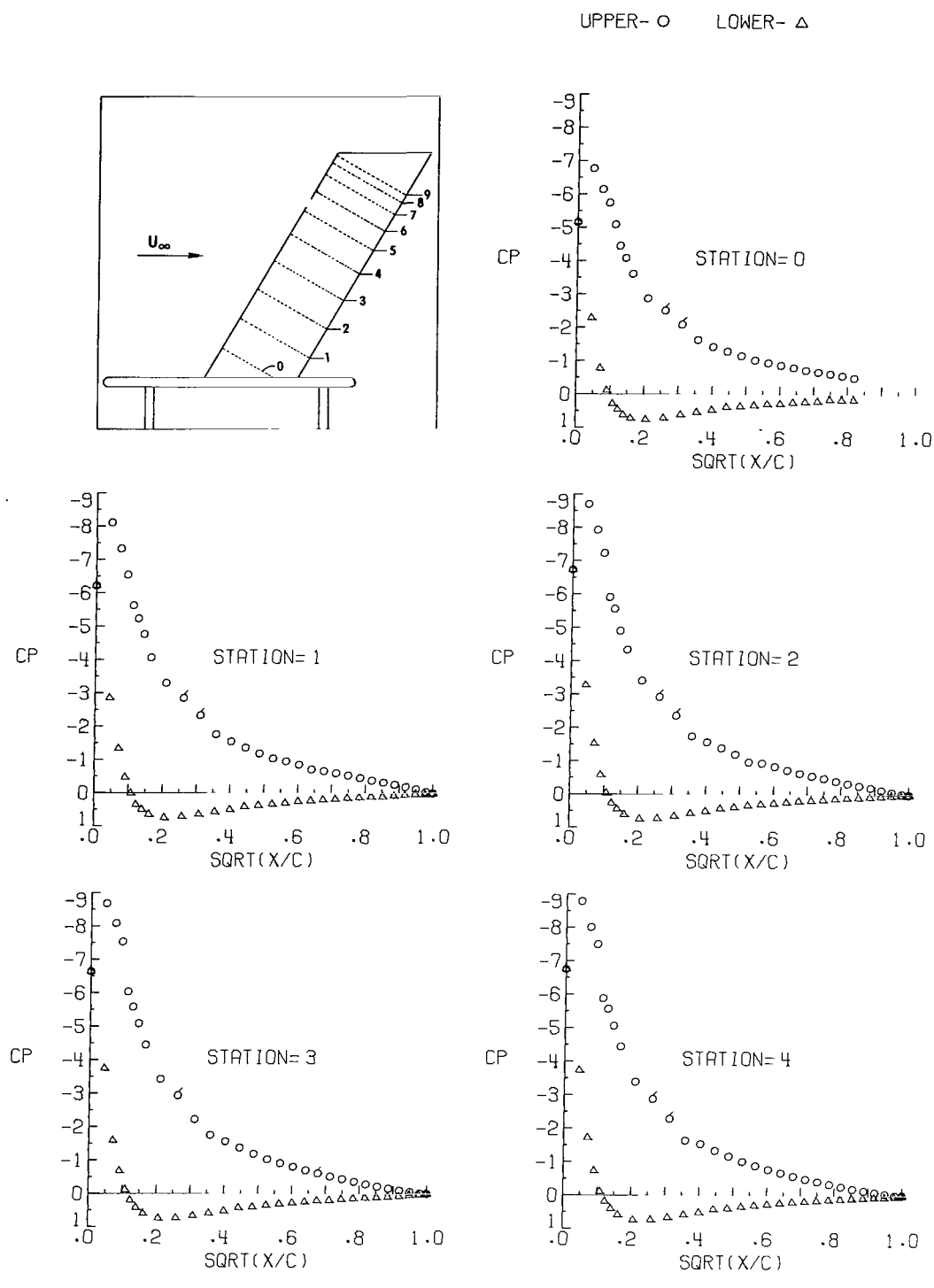

(1) $\alpha = 17.15^{o}$; $q_\infty = 1.47$ kPa (30.79 lb/ft^2).

Figure 6.- Continued.

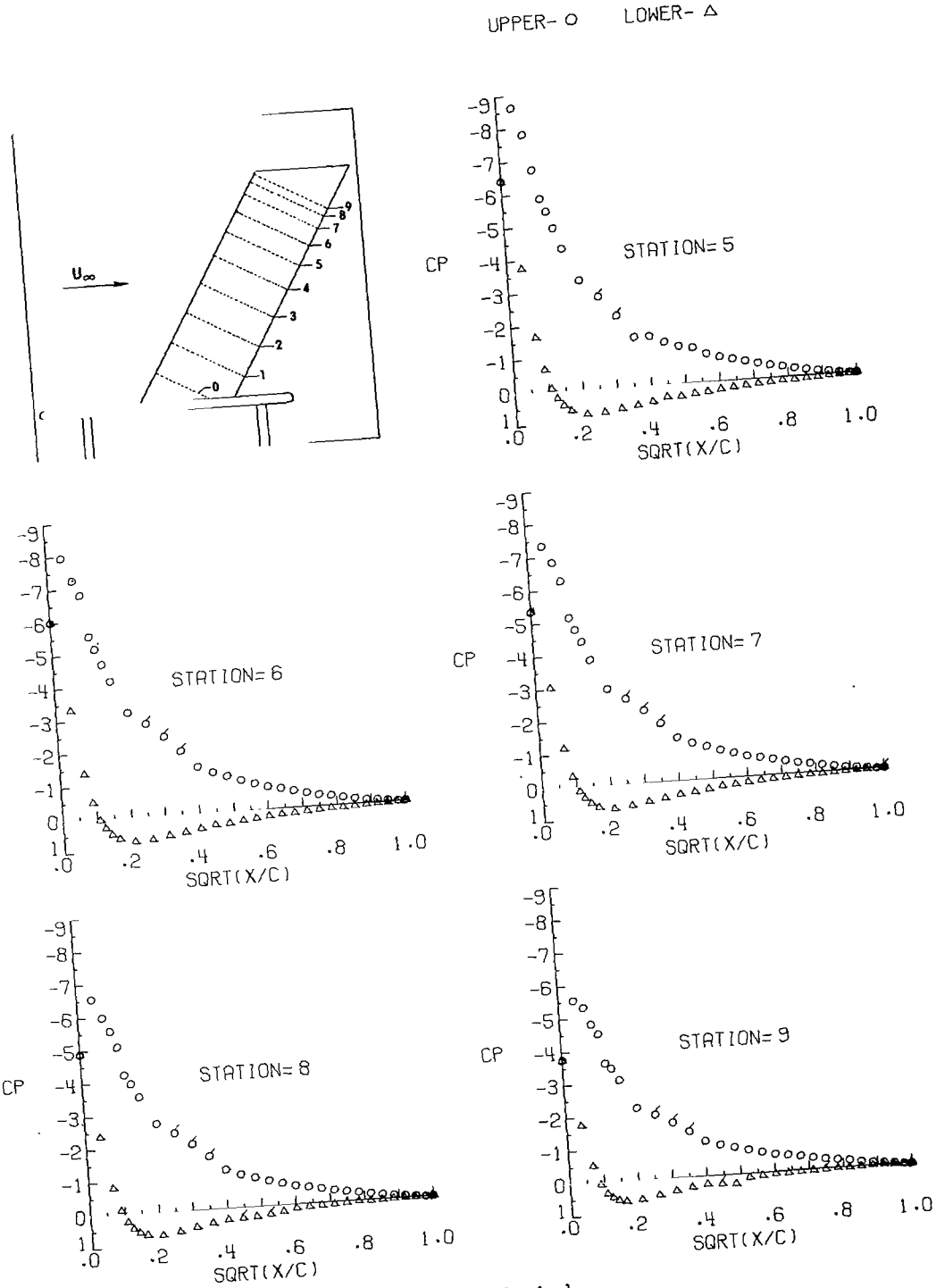

(1) Concluded.

Figure 6.- Continued.

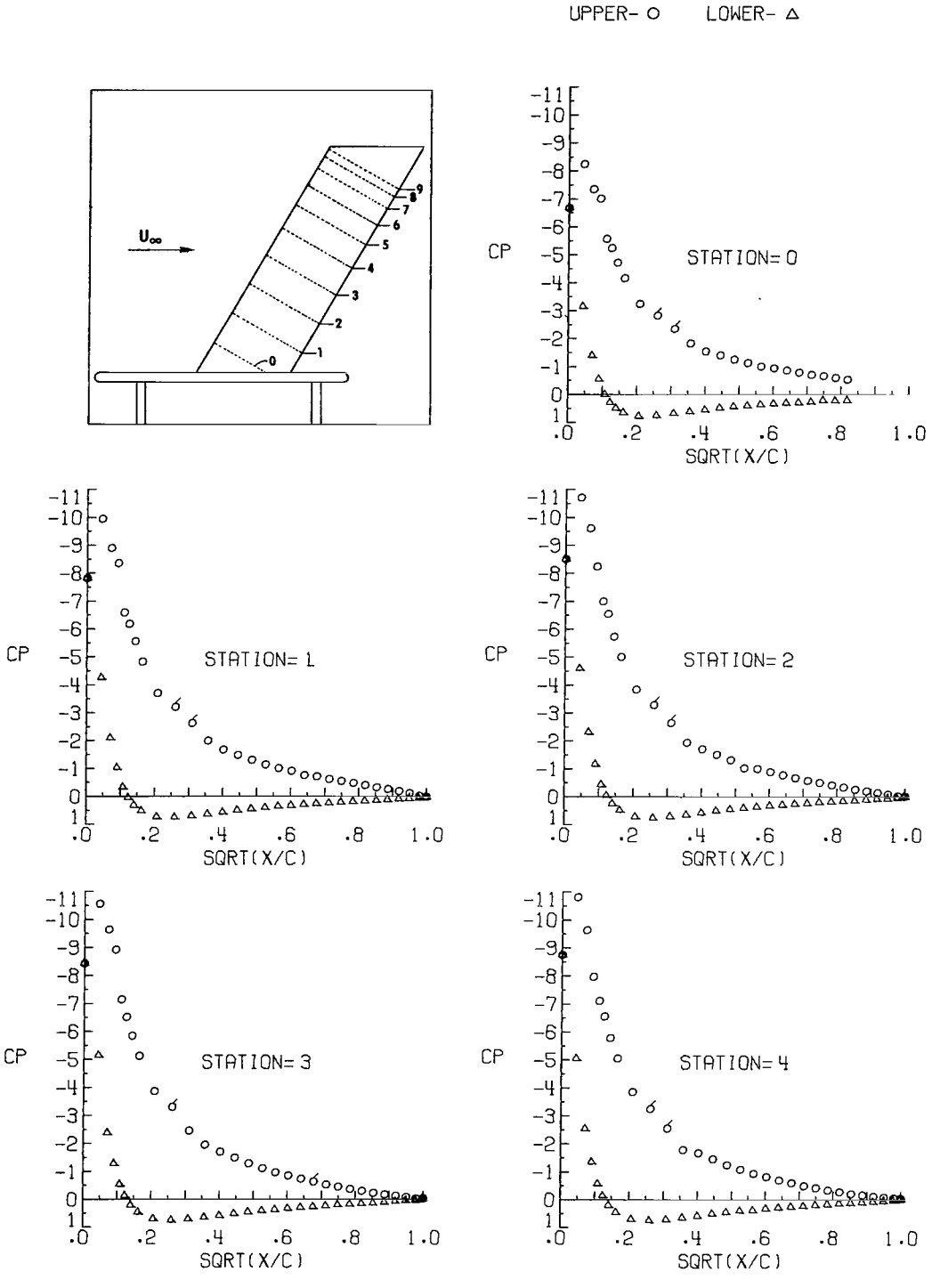

(m) $\alpha = 19.24^{o}$; $q_\infty = 1.48$ kPa (30.97 lb/ft^2).

Figure 6.- Continued.

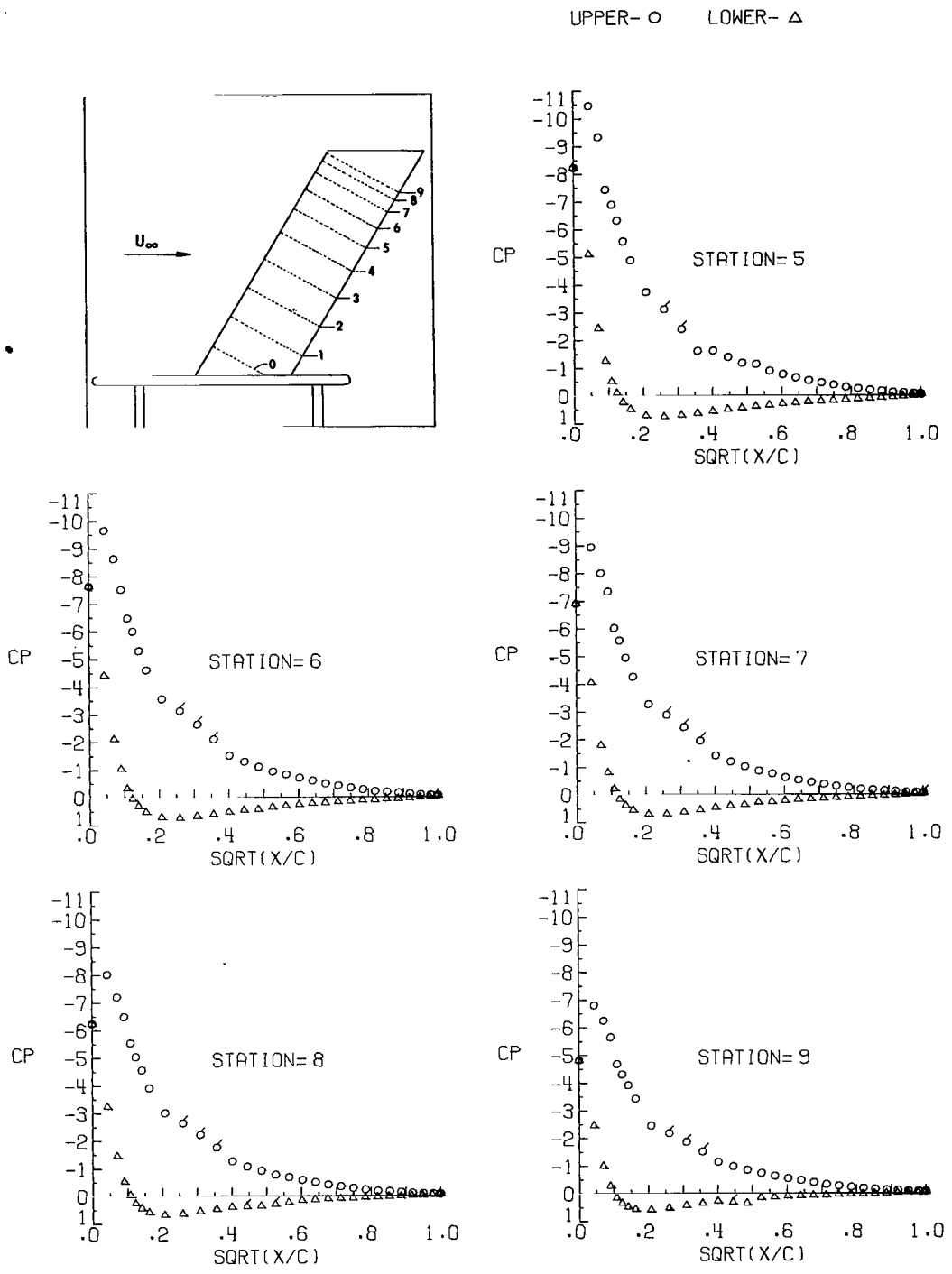

(m) Concluded.

Figure 6.- Continued.

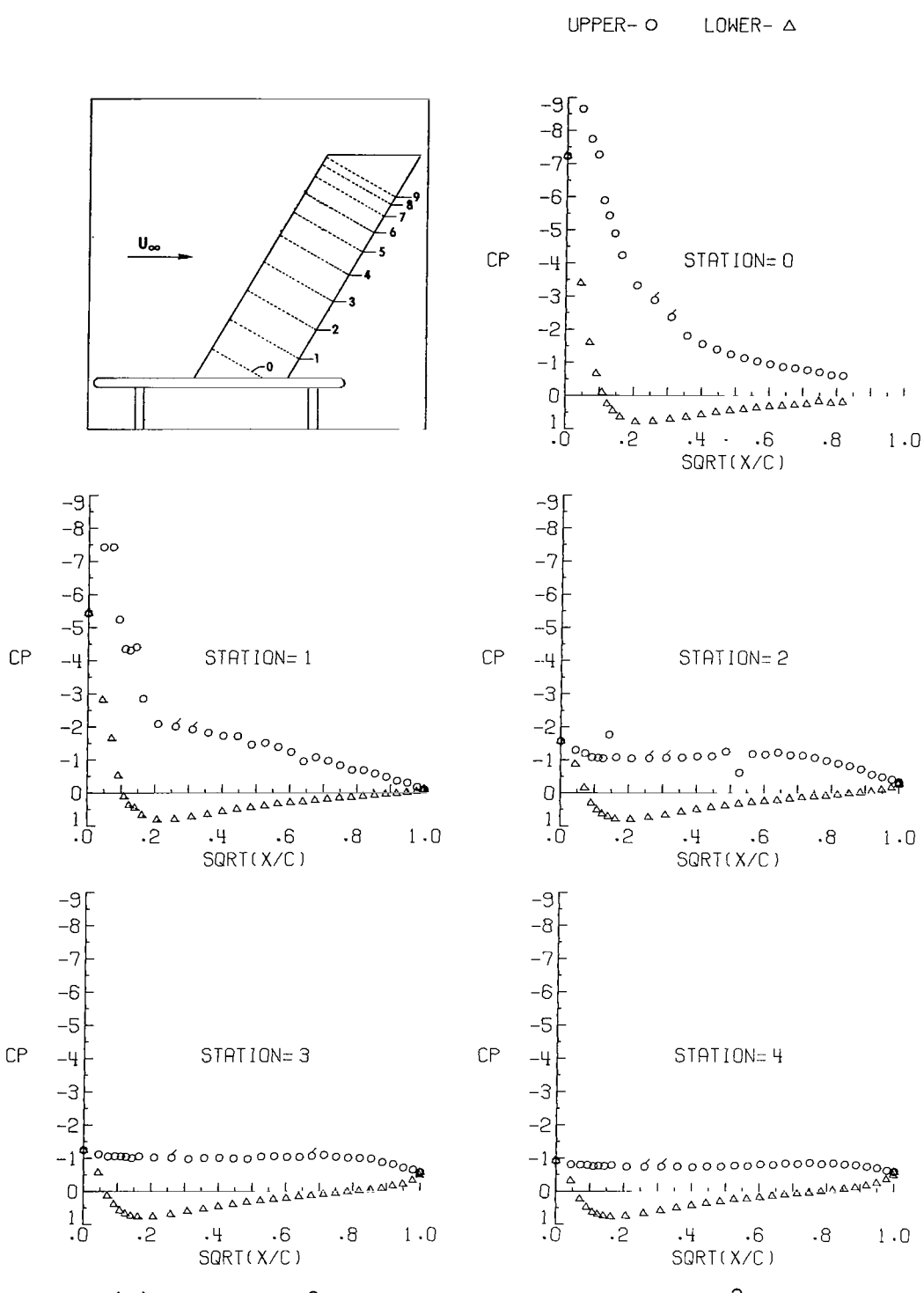

(n) $\alpha = 21.07^{\circ}$; $q_\infty = 1.48$ kPa (30.81 lb/ft^2).

Figure 6.- Continued.

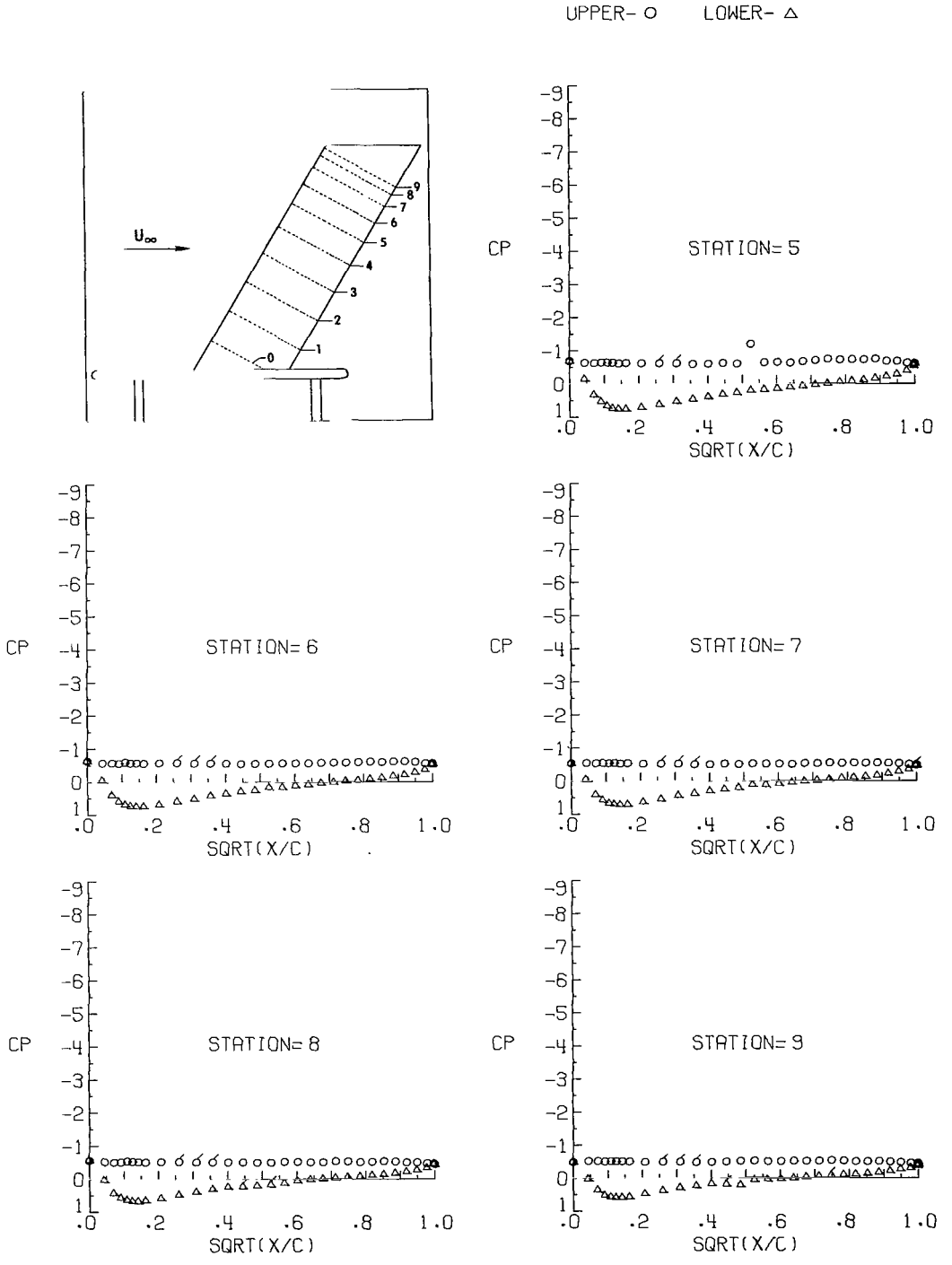

(n) Concluded.

Figure 6.- Concluded.

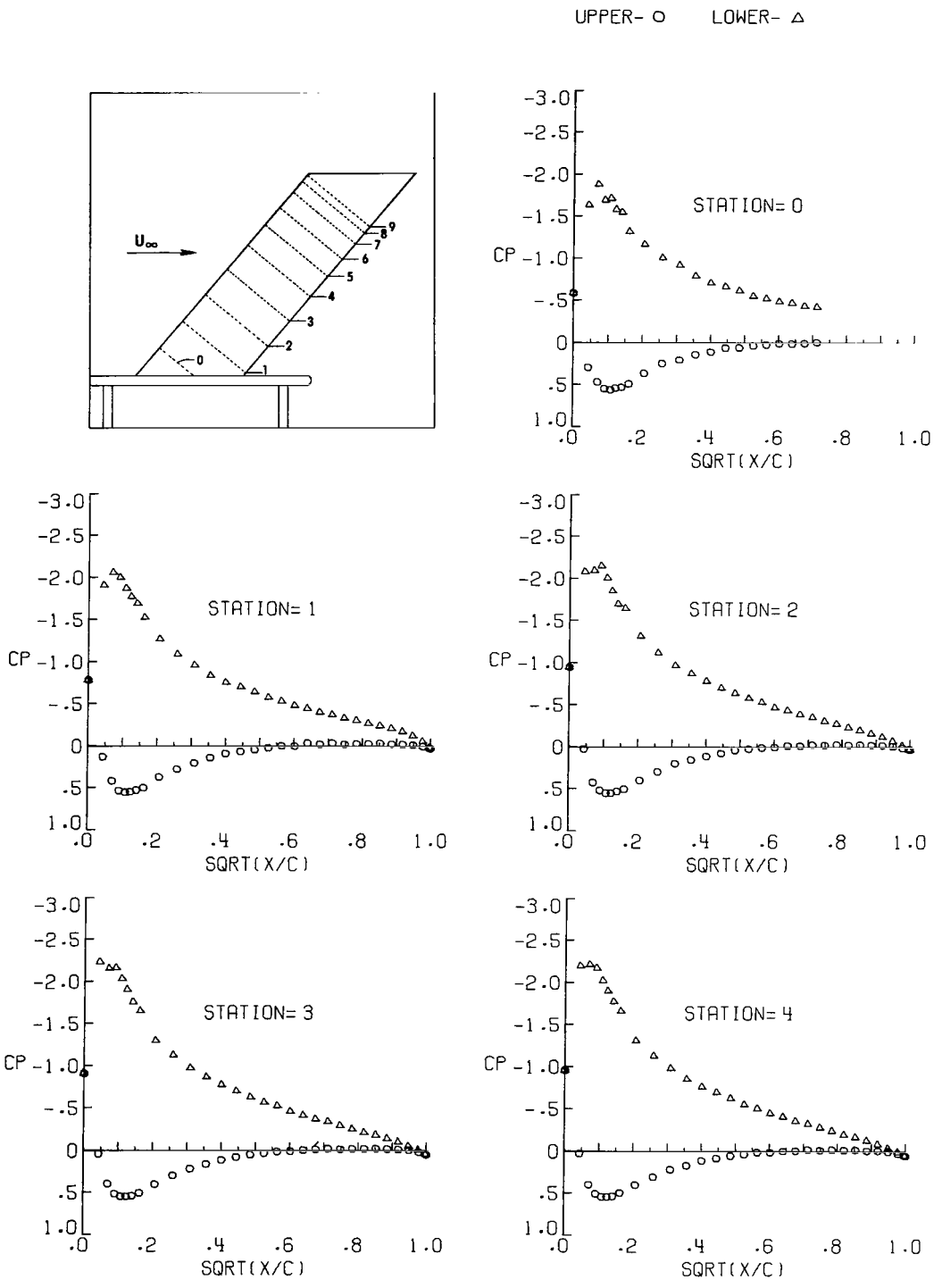

(a) $\alpha = -7.92^{o}$; $q_\infty = 1.48$ kPa (30.86 lb/ft^2).

Figure 7.- Pressure distributions at sweep angle of 40^{o}.

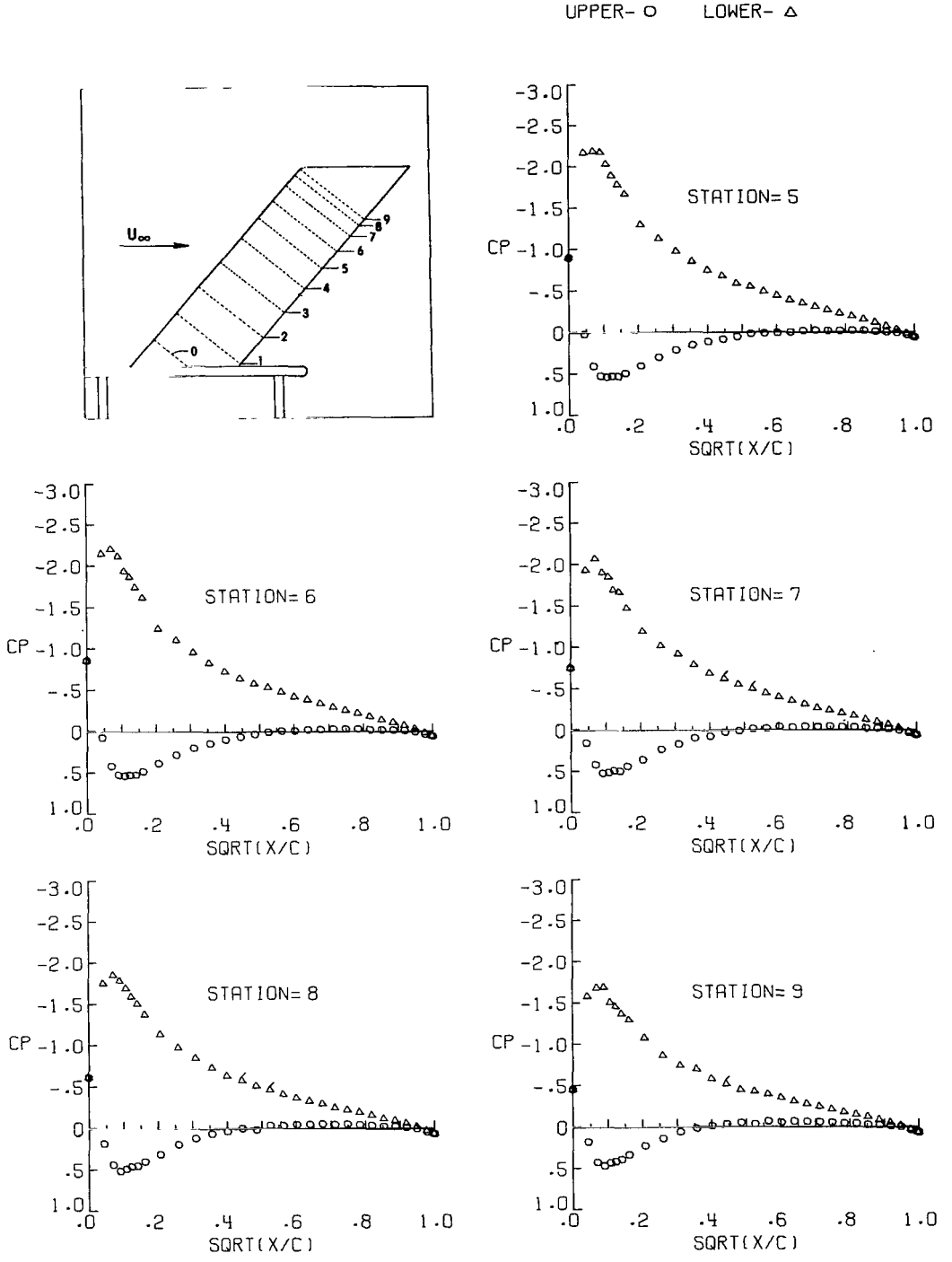

(a) Concluded.

Figure 7.- Continued.

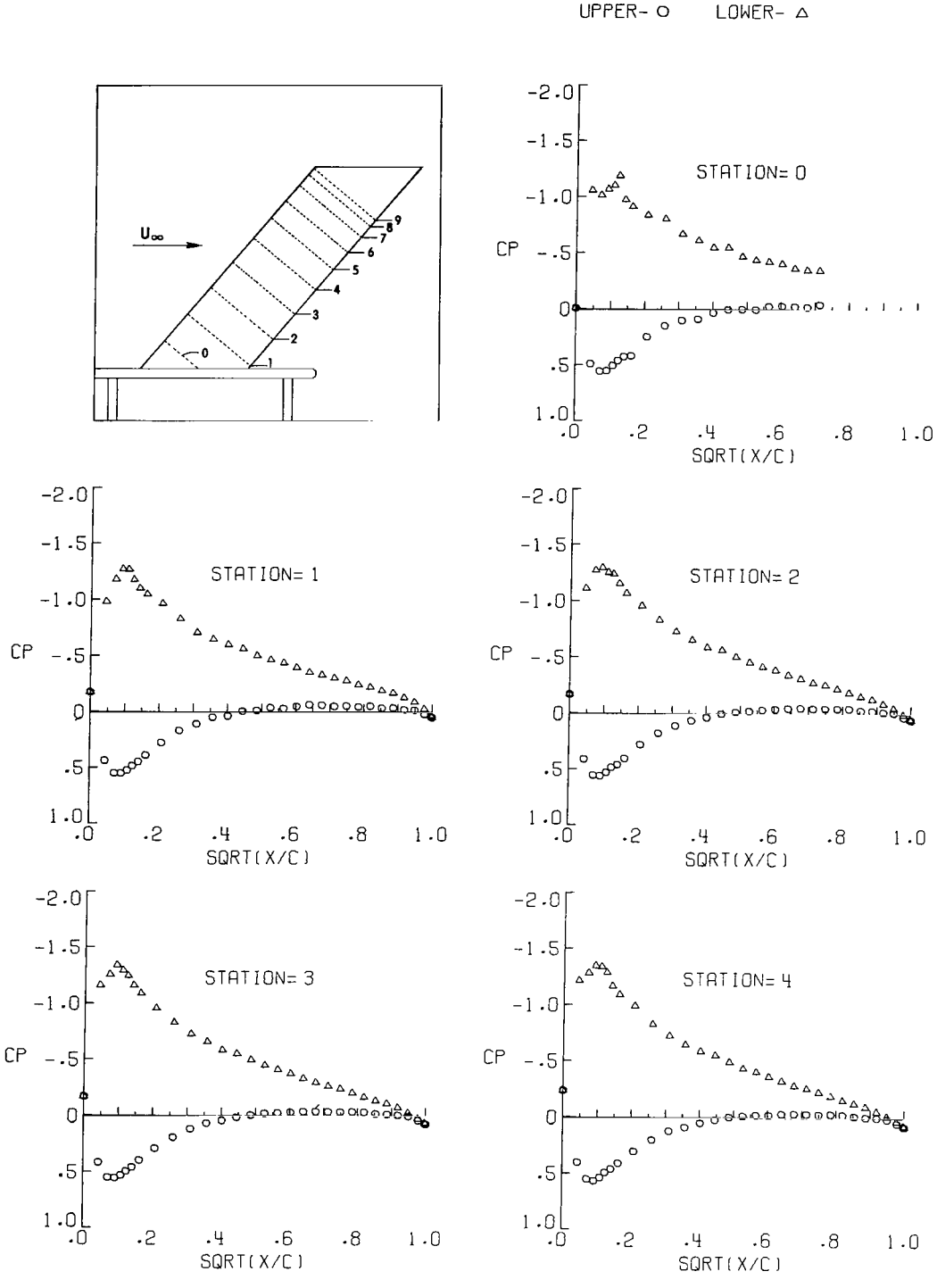

(b) $\alpha = -5.83^{\circ}$; $q_\infty = 1.52$ kPa (31.74 lb/ft^2).

Figure 7.- Continued.

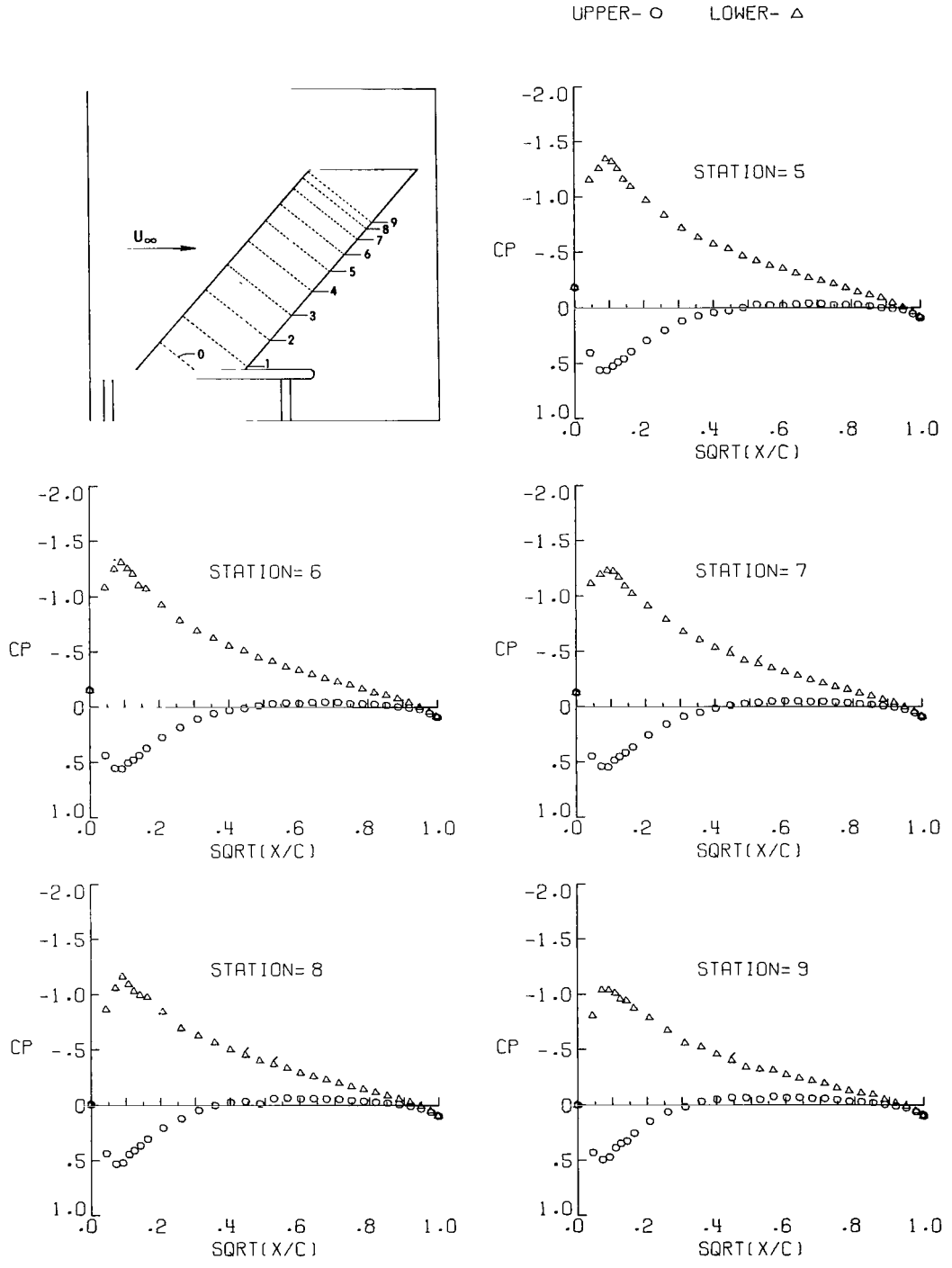

(b) Concluded.

Figure 7.- Continued.

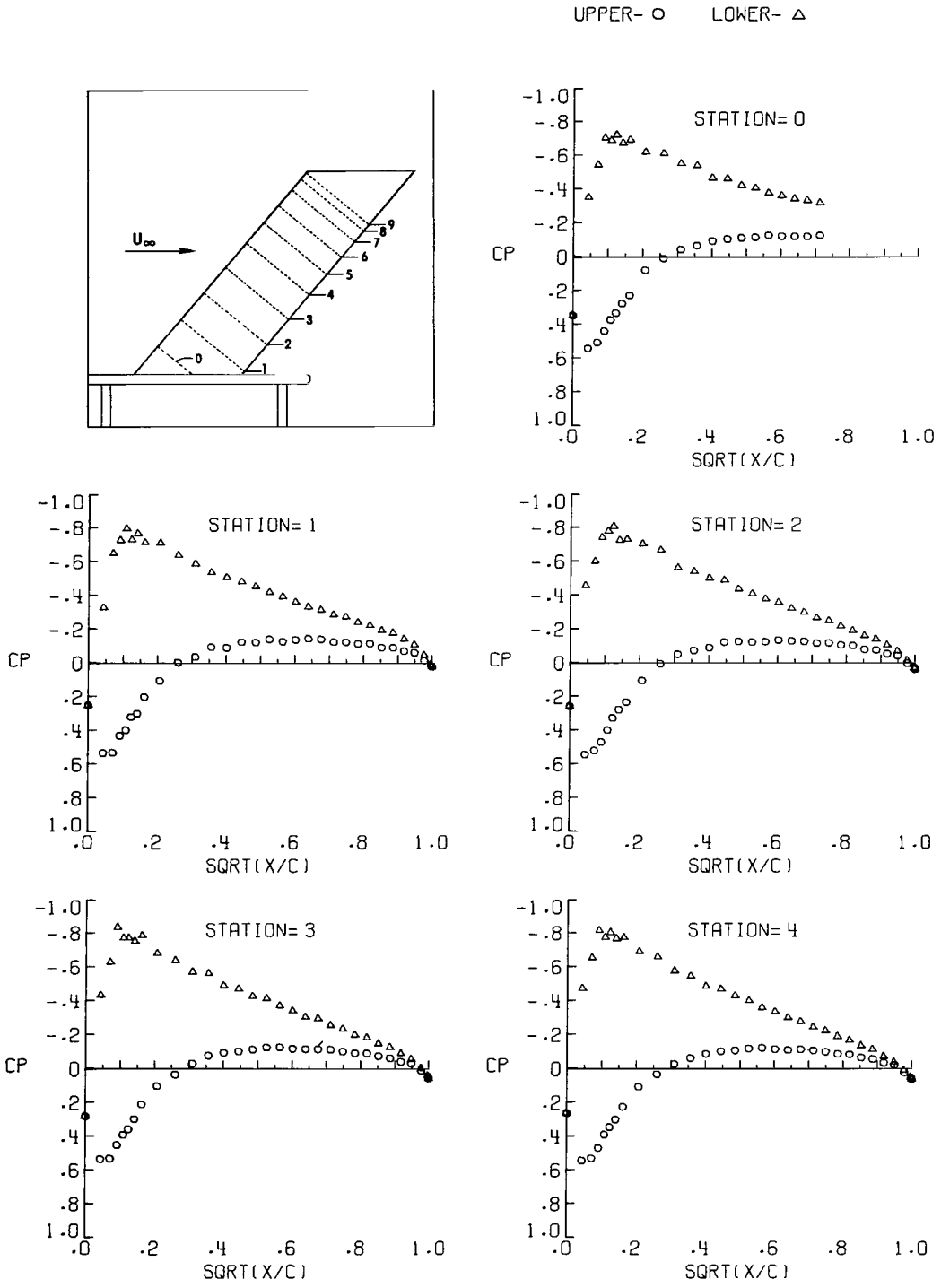

(c) $\alpha = -3.73^{\circ}$; $q_\infty = 1.48$ kPa (30.99 lb/ft^2).

Figure 7.- Continued.

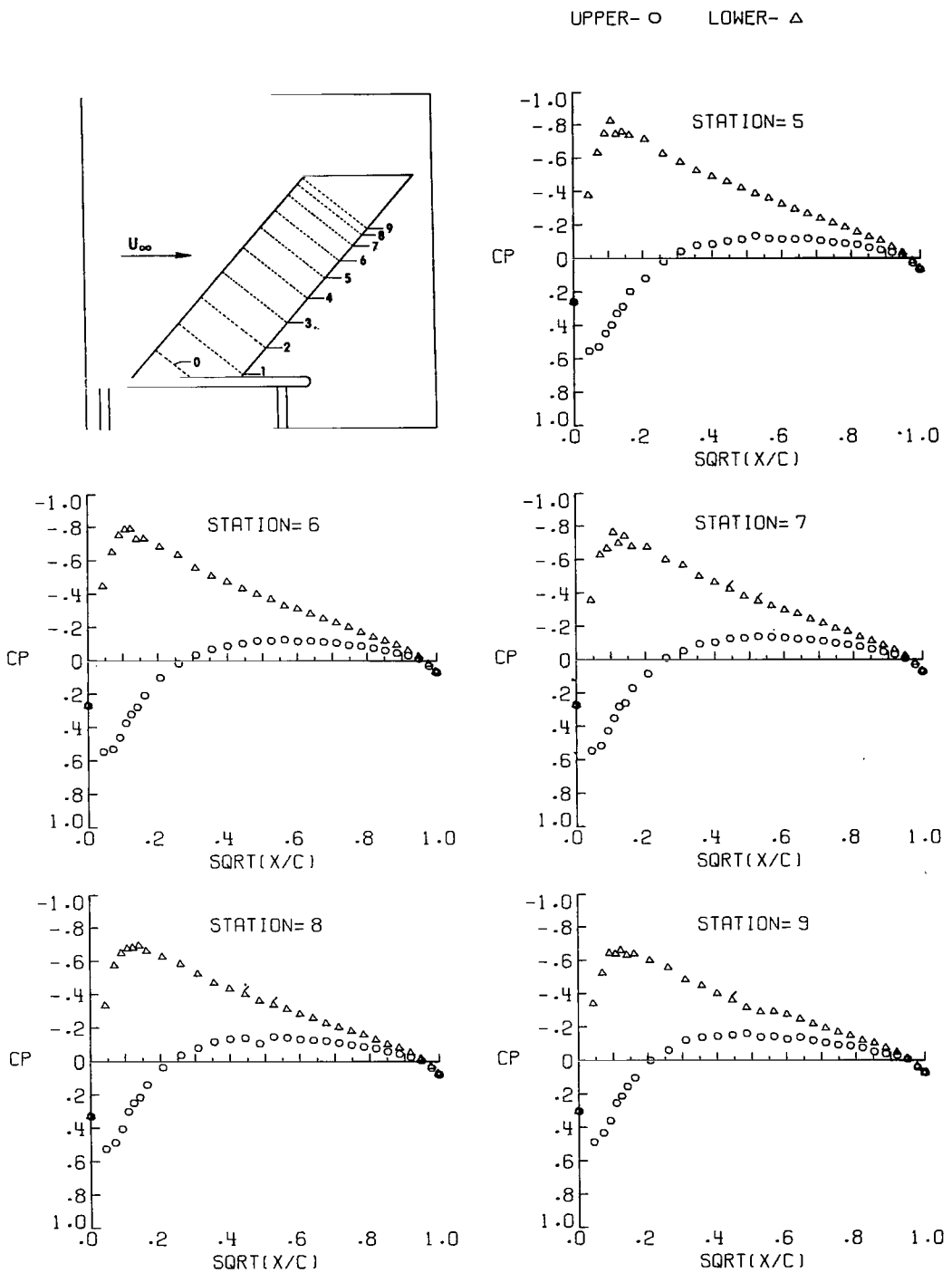

(c) Concluded.

Figure 7.- Continued.

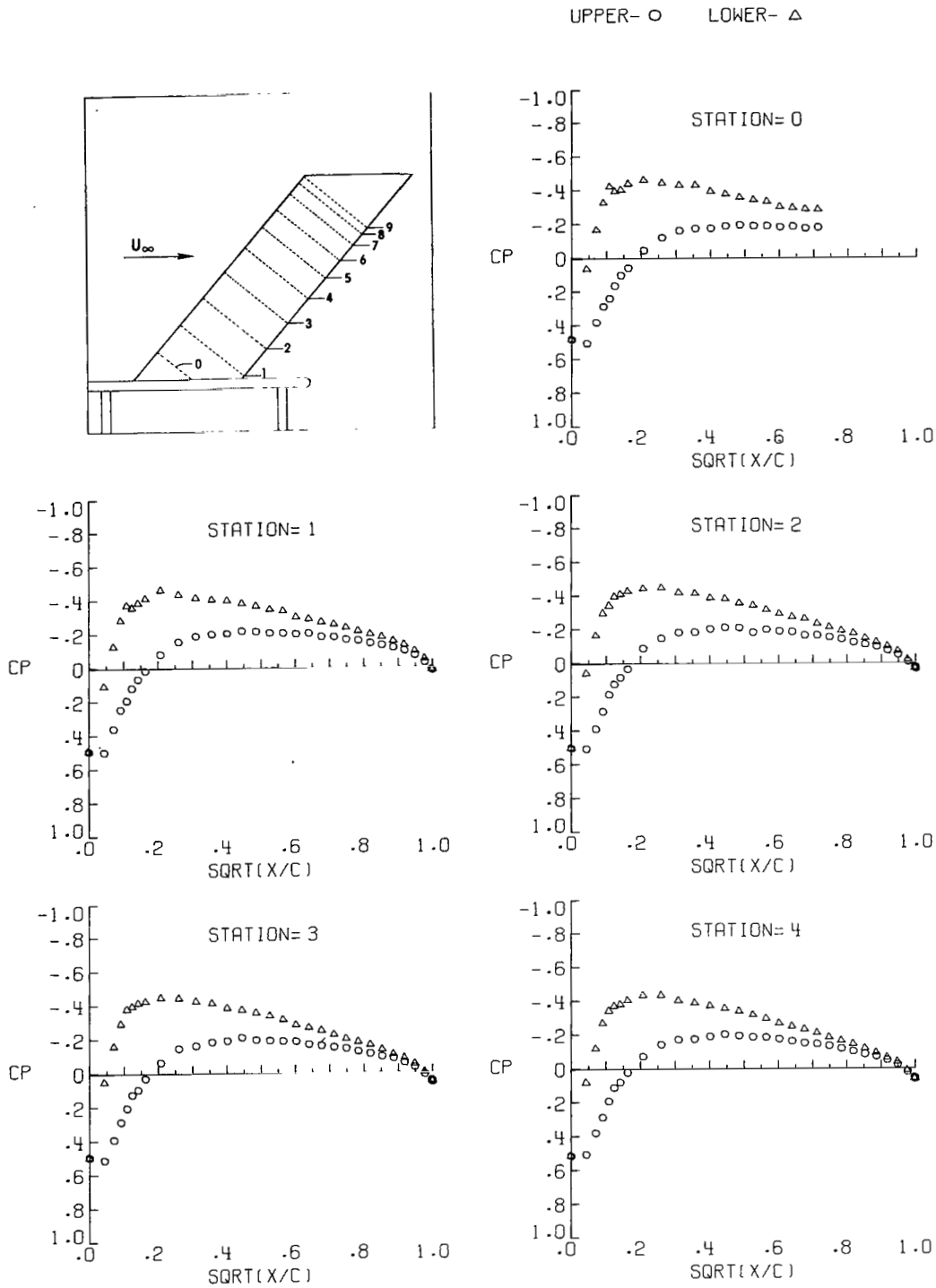

(d) $\alpha = -1.67^{o}$; $q_\infty = 1.48$ kPa (30.81 lb/ft^2).

Figure 7.- Continued.

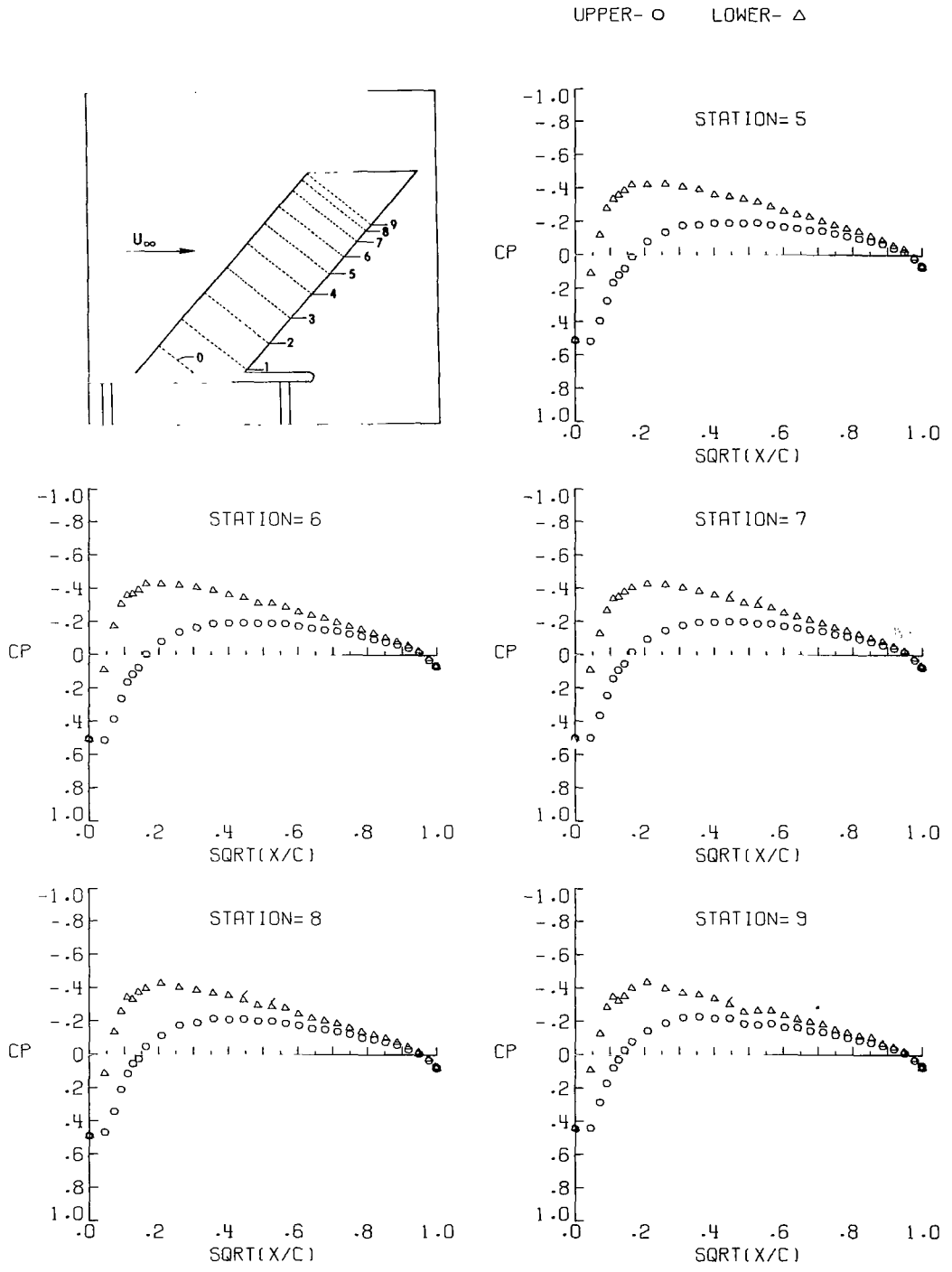

(d) Concluded.

Figure 7.- Continued.

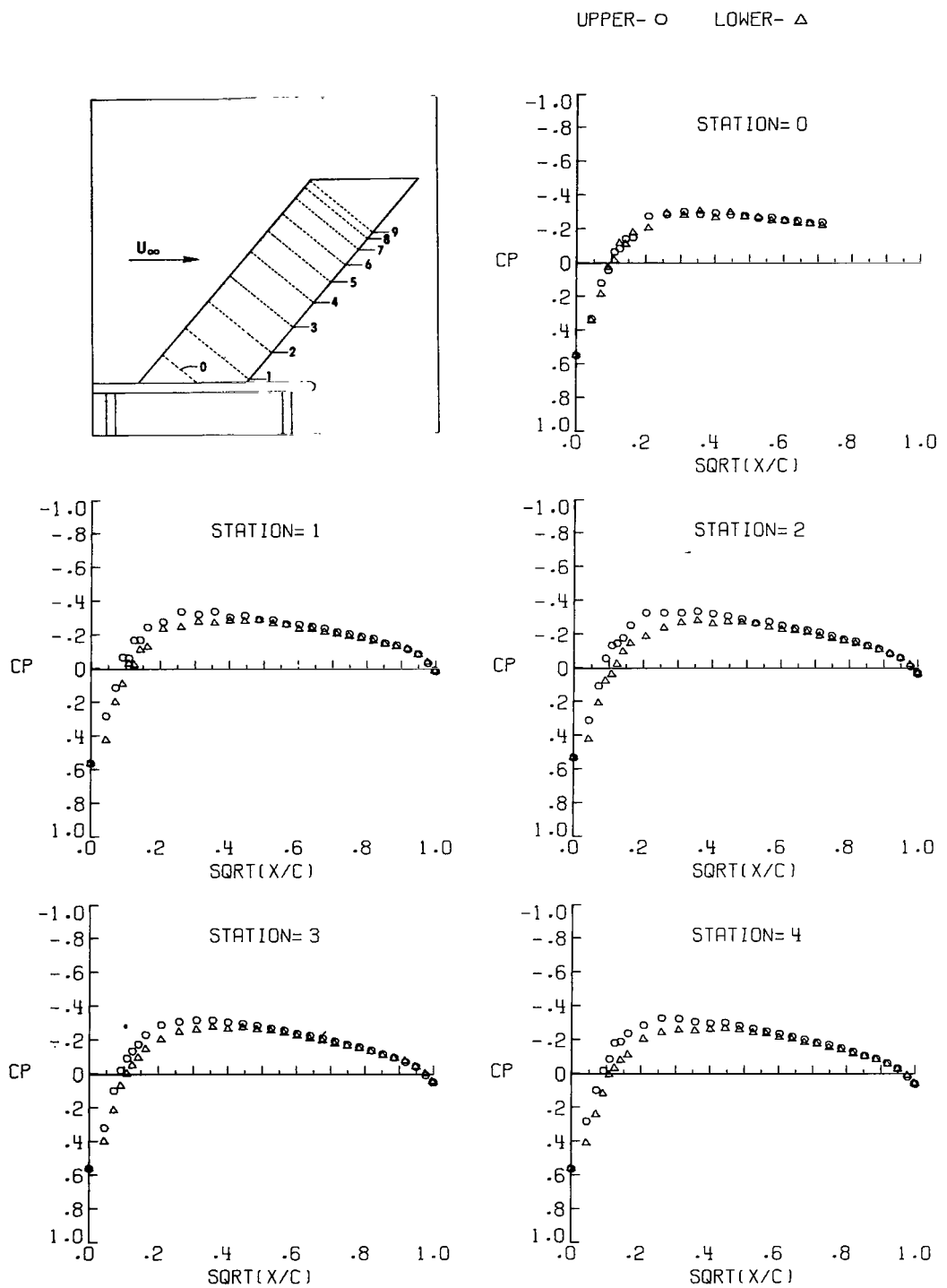

(e) $\alpha = 0.39^{o}$; $q_\infty = 1.47$ kPa (30.73 lb/ft^2).

Figure 7.- Continued.

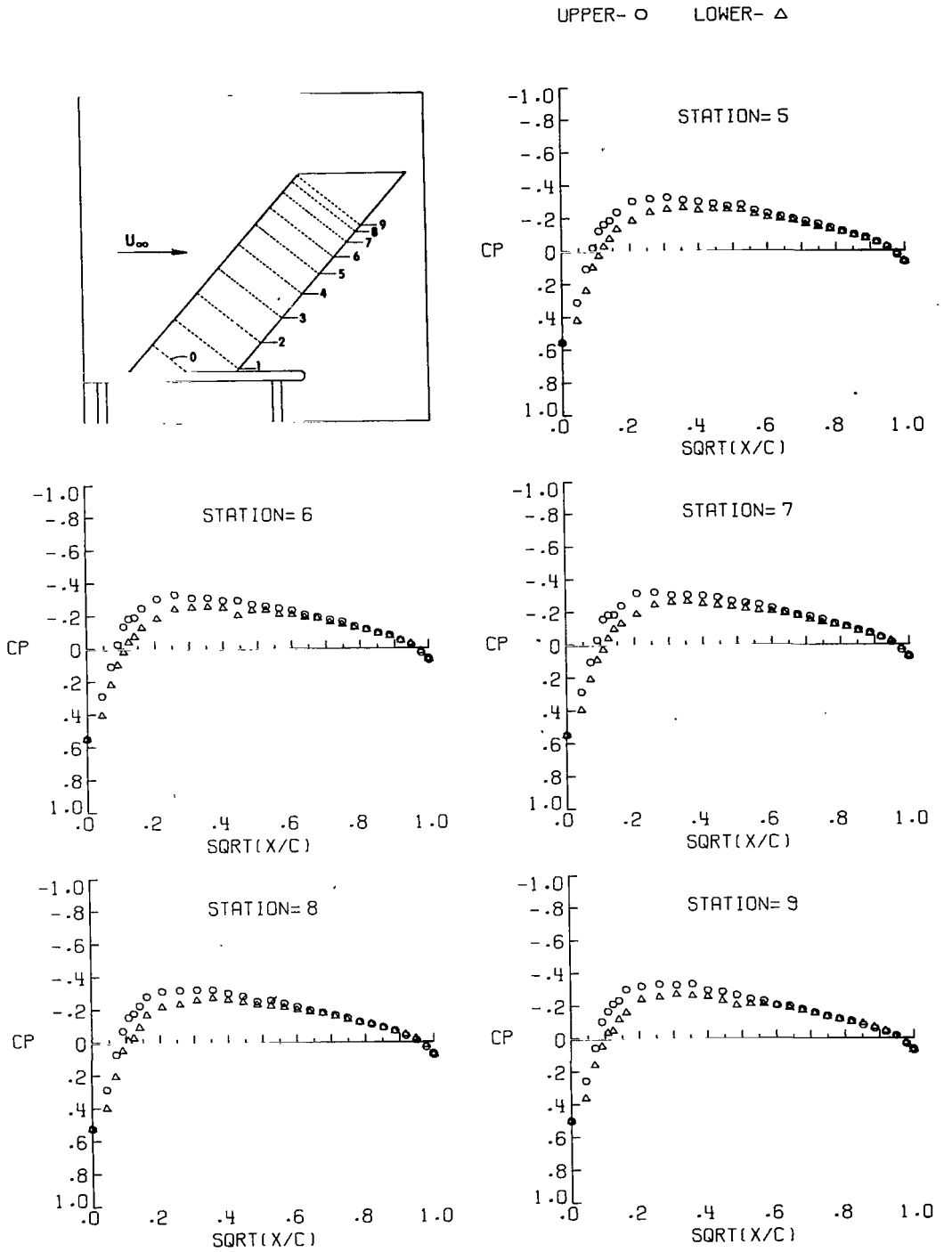

(e) Concluded.

Figure 7.- Continued.

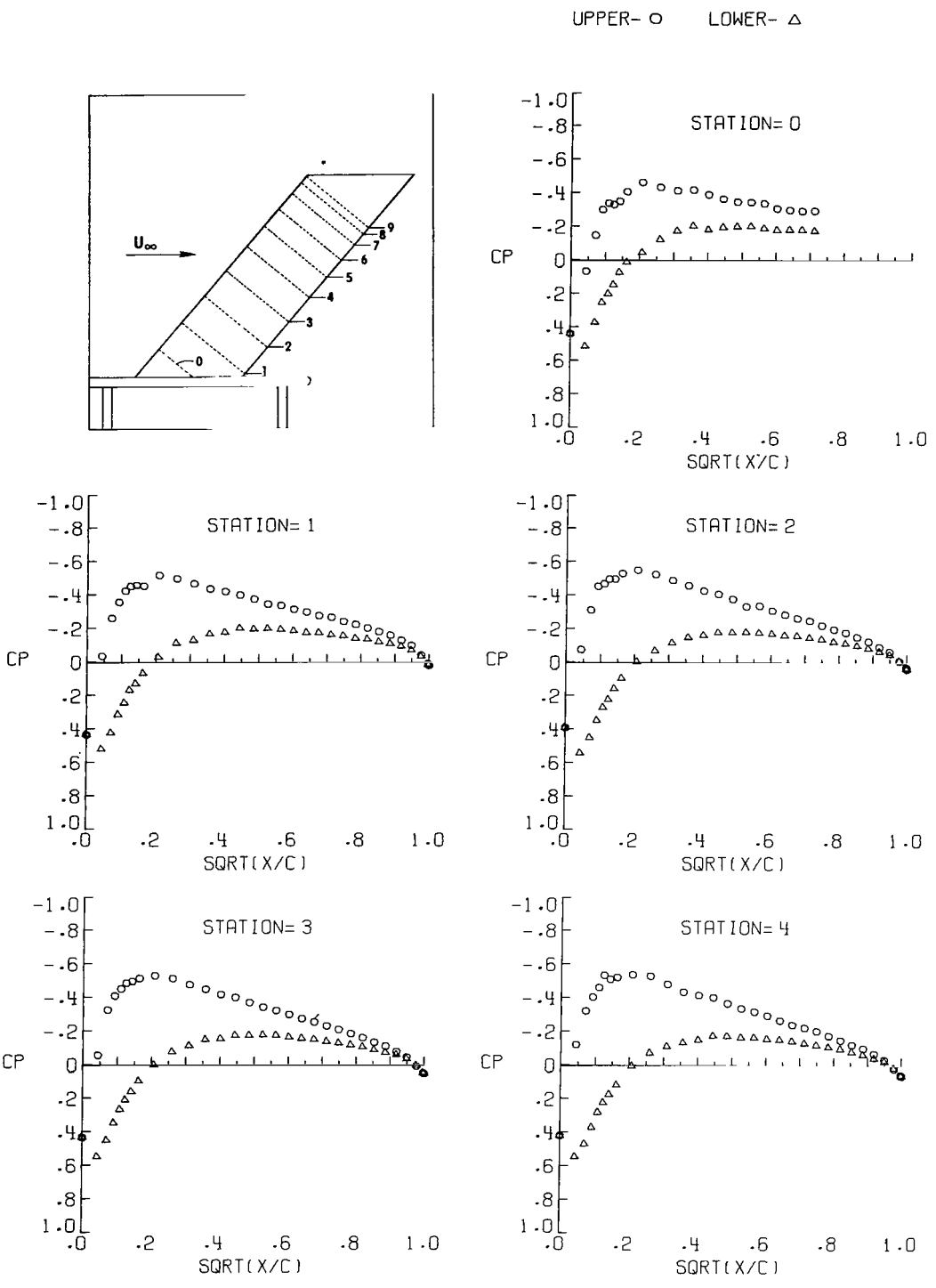

(f) $\alpha = 2.47^{\circ}$; $q_\infty = 1.47$ kPa (30.78 lb/ft^2).

Figure 7.- Continued.

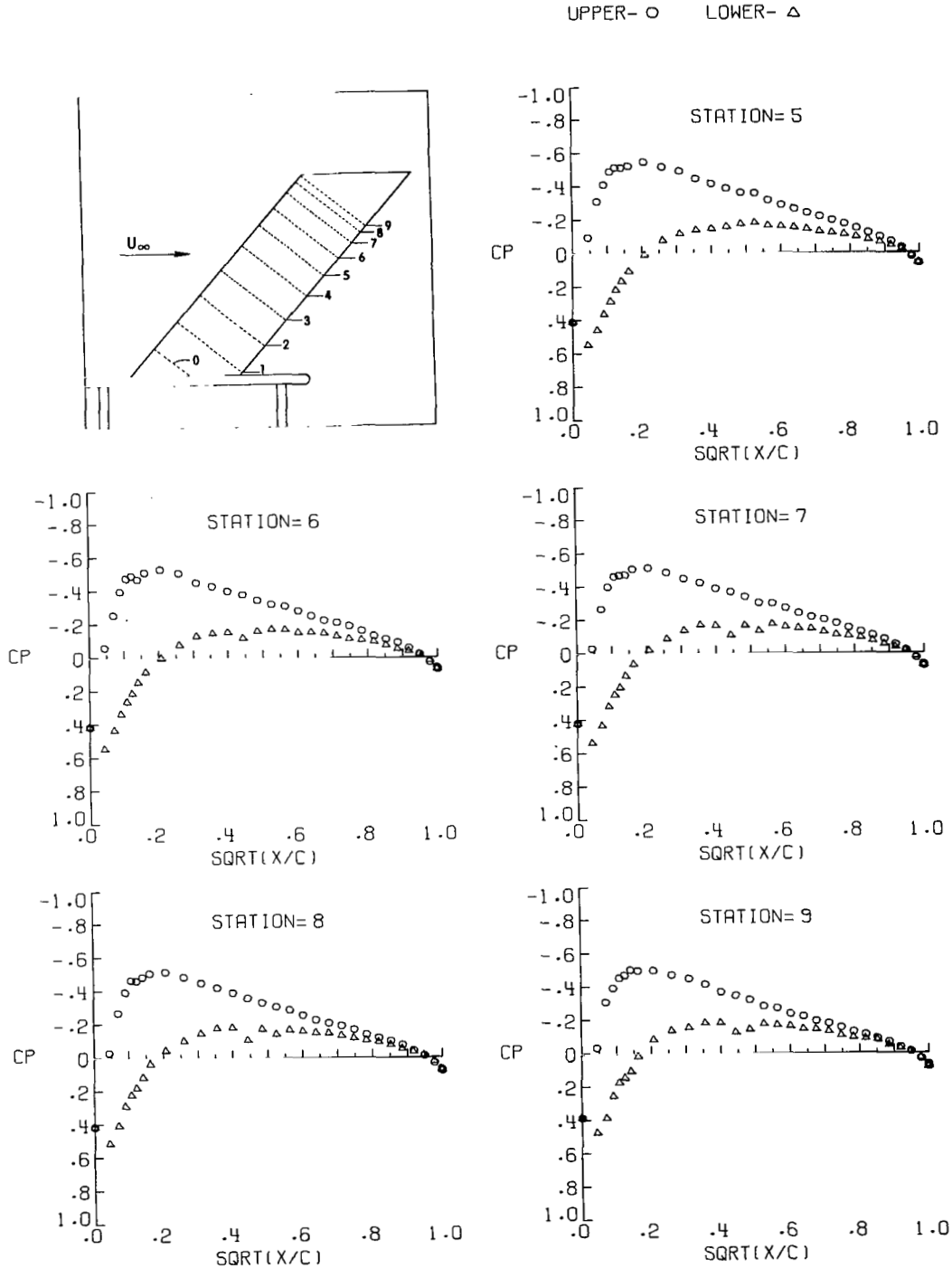

(f) Concluded.

Figure 7.- Continued.

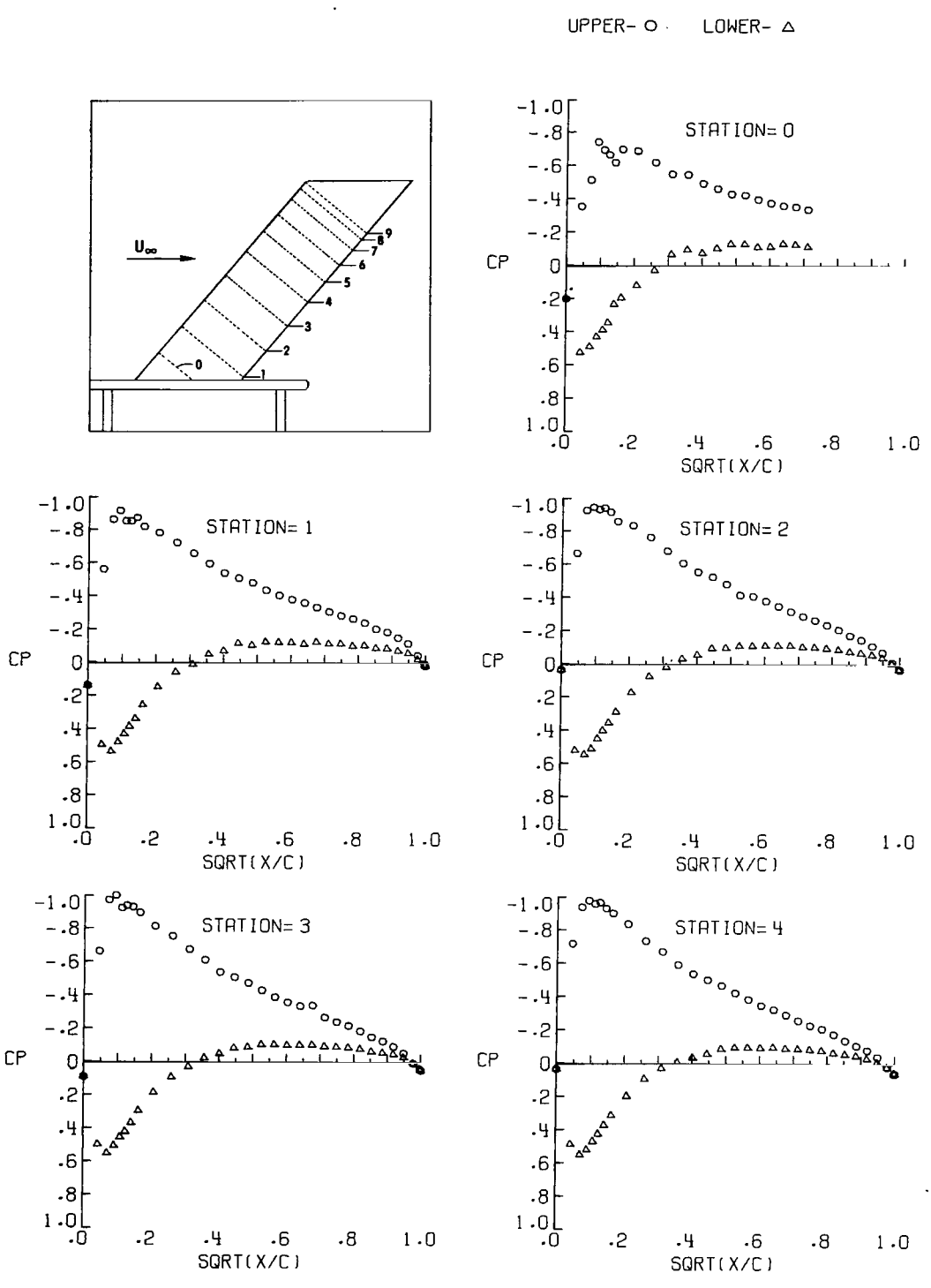

(g) $\alpha = 4.57^{\circ}$; $q_\infty = 1.48$ kPa (30.87 lb/ft^2).

Figure 7.- Continued.

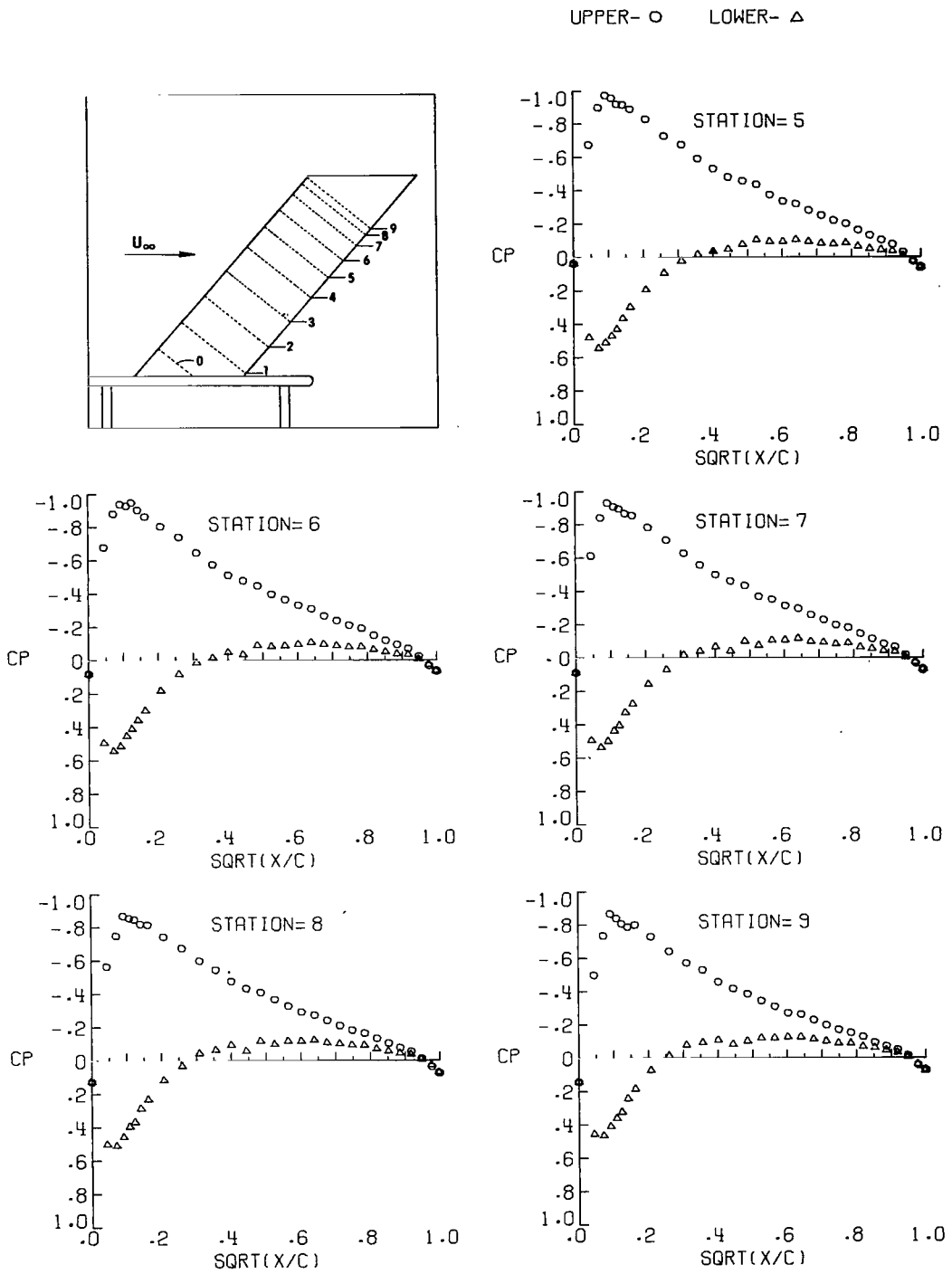

(g) Concluded.

Figure 7.- Continued.

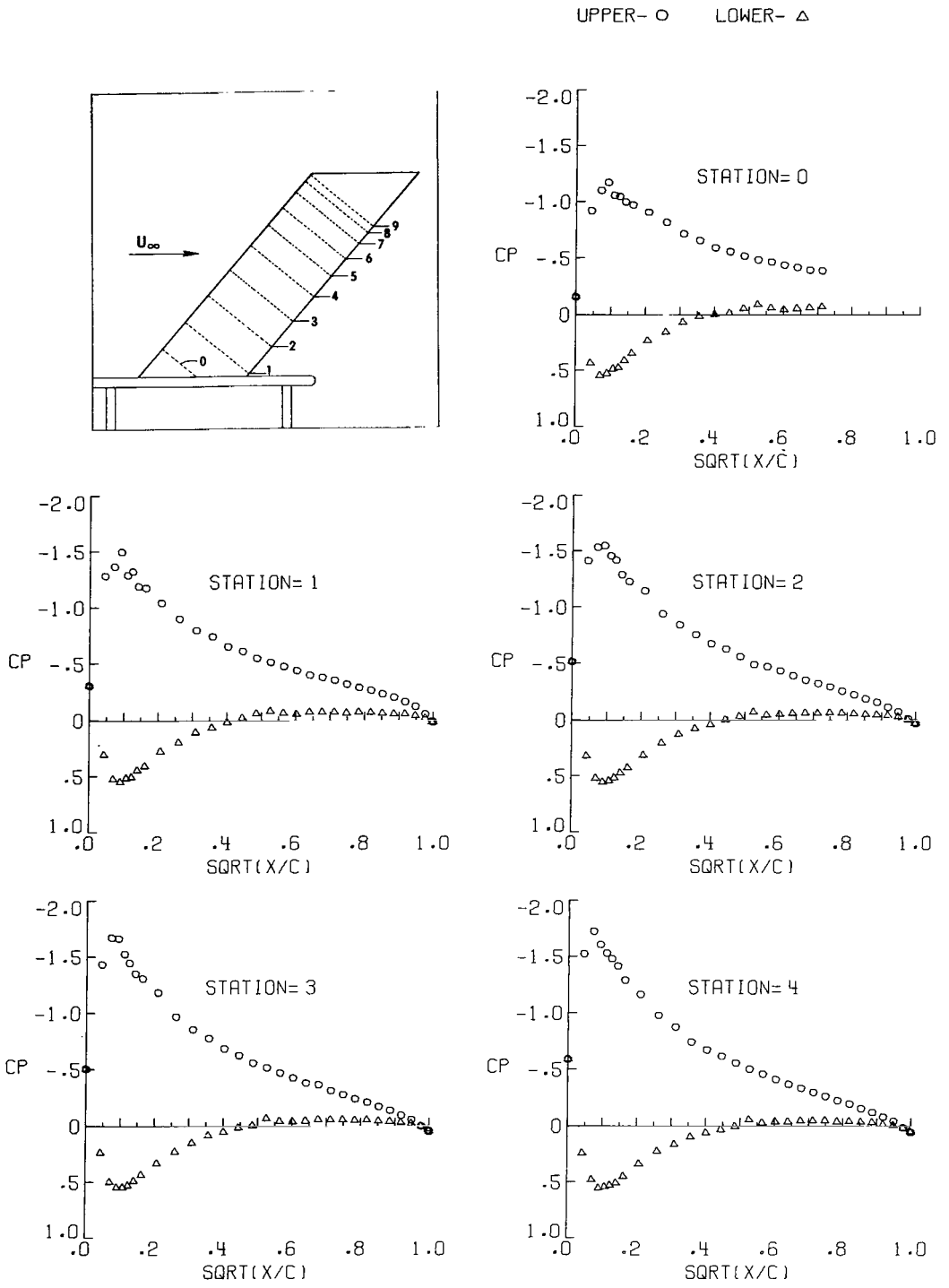

(h) $\alpha = 6.65^{\circ}$; $q_\infty = 1.47$ kPa (30.67 lb/ft^2).

Figure 7.- Continued.

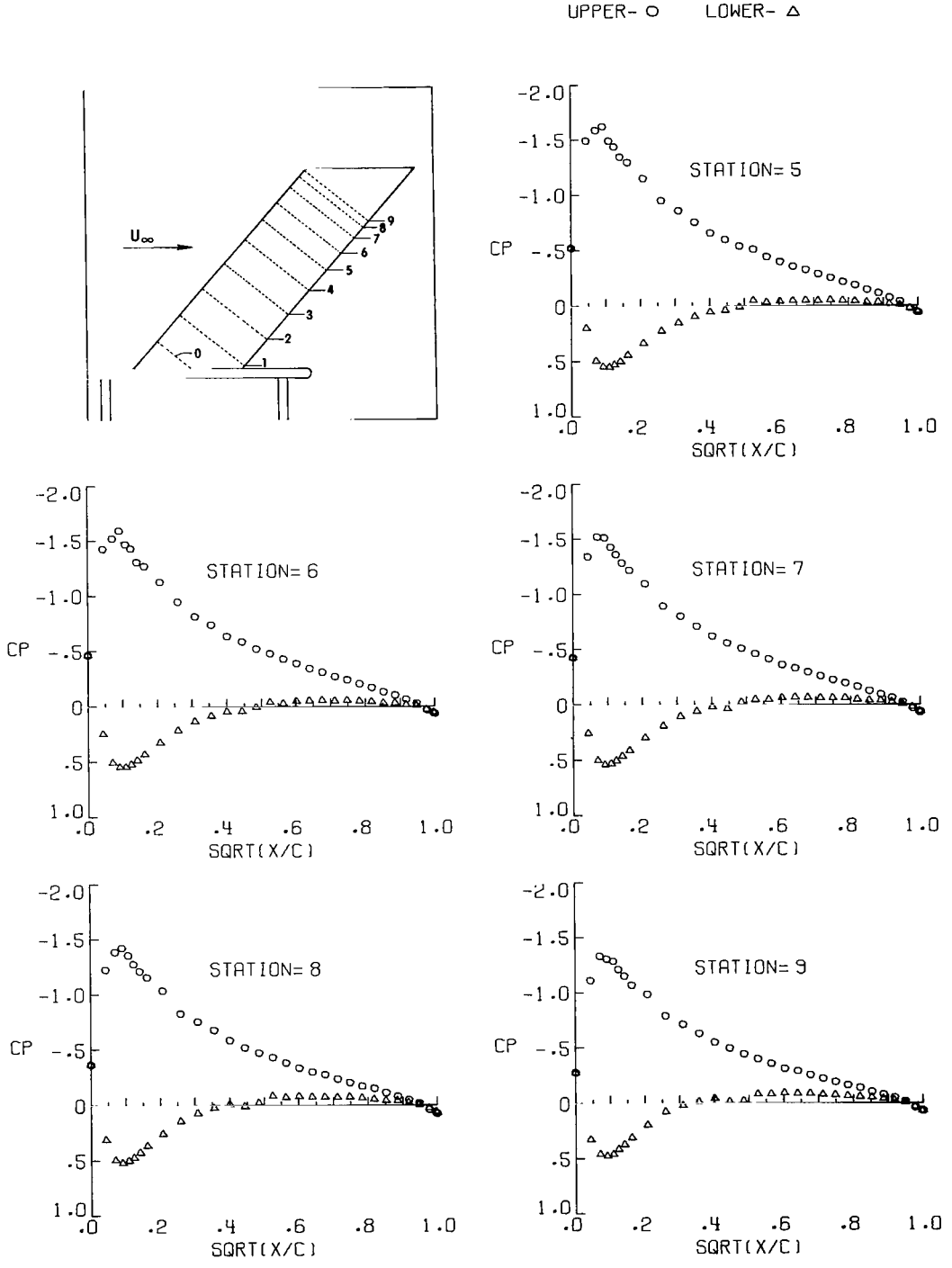

(h) Concluded.

Figure 7.- Continued.

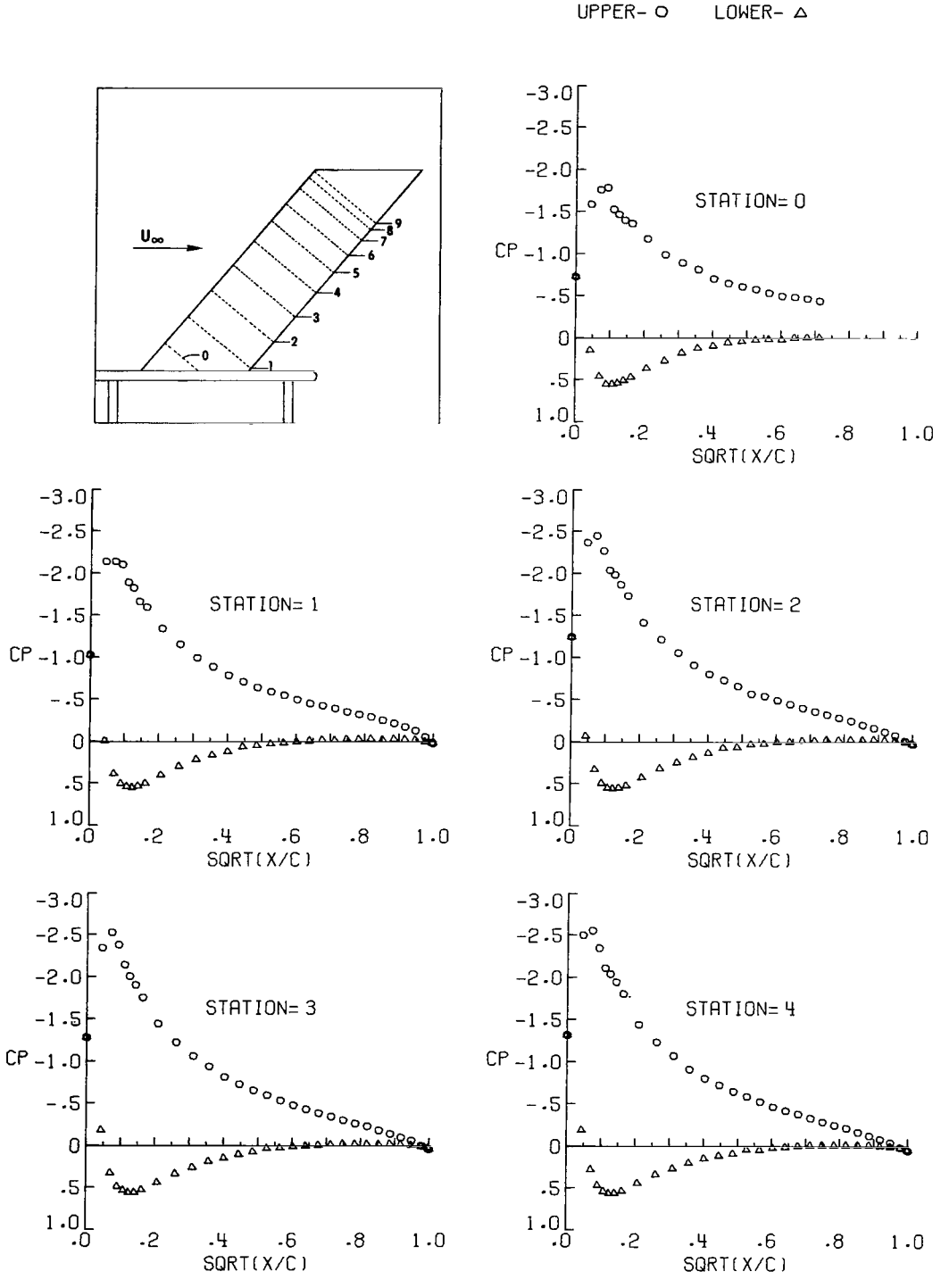

(i) $\alpha = 8.72^{o}$; $q_\infty = 1.48$ kPa (30.81 lb/ft^2).

Figure 7.- Continued.

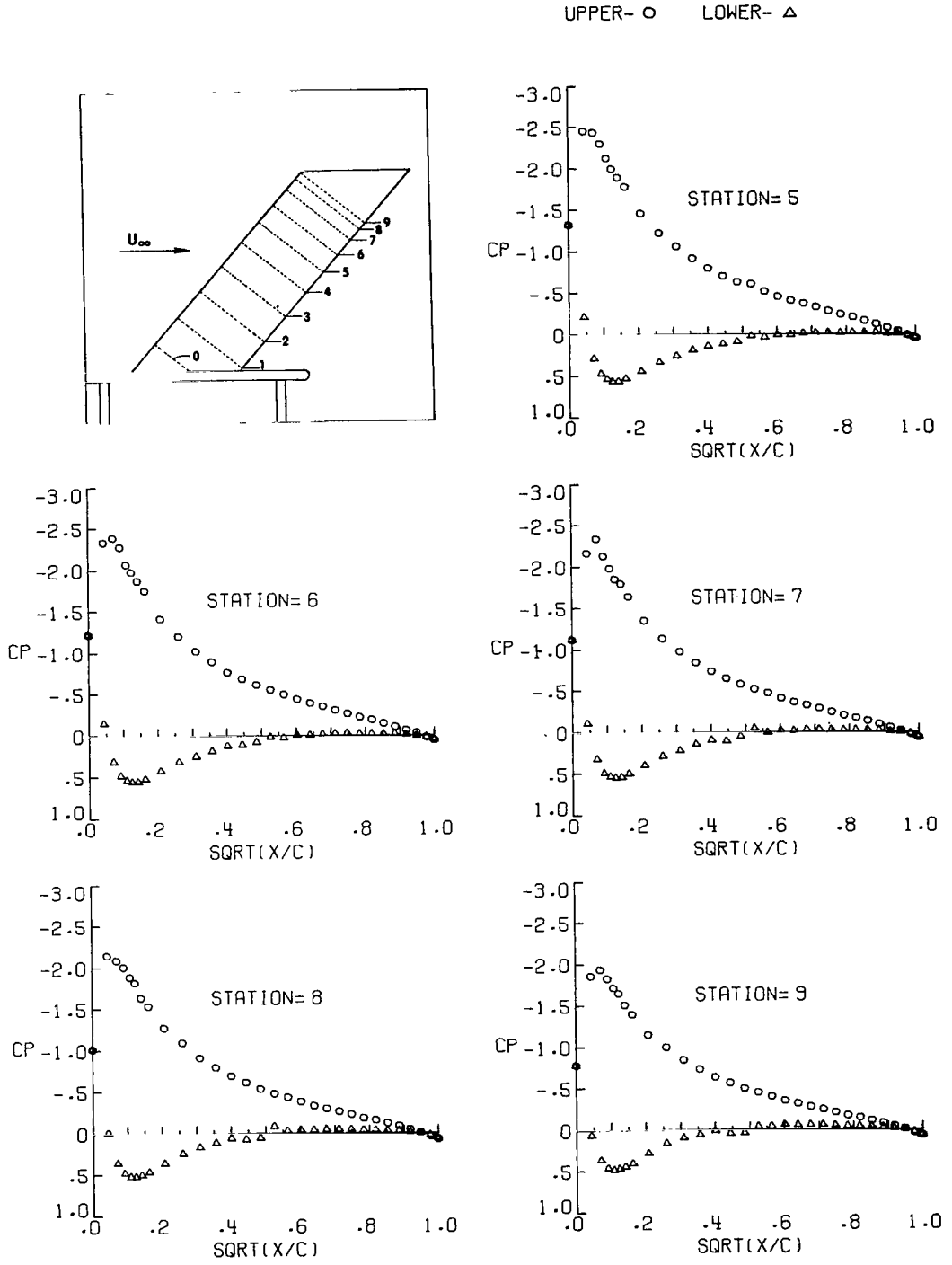

(i) Concluded.

Figure 7.- Continued.

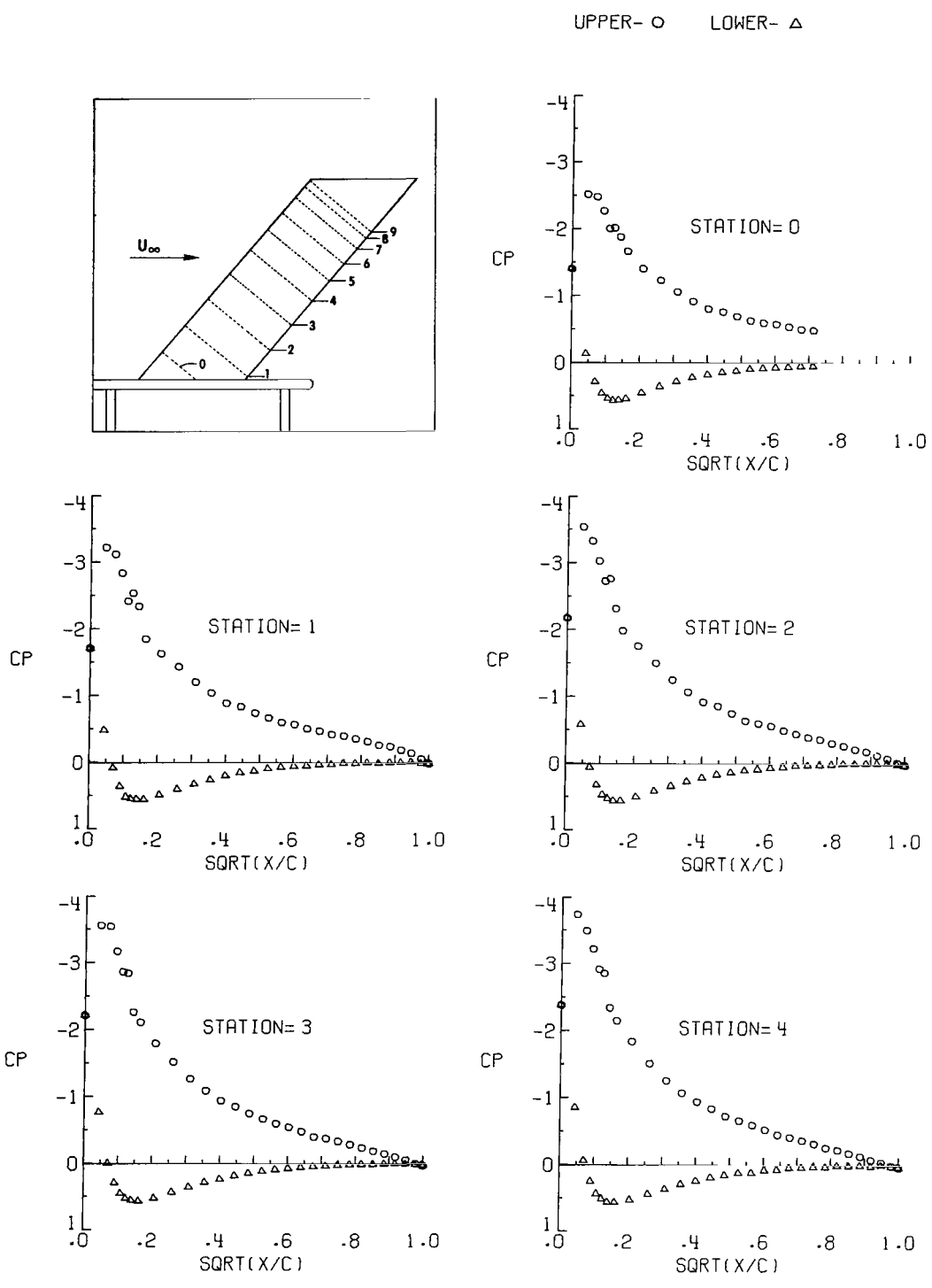

(j) $\alpha = 10.81^{\circ}$; $q_\infty = 1.47$ kPa (30.81 lb/ft^2).

Figure 7.- Continued.

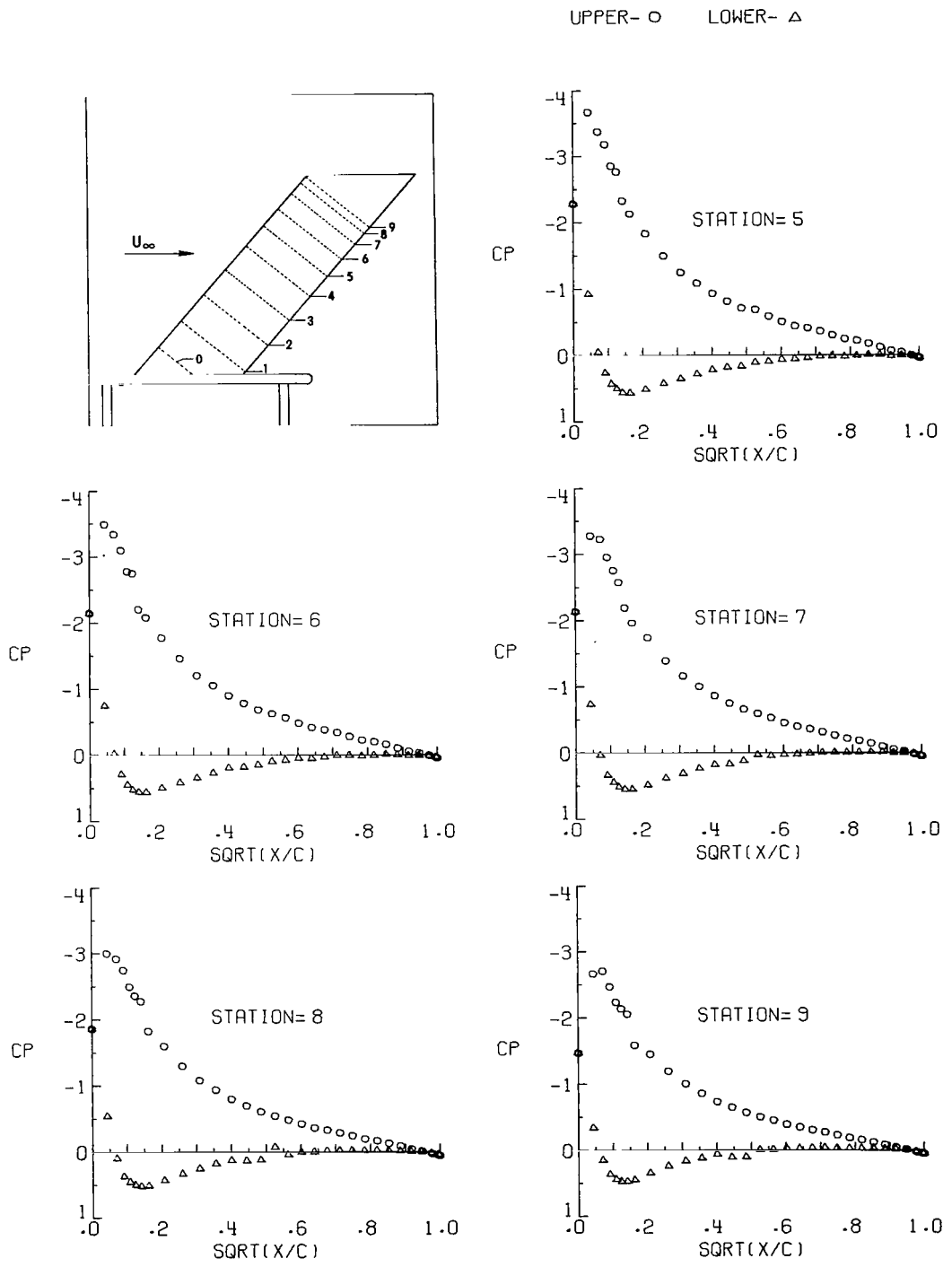

(j) Concluded.

Figure 7.- Continued.

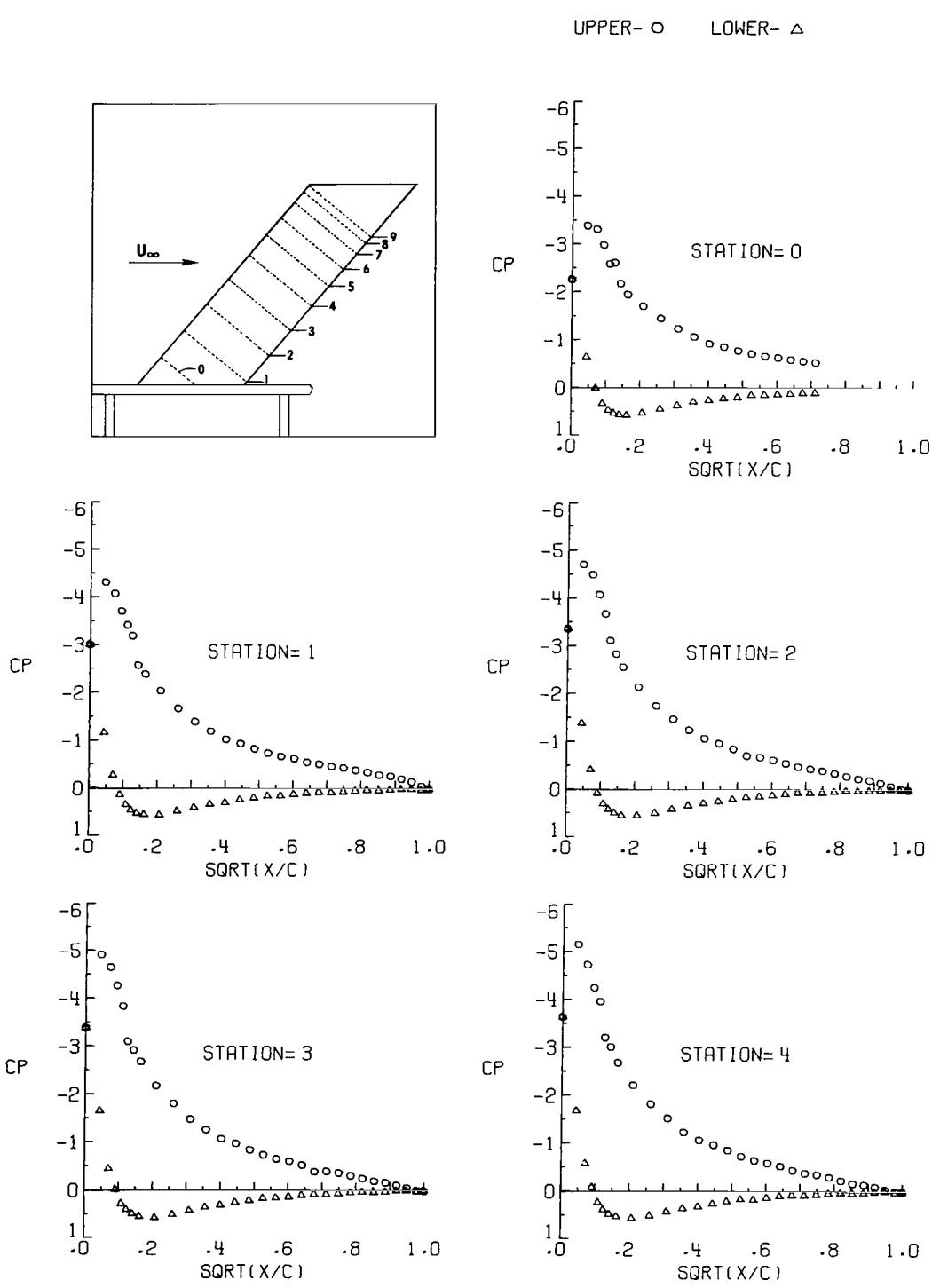

(k) $\alpha = 12.90^{o}$; $q_\infty = 1.48$ kPa (30.86 lb/ft^2).

Figure 7.- Continued.

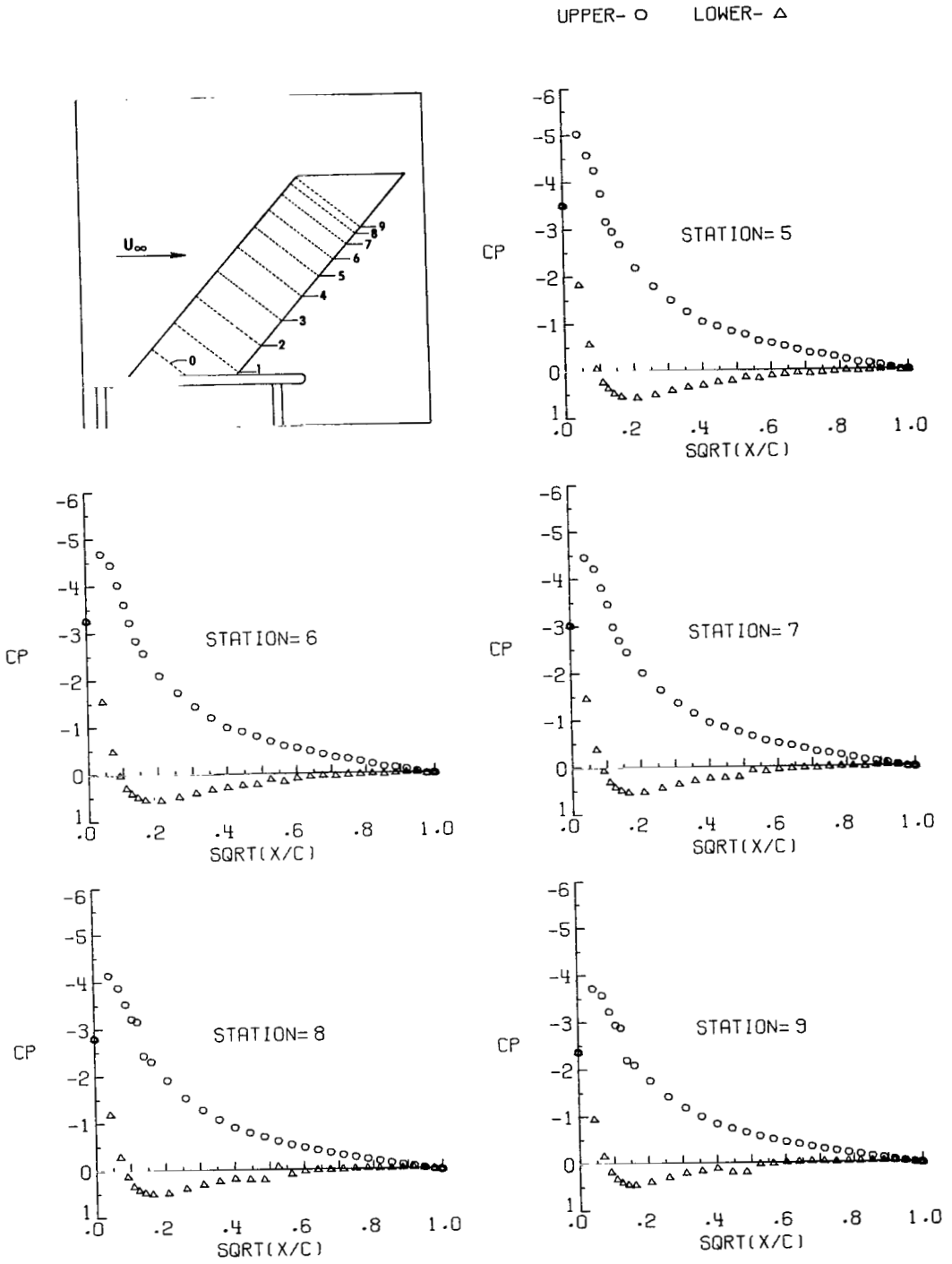

(k) Concluded.

Figure 7.- Continued.

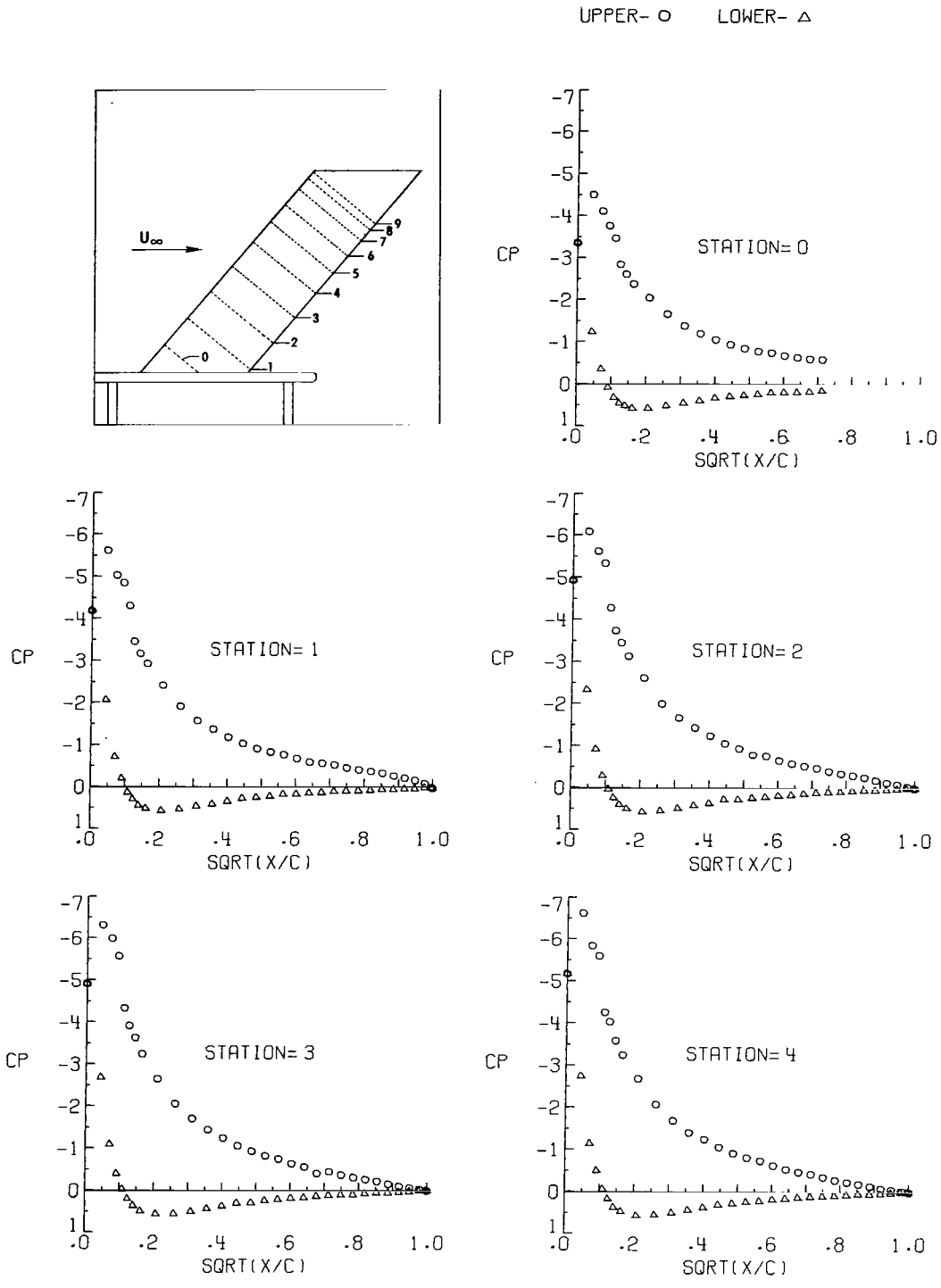

(l) α = 14.98°; q_∞ = 1.48 kPa (30.82 lb/ft^2).

Figure 7.- Continued.

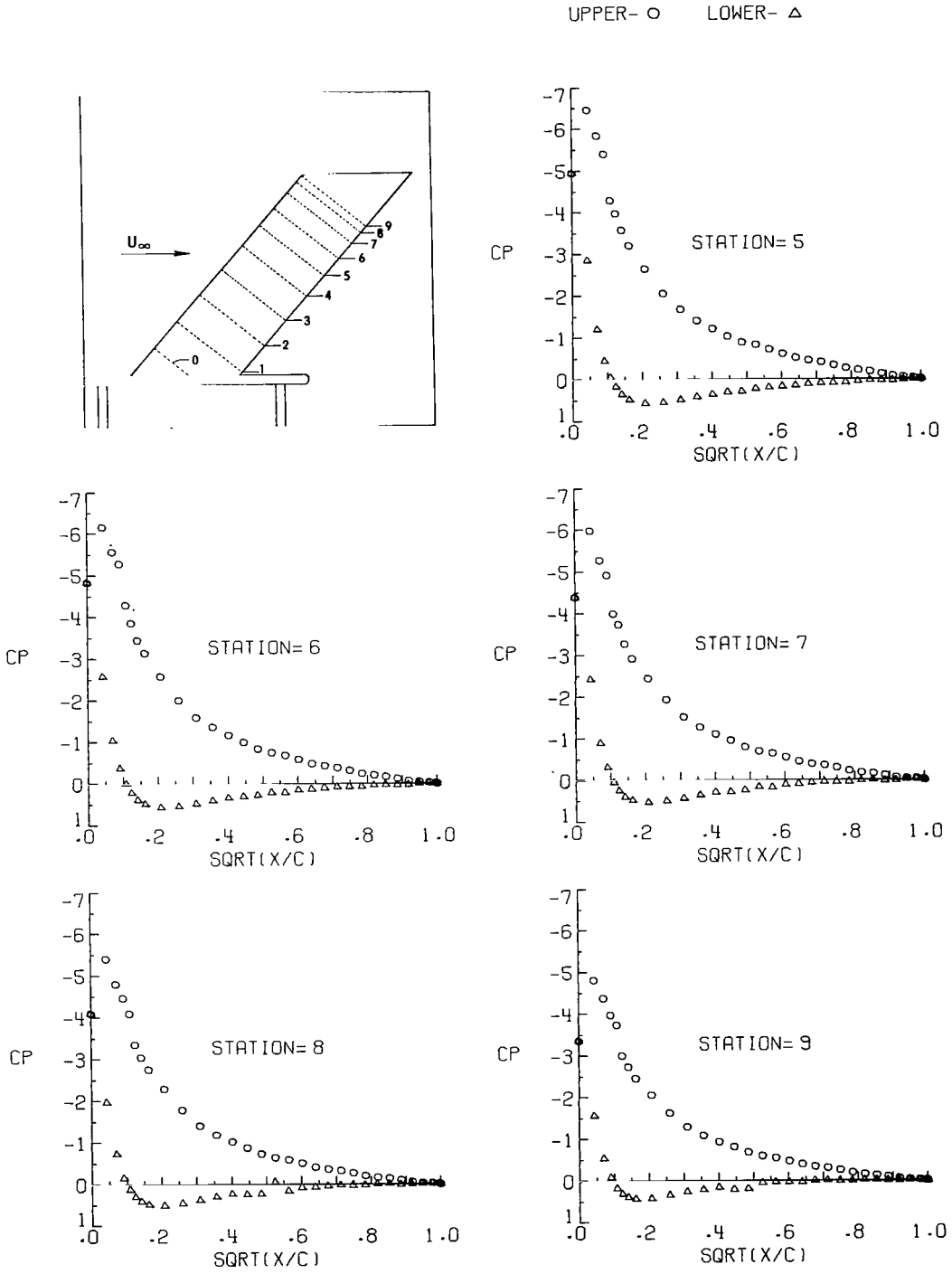

(1) Concluded.

Figure 7.- Continued.

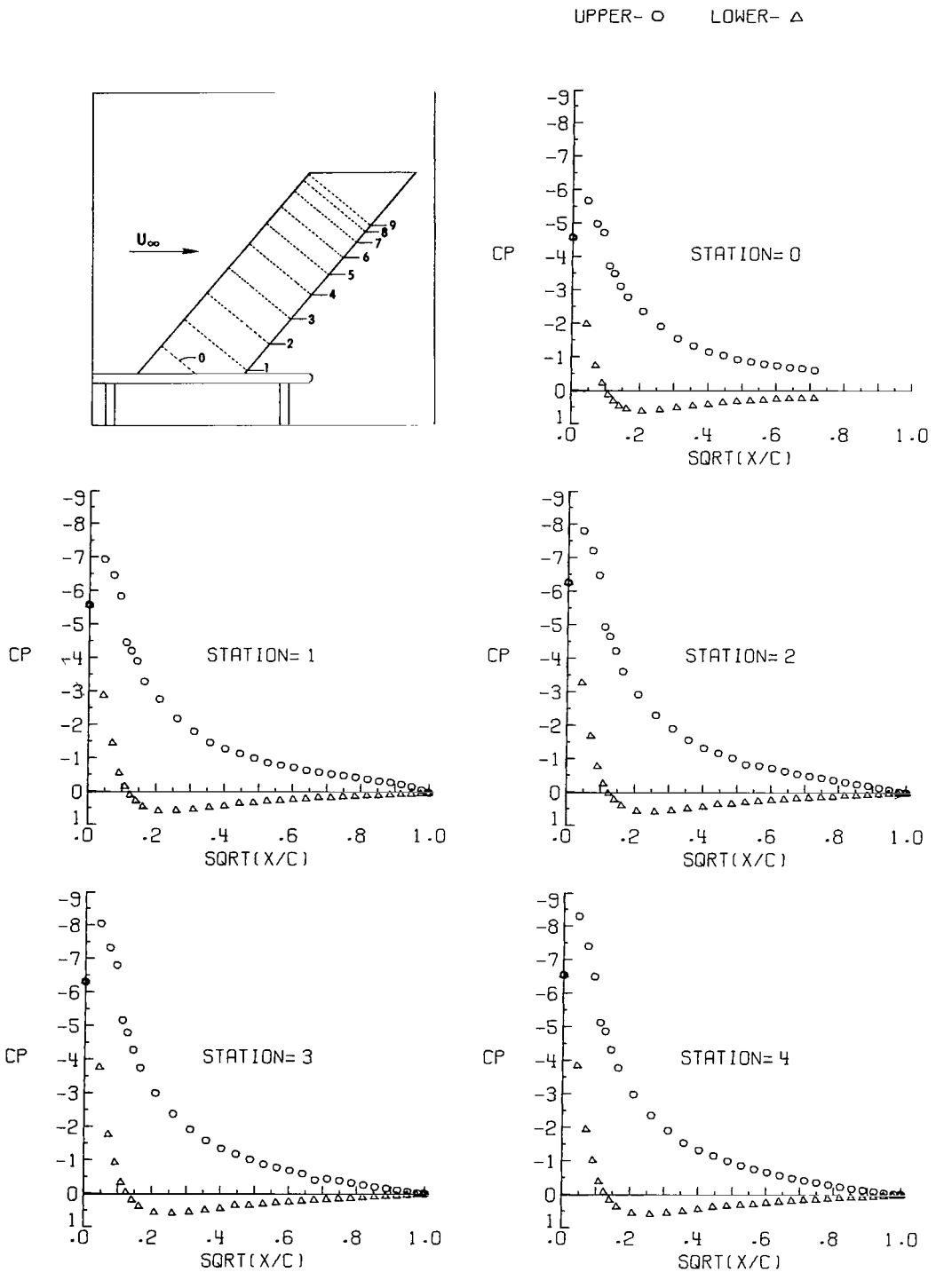

(m) $\alpha = 17.02^{o}$; $q_{\infty} = 1.48$ kPa (30.89 lb/ft^2).

Figure 7.- Continued.

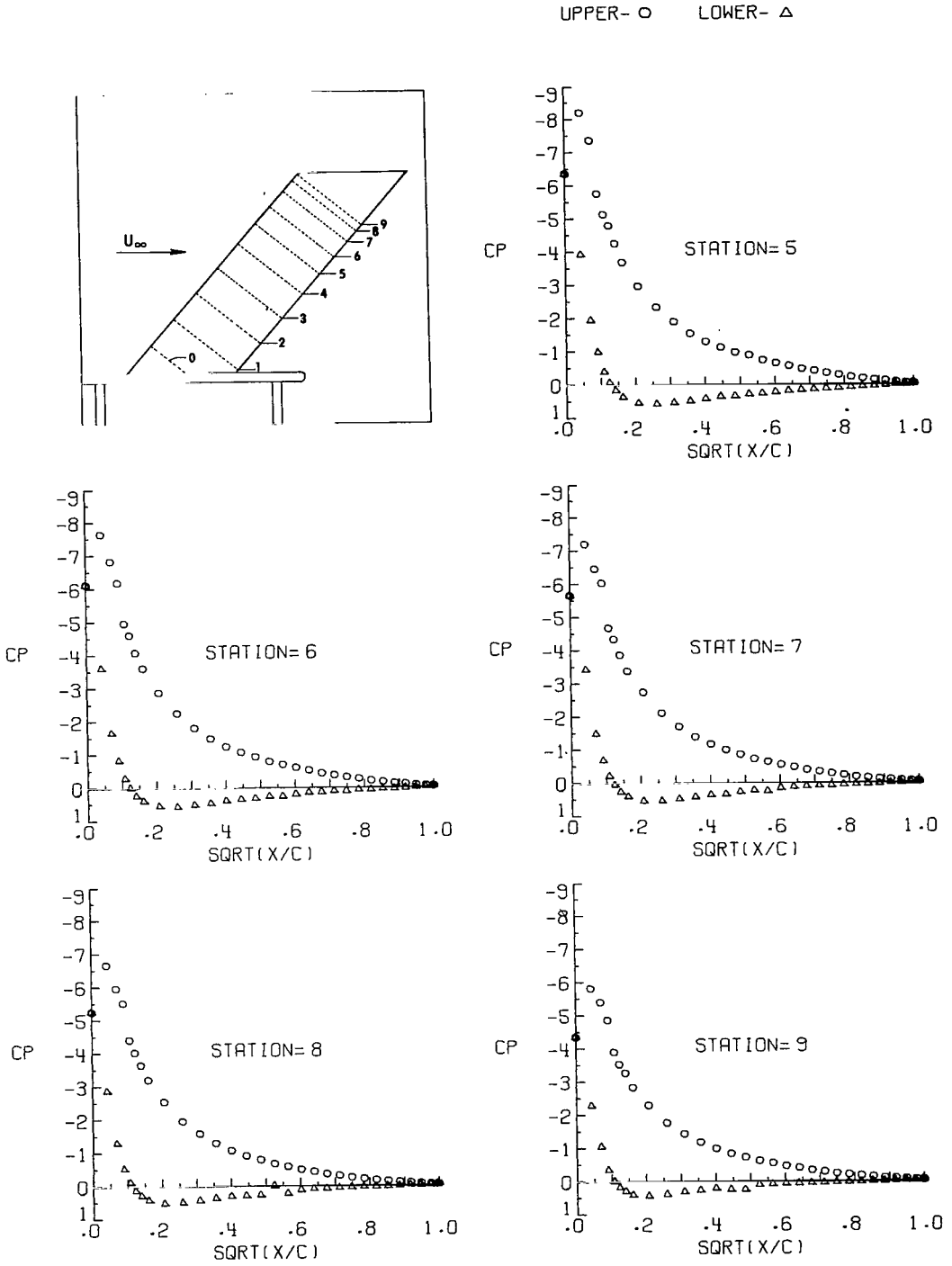

(m) Concluded.

Figure 7.- Continued.

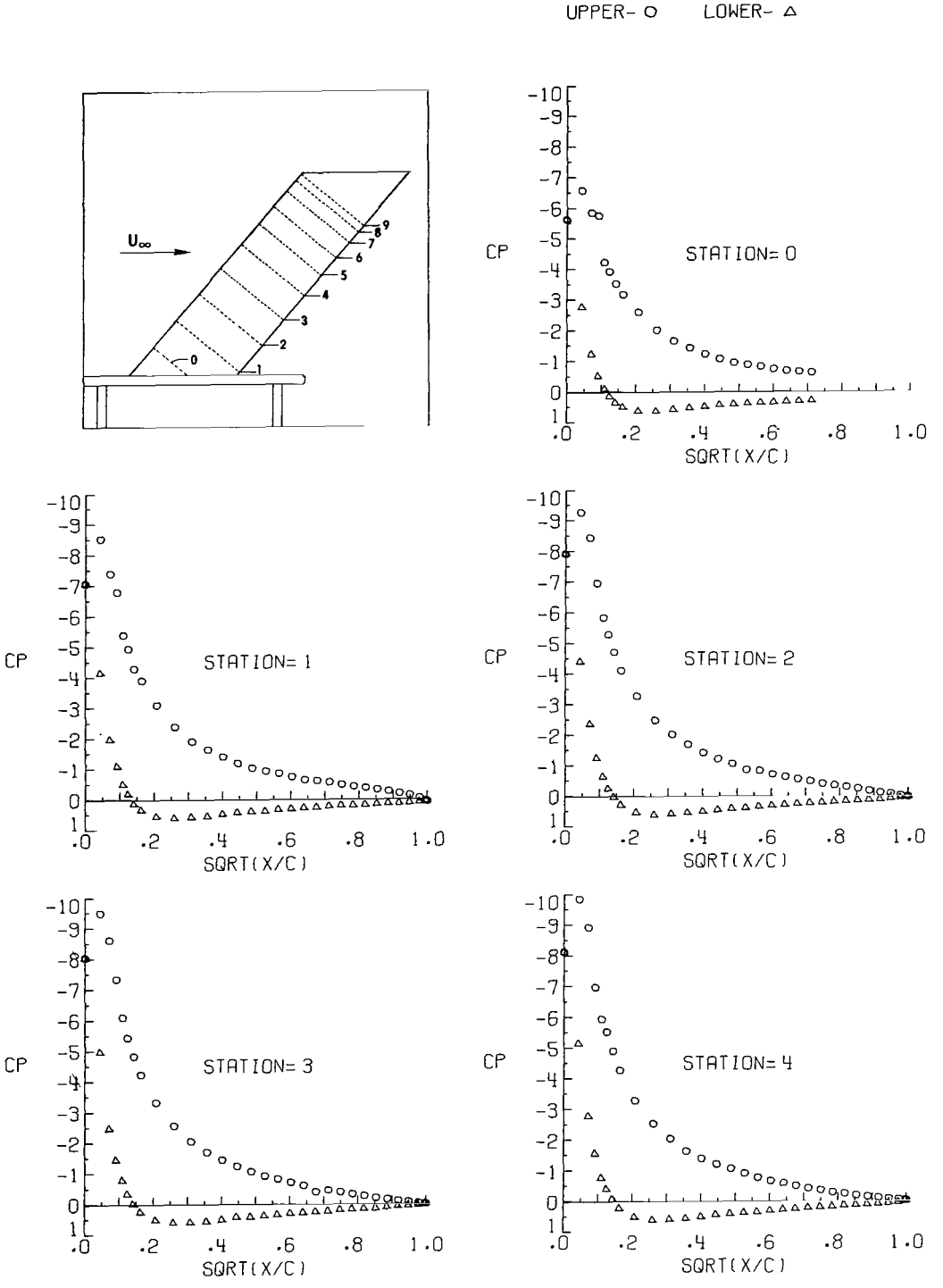

(n) $\alpha = 19.08^{o}$; $q_\infty = 1.51$ kPa (31.54 lb/ft^2).

Figure 7.- Continued.

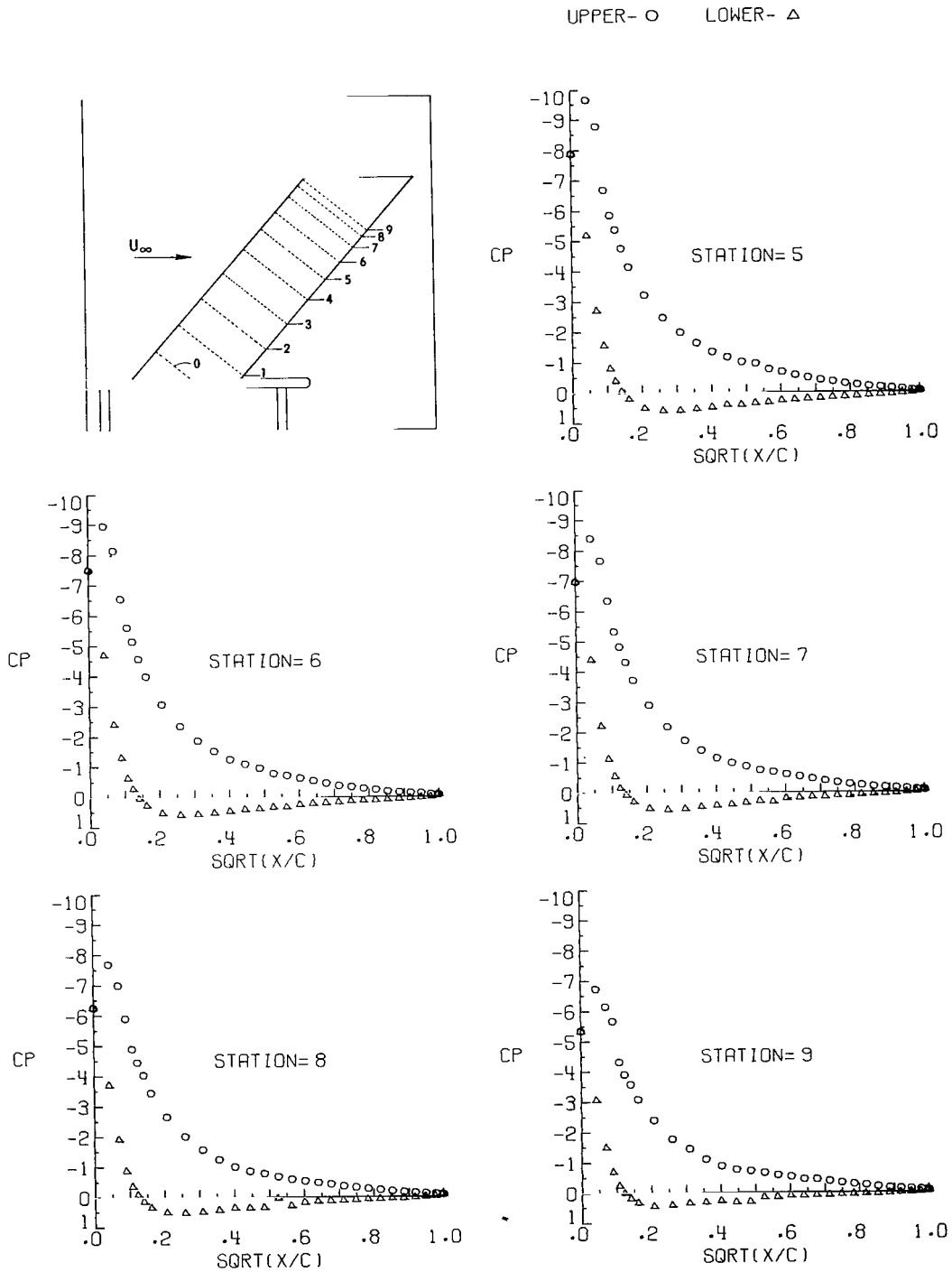

(n) Concluded.

Figure 7.- Concluded.

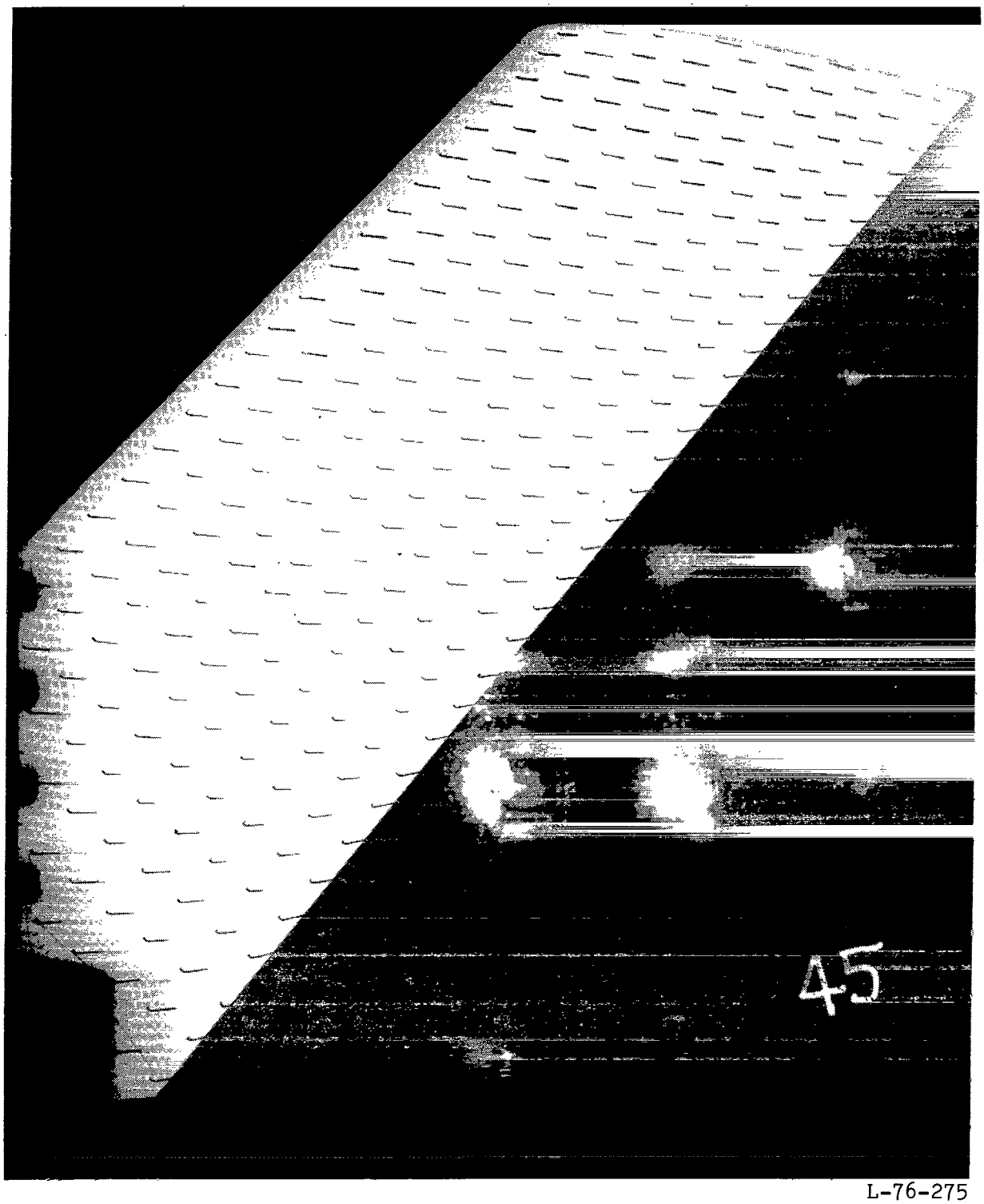

L-76-275

(a) $\alpha = 0.39^{\circ}$.

Figure 8.- Flow visualization using tufts. $\Lambda = 0^{\circ}$.

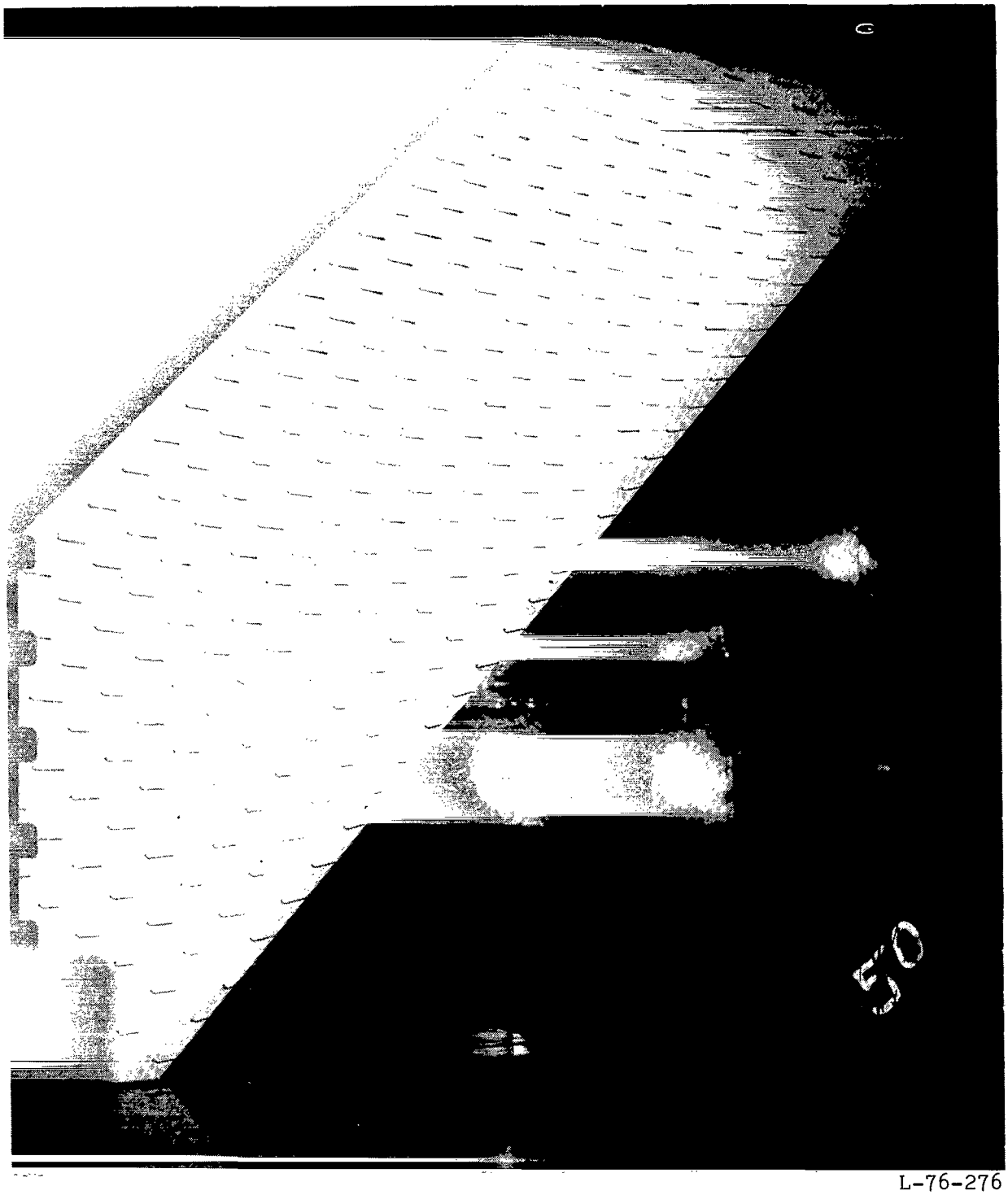

L-76-276

(b) $\alpha = 4.57^{\circ}$.

Figure 8.- Continued.

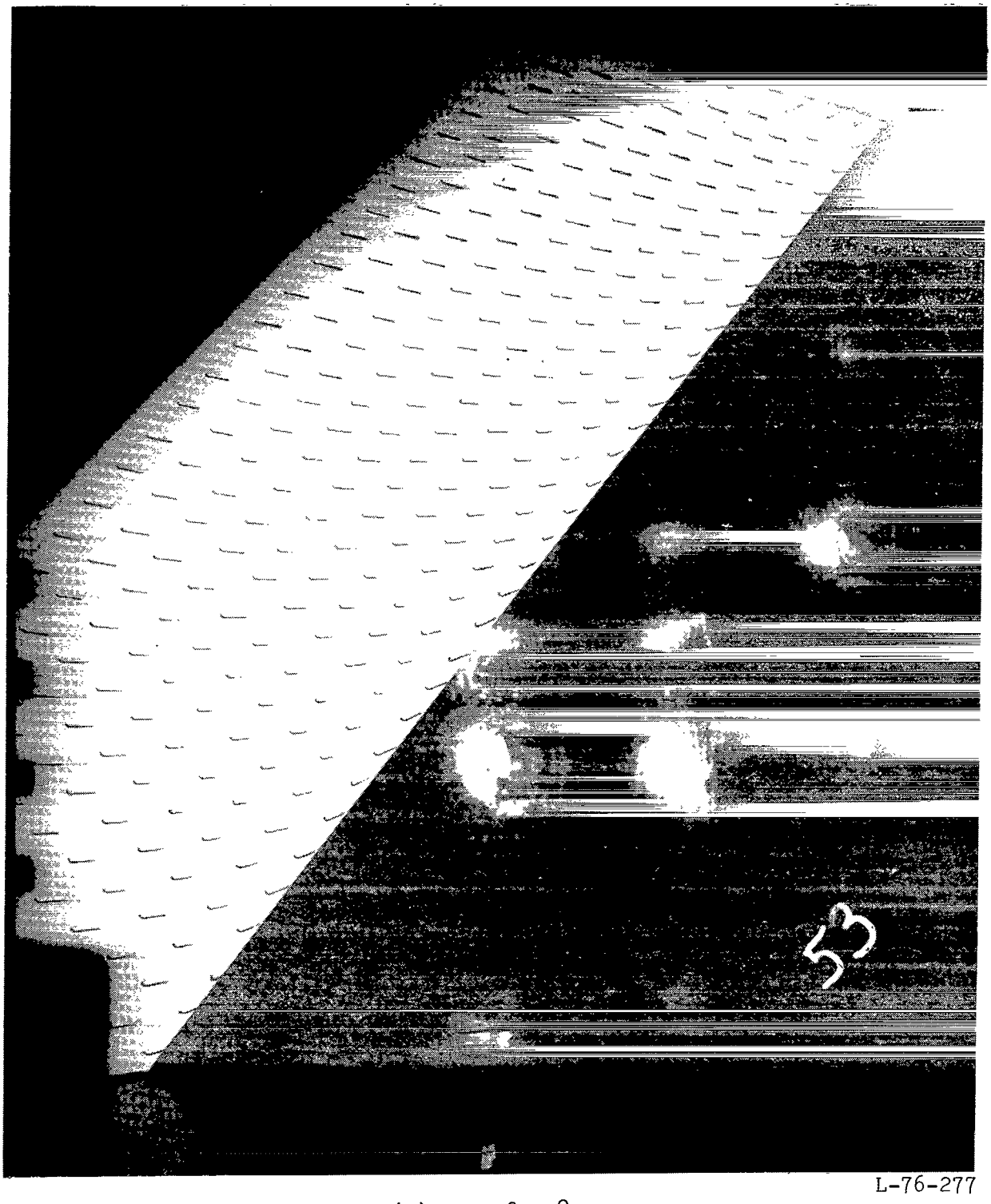

L-76-277

(c) $\alpha = 8.72^{o}$.

Figure 8.- Continued.

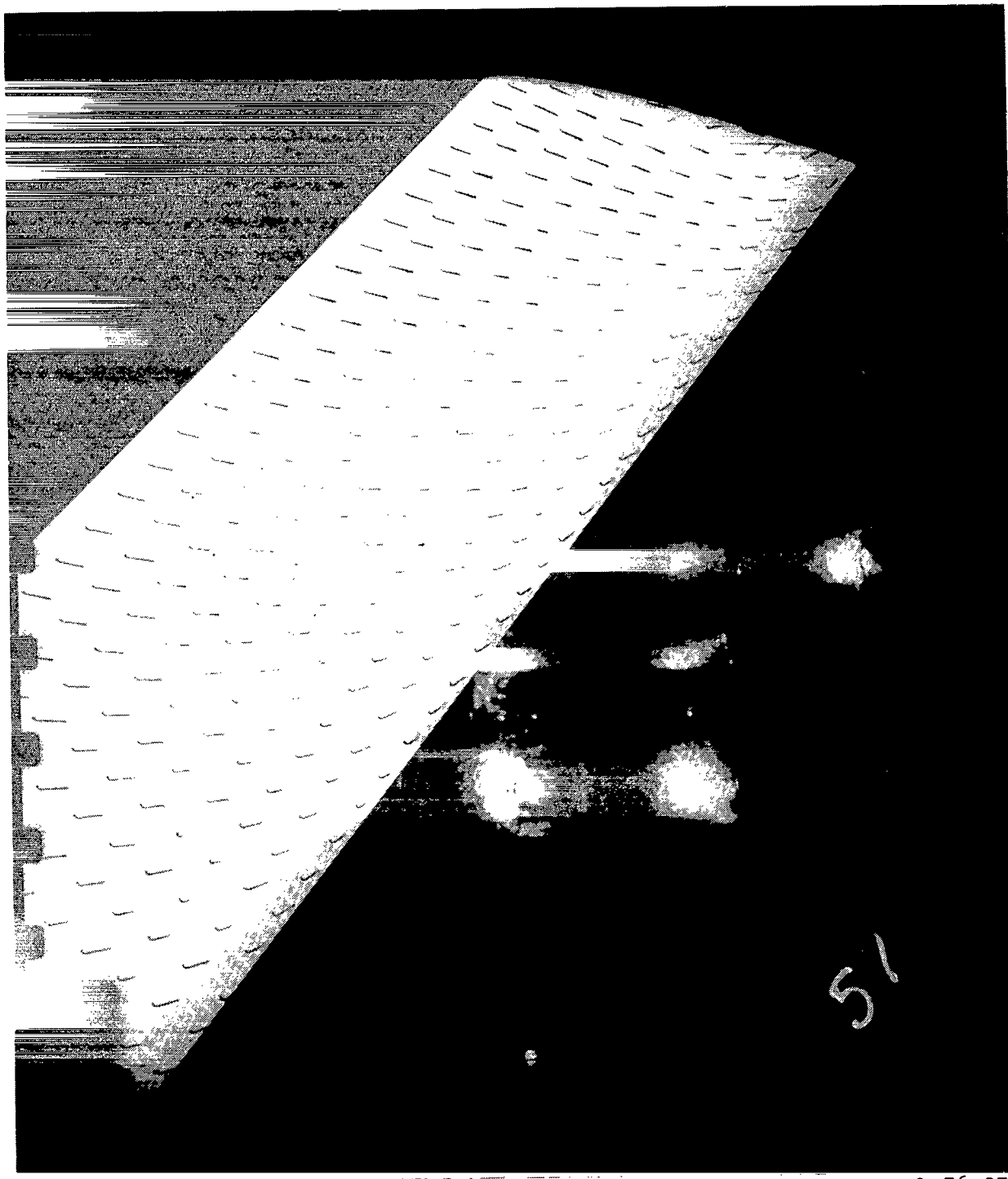

L-76-278

(d) $\alpha = 12.90^{o}$.

Figure 8.- Continued.

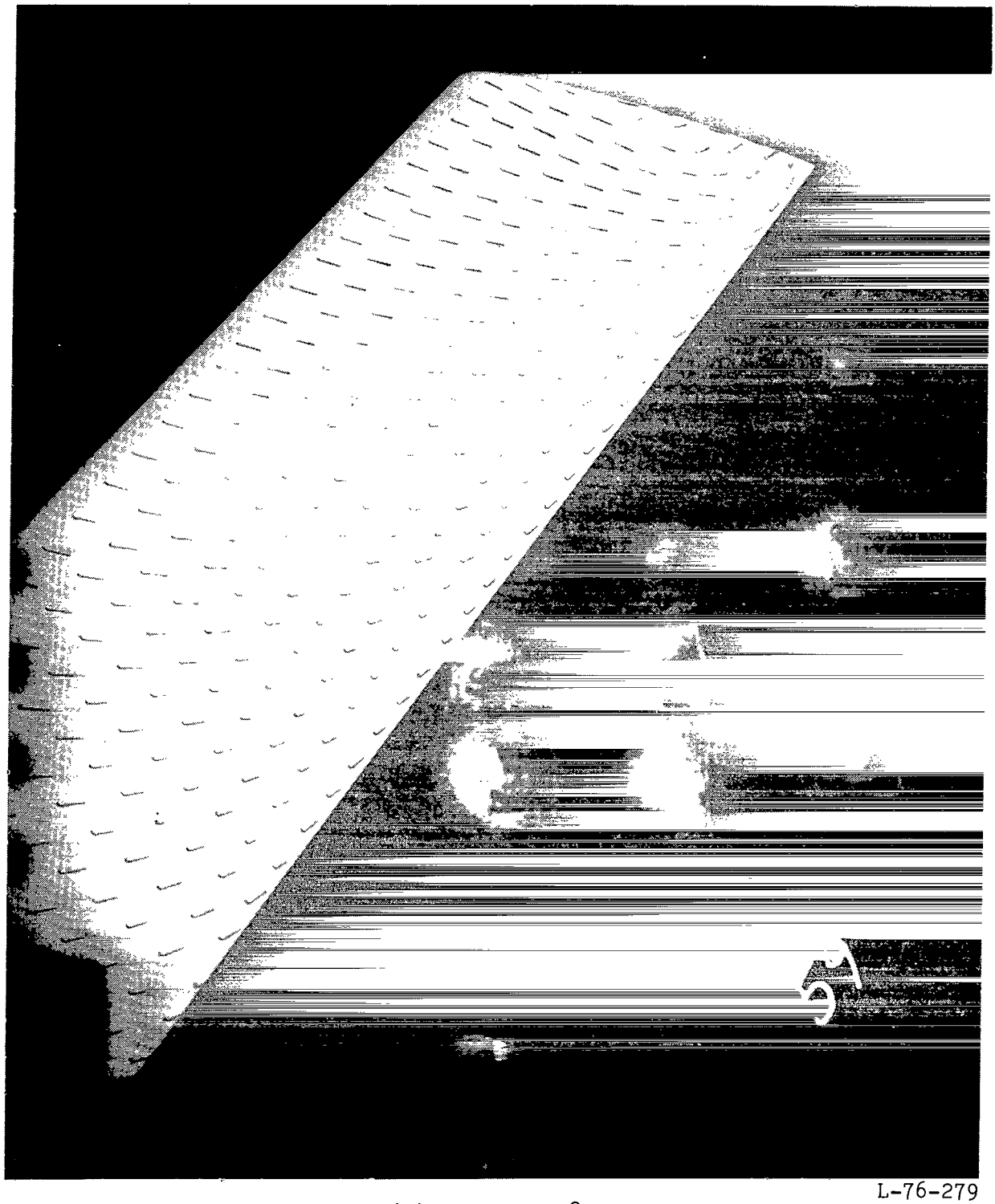

L-76-279

(e) $\alpha = 14.98^{\circ}$.

Figure 8.- Continued.

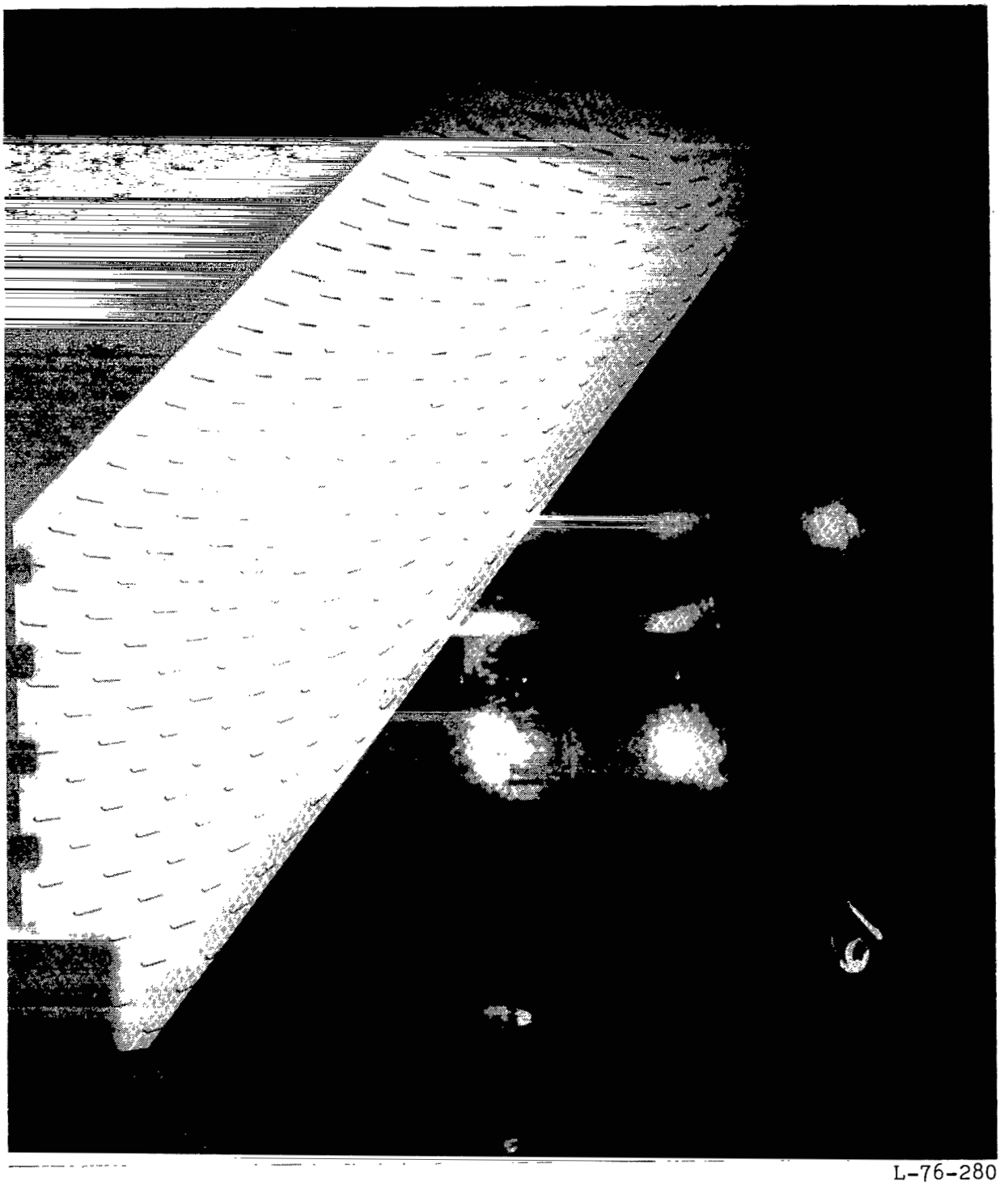

L-76-280

(f) $\alpha = 17.02^{\circ}$.

Figure 8.- Continued.

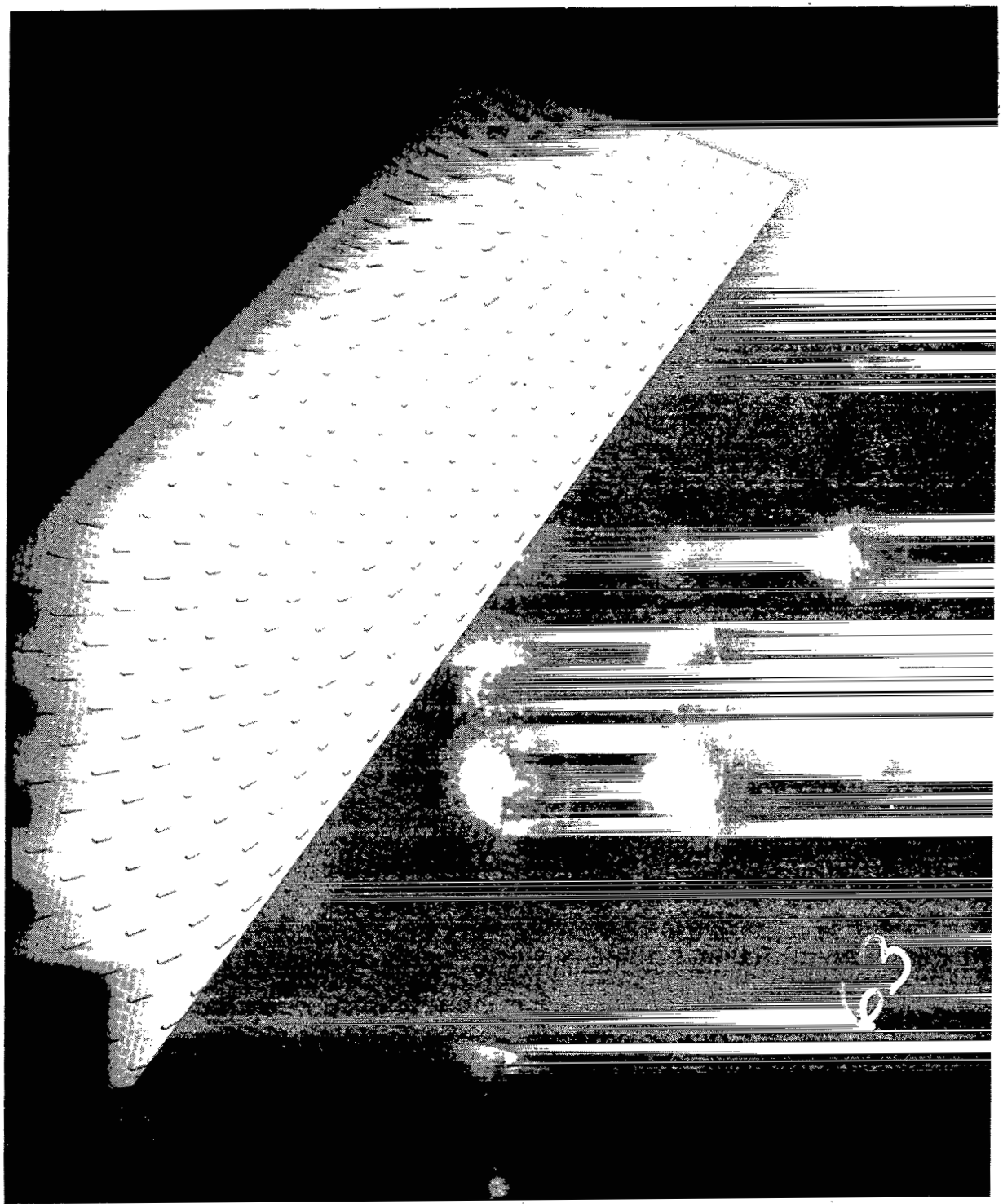

L-76-281

(g) $\alpha = 19.08^{\circ}$

Figure 8.- Concluded.

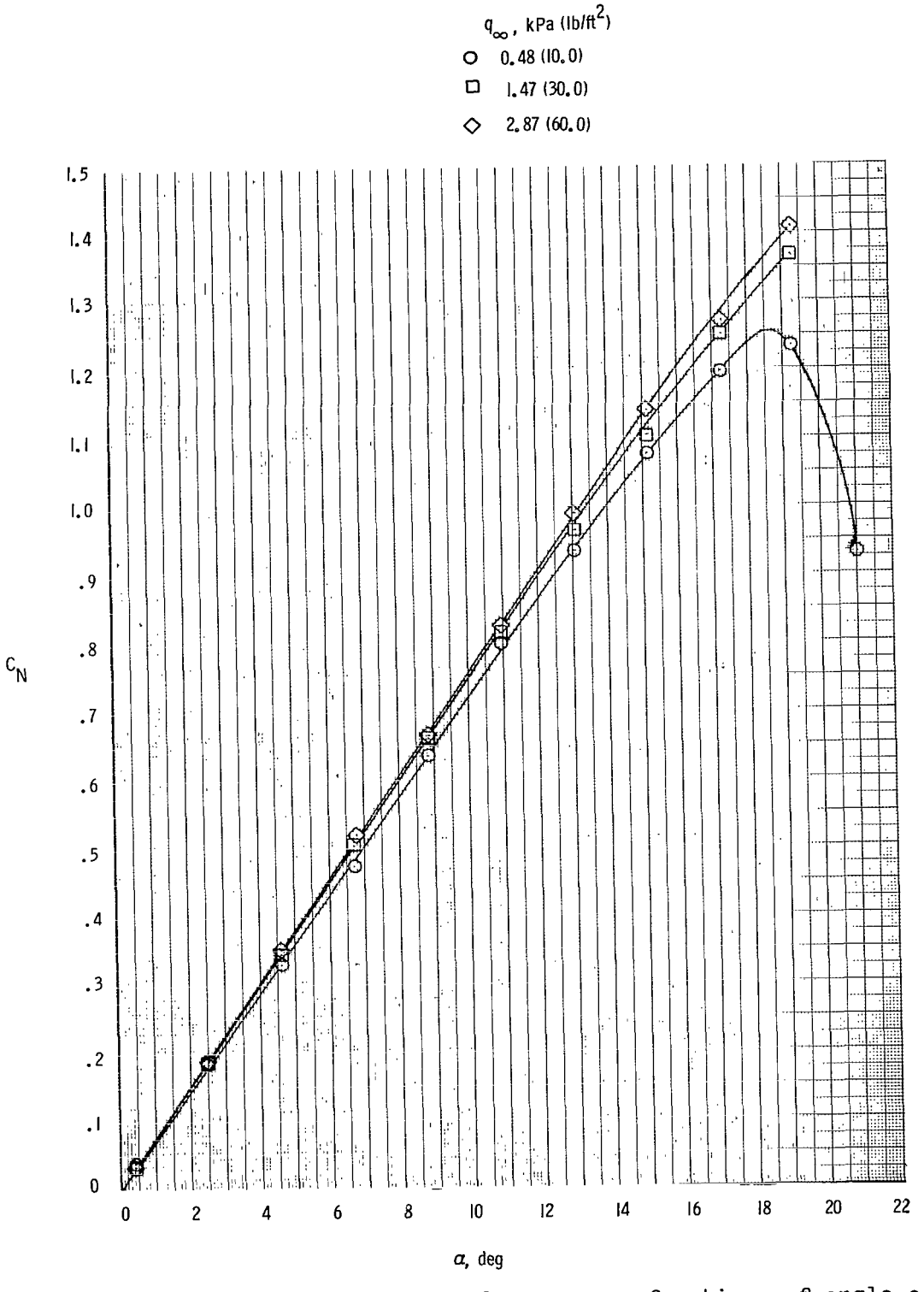

Figure 9.- Comparison of total normal forces as functions of angle of attack at different free-stream dynamic pressures. $\Lambda = 0^o$.

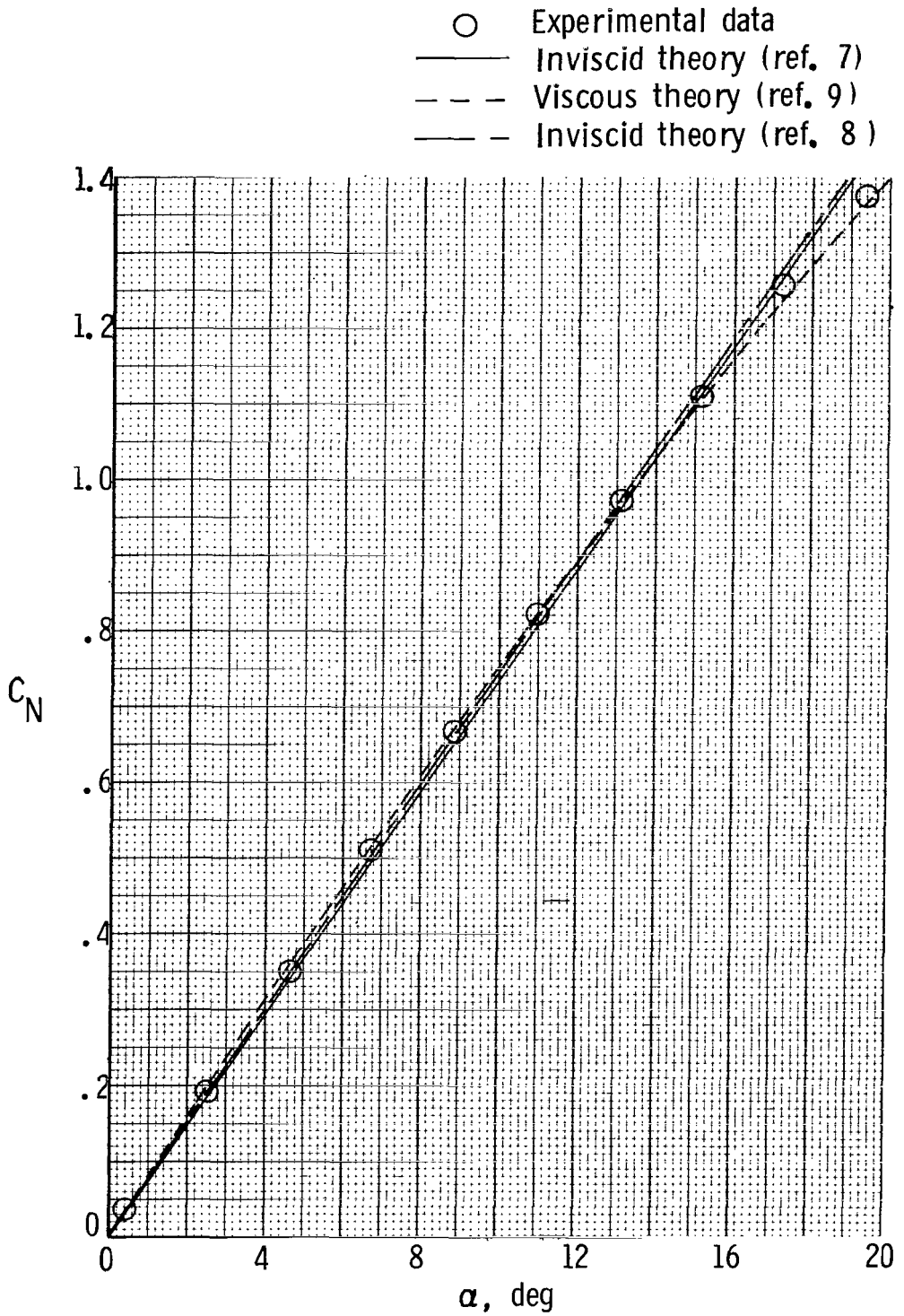

Figure 10.- Comparison of total normal forces as functions of angle of attack for experiment and theory. $\Lambda = 0^{\circ}$.

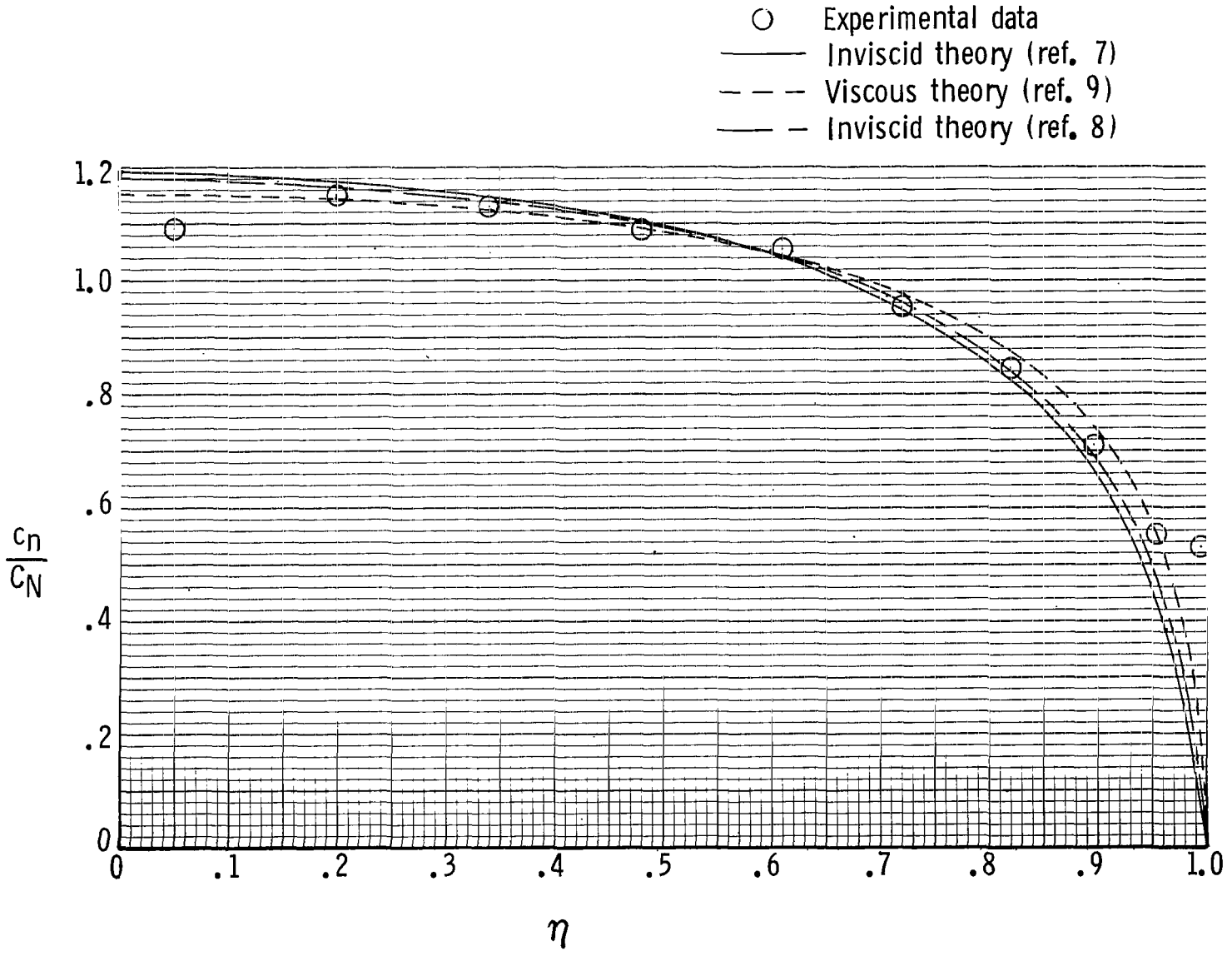

Figure 11.- Comparison of span-load distributions between experiment and theory. $\Lambda = 0^{\circ}$; $\alpha = 6.75^{\circ}$.

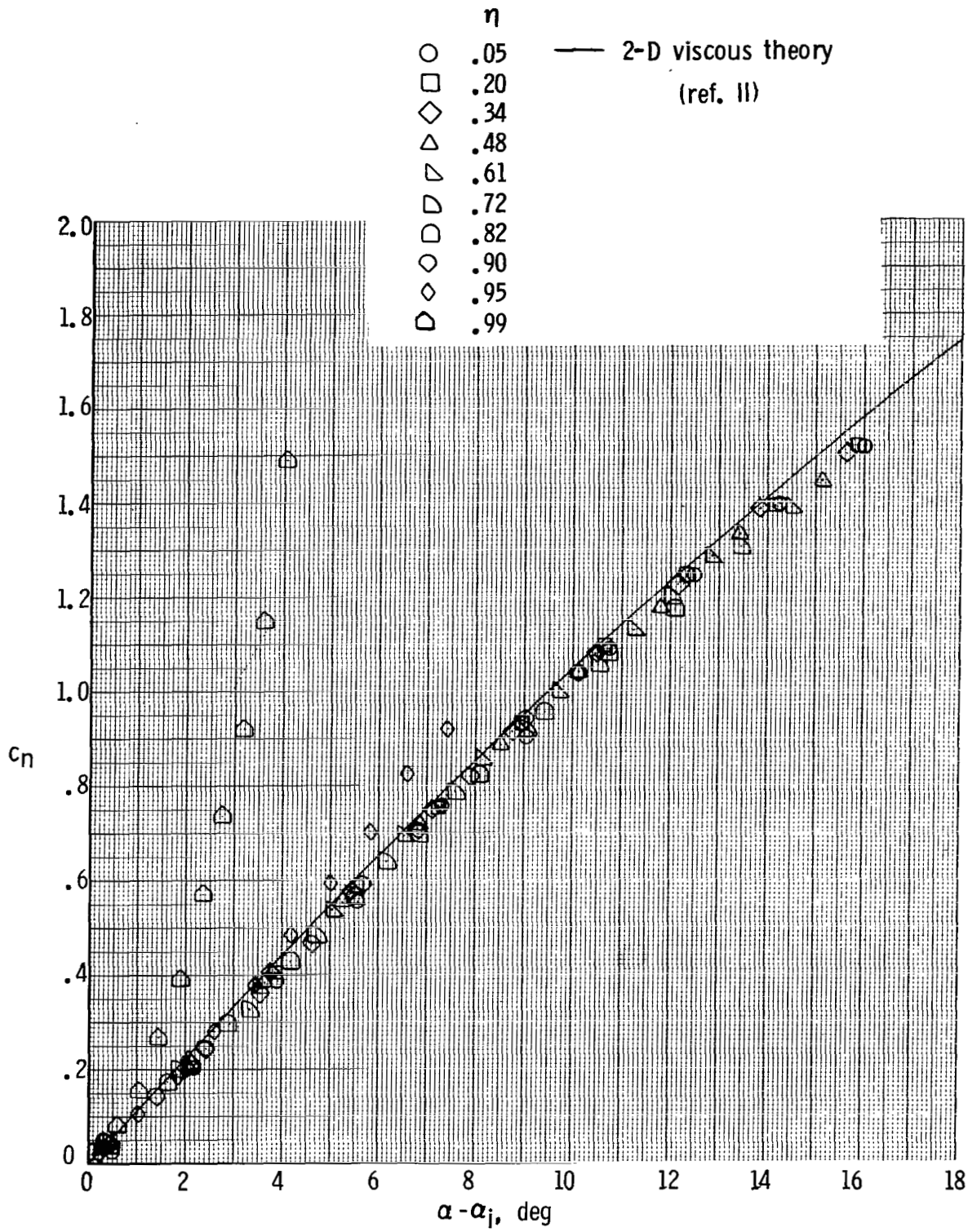

Figure 12.- Comparison of section normal forces as functions of computed local induced angle of attack between experiment and theory. $\Lambda = 0^{\circ}$.

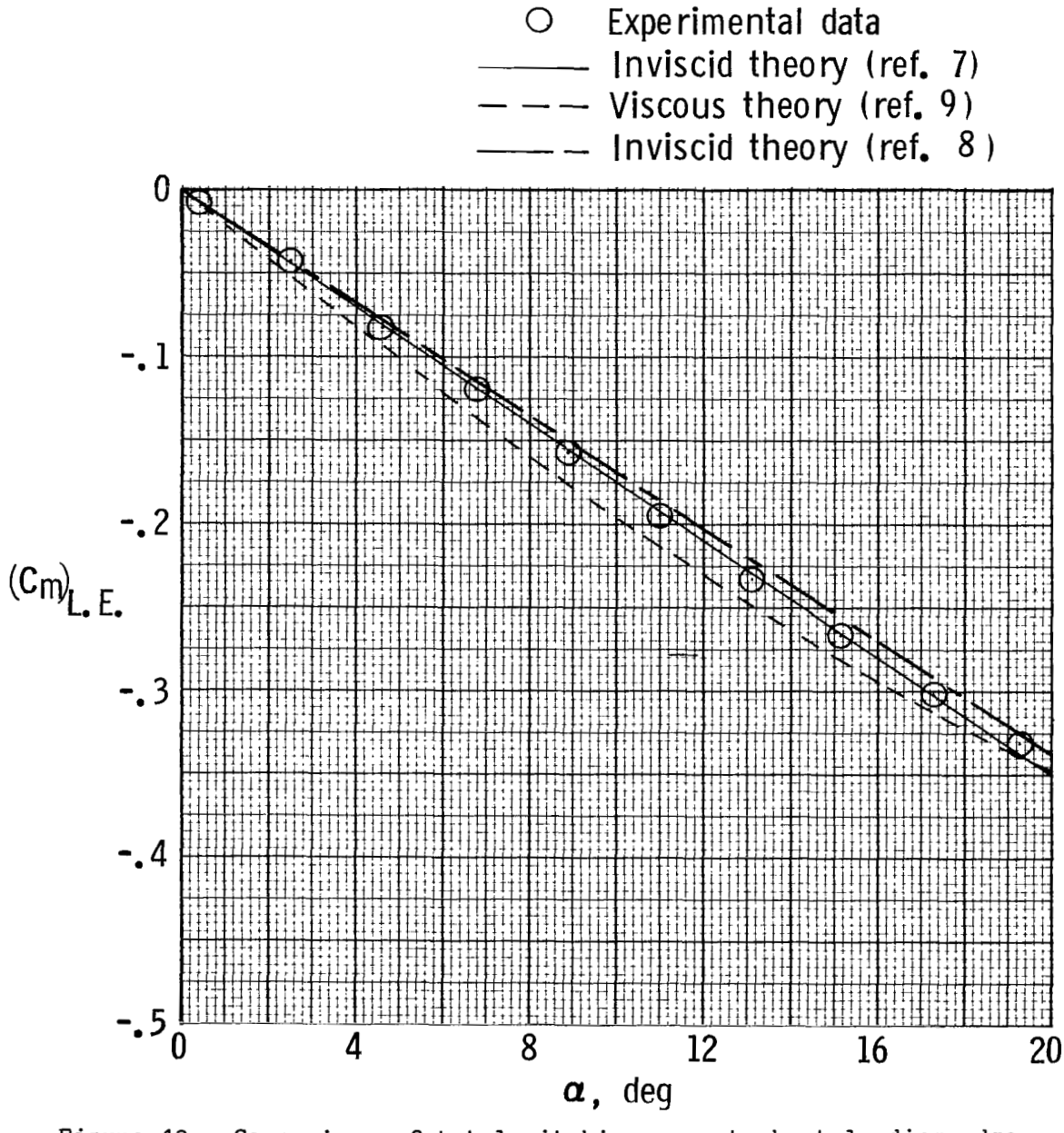

Figure 13.- Comparison of total pitching moment about leading edge for experiment and theory. $\Lambda = 0^{\circ}$.

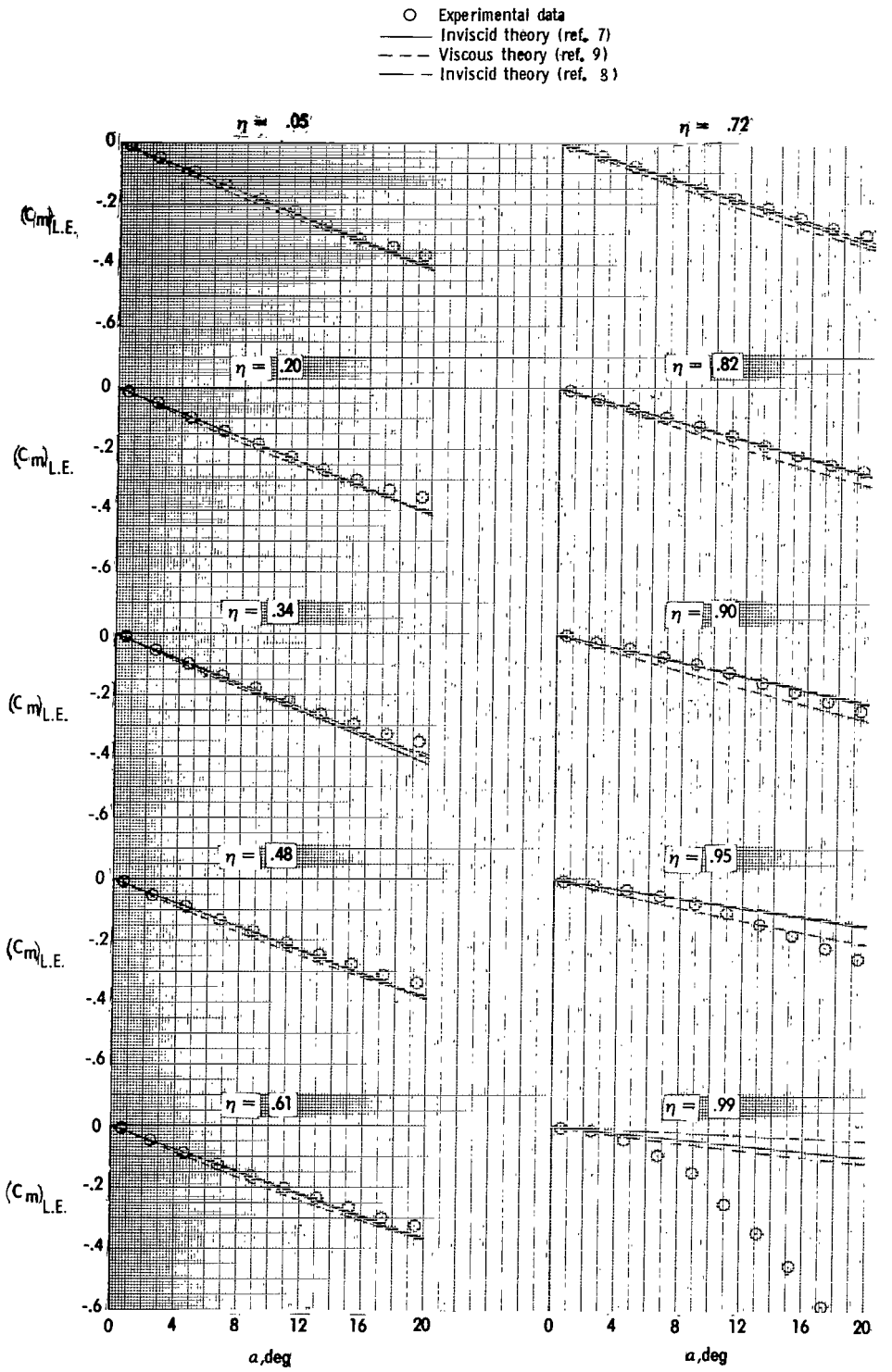

Figure 14.- Comparison of section pitching moments about leading edge for experiment and theory. $\Lambda = 0^{\circ}$.

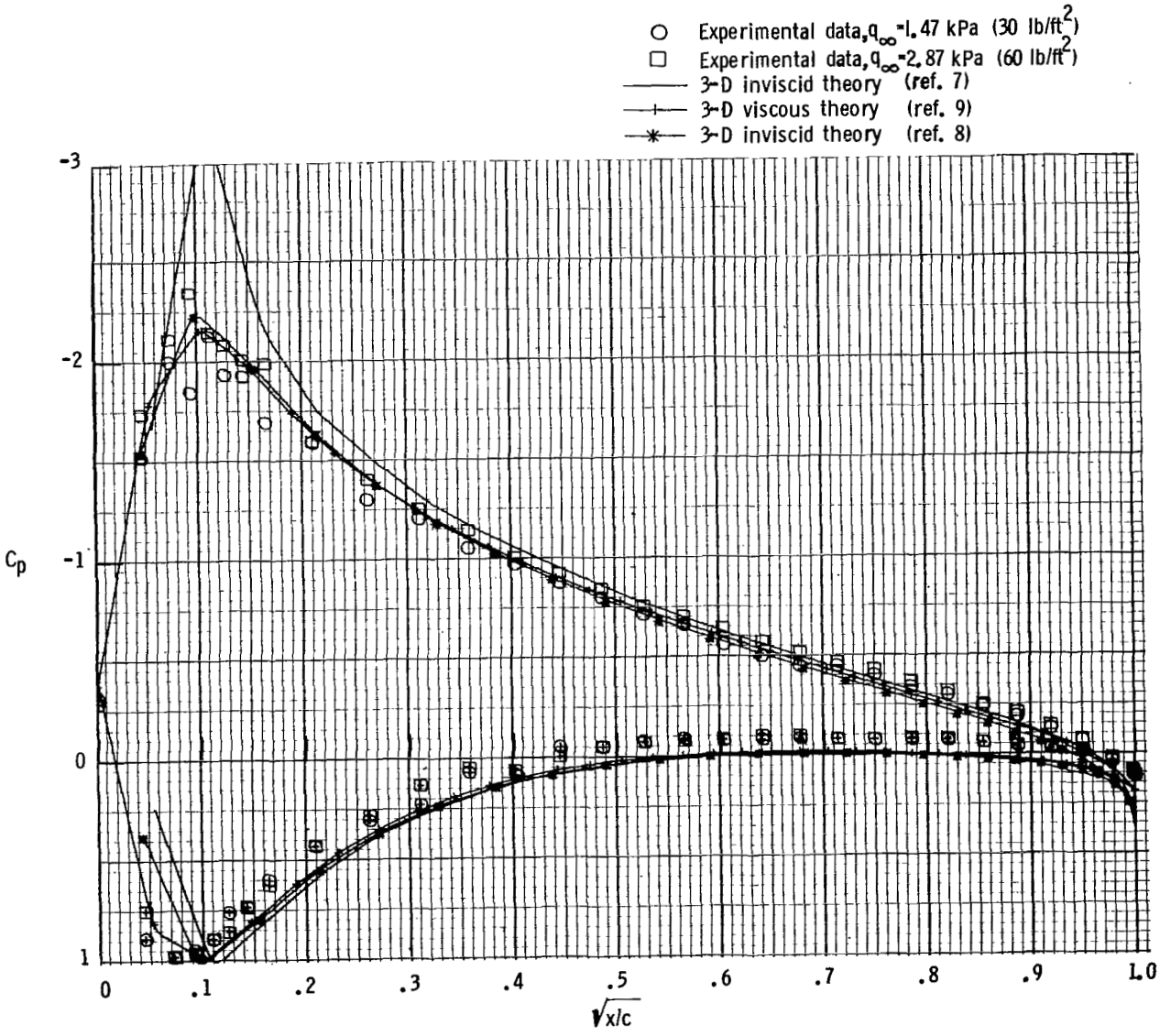

(a) $\eta = 0.05$.

Figure 15.- Comparison of pressure distributions between experiment and theory at $\alpha = 6.75^\circ$. $\Lambda = 0^\circ$.

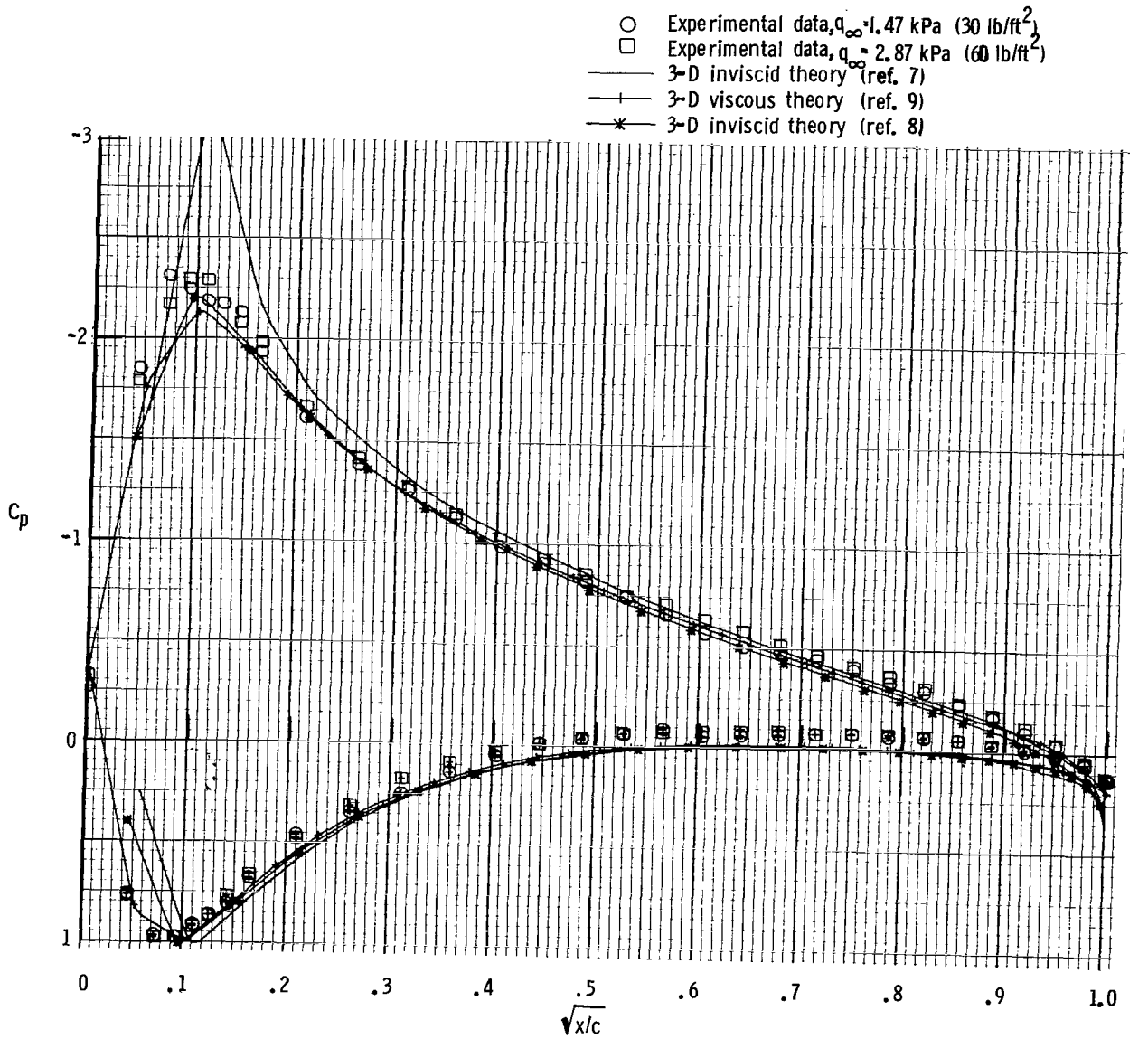

(b) η = 0.20.

Figure 15.- Continued.

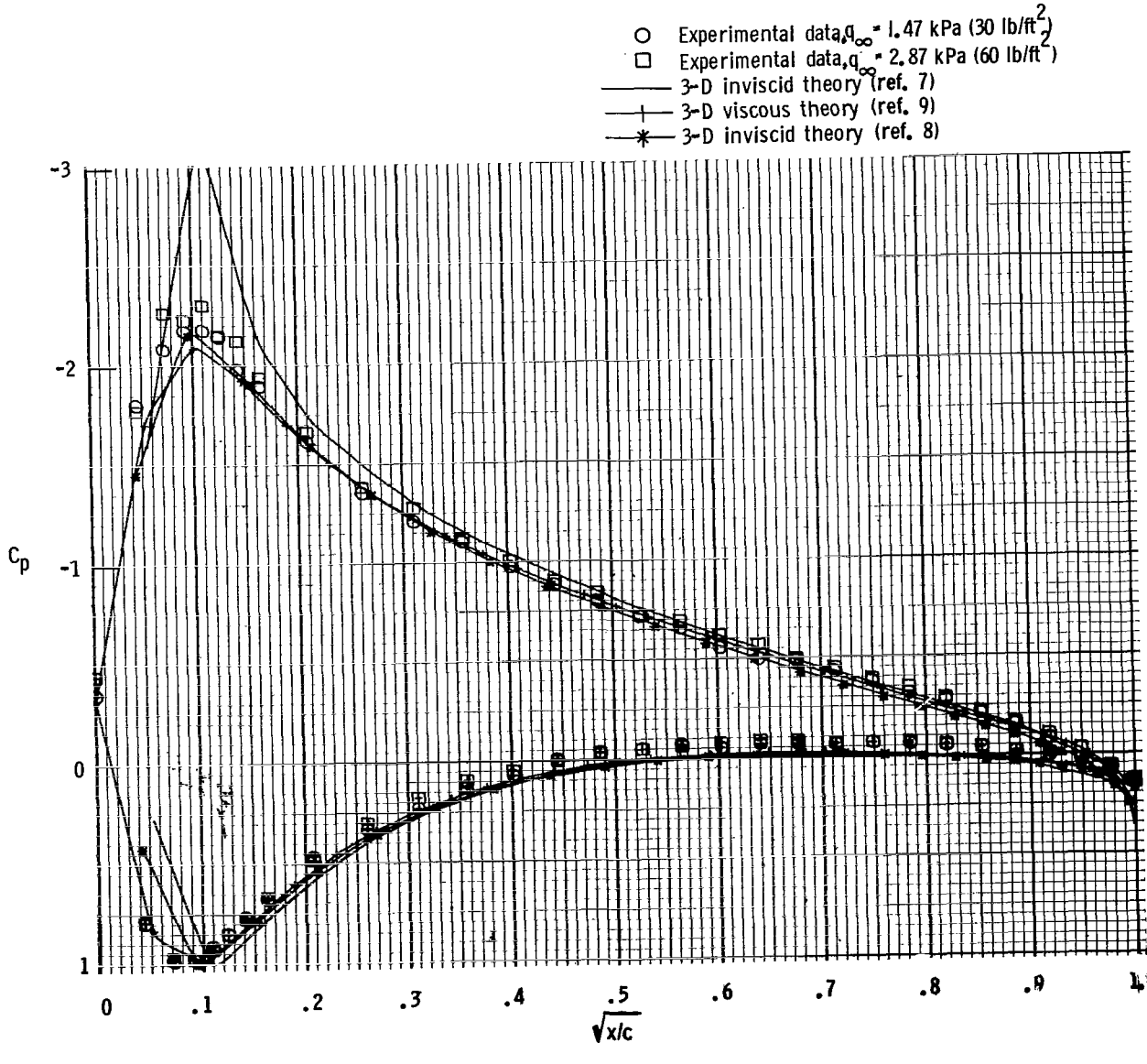

(c) η = 0.34.

Figure 15.- Continued.

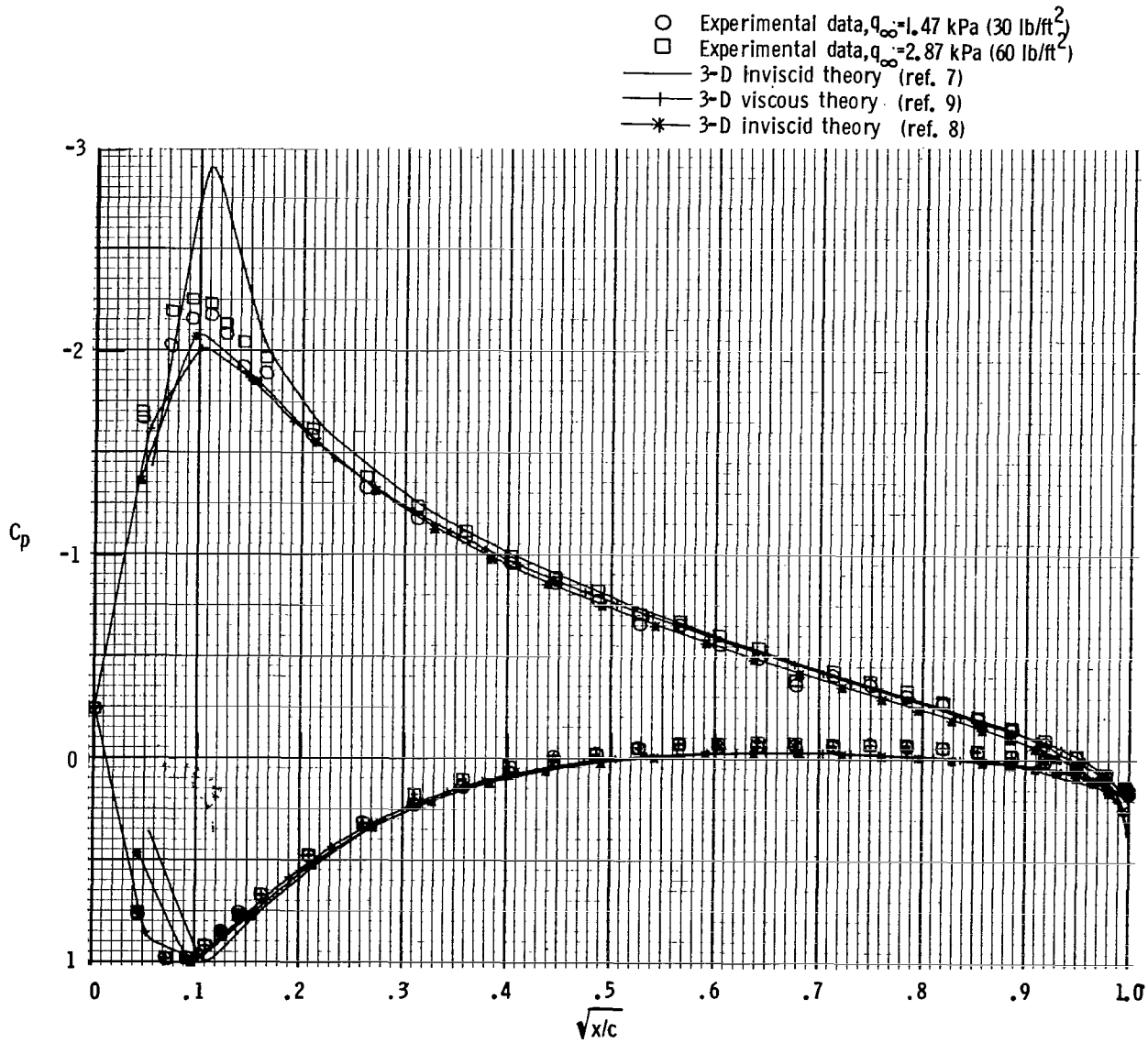

(d) η = 0.48.

Figure 15.- Continued.

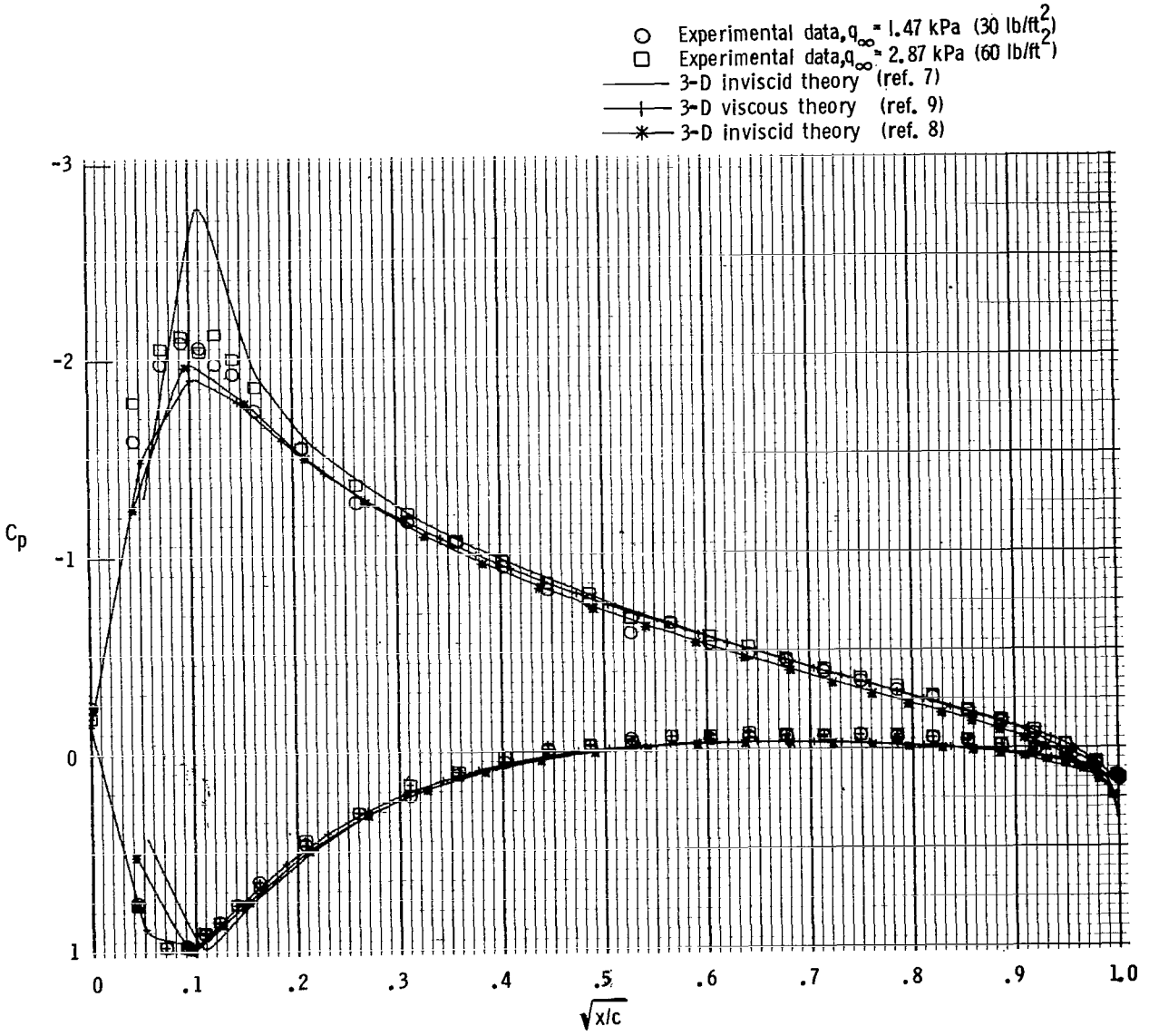

(e) $\eta = 0.61$.

Figure 15.- Continued.

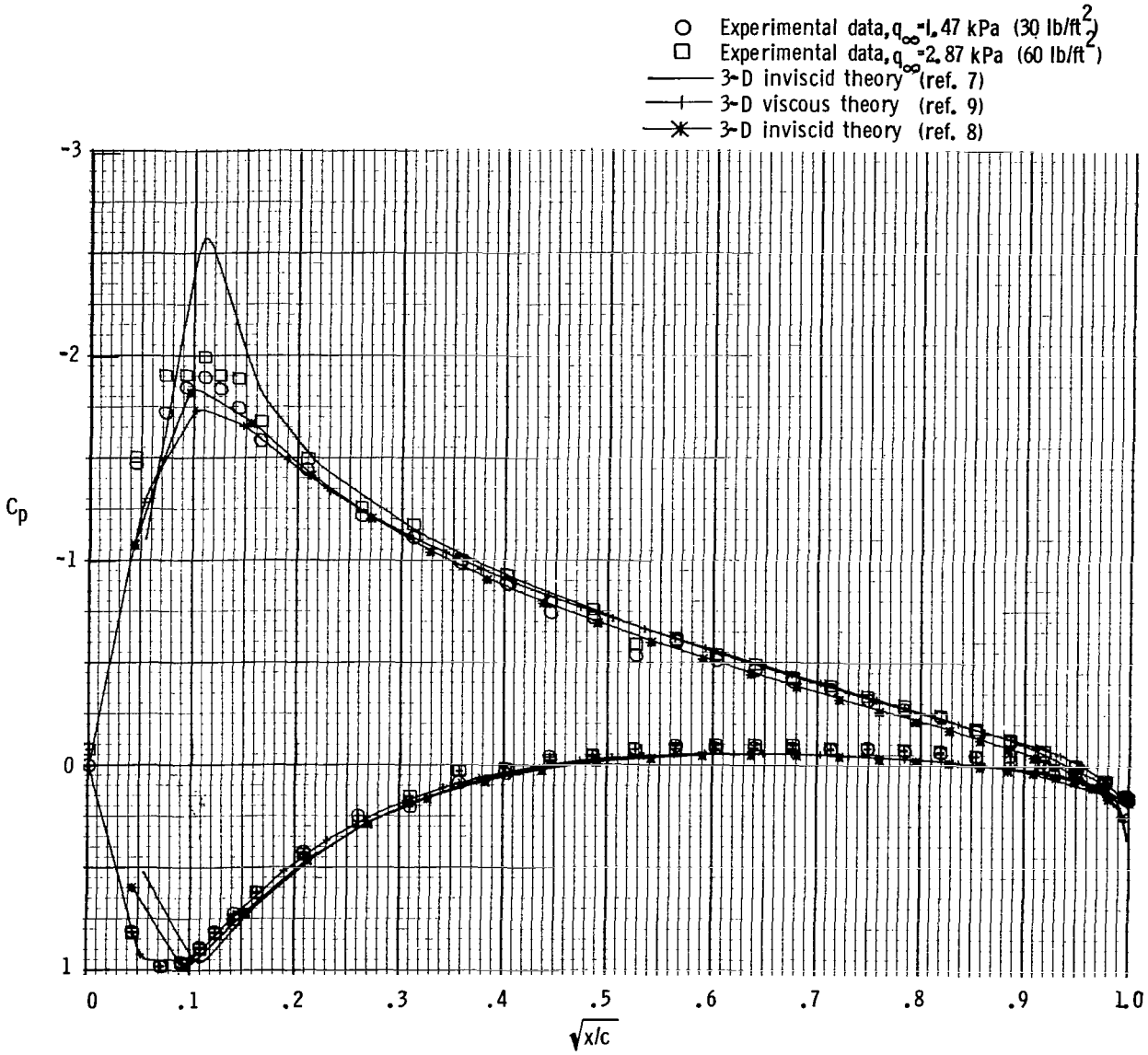

(f) η = 0.72.

Figure 15.- Continued.

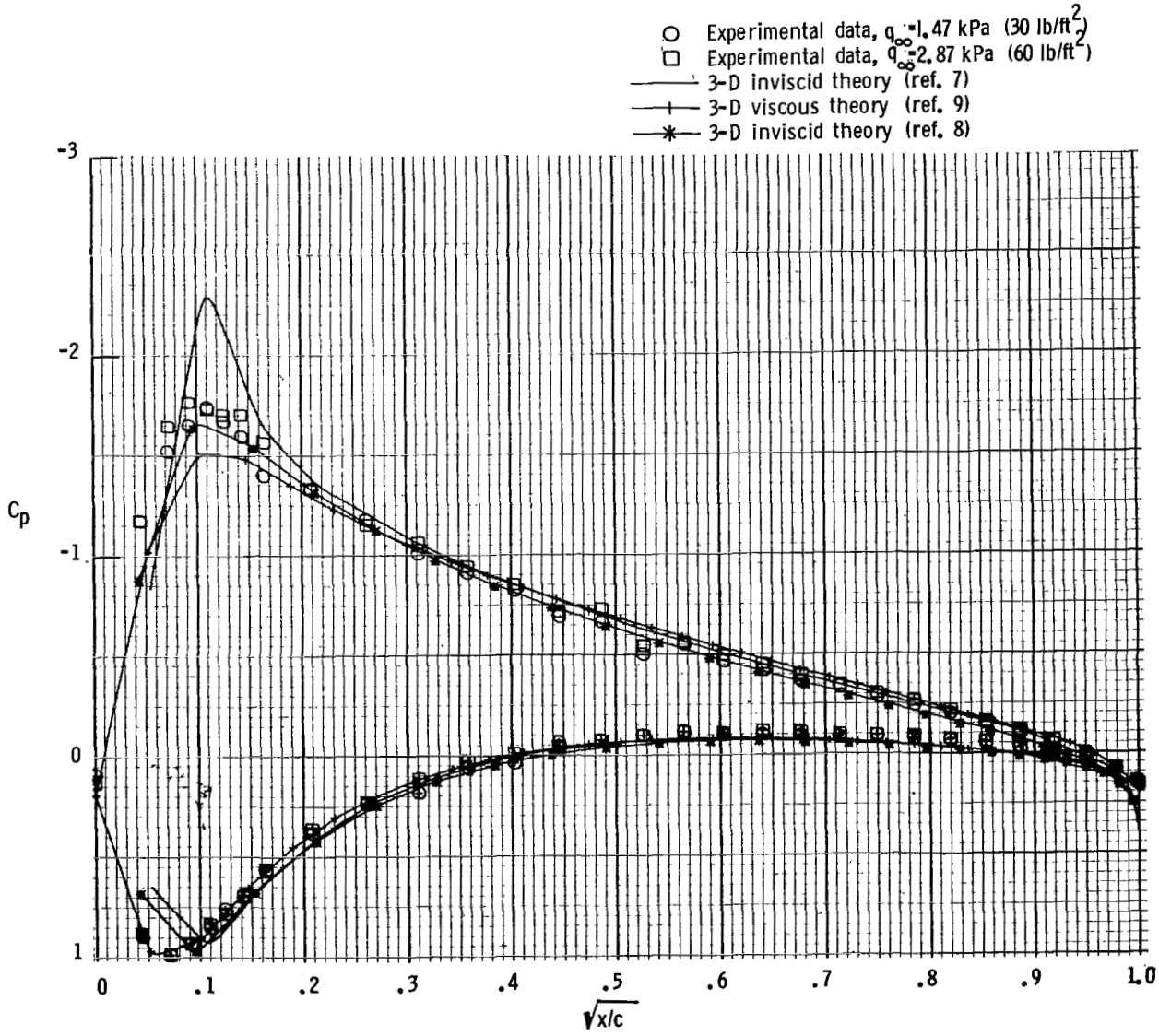

(g) η = 0.82.

Figure 15.- Continued.

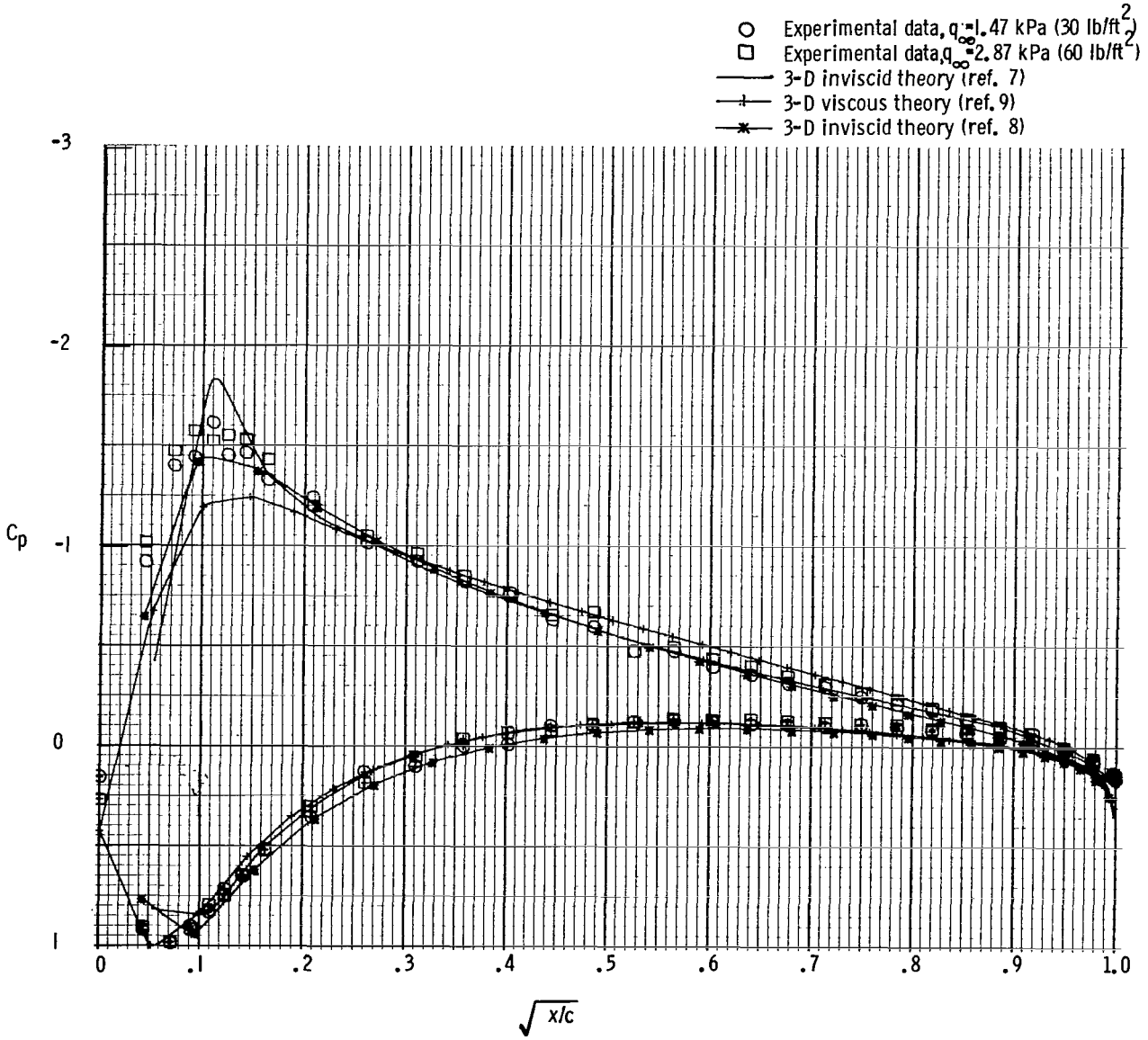

(h) η = 0.90.

Figure 15.- Continued.

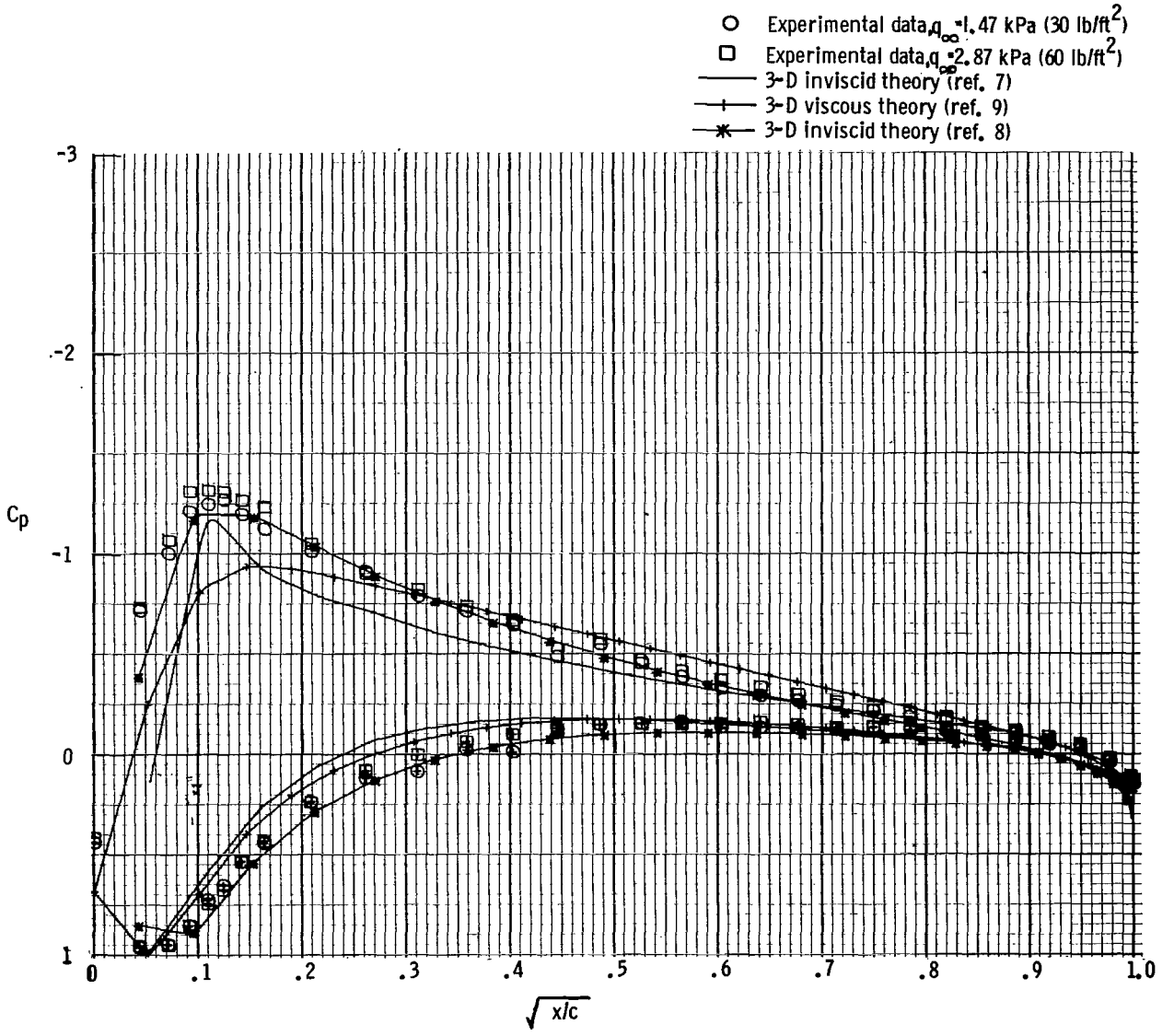

(i) η = 0.95.

Figure 15.- Continued.

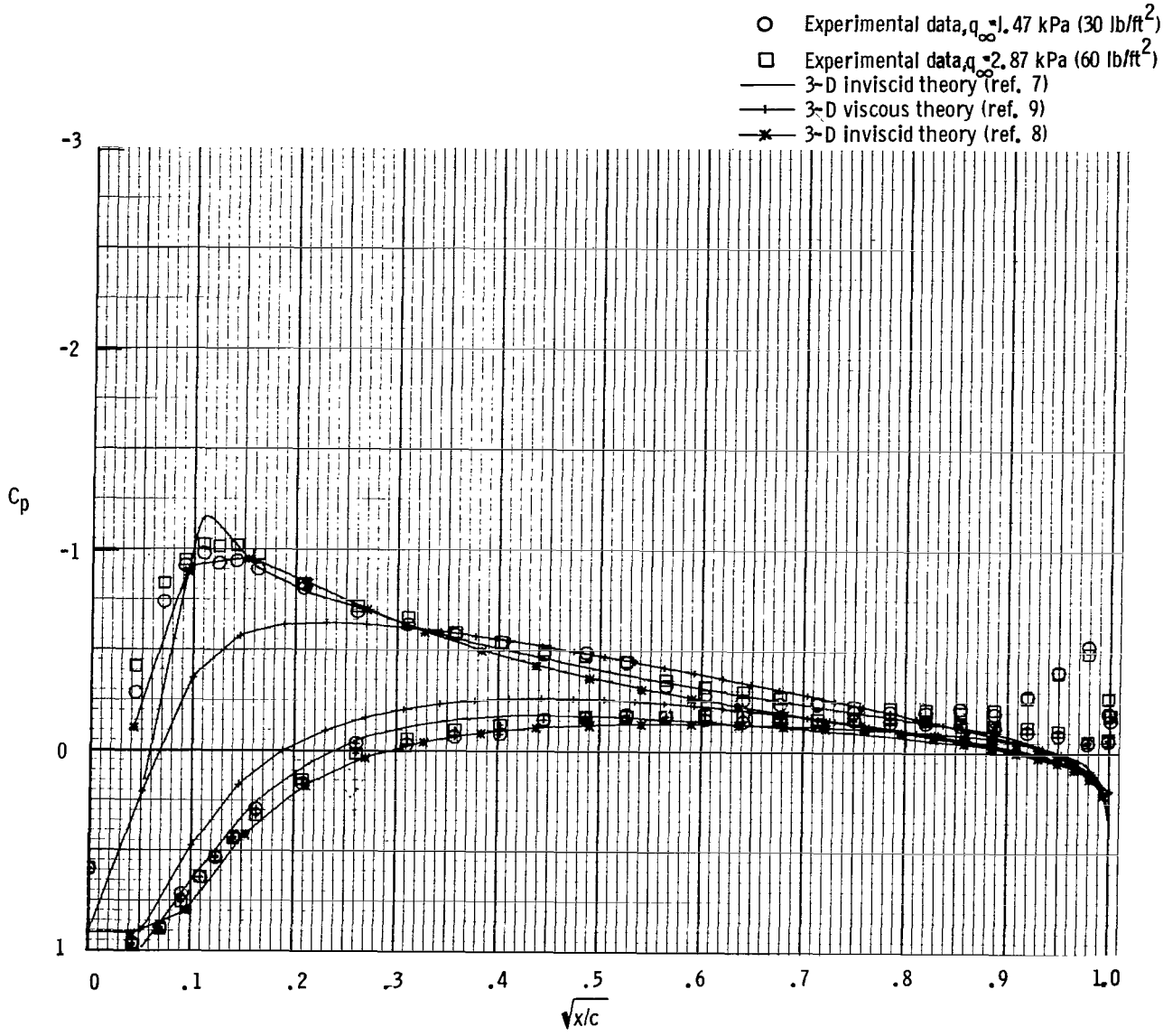

(j) η = 0.99.

Figure 15.- Concluded.

NASA-Langley, 1976 L-10969

"The aeronautical and space activities of the United States shall be conducted so as to contribute . . . to the expansion of human knowledge of phenomena in the atmosphere and space. The Administration shall provide for the widest practicable and appropriate dissemination of information concerning its activities and the results thereof."

—NATIONAL AERONAUTICS AND SPACE ACT OF 1958

NASA SCIENTIFIC AND TECHNICAL PUBLICATIONS

TECHNICAL REPORTS: Scientific and technical information considered important, complete, and a lasting contribution to existing knowledge.

TECHNICAL NOTES: Information less broad in scope but nevertheless of importance as a contribution to existing knowledge.

TECHNICAL MEMORANDUMS: Information receiving limited distribution because of preliminary data, security classification, or other reasons. Also includes conference proceedings with either limited or unlimited distribution.

CONTRACTOR REPORTS: Scientific and technical information generated under a NASA contract or grant and considered an important contribution to existing knowledge.

TECHNICAL TRANSLATIONS: Information published in a foreign language considered to merit NASA distribution in English.

SPECIAL PUBLICATIONS: Information derived from or of value to NASA activities. Publications include final reports of major projects, monographs, data compilations, handbooks, sourcebooks, and special bibliographies.

TECHNOLOGY UTILIZATION PUBLICATIONS: Information on technology used by NASA that may be of particular interest in commercial and other non-aerospace applications. Publications include Tech Briefs, Technology Utilization Reports and Technology Surveys.

Details on the availability of these publications may be obtained from:

SCIENTIFIC AND TECHNICAL INFORMATION OFFICE

NATIONAL AERONAUTICS AND SPACE ADMINISTRATION

Washington, D.C. 20546